Numerical-Experimental Analysis of CFRP Specimen under Multi-Directional Thermo-Mechanical Loading

MSc Thesis

Nachiket Dighe

TU Delft

DLR Deutsches Zentrum für Luft- und Raumfahrt

Numerical-Experimental Analysis of CFRP Specimen under Multi-Directional Thermo-Mechanical Loading

January-August, 2025

by

Nachiket Dighe

to obtain the degree of Master of Science at the Delft University of Technology

Student number:	5289793
Daily university supervisor:	Dr. Bilim Atli-Veltin
Main university supervisor:	Prof. Clemens Dransfeld
Company supervisor:	Dr.-Ing. Josef Koord
Faculty:	Aerospace Engineering

Cover Image: Test Specimen Compartment of the Bulge Rig.
Image taken from the 2024 Innovation Report of DLR Institute of Lightweight Systems

TU Delft

DLR Deutsches Zentrum für Luft- und Raumfahrt

Delft University of Technology
Faculty of Aerospace Engineering
Department of Aerospace Structures and Materials

GRADUATION COMMITTEE

Dated: 29-08-2025

Chair holder:

Dr.ing. S.G.P.(Saullo) Castro

Committee members:

Prof. C.A. (Clemens) Dransfeld

Ir. J. (Jos) Sinke

Dr.-Ing. J. (Josef) Koord

Preface

First and foremost, I would like to thank Prof. Christian Hühne for facilitating an excellent thesis opportunity in the department of Composite Design (DLR).

This thesis would not have been possible without the exceptional mentorship of my main DLR supervisor- Dr. Josef Koord. Dr. Koord's ambitious leadership, enriched with clear consistent communication, ensured a efficacious workflow throughout the duration of the thesis. I would also like to thank my TU Delft supervisors- Prof. Clemens Dransfeld and Dr. Bilim Atli-Veltin- for their trust, encouragement and guidance.

I am deeply grateful to Patrick Makiela (DLR), for his close engagement with the development of my numerical models. Thanks to Mr. Makiela's experienced feedback, it was possible to rapidly troubleshoot issues in that would have otherwise taken significantly longer to overcome. In addition, Harsh Bordekar (DLR/TU Braunschweig) sharing contextual insights into the research topic. Mr. Bordekar's passionate lens gave me a new perspective on my own work.

Over and above that, a large number of skilled and specialised experimentalists at the DLR enabled the multi-sensor test campaign. The impeccable organisation work from both Roman Beck and Rebekka Hauser ensured that everything ran smoothly in the laboratory. I would like to thank them both for conducting the bulge tests. Mr. Beck and Ms. Hauser also maintained an open and approachable attitude, thus supporting me with their close supervision at the DLR. In addition, the DIC setup and measurements were conducted by Ary Zipfel. Alix Landemaine subsequently prepared the DIC data for further analysis. Yannick Boose, Thomas Gesell and Robert Prussak provided invaluable instruction to correctly integrate the fibre-optic sensors for cryogenic environments. Jens Kosmann supported in extracting T-scan data to verify the positioning of the fibre-optic sensors. Bernd Friederichs performed the ultrasound inspection. CNC milling of the specimen was completed by Dirk Holzhüter. Finally, I am indebted to the exceedingly helpful team of technicians: Niklas Drews, Cordelia Koch, Chrisine K"onig, Mareike Stegmaier and Leila Richter. Countless practical tasks could not have been finished without their expertise.

An equally important aspect of life that I cherish is the sense of community in Braunschweig, that was established many fellow students. I would like to take the opportunity to appreciate many of my close friends, who are now spread across the world, for being who are they. Lastly, I am thankful for my loving family. It is my parents especially who have supported me unconditionally, and held the space to let me follow my dreams.

Contents

List of Figures

List of Tables

Nomenclature

Abbreviations

Abbreviation	Definition
AE	Acoustic Emissions
ALLAE	ALL Artificial Energy
ALLCCSD	ALL Contact constraint Stabilisation Dissipation
ALLSE	ALL Strain Energy
ASM	Multi-purpose leak detector from Pfeiffer Vacuum
BK	Benzeggagh-Kenane
CAD	Computer Aided Design
CDM	Continuum Damage Modelling
C3D8R	Continuum 3D-stress 8-node Reduced-integration
C3D8	Continuum 3D-stress 8-node Full-integration
C3D20R	Continuum 3D-stress 20-node Reduced-integration
CFRP	Carbon Fibre Reinforced Polymer
CLT	Classical Laminate Theory
CNC	Computer Numeric Control
COD	Crack Opening Displacement
CPU	Central Processing Unit
CT	Cryogenic Temperature (< -150 [°C])
CTE	Coefficient of Thermal Expansion
CZM	Cohesive Zone Modelling
DCB	Double-Cantilevered Beam
DIC	Digital Image Correlation
DLR	Deutsches Zentrum für Luft- und Raumfahrt
ENF	End-Notched Flexure
ESL	Equivalent Single Layer
FDST	First-Order Shear Deformation Theory
FEM	Finite Element Method
FOSS	Fibre-Optic Strain Sensor
HBK	Hottinger Brüel & Kjær
He	Helium
JAXA	Japan Aerospace Exploration Agency
LH_2	Liquid Hydrogen
LN_2	Liquid Nitrogen
LW	Layer-Wise
MMB	Mixed-Mode Bending
NASA	National Aeronautics and Space Administration
QDC	Quadratic Delamination Criterion
RT	Room Temperature (20 [°C])
SC8R	Shell Continuum 8-node Reduced-integration
UMAT	User-defined MATerial model for Abaqus/Standard
USA	United States of America
VCCT	Virtual Crack Closure Technique
WWFE	World-Wide Failure Exercise
XFEM	Extended Finite Element Method

Symbols

Symbol	Definition	Unit
a_i	Polynomial coefficient	[-]
d	Diameter	[mm]
$d_{nominal}$	Nominal Bolt Diameter	[mm]
l	Lubrication factor	[-]
n_{bolts}	Number of bolts	[-]
r, θ	Principle directions in polar coordinate system	[-]
t	Time	[s]
x, y, z	Principle directions in global cartesian coordinate system	[-]
u, v, w	Displacements in cartesian coordinate system	[mm]
w_{cz}, w_{gz}, w_{sz}	Width of contact zone, gap zone and support zone	[mm]
E	Energy	[J]
E_{ij}	Stiffness	[MPa]
F	Force	[N]
F_{clamp}	Clamping force	[kN]
$F_k(x)$	Near-tip asymptotic function	[-]
G_{ft}, G_{fc}	Intra-laminar fracture toughness fibre tensile, and compression	[N/mm]
G_{mt}, G_{mc}	Intra-laminar fracture toughness matrix tensile, and compression	[N/mm]
G_s	Intra-laminar fracture toughness in shear	[N/mm]
$G_{IC}, G_{IIC}, G_{IIIC}$	Inter-laminar fracture toughness in modes I, II, III	[N/mm]
G_C	Critical energy release rate	[N/mm]
G_T	Total energy release rate	[N/mm]
K_{bolt}	Bolt factor	[-]
K_{nn}, K_{ss}, K_{tt}	Contact stiffness in normal, shear and transverse direction	[MPa]
P_p, P_v	Pressure on supply side, and gas analysis side	[Pa]
Q_L	Leakage Rate	[mbar l/s]
T	Temperature	[° C, K]
W	Weight	[N]
α	Coefficient of thermal expansion	[/K]
$\delta_n, \delta_s, \delta_t$	Tractions in normal, shear and transverse direction	[mm]
ϵ	Strain	[-]
$\epsilon_{11}, \epsilon_{22}$	Strain in local coordinate system (lamina)	[-]
$\epsilon_{xx}, \epsilon_{yy}$	Strain in global coordinate system (laminate)	[-]
η	Benzeggah-Kenane exponent	[-]
η_{vr}	Viscosity coefficient	[s]
κ	Strain-gauge factor	[-]
μ_d, μ_s	Dynamic, static friction coefficient	[-]
ν_{ij}	Poisson ratio	[-]

Summary

The aviation industry is a significant contributor to environmental challenges, accounting for around 2% of global carbon dioxide emissions and up to 4% of global warming. To align with the European Union's ambitious Green Deal and achieve climate neutrality by 2050, substantial advancements in sustainable aviation technologies are imperative. Liquid hydrogen has emerged as a promising alternative fuel, offering high gravimetric energy density. However, its low volumetric energy density necessitates the development of large, lightweight cryogenic fuel tanks.

Carbon-Fibre Reinforced Polymer (CFRP) is widely regarded as the state-of-the-art material for such tanks due to its exceptional stiffness-to-weight ratio. Nonetheless, CFRP faces critical challenges, including hydrogen leakage and permeation. The leakage of hydrogen molecules through tank walls poses significant safety risks, particularly in linerless composite designs. Addressing these technical challenges is crucial for the safe and effective integration of liquid hydrogen in sustainable aviation.

The German Aerospace Centre (DLR) is at the forefront of tackling these challenges, with its Institute of Lightweight Systems developing state-of-the-art test setups to facilitate the development of hydrogen fuel tanks. Among these experimental facilities is the bulge test rig, that performs element-level tests representative of the spherical end-cap structure of a hydrogen tank. The specimen is clamped and sealed using indium, and submerged into a cryogenic bath of LN_2. One side of the specimen is pressurised using helium. On the gas analysis side, a turbo-molecular pump creates a high vacuum to enable the quantification of helium leakage rate by mass spectrometry. Overall, the bulge element testing is a complex procedure. The effects of various boundary conditions on test results, especially clamping and cryogenic cooling, are not yet precisely understood. Purely experimental investigations have blind-spots that can be overcome through insights from numerical modelling.

Therefore, the goal of this thesis is to simulate, verify and validate a digital model of the bulge element. The digital model can then be used for parametric design studies or for the design of experiments. The model simulates the bulge test as accurately as possible. The multi-axial thermo-mechanical stress state is reflected through the choice of boundary conditions. In addition, the model captures the interaction of the test specimen with the test setup. This sheds insights into slippage of the specimen (if any). Furthermore, the model aids localising damage, by incorporating the intra and inter-laminar damage initiation using the LARC05 and Quadratic Delamination Criteria (QDC). Ideally, no damage should occur near the clamping region, as that may lead to an undesired, premature failure of the bulge test specimen.

A range of bulge tests are subsequently conducted at the DLR. Different specimen configurations are tested to understand the influence of curvature, reinforcement and temperature. Concurrently, strain data is acquired extensively for each test. Multiple sensor systems- namely digital image correlation, fibre-optic strain sensors, and strain gauges- are used. The strain sensors show excellent agreement with one another at room temperature. To accurately assess the strains in a cryogenic environment, temperature compensation of sensors is required. In this thesis, the temperature compensation of strain gauges is conducted analytically. However, the signals obtained from fibre optic sensors at cryogenic temperature were considered too noisy for further analysis. Post-mortem damage assessment of bulge specimen were conducted using optical microscopy and ultrasounds. In short, damage was observed in un-reinforced specimen at room temperature.

Subsequently, the experimental measurements were compared with the predictions of the numerical model. Displacement fields from DIC, for example, were used to tune the non-linear contact model. The resulting strains from the tuned model were compared in detailed with the experimentally obtained strains. Doing so quantifies the validity of the numerical model.

Finally, parametric design studies were conducted using the validated numerical model. The effect of slippage, reinforcement design, material and laminate thickness was studied. It is envisioned that the parametric study aids the design of more representative bulge specimen.

1

Introduction

The context of the research topic is introduced in this chapter. The research questions are derived through a funnel down technique. Based on these research questions, a road-map for the remainder of the thesis is established.

Contents

1.1. Role of liquid hydrogen in sustainable aviation

Aviation contributes to 2% of the carbon-dioxide emissions and up to 4% of global warming [15]. Sweeping developments are required in sustainable aviation to attain climate-neutrality by 2050, the heart of the European Union's Green Deal [54].

The development of alternative propulsion systems is crucial in reducing the carbon-footprint of air travel. While electric batteries are gaining popularity in industries like automotive, their low energy density hinders their use for long-haul flights. Hydrogen solves the issue of a low-gravimetric energy density. Its low-volumetric energy density is partially improved by cryogenically storing it in liquid state, instead of a gas at high pressure.

Key players in the aviation industry, such as Airbus, DLR, H2FLY, and ZeroAvia, have recognised the potential of LH_2 and are investing heavily in its development. Airbus, for example, is working on hydrogen-powered aircraft under its ZeroE initiative, which aims to create a hydrogen-powered commercial airliner by 2040. Likewise, H2FLY, based in Germany, has already conducted successful test flights using hydrogen fuel cells, demonstrating the feasibility of LH_2 for regional aircraft.

(a) Airbus's ZeroE Project [4]

(b) DLR EXACT's fleet [20]

(c) H2Fly's HY4 Project [25]

(d) MTU Aero Engines participates in EU-wide HEROPS program [55]

Figure 1.1: Examples of companies developing hydrogen systems to promote sustainable aviation in the EU

1.2. Large, Lightweight Cryogenic Fuel Tanks

The low-volumetric energy density of hydrogen even in its liquid state demands large, cryogenically compatible fuel tanks.

For optimal thermal insulation, cryogenic fuel tanks encompass a 'thermos-flask' concept (Figure 1.2. It comprises of an inner and outer tank wall, separated by an insulating layer of vacuum. Multi-layer insulation further reduces heat exchange.

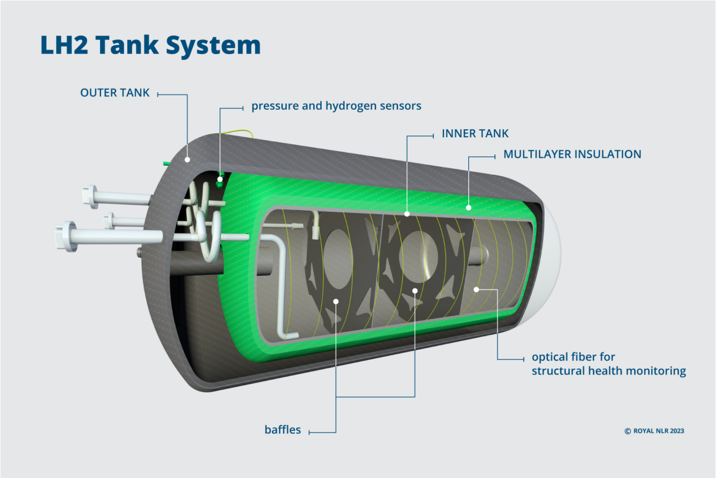

Figure 1.2: Illustration of the cryo-compressed, double-walled hydrogen fuel tank concept [57]

In addition, LH_2 fuel tanks need to be as lightweight as possible. Stainless steel, despite its high resistance to hydrogen embrittlement [66], has to be ruled out. Aluminum is an appropriate choice for lightweight design. With that said, the state-of-the-art tank construction comprises of CFRP without a liner. CFRP has an excellent strength and stiffness-to-weight ratio, offering up to a third of weight savings compared to an aluminum tank [84].

1.3. Safety concerns with the loss of hydrogen from fuel tanks

Unfortunately, state-of-the-art linerless CFRP LH_2 tanks are susceptible to fuel losses. This can be catastrophic in the context of a commercial aircraft. Firstly, only 4% GH_2 in an air mixture is considered to be flammable, as it violently combusts with atmospheric oxygen [58]. Moreover, a loss of LH_2 in the fuel tank may increase the boil-off rate and unexpectedly raise the tank's pressure. This increases the risk of a tank burst.

In fact, the catastrophic failure of the X-33 tank by Lockheed Martin in 1999 revealed the detrimental impact of hydrogen fuel loss. A leak was detected through the inner tank wall. The forensics of this accident prompted research interest in understanding cryo-pumping phenomena, an important safety aspect that was not previously considered during tank design. [60]

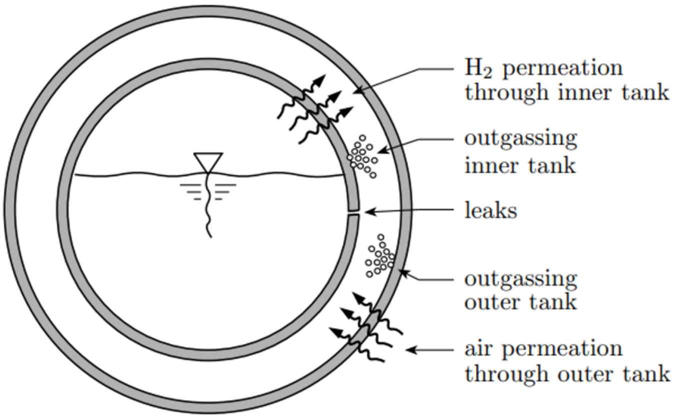

Figure 1.3: Schematic of permeation and leakage in double-walled 'thermos-flask' concept of a LH_2 tank [72]

Two distinct hydrogen transport phenomena are responsible for fuel loss: permeation and leakage. Figure 1.4 visualises the differences between permeation and leakage.

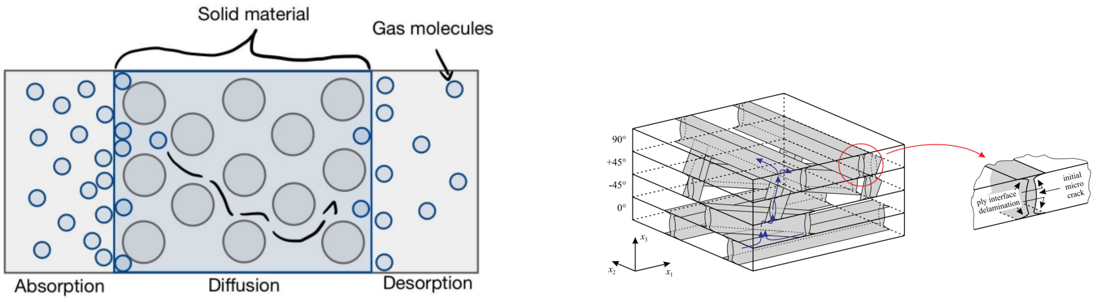

(a) Permeation: Diffusion driven transport in a solid [46]

(b) Leakage: gas transport through defects, such as a microcrack network [33]

Figure 1.4: Hydrogen transport mechanisms through a thin CFRP tank wall

1.3.1. Permeation

Permeation is defined as the diffusion driven mass transport in a solid medium. In the context of a hydrogen tank, a concentration gradient is setup between the inner tank wall and the insulating vacuum layer between the double layered tank wall. Adsorption, diffusion and desorption govern permeation. [16], [72] As the focus of this thesis is on leakage, permeation shall not be discussed further. The reader is referenced to Fahjen [16] and Schultheiß [72] for an in-depth account of permeation.

1.3.2. Leakage

Leakage is a passage of gas molecules along a matrix crack and/or delamination network that runs through the thickness of the laminate. Such a damage state arises due to thermo-mechanical stress. It may initiate during autoclave manufacture, whereby the cure temperature is typically raised to 180 [°C]. Gaps, voids, and other defects may form that could be enlarged during demoulding. The cyclic thermal loading from room temperature to cryogenic temperature (-253 [°C]), on top of pressurisation load, leads to the growth of the micro-crack network. [90]

1.4. Building Block Approach

A building block approach (Figure 1.5) is necessary for the safe structural development of LH_2 aircraft fuel tanks. While it is of utmost importance to reduce permeation/leakage, these phenomena must be thoroughly understood on increasing levels of structural complexity.

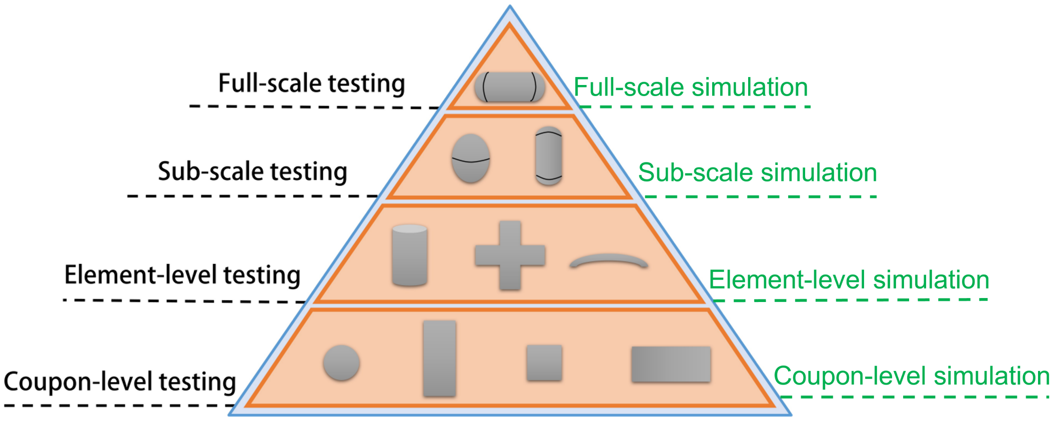

Figure 1.5: Building block approach for development of a composite LH_2 tank. Adapted from [46]

Coupon level tests aim to provide material characterisation; corresponding simulations help in verifying the modelling strategy. An emphasis is placed on creating a database for cryogenic temperature. Permeation tests on flat, pristine specimen help obtain solubility, diffusivity and permeability coefficients at room and cryogenic temperature [16], [67]. Leakage is expected when the laminate is damaged, say after repeated cryo-cycling [26]. Cryogenic environment can be achieved by submersion cooling (77 [K] using LN_2, 20 [K] using LH_2, 4 [K] using LHe). Alternatively, special cryostats [30], [72] may be used. At the coupon level, mechanical (tensile) tests can be performed after thermal (cryogenic exposure) loading. [30]

It is clear that coupon tests cannot capture the bi-axial stress state representative of the tank. Element level testing is necessary for more representative results, without increasing the costs too much. To overcome this, JAXA [26] has developed the cruciform element that can be pulled in two directions simultaneously. The limitation of the cruciform element is that it is flat. Tank curvature is not accounted. The cylindrical part of the tank can be mimicked using tubular specimen [88]. The double-curved geometry of the spherical part of the tank is represented by bulge elements [14], [28], [61]. The ability of the bulge rig to test curved specimen, with simultaneous thermo-mechanical loading, renders it a highly representative element-level test (further explained in section 1.5).

Sub-scale and full-scale tank testing are required to certify tanks for aerospace applications. There are several examples of sub-scale and full-scale testing conducted on linerless CFFRP tanks for space applications. For instance, ESA funded Phoebus project between MT Aerospace and Ariane Group measured leakage/permeation on a sub-scale prototype of upper stage liquid oxidiser tank [87]. Finally, it is worth re-mentioning the (failed) test campaign of the full-scale X-33 tank [60].

Alas, it is clear that sub/full-scale testing is prohibitive. Sub/full-scale testing require the development of large, complicated and costly test fixtures. In addition, an entire tank may be destroyed in a single test. This means that sub/full-scale testing is costly, and are often reversed for validating a final structural design. However, to aid the development process itself, representative element-level testing needed. Such element-level tests should be representative, thus mimicking not only the geometry but also the stress state of a tank structure. Further given the stricter requirement of allowable leakage for aircraft tanks [67], it is necessary to thoroughly charactertise leakage at element-level to obtain the necessary scientific insights to design safe, linerless CFRP tanks.

1.5. State-of-the-art element level testing

There are several types of element level test setups, such as the cruciform, small cylinder and bulge. Lentner [46] compares these test methods in detail. This thesis will solely focus on the bulge test, as that is the rig available at the DLR. The working principle of the bulge test rig is illustrated in Figure 1.6a. A representative (curved) shell of the tank's dome is clamped. One side of the specimen is supplied with helium. Specifically, up to 20 $[\text{bar}]$ of helium pressure can be applied to simulate the mechanical load experienced by the tank. Simultaneously, the thermal load is generated by immersing the entire setup in a cryogenic dewar of LN$_2$. As a result, a thermo-mechanical stress state can be created on the bulge specimen.

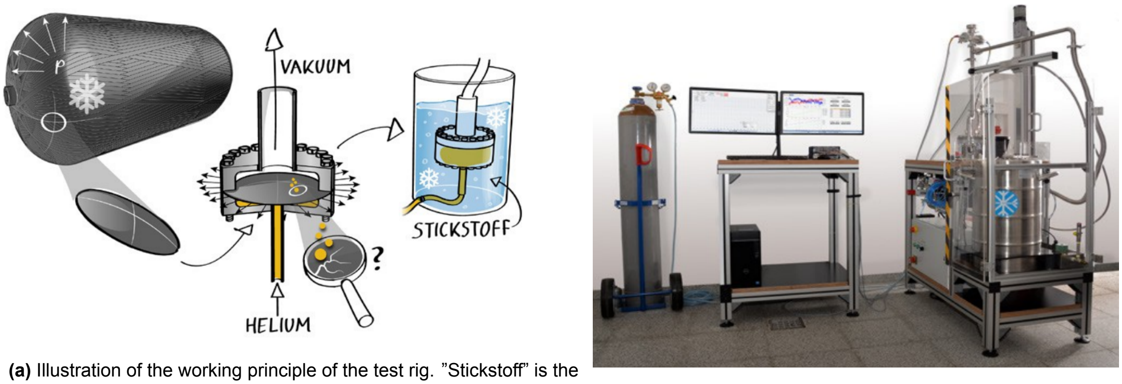

(a) Illustration of the working principle of the test rig. "Stickstoff" is the German word for nitrogen.

(b) Photograph of the physical test rig

Figure 1.6: State-of-the-art bulge test setup at the DLR [85]

It is possible that the thermo-mechanical stress state of the specimen leads to crack network. Leakage is a likely consequence of an extensive crack network. The leak rate of the tracer helium gas can be quantified precisely. This is done by connecting one side of the specimen to a leak detector, as shown in Figure 1.7. The leak-rate or the integral chamber method is illustrated in Figure 1.7a. The specimen is clamped, and pressurised with a tracer gas on one side (PRE). Vacuum (VAC) is applied on the other side. The leak-detector is connected on the VAC side.

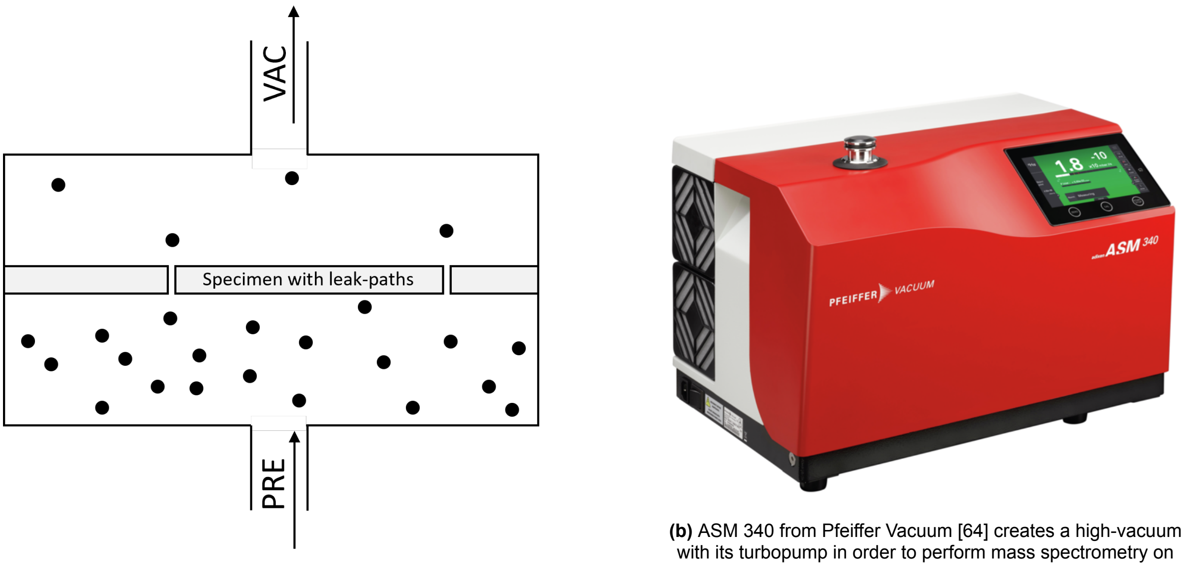

(a) Illustration of the integral chamber/leak-rate method

(b) ASM 340 from Pfeiffer Vacuum [64] creates a high-vacuum with its turbopump in order to perform mass spectrometry on helium gas

Figure 1.7: State-of-the-art leak-detector method used to precisely measure tracer gas leakage rate

Other methods of measuring leakage include monitoring the change in volume (volumetric) or pressure (manometric) on the gas analysis side of the specimen. However, these measurement techniques are not as accurate as the leak-rate method [90], [46]. This is because calibration is needed to compute the leak-rate and one must carefully check that leakage is in fact caused by the tracer gas (eg: not due to a leak in setup that causes ambient air to rush in). Therefore, they are not used in the bulge test setup, and shall not be mentioned elsewhere in this thesis.

1.6. Digital model of the bulge test

At the start of this thesis, the physical bulge setup was operationally in-service. Hauser [28] had conducted preliminary bulge tests as well. Concurrently, Lentner's [46] numerical analyses shed light into influence the key design parameters on the performance of the bulge specimen.

To continue deepening one's understanding of this novel test bench, further numerical-experimental analyses are required. A digital model, incorporating both numerical and experimental data, is therefore envisioned as the primary scope of this thesis. Figure 1.8 illustrates the interaction of the existing physical model with the planned digital model. In the context of this thesis, the digital model is a physics-based, finite element representation of the bulge test in Abaqus. Any automated exchange of (real-time) digital/experimental data, by means of any (cloud-based) software architecture, is beyond the scope of the thesis.

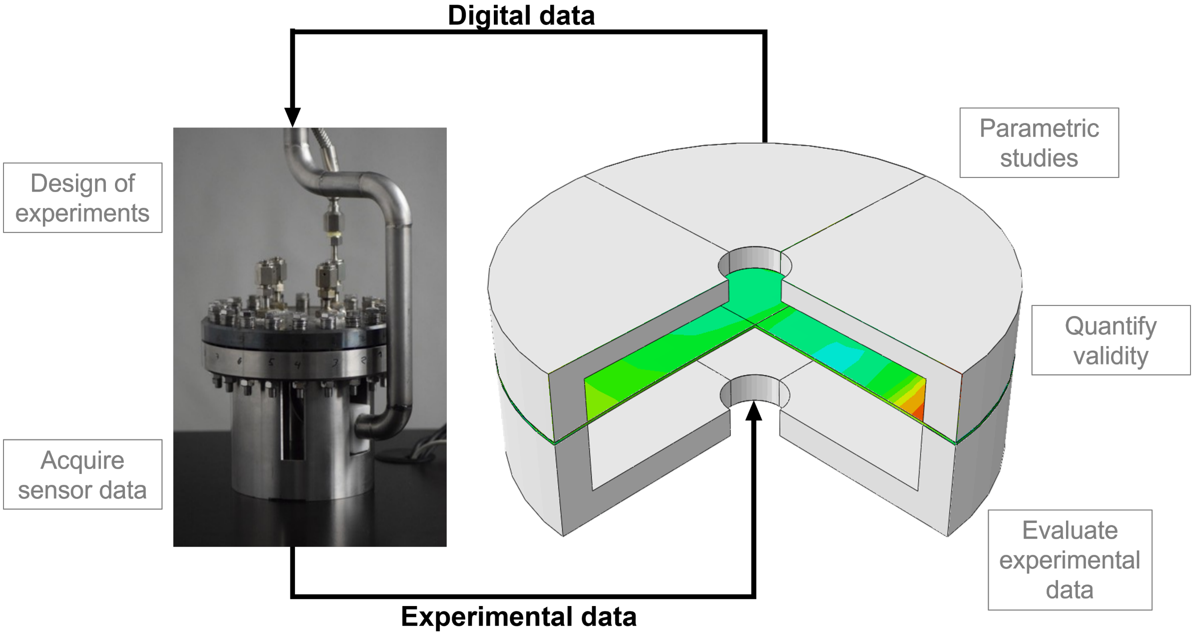

Figure 1.8: Digital model concept

Figure 1.8 illustrates the overall workflow adopted in this thesis. Based on an initial design of experiments, a preliminary digital model is developed. Bulge tests are conducted in parallel to acquire sensor data. The experimentally acquired data is processed and subsequently compared with the corresponding predictions of the digital model. These numerical–experimental comparisons serve two principal purposes: to calibrate and validate the digital model, and to examine the influence of the test variables within a combined modelling–experimental framework. Following validation, the digital model is employed to conduct parametric studies, thereby enabling the investigation of variables that were not directly tested yet. The outcomes of these studies are anticipated to inform and refine the design of subsequent experiments.

1.7. Research questions

The central theme of this thesis is the development of a digital model. With that in mind, the main research question is phrased as follows:

How to simulate and validate an accurate, digital representation of the element-level bulge test?

Several sub-research questions need to be posed to realise the digital model concept. These are categorised into three groups. The first group of sub-questions concerns the numerical methodology. The second group outlines the experimental methodology. The third group of questions encompasses experimental, experimental-numerical and numerical analyses.

1) ***How to implement a finite-element model, using existing numerical methods, to mimic the bulge test?***
    - a: *What numerical boundary conditions accurately represent the physical bulge specimen, that is clamped inside the test setup?*
    - b: *What loading sequence can create the thermo-mechanical stress state of the bulge specimen?*

   c: *What modelling choices or improvements increase the computational efficiency of the digital model?*

2) *What experimental data can be acquired through bulge testing?*

   a: *What parameters should be constrained and varied to derive a test matrix?*

   b: *What sensor system(s) should be used to measure the strain field of the specimen?*

   c: *What inspection technique(s) should be employed to assess damage in the specimen?*

3) *How should numerical–experimental results be analysed?*

   a: *How can experimental data be processed before further analysis?*

   b: *How can experimental measurements quantify the validity of the digital model?*

   c: *What conclusions can numerical–experimental analyses provide on the influence of the variables of the test matrix?*

   d: *How can simulation-driven parametric studies contribute to a more representative design of experiments?*

1.8. Report outline

The report outline is visualised in Figure 1.9, depicting the inter-dependencies of the chapters. The research questions (RQs) addressed in each chapter are also stated.

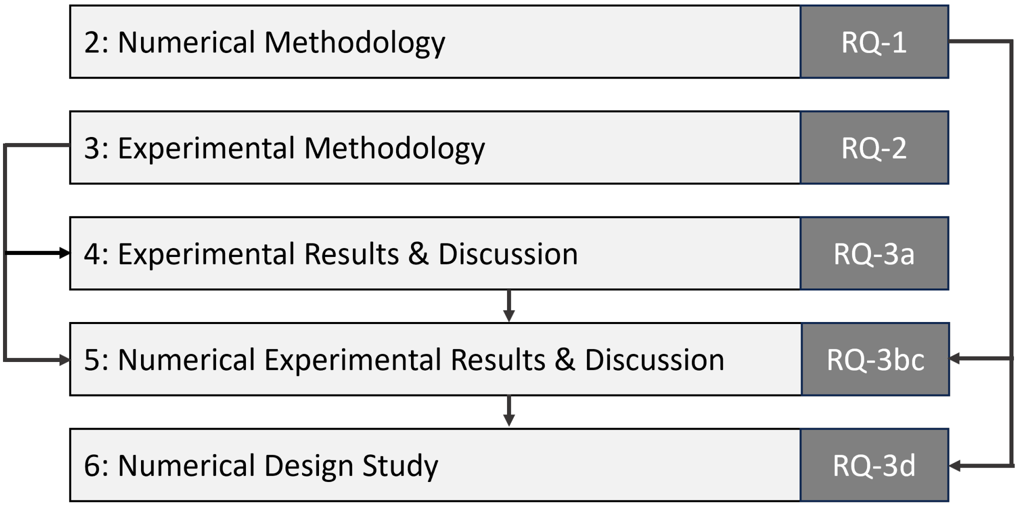

Figure 1.9: Outline of the report

The numerical methodology is outlined in chapter 2. The modelling priorities are identified. These priorities are determined from the state-of-the-art numerical [46] and experimental [28] research carried out on the bulge test setup at the DLR. The modelling strategy of both the CFRP test specimen and the bulge test setup is explained in detail.

Chapter 3 presents the methodology driving the bulge test campaign. The focus of this experimental campaign was to extensively acquire sensor data, to compare with the results of the digital model. A preliminary understanding of the digital model is essential to determine the breadth and depth of data collection. Therefore, the thesis follows an unconventional structure, with the experimental methodology being presented after the numerical one. Specifically in chapter 3, the test matrix, sensor selection & positioning, and damage inspection techniques are established.

Subsequently, the acquired raw data of the bulge test campaign is presented in chapter 4. Due to the volume of data being collected, it was necessary to pre-process, curate and interpret the experimental measurements before proceeding with further analysis. By solely considering the experimental data, it is possible to obtain an overview of the test results. A preliminary qualitative assessment can be made on the influence of the variables of the test matrix.

Detailed numerical and experimental analyses are conducted in chapter 5. Firstly, potential measurement errors in the experimental data are addressed, and to some extent, corrected. The results of room temperature tests are then used to tune the uncertain parameters of the numerical model. Following on, the strain fields of the experiments are compared with the ones of the numerical model to quantify the validity of the latter. Simultaneous consideration of experimental measurements and numerical predictions lead to the quantification of the influence of test specimen configuration.

Finally, numerical design studies are simulated with the validated digital model in chapter 6. Only a limited number of parameters of interest are varied. The most influential parameters are selected based on the engineering judgment built during preceding stages of this thesis. It is envisioned that some of these numerical results may contribute to an improved, and more representative design of element-level bulge tests.

2

Numerical Methodology

This chapter explains the setup of the digital model in detail. The modelling objectives are identified based on state-of-the-art experimental and numerical observations from previous studies. Guided by these goals, the step-by-step implementation of the model in Abaqus, using the available numerical methods, is described.

Contents

2.1. Objectives of the numerical model

The main scientific objective of the bulge setup's numerical model is to gather a deeper understanding of the boundary conditions imposed by the test setup on the test specimen.

In order to study the boundary conditions of the test setup, the interaction between the test specimen and the test setup should be modelled as realistically as possible. Therefore, it is necessary to not only accurately model the CFRP bulge specimen but also the interacting clamps (see Figure 2.1-2.2). In other words, the boundary conditions of the test specimen are not idealised in this study. Many modelling studies, involving coupon or element level tests, impose homogeneous kinematic boundary conditions (eg: encaster, roller, or a pin support) on the specimen. [13], [34], [41], [49], [82] Doing so circumvents the need to model the test fixtures. This simplification is acceptable if the effect of the test fixture on the specimen is known, or if it can be proven that the effect of the test fixture is negligible. For the bulge test, this remains an open question. Such a research gap shall be addressed in this chapter.

In addition, a major objective of the bulge test rig is characterising leakage in CFRP specimen. For a representative comparison with a tank dome structure, leakage should occur within the equal biaxial strain zone located at the centre of the bulge specimen. Unfortunately, preliminary experiments conducted by Hauser [28] reveal otherwise. Cross-ply and quasi-isotropic laminates tested at cryogenic temperature did not exhibit any leakage, even at the maximum pressure load of 20 [bar]. In principle, an obvious solution appears to increase the pressure load. However, in practice, doing so requires replacing expensive, safety-critical components (such as valves, pipes, and pressure regulators) to allow the test rig to operate to higher pressure loads. Given the practical difficulty in modifying the test setup, an easier solution may be found in modifying the test specimen. Thus, the desired test specimen exhibit leakage, without changing the current operational constraints of the bulge setup. It is known that leakage is caused by micro-crack networks. [24], [26] Cracks propagate as stresses exceed the material strength. In this thesis, the (temperature-dependent) strength of materials is taken on existing databases. Stresses and strains are computed using FEM. This means that numerical predictions of stresses and strains, even without accounting for computationally expensive progressive damage, can potentially be used to build an engineering judgment about whether a specimen is likely to leak before it is tested.

In bulge testing, another challenge in characterising leakage is the onset of premature clamp-induced damage. Early studies of Estrada et al. [14] and Oliver [61] reveal that clamped boundary conditions of the bulge setup result in a local stress concentration. This means that even if the test rig was upgraded to safely operate at higher pressure loads or even if leakage was measured, it is likely to occur in the clamping zone. The clamping zone, comprising of large out-of-plane compressive stresses, does not correctly represent the biaxial strain state of a tank dome. Thus, leakage/damage in this clamping zone renders the bulge test invalid. Drawing an analogy to the tensile testing of CFRP specimen, the ASTM standard [5] states that test data should be excluded from analysis if the test coupon fails inside the gripping area due to a stress concentration and not in the desired gauge section. The described clamp-induced damage was reported by Hauser [28], who tested a cross-ply laminate at room temperature. Hauser's ultrasound C-scans showed delamination near the clamping zone, which likely resulted in premature leakage. As the leakage region was localised outside the region of interest, the leakage measurements from Hauser's tests are not valid. [5]. Moreover, numerical studies from Lentner [46] revealed that the clamping pressure induced large stress concentrations, leading to tensile fibre failure outside the region of interest. Lentner further demonstrated that a reinforcement ring partially reduced the damage induced by the clamps. In this thesis, specimen with and without reinforcement shall be modelled. The model should also be able to provide a statement on the stress concentration due to the clamp.

In summary, state-of-the-art numerical and experimental investigations [28, 46] indicate that improvements are needed in the design of bulge test specimen, particularly to ensure that leakage can be localised within the biaxial strain zone. With this in mind, one objective of the digital model is to support the design process of future bulge test specimens. This central objective is further divided into smaller, more specific objectives. Table 2.1 presents a top-level breakdown of these modelling objectives. Each requirement, together with its rationale and the corresponding modelling choice, is stated explicitly to form the foundation of the numerical methodology developed in the remainder of this chapter.

Table 2.1: An overview of the requirements, rationale and modelling choices of the numerical model

	Requirement	Rationale	Modelling Choice
MODEL-REQ-01	The model shall be computationally efficient.	The model should be able to conduct parametric design studies and accompany test campaigns.	Computationally expensive analyses- namely progressive damage, transient thermal, and plasticity-induced sealing- are omitted.
MODEL-REQ-02	The model shall capture the interaction of the test setup with the test specimen.	The model should be able to help understand how the boundary conditions of the test setup affect test results.	The test setup's clamps are modelled as deformable solids; mechancical contact between the clamps and specimen is modelled; force-controlled loading mimics the clamping pressure.
MODEL-REQ-03	The model shall localise damage.	The model should be able to predict where damage may occur, in order to design specimen that fail in the region of interest. The model should be able to predict the failure load of a specimen, to a priori estimate the maximum pressure load during a test.	Inter and intra laminar damage initiation of the CFRP specimen is modelled; a mesoscale (ply-by-ply) discretisation is selected.
MODEL-REQ-04	The model shall incorporate multi-axial thermo-mechanical loading.	The model should be able to accurately represent the pressure and temperature loads on the specimen.	Temperature dependent material properties are used; a homogeneous cryogenic cooling step is incorporated; continuum/conventional shell mesh elements are never used as they are not appropriate choices for loading dominated in the out-of-plane direction.

Table 2.1 prioritises the need for accurately modelling the linear, elastic response of CFRP bulge specimen under multi-axial thermo-mechanical loading. In other words, computational resources will not be directed into predicting the damage tolerance or leakage performance of the laminate. Conventional conductance leakage models [70], [44], [89] rely on the output from highly computationally intensive progressive damage models (such as hybrid XFEM-SCZM [23], [30]). Such modelling methodology, originally proposed by Grogan [24], requires a priori knowledge of a large number of parameters (eg: crack density, leak conductance, etc) that are costly to determine experimentally.

At least at the time of writing, leakage/progressive damage modelling on the CFRP bulge specimen is not considered a productive use of resources for three main reasons. Firstly, the size of the region of interest is not quantified. The region of interest in element level characterisation is described as one where both in-plane components of true strain are equal (practically speaking within an acceptable tolerance, such as 5%). The size of this biaxial zone can vary, not only for different laminates but also through the thickness of a given laminate. In the case of that the size of the region of interest is not known, it is not possible to precisely determine how much of the specimen should be ”enriched” numerically. ”Enrichment” refers to the meshed regions in FEM that undergo progressive damage. Trivially, it is not computationally efficient (or even feasible) to perform such high fidelity damage modelling on the entire specimen- as most of it does not represent the strain state of the tank structure. Secondly, even if the damage/leakage model is correctly implemented, leakage paths currently only exist near the clamping zone [28] and not inside the biaxial region of interest. This means that the leakage predicted numerically and the leakage measured experimentally will take place at different locations in the CFRP specimen, and due to different load cases (experimentally due to the stiffness jump caused by the specimen leaves the clamping region and numerically due to the pressure/temperature loads). As a result, no direct leakage comparison can be meaningfully established between numerical and experimental results. Thirdly, even the strains predicted by simulation are not validated by experiment. Errors in the linear elastic strain response are expected to carry over (and even amplify) in non-linear material analyses. Therefore, the validation of the strain field is considered as a pre-requisite before starting damage modelling on the bulge specimen.

The numerical model that is conceived in this thesis aims to provide information on the three aforementioned sources of epistemic uncertainty. The validity of the model's strain and damage initiation prediction is quantified by comparing to experimental results in chapter 5. This will help assess the suitability of the model, as a baseline for design studies or further modelling. chapter 4 and 5 shares the insights needed to induce damage in the region of interest, while chapter 6 numerically quantifies the size of this region for various test configurations.

Keeping these modelling objectives in mind, the remainder of this chapter explains the numerical model in detail. section 2.2 introduces the thermo-mechanical loading sequence and the associated boundary conditions. section 2.4 explains the interactions between the test setup and the specimen. section 2.5 focuses on the modelling of the composite specimen. Damage initiation is described in section 2.6.

2.2. Overview of loading steps and boundary conditions

Prior to the setup of the FEM model, a simplified CAD model was derived from the technical drawings of the bulge setup. An isometric cut-view of the bulge compartments is shown in Figure 2.1. The corresponding cross-section is labelled in Figure 2.2.

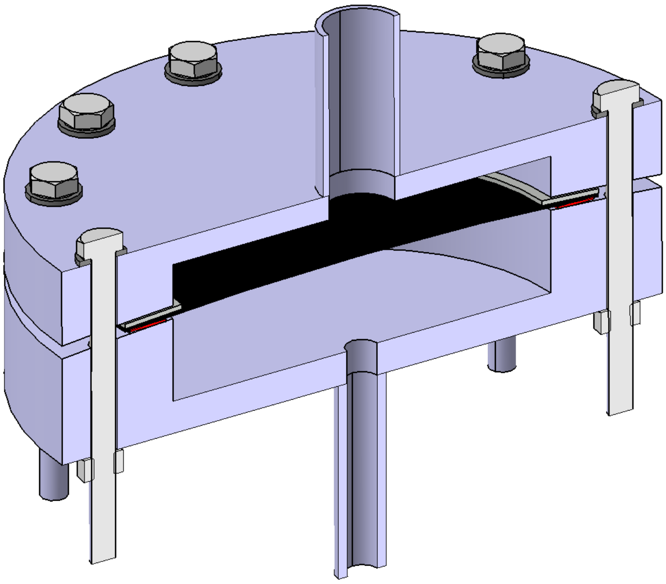

Figure 2.1: Isometric cut-section view of the bulge compartments

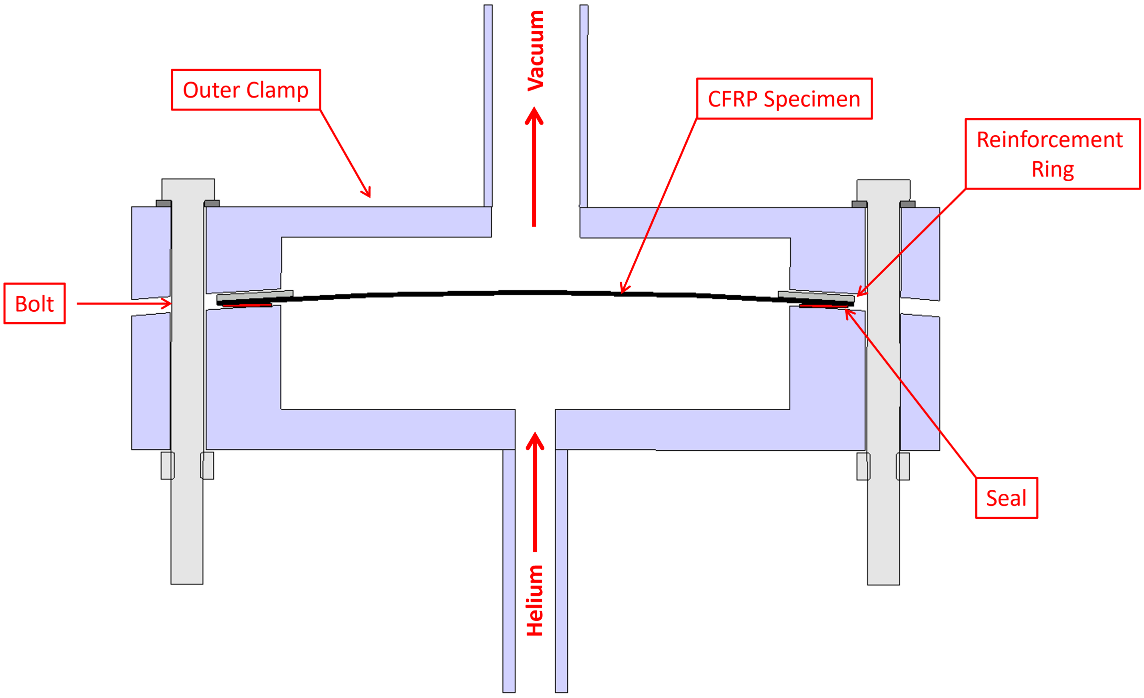

Figure 2.2: Labelled cross-section of the bulge compartments, based on a simplified CAD model

It can be seen from Figure 2.2 that a (double curved) CFRP specimen is clamped between the inner and outer clamp. During the clamping procedure, the bolts are gradually tightened. The clamping pressure generated by the applied bolt torque plastically deforms the indium, thus creating a hermetic seal between the specimen and the setup.

Both compartments are evacuated after clamping. This is because leakage measurements using the leak-detector technique rely on conducting mass spectroscopy on a tracer gas such as helium. Therefore, a vacuum must always be maintained on the gas analysis/outer side of the specimen. At the same time, helium gas is supplied on the inner side of the specimen. Up to 20 $[\mathrm{bar}]$ of gas pressure can be applied to one side of the specimen, to mimic the mechanical loading of a hydrogen tank. The cryogenic environment is reproduced by submerging the entire assembly in a dewar of LN_2 (not shown in Figure 2.2).

The bulge test is modelled in Abaqus using three distinct Static, General loading steps. An additional step is initially used to simulate the cooling down of only the CFRP specimen in the autoclave. Table 2.2 summarises this thermo-mechanical loading sequence, based on the previous numerical studies of Lentner [46].

Table 2.2: Overview of the loading steps

Step	Temperature [K]	Pressure [bar]	Clamping force [kN]
Initial	407 (HT)	0	0
Autoclave cooling	293 (RT)	0	0
Clamping	293 (RT)	0	126 (F_{RT})
Cryogenic cooling	77 (CT)	0	426 (F_{CT})
Pressurisation	77 (CT)	20 (P_{He})	426 (F_{CT})

It should be clarified that the individual bolts and indium sealing, as shown in Figure 2.2, are not modelled. The clamping force created by the bolt torque is analytically estimated, and corrected for thermal effects. The detailed calculation is provided in subsection 2.4.2. In addition, no clear benefit could be identified by modelling the indium seal. As they are known to work well experimentally, it was not deemed necessary to conduct any sealing/pressure over-closure analysis to improve their performance.

Following on, subsection 2.2.1-2.2.5 will describe the boundary conditions used in each step given in Table 2.2.

2.2.1. Initial step

There are two unconnected regions during the initial step. The first region consists of the specimen resting on top of the inner clamp. The second region comprises only of the outer clamp, that is separated from the surface of the specimen by a clearance of 1 $[\text{mm}]$. Strictly speaking, there has been no purpose of the clamps/reinforcement ring so far. This is because the specimen is not physically interacting with the test setup yet. However, all parts in Abaqus had to be instantiated from the beginning of the simulation. It was not possible to 'activate' certain parts after a given load step. The work-around for controlling the active parts during a loading step is manipulating their boundary conditions.

The boundary conditions are shown by Figure 2.3.

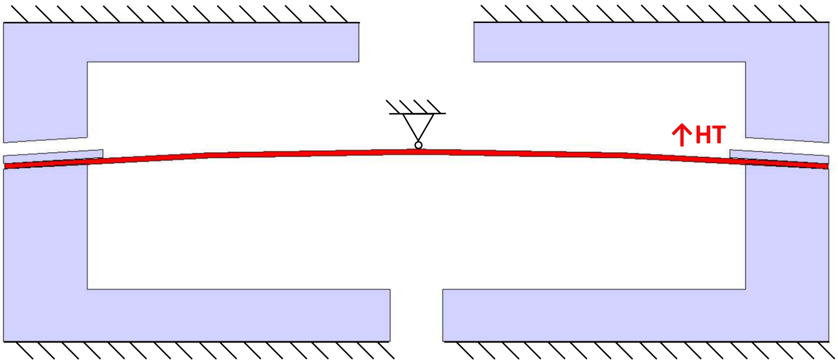

Figure 2.3: Boundary conditions of the initial step

One node at the centre of the specimen is encastred (U1 $=$ U2 $=$ U3 $=$ UR1 $=$ UR2 $=$ UR3 $= 0$). One surface of both clamps is also encastred (U1 $=$ U2 $=$ U3 $=$ UR1 $=$ UR2 $=$ UR3 $= 0$) to ensure static determinacy.

A predefined temperature field is applied only to the CFRP specimen (excluding the reinforcement ring). During the initial step, the magnitude of the temperature field is equal to the maximum cure cycle temperature of IM7/8552 [32]. The cure cycle is provided in chapter 3.

2.2.2. Autoclave cooling

During the autoclave cooling step, the temperature of the CFRP specimen is linearly decreased to room temperature. A linear ramp down is realistic because autoclaves often exhibit controlled cooling to avoid thermal shocks in laminates. These may cause manufacturing-induced cracks, especially in thicker laminates where the surfaces may cool faster than the middle.

On top of that, the clearance between the specimen and outer clamp is linearly decreased such that contact is established at the end of the step. This is achieved by prescribing an out-of-plane displacement on the outer clamp, that is equal in magnitude to its initial clearance $(\text{U2} = -1)$. All other boundary conditions remain the same as the previous step (see Figure 2.3). The boundary conditions at the end of this simulation step are visualised in Figure 2.4. It can be confirmed that all parts of the model are connected.

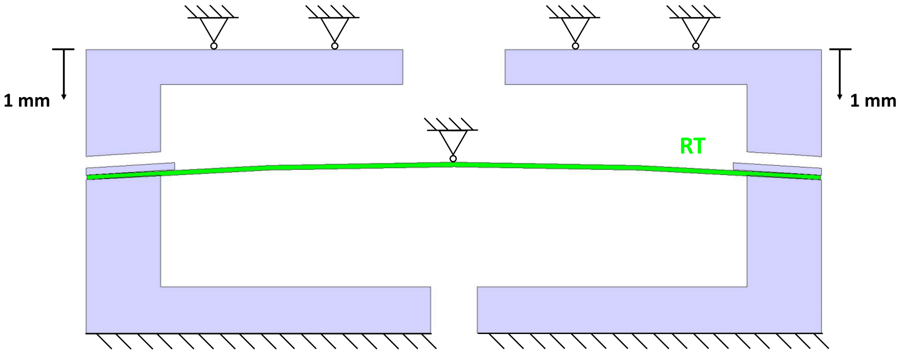

Figure 2.4: Boundary conditions of the autoclave cooling step

2.2.3. Clamping

A clamping force is applied. The magnitude of the force is linearly increased, to mimic the gradual increase in the physical bolt torque. The force is uniformly applied on the surface of the outer clamp, as shown in Figure 2.5.

A predefined temperature field is applied to the entire assembly, to enforce that the loading step takes place at room temperature.

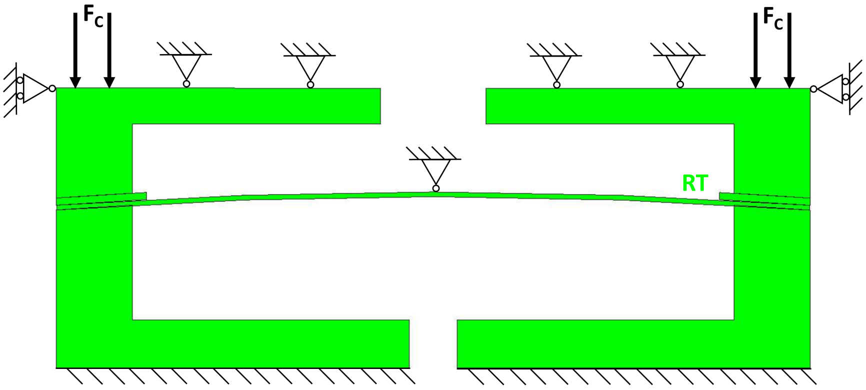

Figure 2.5: Boundary conditions during the clamping step

The encastred boundary condition at the central node of the specimen is deactivated. One surface of the inner clamp remains encastred (U1 $=$ U2 $=$ U3 $=$ UR1 $=$ UR2 $=$ UR3 $= 0$). One surface of the outer clamp is free to move vertically (U2 is free). The deformation in the vertical direction, once contact has been established, is dependent on the clamping force. All other degrees of freedom on the surface of the outer clamp are constrained (U1 $=$ U3 $=$ UR1 $=$ UR2 $=$ UR3 $= 0$).

2.2.4. Cryogenic cooling

Homogeneous cooling is applied to model the thermal effects of cryogenic immersion. This is done by modifying the temperature of the predefined temperature field, from RT to CT. For the sake of modelling simplicity, a linear ramp down is used.

The boundary conditions in this step remain unchanged from the previous step. Only the magnitude of the temperature field and clamping force is changed.

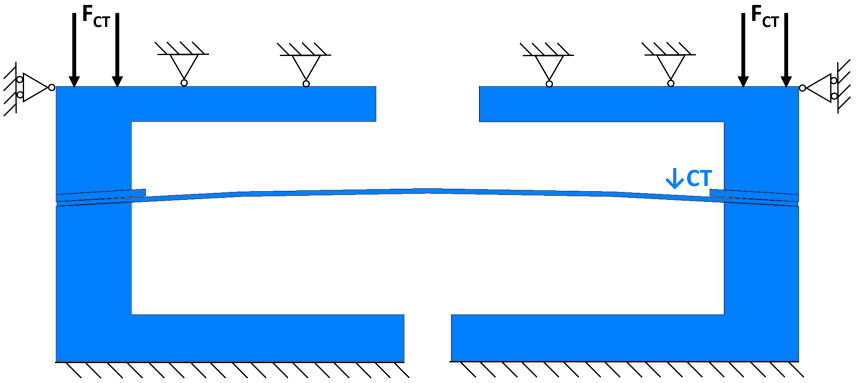

Figure 2.6: Boundary conditions of the cryogenic cooling step

2.2.5. Pressurisation

A pressure load is applied to the inner surface of the CFRP specimen, as shown in Figure 2.7. All other boundary conditions are propagated from previous steps.

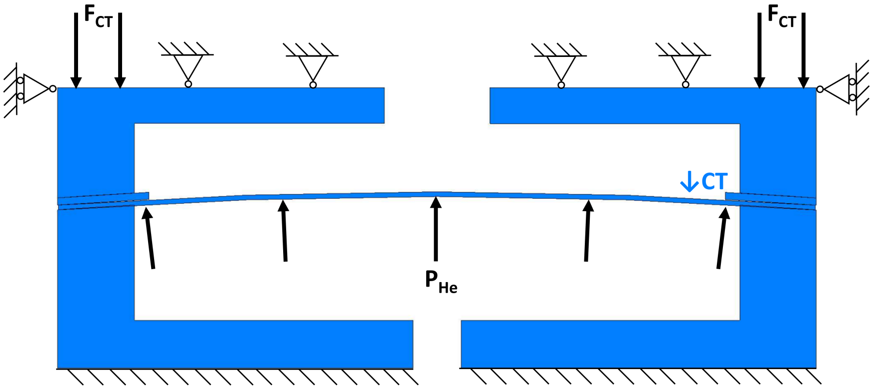

Figure 2.7: Boundary conditions of the pressurisation step

2.3. Overview of software/solver settings

In the previous section, the boundary conditions of the loading steps have been described. This section will focus on the numerical controls used in each step (subsection 2.3.2). In addition, a brief note on the choice of software is provided in subsection 2.3.1.

2.3.1. Software

Abaqus/Standard 2023 is selected.

Abaqus/Standard was selected over Abaqus Explicit, because the initial research scope was discrete damage modelling using XFEM. XFEM is not yet implement in Abaqus/Explicit. In addition, the problem is (quasi)-static, so higher frequency terms were not expected. This means that it was not necessary to use small time increments to capture the solution response due to the higher frequency terms. Consequently, implicit Abaqus/Standard schemes- that allowed larger stable time increments than Abaqus/-Explicit ones- were preferred.

The full-academic license for the 2023 version was available at the DLR. As the thesis did not use legacy code, namely (V)UMATs developed in an older Abaqus version, there was no specific reason to not use the latest available software. Further bearing in mind that the original goal of the thesis was using XFEM, the 2023 version was reported to demonstrate improved convergence performance (due to improvements in the level-set method used to describe a crack) [81].

2.3.2. Solver

All loading steps are Static/General. All steps use a non-linear implicit solver (NLGEOM=ON) - full Newton/Raphson method. Despite the absence of damage evolution, non-linearities in the model arise from contact boundary conditions and large displacements of the specimen.

Results from the previous iteration are linearly extrapolated onto the current one. No numerical difference was observed by turning off the extrapolation.

Based on the experience gained throughout the duration of the thesis, the default solver settings were modified for every step. These recommendations are given in Table 2.3. Each step has a normalised time period of 1.

Table 2.3: Recommended solver setting for each step

Loading step	Initial time increment	Min. time increment	Max time increment	Max number of iterations
Autoclave cooling	0.01	0.001	0.1	1000
Clamping	0.001	1e-6	0.1	1000
Cryogenic cooling	0.01	1e-5	0.1	10000
Pressurisation	0.01	1e-6	0.05	10000

The initial time increments were deliberately set to a lower value, to ensure the start of the loading ramps did not cause sudden numerical instabilities. From numerical experience, the recommended maximum time increments in Table 2.3 do not lead to diverging results. Fairly large minimum time increments/low number of maximum iterations were set. This was deliberately done to troubleshoot modelling mistakes without wasting excessive computational time. From numerical experience, a model that was correctly setup did not need more than 200 iterations/step to converge. In other words, convergence was judged highly unlikely if the time-step started dropping below 0.005.

On top of that, automatic stabilisation was turned on for all loading steps. It was required to stabilise the rigid body motion of the unconnected regions prior to the establishment of contact. The default adaptive automatic stabilisation settings were used. A dissipation energy fraction of 0.0002 was specified. This means that the artificial damping factor was adapted by the solver, to ensure that the artificial energy did not exceed a certain proportion of the real (strain) energy. To quantify the effect of automatic stabilisation, the ratio of the static dissipation energy (ALLSD) to elastic strain energy (ALLSE) was compared at the end of the simulation. It was found that ALLSD/ALLSE $= 0.02\% << 5\%$, a negligible amount [2].

2.4. Modelling the interaction of the test specimen with the test setup

As explained earlier in section 2.1, a modelling priority is to understand the influence of the test setup's boundary conditions on the test specimen. With that in mind, the modelling of the clamps and their interactions with the specimen shall be described in detail in this section.

2.4.1. Clamps

Both the inner and outer clamps are modelled as deformable 3D solids (C3D8R elements).

Geometry

The geometry that was modelled in Abaqus is based on the CAD shown in Figure 2.2. A 'defeatured' geometry is used. Specifically, the vacuum/pressure pipes are not modelled. The bolt holes are also neglected. In fact, only the part of the clamp that extends till the edge of the bulge specimen is modelled.

The clamps shown in Figure 2.2 are specially designed for the curved specimen. Precisely machined adapter plates match the local radius of curvature of the curved specimen. Matching the curvature of the clamp with the specimen is shown to reduce the clamp-induced stress concentration [14]. These adapter plates are not necessary for testing flat specimen. Removing these adapter plates reduces the thickness of the clamps by 5 [mm]. This reduction in the thickness of the clamp, for flat specimen, is taken into account.

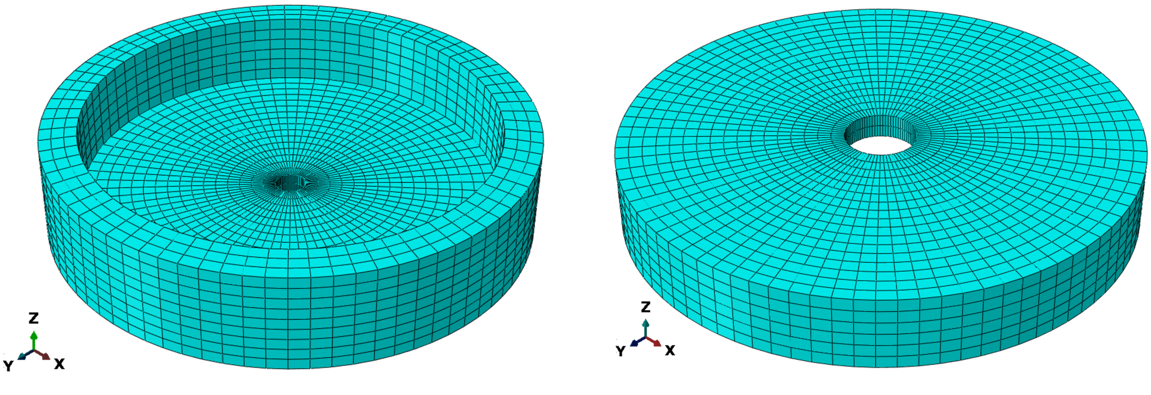

(a) Meshed isometric view of inner clamp. Mesh size = 4 [mm], number of elements = 6150

(b) Meshed isometric view of outer clamp. Mesh size = 4 [mm], number of elements = 4165

Figure 2.8: Geometry and mesh of inner/outer clamps

Mesh

The clamps are meshed using reduced integration, linear solid elements (C3D8R) with enhanced hourglass control. Structured hexahedral mesh is created using the sweep method. Using the advacing front or medial axis mesh generation algorithm did not result in any observables differences in the mesh. No additional partitions were used. The curvature control of the mesh generated was not modified from the default. A global mesh size of 4 [mm] is selected. It will later be seen in subsection 2.5.4 that the average global mesh size of the clamps is double that of the specimen. The coarser mesh of the clamp reduces unnecessary computational cost. After all, it is still of interest to predict the stress/strain accurately in the specimen, and not the clamps. However, an excessively coarse mesh is also avoided to reduce numerical issues associated with highly non-conformal meshes.

Material

The clamps are made up of Invar-36, an alloy of nickel and iron.

Temperature dependent material properties of Invar-36 are used in the FEM model. These properties are summarised in Table 2.4.

Table 2.4: Temperature dependent elastic and thermal expansion properties of (annealed) Invar-36 [59]

Temperature [K]	E [GPa]	ν [-]	α [K^{-1}]
77 (CT)	133	0.29	2.16×10^{-6}
293 (RT)	141	0.29	1.26×10^{-6}

2.4.2. Clamping force

The clamping force is estimated analytically. The magnitude of the bolt pre-load at room temperature (F_{RT}) is governed by a known applied bolt torque, and type of the bolt selected. The condition of the bolt is translated into a torque coefficient, based on empirical relationships [10].

Considering that the test setup is cryogenically cooled, Hooke's law is used to estimate the change in preload due to thermal effects (F_{CT}).

Estimate of the pre-load at room temperature

The total bolt pre-load (F_{RT}) is related to the individual bolt torque (T) by Equation 2.1.

$$F_{RT} = \frac{n_{\text{bolts}} \cdot T}{K_T \cdot d_{\text{nom}} \cdot (1 - l)} \tag{2.1}$$

where n_{bolts} is the number of bolts, d_{nom} is the nominal bolt diameter, l is the lubrication factor and K_{bolt} the torque coefficient.

As far as the author's practical knowledge of the bulge test setup is concerned, its bolts were not intentionally lubricated. Therefore, the effect of any (unknown) lubrication is not taken into consideration, by simply setting $l = 0$.

The bolt parameters that were known beyond a reasonable doubt are given in Table 2.5.

Table 2.5: Known bolt parameters

$\mathbf{n_{bolts}}$	$\mathbf{d_{nom}}$ **[m]**	**T [Nm]**
20	8.0×10^{-3}	14.0

The torque coefficient K_T still has to be estimated. To obtain a realistic estimate, the friction generated due to the lead angle of the threads and due to the bolt collar are considered. This is shown in Equation 2.2. [10]

$$K_{\text{bolt}} = \left(\frac{r_t}{d}\right)\left(\frac{\tan\lambda + f_t \sec\theta}{1 - f_t \tan\lambda \sec\theta}\right) + \frac{r_c f_c}{d} \tag{2.2}$$

where r_t is the mean thread radius, r_c is the mean collar radius, λ is the thread lead angle, θ is the thread half angle, f_t is friction coefficient between thread surfaces and f_c is friction coefficient between collar surfaces.

r_t is taken as an average of the bolt nominal (d) and minor diameter (d_m). The collar area is the bearing face, the face of the nut, that is rotated during installation. The width across the flats of a nut is generally 50% more than the nominal diameter. The relations of these geometric parameters is provided by Equation 2.3. [78]

$$\begin{aligned} r_t &= \frac{(d_{\text{nom}} + d_{\text{minor}})/2}{2} = \frac{d_{\text{nom}} + d_{\text{minor}}}{4} \\ r_c &= \frac{d_{\text{nom}} + 1.5\, d_{\text{nom}}}{2} = 0.625\, d_{\text{nom}} \\ \tan\lambda &= \frac{l}{2\pi r_t} = \frac{1}{2\pi r_t(\text{TPM})} \end{aligned} \tag{2.3}$$

I is the lead length, and is the reciprocal of the Threads Per Meter (TPM). For a standard (coarse) thread, Shigley [10] suggests the following thread properties.

Table 2.6: Standard (coarse) thread properties

ϑ [°]	d_{minor} [m]	TPM [m^{-1}]
30	6.65×10^{-3}	800

Shigley further recommends the use of $f_t = f_c = 0.15$, as commonly used for hard steel-on-steel contact. Substituting the parameters stated in Table 2.6 into Equation 2.3, $K_T = 0.278$ is obtained. This results in $F_{RT} \approx 126$ [kN]

Estimate of the change in pre-load due to cryogenic cooling

The cooling of the bulge test setup changes the pre-load of the bolts. This is attributed to the CTE mismatch between the bolt and the joint. As the stainless steel bolts have a higher CTE than the invar joints, the bolts are expected to contract more. Consequently, an increase in the pre-load is expected due to the cooling.

Bickford [9] suggests the use of Hooke's law (Equation 2.4) to approximate the change in bolt tension due to the thermal differential between the bolt and the joint.

$$\Delta F = n_{\text{bolts}} \frac{A_S E}{L_E} \left(\Delta L_J - \Delta L_B\right) \tag{2.4}$$

where ΔF is the change in the bolt force due to the thermal differential, E is the Young's modulus of the bolt, A_S is the tensile stress area, L_E is the effective bolt length, ΔL_J is the change in the length of the joint and ΔL_B is the change in the length of the bolt.

The tensile stress area (A_S) refers to the threaded portion of the bolt that resists tensile forces when the bolt is tightened. For a metric bolt, $A_S = 36.3$ [mm^2]. [9]

The effective length (L_E) refers to the part of the bolt that carries tensile load. The tensile load is carried at least between the underside of the bolt head and the top surface of the nut. As the tensile load gradually decreases to zero through the length of the bolt head and the nut, half the width of the bolt head and nut are also considered to carry the bolt load. [9] For the bulge setup, $L_E \approx 80$ [mm], as measured by the author.

The young's modulus of the bolt is taken as the average stiffness of stainless steel at room temperature (293 [K]) and cryogenic temperature (77 [K]).

Table 2.7: Young's modulus of a stainless steel bolt at RT and CT

E_{RT} [GPa] [48]	E_{CT} [GPa] [83]	E_{avg}[GPa]
194	200	197

Estimating ΔL_B and ΔL_J requires knowledge of the CTE of the constitutive materials of the bolt and joint respectively. The joint consists of: inner/outer Invar-36 clamps, CFRP specimen and a column of stainless steel washers. The bolt, as mentioned earlier, is made of stainless steel. The secant CTE (α_{mean}) of the relevant materials is tabulated in Table 2.8. The secant CTE is estimated as the arithmetic mean of the tangent CTE found at RT and CT. This approximation had to be made because it was not possible to mathematically reconstruct the shape of the tangent/instantaneous CTE from the published sources [50], [59], [71]. Thus, it was assumed that the CTE varies linearly between RT and CT. For the CFRP (namely IM7/8552), the transverse CTE is taken to be the CTE in the out-of-plane direction.

Table 2.8: Estimate of the CTE for the constitutive materials of the bolt/joint assembly

Material	α_{RT} [K $^{-1}$]	α_{CT} [K $^{-1}$]	α_{mean} [K $^{-1}$]
Stainless steel [50]	1.57×10^{-5}	1.00×10^{-5}	1.29×10^{-5}
Invar [59]	1.26×10^{-6}	2.26×10^{-6}	1.71×10^{-6}
CFRP [71]	3.38×10^{-5}	1.87×10^{-5}	2.63×10^{-5}

The change in bolt and joint length are then given by Equation 2.5. Calculating ΔL_B is straightforward as only the contraction of the bolt needs to be calculated. ΔL_J, on the other hand,

$$\begin{aligned} \Delta L_B &= \alpha_{\text{mean}} L_{0,B} \Delta T \\ \Delta L_J &= \sum \alpha_{\text{mean,i}} L_{0,i} \Delta T \\ \text{where}: \quad & \Delta T = 77 \text{ K} - 293 \text{ K} = -216 \text{ K} \end{aligned} \tag{2.5}$$

where $L_{0,i}$ is the initial length, and $\Delta L_{0,i}$ is the change in length.

Using Equation 2.5 and the mean CTE values given in Table 2.8, values for ΔL_B and ΔL_J are computed. The initial bolt length is taken as the effective bolt length $(L_{0,B} = L_E)$. The joint is comprises of all components between the underside of the bolt head and the nut. These include washers, clamps and the specimen. Finally, all required parameters are substituted into Equation 2.5 to compute ΔF_T.

Table 2.9: Estimated magnitude of clamping force at room and cryogenic temperature, used as input for force-controlled quasi-static loading in Abaqus

F_{RT} [kN]	ΔF_T [kN]	F_{CT} [kN]
126	300	426

2.4.3. Contact model

The purpose of the contact model is to accurately predict specimen slippage. The interaction surfaces and properties are described in subsection 2.4.3 and subsection 2.4.3.

Interacting surfaces

Contact interactions are used between the specimen and the clamps.

Namely, surface-to-surface interactions are defined. Finite sliding is used to allow for arbitrary separation,sliding and rotation of the contact surfaces. Small sliding is not used. The finite sliding contact formulation, unlike small sliding, eliminates the assumption for small relative motion between the contact surfaces. There is an extra computational cost associated with using finite sliding. However, as the model only has two contact interactions, the increase in computational time is expected to marginal. [1]

The surface-to-surface discretisation method is selected. It predicts contact stress and pressures more accurately than node-to-surface discretisation. This is because surface-to-surface discretisation considers contact in an ”averaged” sense over a finite region. This reduces interpenetration of the surfaces, at the position of the discretised nodes. [2]

The surfaces of the clamps are selected as the master surfaces for several reasons. Firstly, the mesh of the clamps is coarser than that of the specimen. This means that the projection of normals from the master surface are expected to remain more orthogonal to the slave surfaces. This is especially true for the nearest-neighbour interpolation technique. Moreover, the clamp is more stiff than the specimen. Consequently, the surface of the clamp surface should change its shape less than that of the specimen's surface. This in turn should minimise the change in the direction of the contact projections, presumably improving numerical stability. [77]

Interaction properties

Normal and tangent contact properties have to be specified. In addition, a small amount of damping is required for numerical stability.

Normal contact Concerning the normal behaviour, "hard" contact is used. The default constraint enforcement method in used. In Abaqus/Standard and Abaqus/Explicit, the default settings internally select the Penalty method. [2] Technically, the model can be refined by inputting a pressure-overclosure relationship to account for the plastic deformation of the indium seal. A detailed sub-model can be established to obtain the relationship between contact pressure and clearance. However, as already explained in section 2.1, modelling the sealing is not of interest in this thesis.

Tangential contact The tangential behaviour is governed by friction. The Penalty method is selected, with a specified coefficient of static friction (μ_s). It is important to clarify μ_s must be defined for the material of the specimen and the seal (not the clamp!). Otherwise, slippage will be under-predicted. This is because indium seal has an extremely low friction coefficient, far lower than that of the Invar clamps. One study reports that $\mu_s \approx 0.05$ for indium surfaces [63]. In fact, indium coatings have been investigated to improve lubrication/reduce wear on metals. [73], [86] Unfortunately, the friction coefficient of indium has only be published for coatings applied on steel surfaces. Often, the indium in the coating wears out due to cold annealing (recall that indium has low yield stress, around 2 [MPa] at room temperature [69]). Therefore, the accuracy of the friction coefficients has to be questioned. Furthermore, it is not clear if the friction coefficient obtain for Indium-steel surfaces is valid for indium-CFRP surfaces. All in all, the author could not find a satisfactory value of μ_s from literature. Luckily, experimental data analysis is within the scope of this work. It is proposed that displacement fields from DIC is used to obtain μ_s. Such tuning of the (tangential) contact model is done in chapter 5.

Numerical damping The contact model did not converge without damping. Preliminary simulations revealed that numerical instabilities arose during the clamping step. During this step, clamping force is applied. This should result in the establishment of normal contact between all surfaces. No physical gap should exist between surfaces in contact. However, (large) numerical interpenetration errors were discovered in the log files of the simulations.

Incorporating a contact damping coefficient reduced the interpenetration errors, thus improving the convergence. It is only necessary to use damping in the normal direction. In Abaqus, 'tangent fraction' of the damping coefficient was set to zero. This ensures that the tangential contact remains undamped. By extension, numerical damping should not have an influence on slippage results.

The damping coefficient is estimated by Equation 2.6. It should be noted that the damping coefficient is not dimensionless in Abaqus/Standard.[2]

$$\mu_0 \approx \frac{P_c}{v_{rel}}, \qquad \text{where :} \quad P_c = \frac{F_c}{A_c}, \quad v_{rel} = \frac{s_{rel}}{t} \tag{2.6}$$

where P_c, F_c and A_c is the contact pressure, force and area respectively. v_{rel}, and s_{rel} is the maximum relative velocity and separation distance of the contact surfaces. t is the elapsed simulation time for the surfaces to come in contact with each other.

F_c is taken as the clamping force at room temperature from Table 2.9. A_c is computed from Figure 2.8. s_{rel} is the initial clearance of the clamp from the specimen. The clamp covers a distance of s_{rel} within one loading step. All loading steps have a normalised simulation time, so $t = 1$.

Table 2.10: Estimation of the damping coefficient

F_c [N]	A_c [mm^2]	s_{rel} [mm]	t [s]	μ_0 [N s mm^{-3}]
126000	3600	1.0	1.0	35

μ_0 is the estimated damping coefficient.

A clearance (c_0) was subsequently selected. The damping coefficient is zero if the contact separation exceeds the set clearance. The relationship between the damping coefficient and clearance is visualised in Figure 2.9. Note that a linear ramp down of μ_0 was selected. This means that $\eta = 0$. The clearance c_0 of 0.01 was assumed.

Finally, the effect of numerical contact damping was quantified. Damping results in artificial energy. It is only acceptable to use damping if the artificial energy is a small portion of the real energy ($<< 5$%). Figure 2.10 shows the ratio of the ALL Contact Dissipation (ALLCD)/ALL Strain Energy (ALLSE) for varying μ_0.

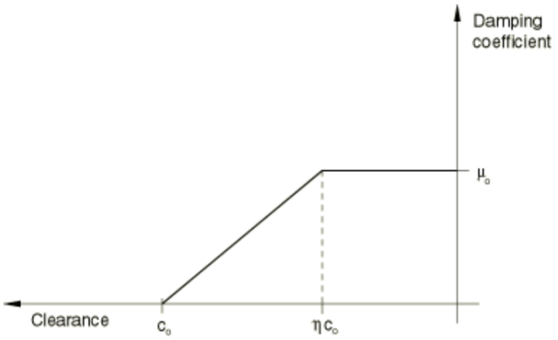

Figure 2.9: Variation of the contact damping coefficient μ_0 with clearance c_0 [2]

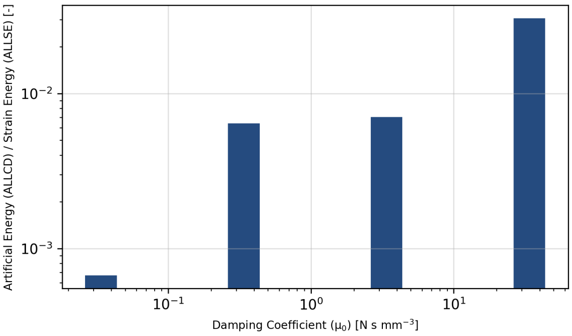

Figure 2.10: Ratio of the artificial energy vs. the elastic strain energy, for various values of the contact damping coefficient

Figure 2.10 substantiates that the influence of damping is negligible. The artificial dissipation is only 3% of the strain energy, for $\mu_0 = 35$. That being said, contact model simulations converged even only 1% of the damping coefficient was used. This reduced the proportion to artificial energy below 1%. Therefore, $\mu_0^{0.1} = 0.35$ shall be used as default. Whenever possible, $\mu_0^{0.01} = 0.035$ was employed to practically neglect the influence of the numerical contact dissipation (0.05% artificial energy).

2.5. Modelling the composite bulge test specimen

A mesoscale, linear elastic model of the CFRP laminate is implemented.

2.5.1. Geometry & coordinate system

The geometry of the bulge specimen is parametrically defined with: diameter (d), curvature (c) and thickness (t). Values of geometrical parameters are explicitly stated in chapter 3, because they are derived from experimental constraints. For validating the numerical model (chapter 5), only one thickness/layup is selected. However, the effect of laminate design and specimen is numerically investigated in chapter 6.

A typical section is visualised in Figure 2.11. Four plies are shown. The laminate/global coordinate system is x, y, z. x,y are the in-plane axes. z is the out-of-plane direction.

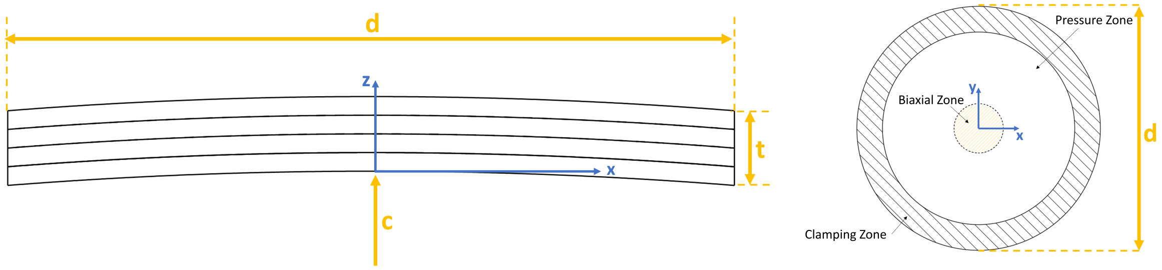

(a) Cross-section view

(b) Top view

Figure 2.11: Typical section of the bulge element (not to scale). The sketch is inspired by the work of Lentner [46].

Another local/lamina (ply) level coordinate system is used. 11, 22 represent the transverse (along fibre) and longitudinal (perpendicular to fibre) directions. 33 is the out-of-plane direction. The local coordinate system of the bottom/inner-most ply is used to define the global coordinate system. Namely, 11 and 22 of the inner-most ply is the global x and y direction of the laminate. The definition of the coordinate system is crucial to the interpretation of results in chapter 4-5.

As $c \to \infty$, the laminate becomes flat. To remove mathematical singularities during modelling, a separate FEM model is set up for flat specimen altogether.

2.5.2. Material properties

The default CFRP material system is IM7/8552. A brief explanation of the material selection is provided in subsection 3.1.2. Temperature dependent material properties of IM7/8552 are summarised in Table 2.11-2.12.

Table 2.11: Temperature dependent elastic properties of IM7/8552 [71]

Temperature [K]	**E_1 [GPa]**	**$E_2 = E_3$ [GPa]**	**$\nu_{12} = \nu_{13}$ [-]**	**ν_{23} [-]**	**$G_{12} = G_{13}$ [GPa]**	**G_{23} [GPa]**
77 (CT)	159	13.3	0.24	0.30	8.65	5.15
293 (RT)	160	9.6	0.27	0.34	5.01	3.56

Table 2.12: Temperature dependent thermal properties of IM7/8552 [71]

Temperature [K]	**α_{11} [K^{-1}]**	**$\alpha_{22} = \alpha_{33}$ [K^{-1}]**
77 (CT)	-1.9×10^{-7}	1.87×10^{-5}
293 (RT)	-5×10^{-8}	3.38×10^{-5}

2.5.3. Reinforcement ring

A reinforcement ring can potentially reduce the clamp-induced damage [46]. The reinforcement ring is bonded to the composite laminate, and is treated as part of the test specimen.

The geometry of the reinforcement ring is defined by its outer diameter (d), curvature (c), width (w), and thickness (t). Its outer diameter and curvature match those of the composite specimen, as shown in Figure 2.11. The width and thickness can vary. chapter 3 provides the properties of the default reinforcement. The default reinforcement is used for quantifying the validity of the model in chapter 4.

The reinforcement ring is meshed using reduced integration, linear solid elements (C3D8R). An average global mesh size of 2 $[\text{mm}]$ is used. This generates 2180 elements. Only hexahedral shaped elements are allowed. These are generated using the sweep technique, using the medial axis algorithm.

The default material of the reinforcement ring is aluminium. Its temperature dependent properties are given in Table 2.13.

Table 2.13: Temperature dependent elastic and thermal expansion properties of aluminium-6061 [79]

Temperature [K]	E [GPa]	ν [-]	α [K $^{-1}$]
77 (CT)	77	0.30	1.85×10^{-5}
293 (RT)	70	0.33	2.36×10^{-5}

A tie constraint is used to join the surfaces of the reinforcement ring and composite laminate. Tie constraint is selected due to its low computational cost. The limitation of the tie constraint is that it cannot model any delamination. To analyse reinforcement/laminate debonding, it is necessary to use cohesive interactions or elements. Even in the absence of a progressive traction-separation laws, cohesive modelling requires tuning of the interface strength and longer computational times. Therefore, they are not selected in this study.

2.5.4. Meshing: An evaluation of accuracy and computational cost

Mesoscale discretisation demands a large number of mesh elements. It is worthwhile to estimate the minimum number of mesh elements that are necessary to generate sufficiently accurate results. Bearing in mind the modelling objectives outlined in section 2.1, the FEM should be able to predict the linear, elastic response of the CFRP specimen. Progressive damage is out-of-scope. This eliminates the need for excessively refined meshes in the region of interest. That being said, stress peaks at the clamps should be captured correctly.

subsection 2.5.4 clarifies the constraints and limitations of the mesh study. subsection 2.5.4 describes a mesh convergence study to determine the global mesh size. Based on the appropriate mesh refinement, Figure 2.5.4 explores various partitioning strategies to effectively mesh a double-curved membrane. Various types of solid elements are considered as well (Figure 2.5.4). Finally, the number of elements per ply are varied in Figure 2.5.4.

Constraints

Solid Elements The reader is reminded that only solid mesh elements are used in this study. (Continuum) shell elements, such as SC8R, are not used. This is because shell elements are not able to account for out-of-plane stresses. The possibility of placing cohesive zones between plies discretised with continuum shell/solid elements is not considered in this study. [82] To keep modelling effort and computational cost low, solid elements of each ply are simply merged together.

Full model The compete geometry of the specimen is discretised. In other words, no symmetric boundary conditions are applied. The author is aware of the possibility of a quarter-model, that benefits from two radial planes of symmetry. However, symmetry was deliberately not used. It risks in the non-linear contact boundary conditions not being correctly reflected in the solution. This could reduce the accuracy of the slippage predictions, which would certainly not be desired.

Previous numerical studies [45], [61], [14] also model the specimen without specimen to correct capture the complex boundary conditions associated with the test rig.

In fact, one analyses in chapter 5 will quantify the degree of axis/point symmetry of the specimen. Therefore, a full model is required.

Mesh convergence study

Five structured hexagonal meshes were generated for the mesh convergence study. Figure 2.12 shows the global mesh size and the number of elements.

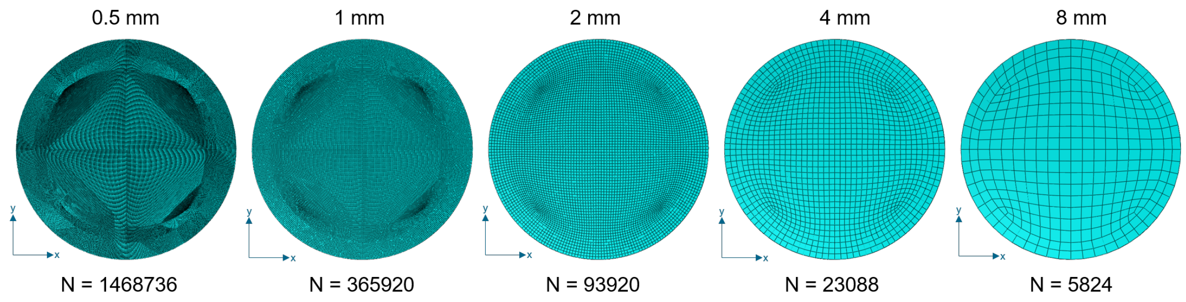

Figure 2.12: Various mesh sizes used for the convergence study

The simulations were run on 6 cores. The simulation with the most refined mesh (0.5 [mm]) was terminated after several days of run-time. Thus, results are not available for this mesh size. This is not considered a huge drawback, because the run-time of a model should be in hours and not days.

Figure 2.13 shows the main results of the mesh convergence study. Figure 2.13a sheds insights into the relative difference of a maximum displacement and stress component for increasing mesh refinement. Figure 2.13b shows the increase in CPU time associated with finer meshes.

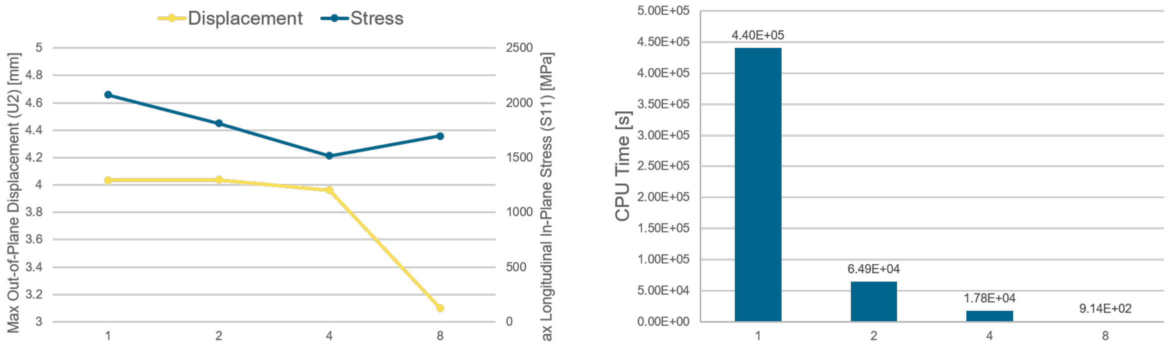

(a) Maximum displacement/stress

(b) CPU time

Figure 2.13: Summary of the results of the mesh convergence study

Consider the displacement in Figure 2.13a. The maximum out-of-plane (U2) displacement always occurs at the centre of the specimen. The discretisation residual is sufficiently minimised for a global mesh size of 2 [mm]. Further reducing the mesh element size to 1 [mm] makes a small difference of 0.1%.

On the contrary, a 2 [mm] mesh cannot sufficiently capture the maximum magnitude of the in-plane longitudinal stress (S11). This is because the value of max S11 increases by 12% as the mesh size is reduced to 1 [mm]. It should now be noted that the maximum longitudinal stress always occurs at near the clamping region. Precisely, there is a stress concentration point where the specimen leaves the clamp. Since the location of the stress concentration is known a priori, the mesh only needs to be refined locally.

Overall, a global mesh size of 2 [mm] is judged to be sufficient. It is recommended that the mesh size is reduced to 1 [mm] at the boundary of the clamping to pressure zone.

For the reader's reference, the components of stress for different paths are provided in Appendix A. However, these raw results do not contribute to the discussion in this section.

Partitioning strategy

The bulge specimen had to be partitioned prior to meshing. Paritions had to be created through the thickness of the laminate (not simply a face)! To do so, a shell was extruded through the thickness of the laminate. The faces of the shell were removed after the partitioning was completed. The cross-section sketches of these shells are given in Figure 2.14.

Green and/or yellow regions are created as a result of the partitioning. Green regions refer to fully structured hexagonal shaped elements. Yellow regions indicate fully hexagonal, hexagonal dominated or tetrahedral elements created using the sweep algorithm. Mesh B (Structured Hex-Tet) uses medial axis sweep for element generation. Mesh D (Unstructured Hex) is generated with the advancing front method.

Only four hexagonal dominated meshes are simulated. Tetrahedrals are used sparingly. Only mesh B uses tetrehedral to improve mesh element quality (higher orthogonality and reduced skewness) in transition regions. Tetrahedrals should not be used to discretise the region of interest. Lentner [45] explored structured meshes that placed tetrahedrals elements in a circle, at the middle of the specimen. The use of tetrahedrals resulted in numerical oscillations in the stress/strain results. Therefore, tetrahedrals should not be used.

For comparable results, a global seed size of 2 $[\text{mm}]$ was used to generate the meshes.

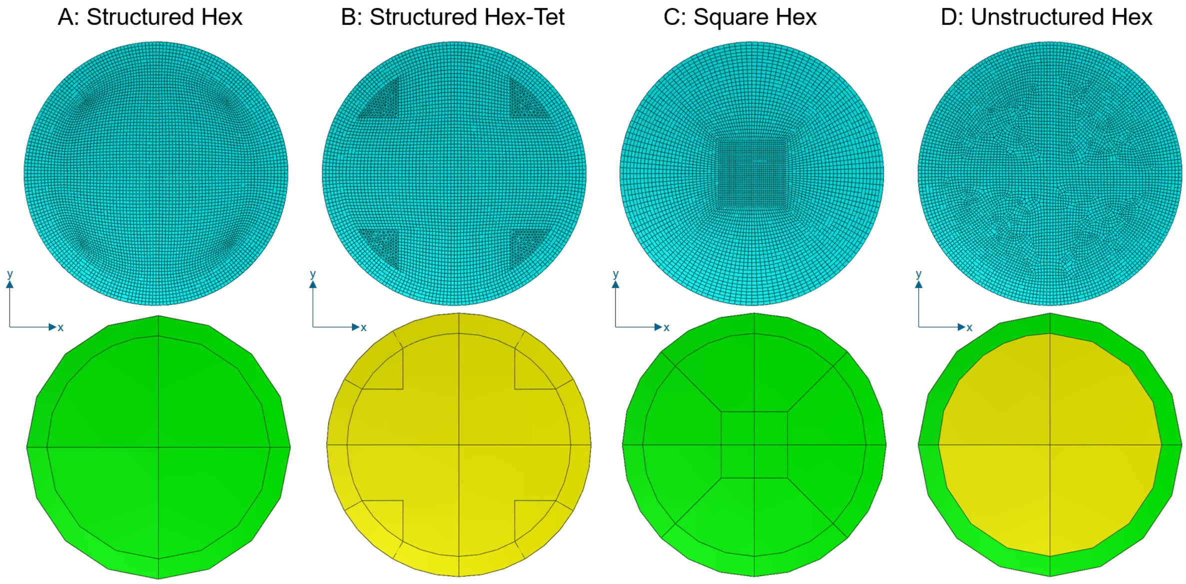

Figure 2.14: Mesh partitioning strategies

Figure 2.14 shows that Mesh A and Mesh C are fully structured. However, both meshes have drawbacks. For mesh A, elements tend to ”pinch” at the four corners. Placing unstructured tets (Mesh B) at the corners appears to alleviate this problem. On the other hand, mesh C can result in a mesh bias at the boundary between the square and circular regions. Lentner [46] showed that Mesh C can result in numerical peaks in the stress/strain. These peaks occur at the transition. However, they are within an (acceptable) 1% margin from the values of Mesh A.

An informed decision on the choice of mesh needs further analysis. Thus, the mesh element quality was compared. Figure 2.15 shows the orthogonality and aspect ratio of all four meshes. The distribution of the ’quad angle’ (min, max, mean) is plotted in Figure 2.15a. The quad angle should be as close as possible to $90°$. The mean aspect ratio is given in Figure 2.15b. The aspect ratio should ideally be 1.

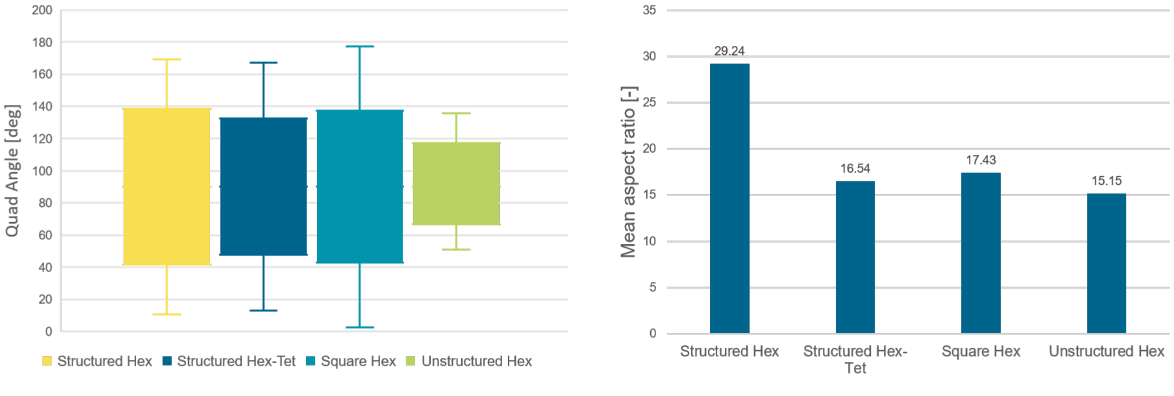

(a) Orthogonality

(b) Aspect ratio

Figure 2.15: Mesh element quality, for a global mesh size of 2 $[\mathrm{mm}]$

Figure 2.15a clearly shows that the best orthogonality is achieved for the unstructured mesh. The square hexahedral mesh has the poorest orthogonality. This is presumably caused by the hexahedral elements right outside the square region.

Figure 2.15b shows large aspect ratios (>5). This is unsurprising for mesoscale models, whereby the element thickness (take 0.125 $[\mathrm{mm}]$ per ply) is an order of magnitude smaller than the in-plane element width (2 $[\mathrm{mm}]$ global size). An aspect ratio of $2/0.125 = 16$ implies a perfect square in the xy plane. All meshes - except the structured hexahedral one- have acceptable average aspect ratio. The worse (higher) aspect ratio of the structured hexahedral mesh can be explained by the skewness of the corner elements.

The simulations with different meshes were run. Stress prediction along the XY path are shown in Figure 2.16. For completeness, stress along X and Y paths are given in Figure A in Appendix A. However, they are left out of discussion in this section.

The global coordinate system is referenced in Figure 2.11. The reason XY path is shown here is to qualitatively visualise any mesh bias. Mesh bias is likely to occurs along a diagonal path, as it traverses more irregularly shaped mesh elements (see Figure 2.14).

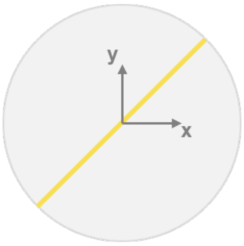

(a) XY-path

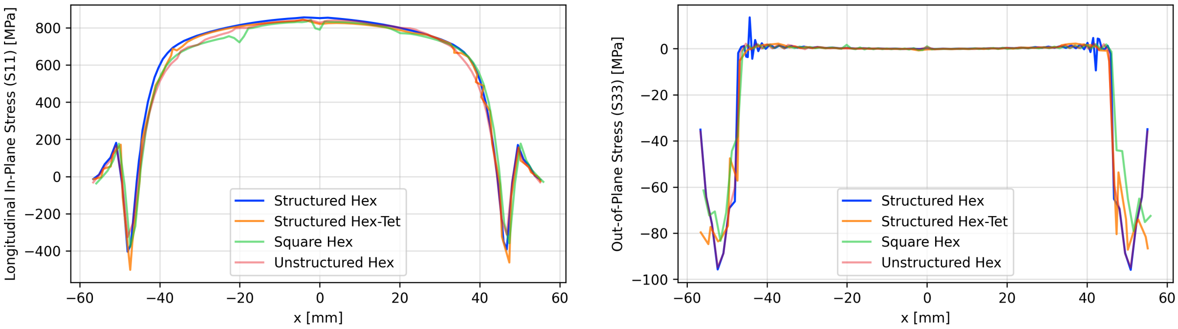

(b) Longitudinal in-plane stress (S11) against the global/laminate's x-ordinate

(c) Out-of-plane stress (S33) against the global/laminate's x-ordinate

Figure 2.16: Components of stress along the global XY-path, for the outer/top-most ply

The in-plane stress peak in Figure 2.16b is well captured by all meshes. The structured hex-tet mesh has the most conservative S33 prediction. Although this is desired, the structured hex-tet suffers from oscillations inside the clamping zone- as shown by Figure 2.16c. Still analysing Figure 2.16b, the unstructured mesh has the least oscillations.

Finally, the total CPU time is compared in Figure 2.17. The effect of parallelisation on the computational time is not considered. However, the same number of cores (n = 6) are used for a fair comparison.

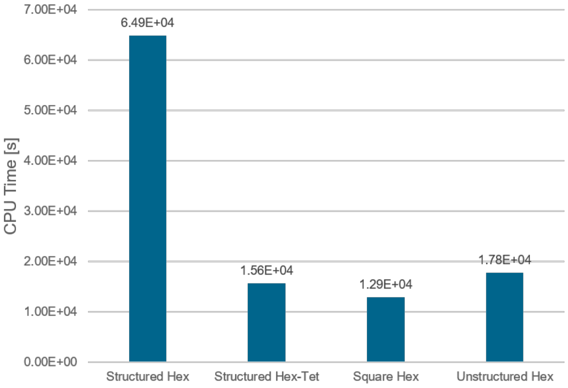

Figure 2.17: CPU time for different mesh partitions

It can clearly be seen that the structured hexahedral mesh is significantly slower (x3.5-5) than the rest. The log files indicated analysis warnings for the poorly meshed corner elements of the structured hexahedral mesh. Presumably, this translates to an increased number of solver iterations to achieve convergence within an implicit time step. Hence, the structured hexahedral mesh is no longer used.

In conclusion, the unstructured hexahedral mesh is selected. It has best mesh element quality, as characterised by the lowest aspect ratio and the highest orthogonality (Figure 2.15. It does not suffer from artificial (out-of-plane) stress oscillations, unlike the structured hex-tet or square mesh (Figure 2.16). Albeit this mesh does not have the lowest runtime, it is at least in the same order of magnitude of other meshes- excluding the structured hexahedral one.

Influence of mesh element type

Two additional types of solid elements are investigated: C3D8 and C3D20R.

C3D8, unlike C3D8R, utilises full-integration. It is of interest to explore whether the use of full-integration is worthwhile. In the following scenarios, reduced integration should be preferred. Firstly, it is possible that the use of full-integration simply leads to shear-locking. As the mechanical loading is bending-dominated, the risk of shear-locking is amplified.[76] In addition, C3D8 will use 2 x 2 x 2 = 8 Gauss integration points. C3D8R uses only 1 integration point in contrast.[1] The question remains whether the increased number of Gauss points sufficiently improves accuracy to justify its increased computational cost.

C3D20R is a quadratic solid element. It has 20 nodes. C3D8R only has 8 nodes. The question arises whether a higher number of nodes results in enhanced accuracy or merely an inefficient use of computational time.

To compare the results from different mesh elements, select components of the stress were plotted along the XY-path. The raw results are depicted in Figure 2.18.

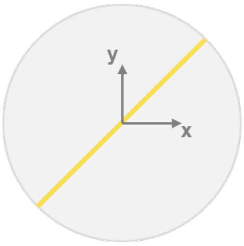

(a) XY-path

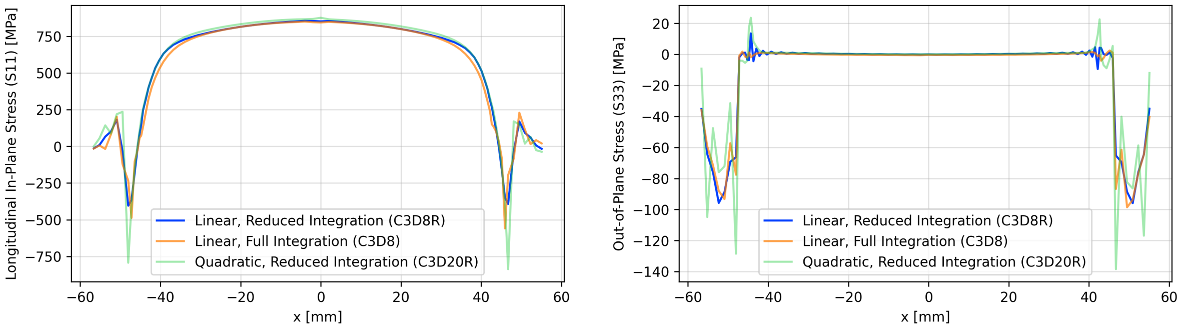

(b) Longitudinal in-plane stress (S11) against the global/laminate's x-ordinate

(c) Out-of-plane stress (S33) against the global/laminate's x-ordinate

Figure 2.18: Components of stress along the global XY-path, for the outer/top-most ply

C3D20R yields the most conservative S11 prediction, according to Figure 2.18b. At the same time, C3D20R elements lead to five S33 within the clamping region (Figure 2.18c). Such a complex peak of S33 could be attributed to stick-slip behaviour- introduced by the contact boundary condition. However, this cannot be further verified. Only one peak in S33 would be expected, as the compressive force of the clamp is relieved inside the unsupported zone. All in all, predictions from C3D20R should be treated with caution.

It can be qualitatively deduced from Figure 2.18 that the behaviour of C3D8R and C3D8 are similar. C3D8 predicts a more negative peak, by around -125 [MPa], in Figure 2.18b. C3D8 also has two S33 peaks in Figure 2.18c. No physical explanation can be found.

The remainder of the results for different paths are given in Figure A in Appendix A. However, to aid the selection of the most suitable solid element, the CPU time must be compared.

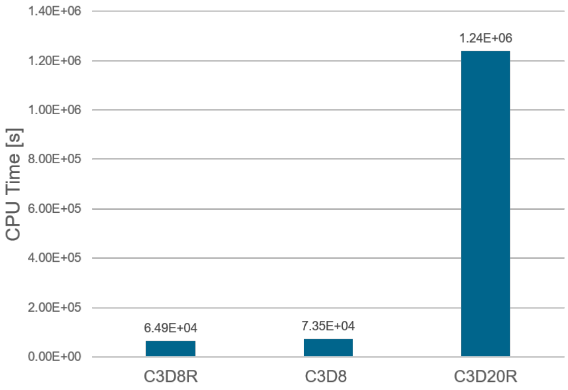

Figure 2.19: CPU time for different solid mesh elements

Figure 2.19 shows that C3D20R increases computational time by a factor of about 50. This is unacceptably large. Any (marginal) betterment in predictive accuracy is offset by its computational infeasibility. As such, C3D20R shall no longer be used in any further analysis within this study.

An additional analysis was performed to quantify the effect of hour-glassing. Reduced integration elements are especially susceptible to it. Abaqus, by default, uses enhanced hour-glassing control C3D8R and C3D20R. However, this means that some artificial energy is generated to stabilise the element against excessive distortion. [2] To be certain that such viscous dissipation is small ($<< 5$% of the real energy), the ratio of ALL Artificial Energy (ALLAE) to ALL Strain Energy (ALLSE) is plotted. Results at the end of the simulation are shown in Figure 2.20.

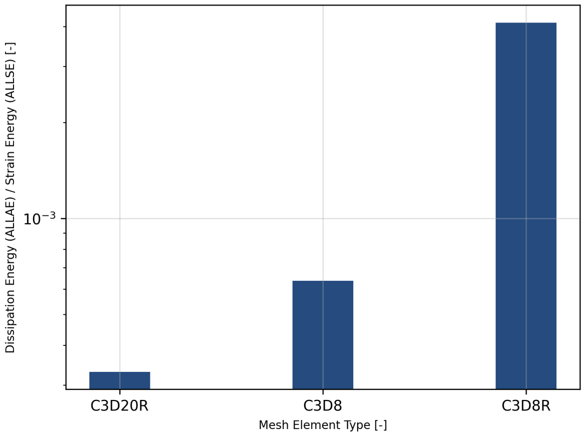

Figure 2.20: Ratio of the artificial energy vs the elastic strain energy, for different solid mesh element types

Figure 2.20 shows no signs of hour-glassing in all solid elements. If significant hour-glassing took place, the fraction of artificial energy would presumably be higher. Even C3D8R, that is supposed to suffer the most from the hour-glassing effect, has a mere 0.4% of artificial dissipation. No additional benefit can therefore be identified from using full-integration.

Ply level discretisation

In a mesoscale model, at least one element should be used in the thickness direction of the ply. It is useful to understand whether increasing the number of elements through the thickness of the ply significantly affects the numerical accuracy.

To observe the effect of mesh refinement in thickness direction, the three components of out-of-plane stress are compared in Figure 2.21. Previous studies have shown that the maximum out-of-plane stress is likely to occur at the transition between the clamped and unsupported zone. Hence, a path through the thickness of the laminate at the transition point is selected. This Z-path is shown in Figure 2.21a.

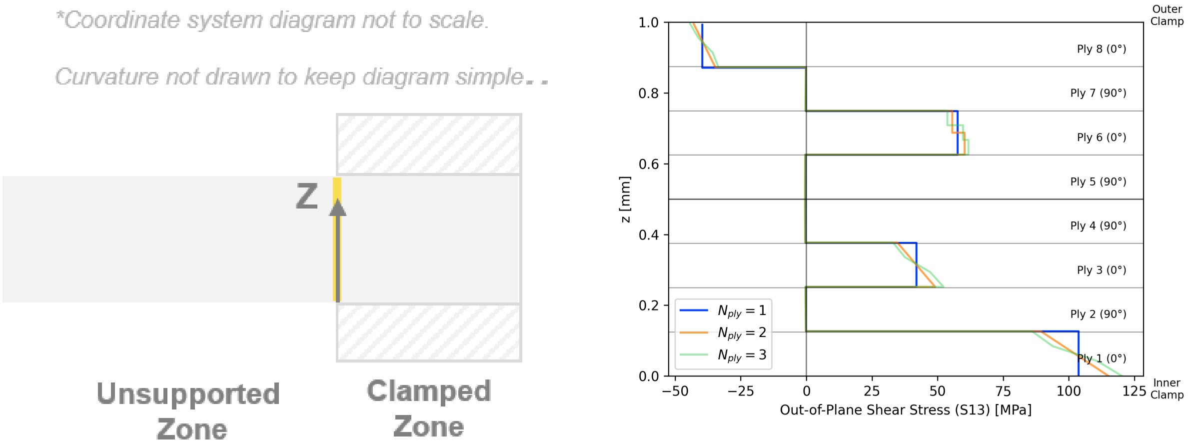

(b) Longitudinal shear stress (S13) through the thickness of the laminate

(a) Z-path

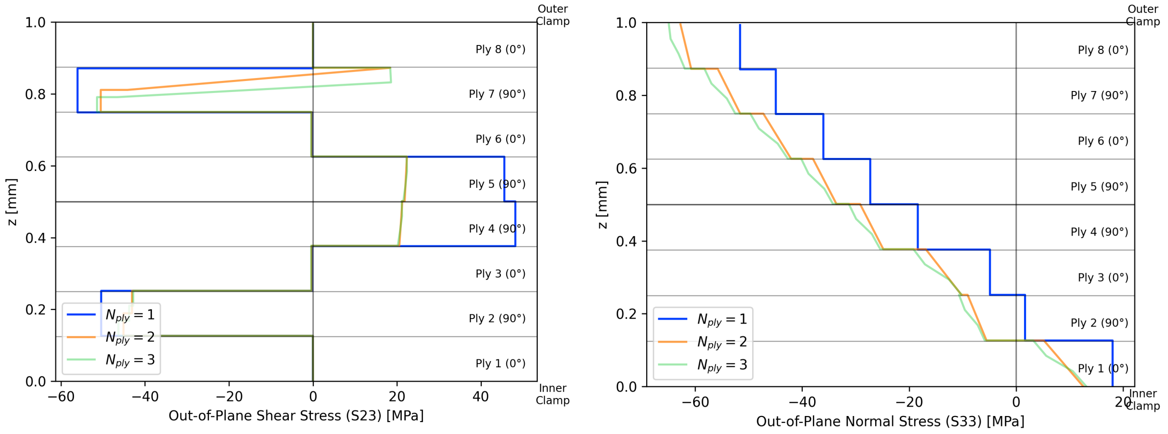

(c) Transverse shear stress (S23) through the thickness of the laminate

(d) Axial stress (S33) through the thickness of the laminate

Figure 2.21: Components of out-of-plane stress along Z-path, at the clamp location

Figure 2.21 shows that using one element per ply thickness results in constant values of stress components in the ply. This is acceptable because of two reasons. Thin plies are used by default. Consequently, large variation of stress through the thickness of the ply is not expected.

Consider Figure 2.21b qualitatively. $n_{ply} > 1$ results in a linear variation of S13 through the thickness of the ply. $n_{ply} = 1$ seems to predict a "mean" value of this stress.

$n_{ply} = 1$, however, overpredicts S23 by up to 25 [MPa] (Figure 2.21c). At the same time, $n_{ply} = 1$ offsets S33 by around 10 [MPa] (Figure 2.21d). The physical or numerical explanation behind these observations cannot be inferred. Considering that the S33 stress peak (for C3D8R) in Figure 2.18c is -95 [MPa], a $+10$ [MPa] equates to a -10.5% difference. This leads to the risk that using $n_{ply} = 1$ may under-predict delamination. Therefore, it may be worthwhile to increase n_{ply} in critical locations for higher fidelity analyses (eg: using traction-separation laws). However, for preliminiary linear, elastic simulations, $n_{ply} = 1$ is decided to be sufficient. It is shown in Figure 2.22 that doubling the number of elements in the thickness direction results in an eight four increase in computational cost. CPU time appears to scale with $O(N^{2.5}) - O(N^3)$. A possible reason for poor scaling of run-time could be attributed to the increasing mean element aspect ratio with increasing mesh refinement.

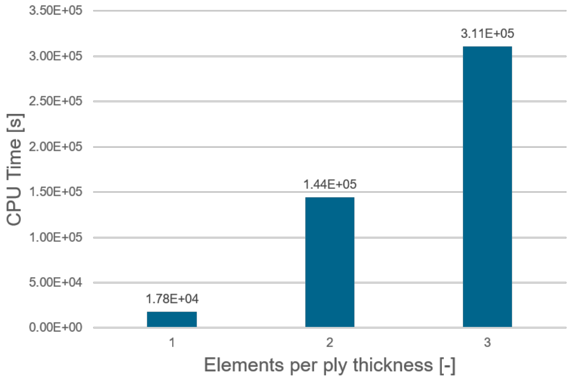

Figure 2.22: CPU time for increasing number of mesh elements in the ply thickness direction

2.6. Modelling damage initiation

Localising damage is a modelling priority. Two broad causes of damage are identified. Damage can be induced by the boundary conditions of the test setup (Figure 2.23). [45], [61], [14] This type of damage is undesired as it leads to the premature failure of the specimen. Alternatively, the thermo-mechanical stress state is observed to induce extensive micro-cracking that progressively leads to leakage (Figure 2.24). [8], [33], [18], [26], [67], [80] The latter case can lead to scientific insights into the damage/leakage performance of composite laminates.

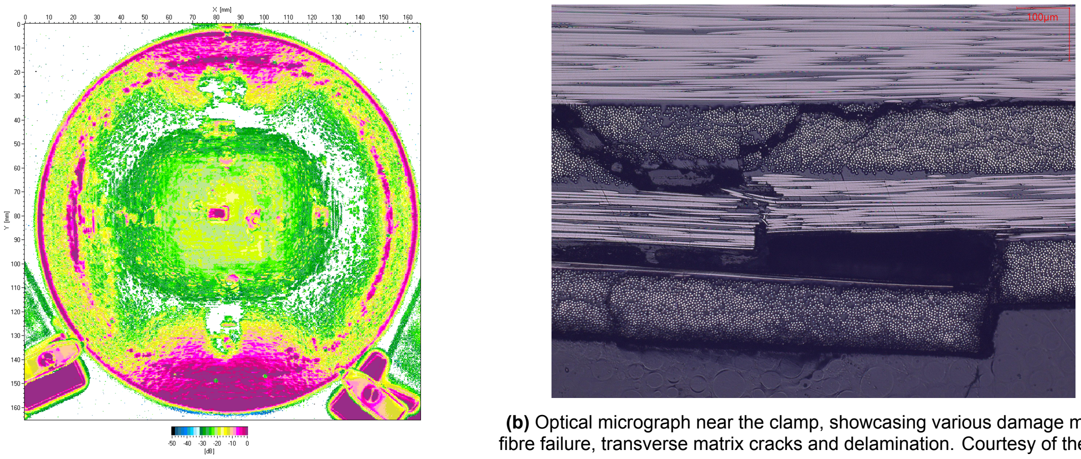

(a) Post-inspection ultrasound unearthing delamination near the clamping region

(b) Optical micrograph near the clamp, showcasing various damage modes: fibre failure, transverse matrix cracks and delamination. Courtesy of the DLR.

Figure 2.23: Damage/leakage observed by Hauser [28] in IM7/8552 bulge specimen, due to the boundary conditions of the test rig

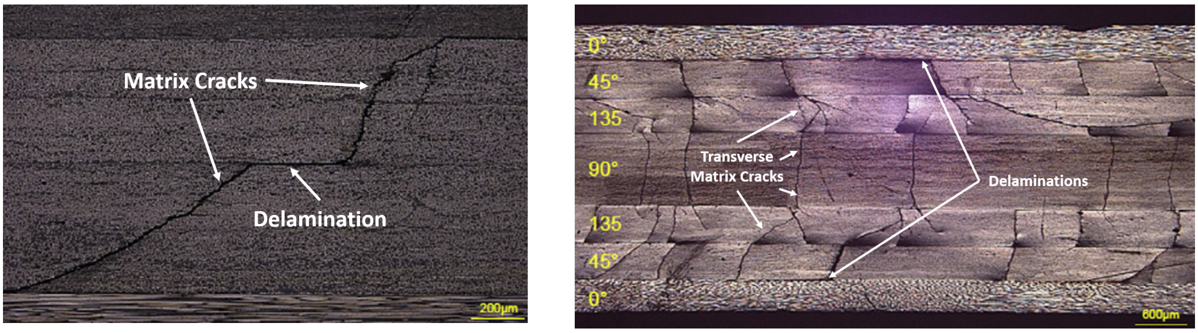

(a) Transverse matrix cracks, in adjacent plies, joined by delamination

(b) Extensive microcrack network (transverse matrix cracks and delaminations) through the laminate's thickness

Figure 2.24: Damage/leakage observed by Grogan [24] in CF/PEEK laminates, due to its thermo-mechanical stress state

Figure 2.23 and Figure 2.24 show that multiple damage modes may occur simultaneously. This means that both intra (within the ply) and inter (between plies) laminar damage modes should be modelled. In order to localise damage while keeping computational cost low, only damage initiation is required. Knowledge of damage initiation can be beneficial in the representative design of bulge specimen. For example, specimen that fail first due to their thermo-mechanical stress state can be designed.

Damage initiation sheds light on the failure load. It is useful to know the failure load of the specimen before testing. In that way, the loading sequence for that particular test can be tailored.

2.6.1. Inter-laminar

A stress or strain based criterion sufficiently captures inter-laminar damage initiation.

Equation 2.7 shows the quadratic stress based initiation criterion (QDC). t_n^0, t_s^o and t_t^o refer to the interface strength in the normal and two shear directions of the interface.

$$\begin{gathered} QDC = \left(\frac{t_n}{t_n^o}\right)^2 + \left(\frac{t_s}{t_s^o}\right)^2 + \left(\frac{t_t}{t_t^o}\right)^2 \\ QDC > 1 \implies \text{intralaminar damage initiation} \end{gathered} \tag{2.7}$$

In Abaqus, a cohesive zone (either interaction or elements) can be placed between plies. In such a case, the QUADS initiation variable is natively displayed in the visualisation module. However, the implementation of cohesive zones (even in the absence of traction-separation) increases computational time. Such increased computational cost cannot be justified if CZMs are only used for delamination initiation and not propagation. An alternative method to compute QDC is used. A post-processing python script is written to access the .odb file. The components of out-of-plane stress are extracted at the integration points of all plies. The stress at the interface is then estimated by averaging the stress of the adjacent plies. Such a technique is beneficial as it allows all solid elements to be merged together, thus eliminating the need for a CZM.

Following on, temperature dependent interface strengths had to be found. Unfortunately, the author could not find publicly available, reliable interface strengths for IM7/8552 at 77 $[\text{K}]$. On the contrary, Koord [41] experimentally characterises interface strength for M21/T700GC and uses them for subsequent inter-laminar progressive damage modelling. Temperature dependent properties are available at $-55°$C $(218$ $[\text{K}])$. While this is significantly higher than cryogenic temperature, the increase in interface strength can already be seen in Table 2.14. In fact, reducing temperature by only 75 $[\text{K}]$ doubles the interface strength. Presumably, interface strength is expected to be even higher than at cryogenic temperature. This means that delamination initiation should be more conservative than reality.

Table 2.14: Temperature dependent interface strength properties of M21/T700GC [41]

Temperature [K]	t_n^o [MPa]	$t_s^o = t_t^o$ [MPa]
218 (LT)	40	120
293 (RT)	20	60

The use of M21/T700GC instead of IM7/8552 further increases conservatism. Völkerink [82] reports higher interface strengths for IM7/8552 at RT, by up to 50%.

Finally, interface strengths are invariant for different ply orientations. [41], [82]

2.6.2. Intra-laminar

An intra-laminar damage initiation criterion is required to predict failure within the ply. The World Wide Failure Exercise (WWFE) I & II [36], [37] recommend the use of Puck, Cuntze or LARC. LARC05 is selected because it is implemented in Abaqus.

LARC05 is able to consider the following damage modes: fibre tensile failure, fibre splitting, fibre kinking and matrix failure. The initiation criteria for these modes are related to the lamina's material strength, according to the relations proposed by Pinho [65].

The temperature dependent material properties of IM7/8552 are given by Table 2.15. These values are used to compute the LARC05 damage initiation.

Table 2.15: Temperature dependent strength properties of IM7/8552 [71]

Temperature [K]	$R_{\parallel}^{T}/X_{T}$ [MPa]	$R_{\parallel}^{C}/X_{C}$ [MPa]	$R_{\perp}^{T}/Y_{T}$ [MPa]	$R_{\perp}^{C}/Y_{C}$ [MPa]	$R_{\parallel\perp}/S$ [MPa]
77 (CT)	2500.4	1500	55	300	120
293 (RT)	2500	1200.1	50.8	252	91.1

In-situ strengths are accounted for internally [65]. Additionally, three other parameters are needed to describe the failure envelope: fracture plane angle, and coefficients of longitudinal/transverse shear friction. Although the fracture plane angle is determined numerically, 53° is assumed. The coefficients of friction are both set to 0.1. [46]

2.7. Outlook

A mesoscale, linear elastic model of the bulge specimen has been developed, incorporating contact interactions to represent the mechanical influence of the test setup. Preliminary results suggest that the model is capable of capturing damage initiation and slippage. However, its predictive accuracy remains to be established.

The subsequent step is to assess the validity of the modelling approach. To this end, numerical strain fields will be compared against experimental measurements in chapter 5. The validation dataset, obtained using multiple sensing techniques as described in chapter 3, provides a basis for a systematic evaluation of model accuracy.

3

Experimental Methodology

The purpose of this chapter is to define the scope of the experimental data acquisition conducted in this study. To this end, the rationale underlying the development of the test matrix is first outlined. The selection and placement of sensors for the different test configurations are then described, followed by a discussion of the available methods for post-test damage assessment. Finally, a high-level overview of the bulge test procedure is provided. The overall aim of this chapter is to ensure that the experimental campaign yields data of sufficient depth and quality to enable detailed analysis and meaningful comparison with the numerical model.

Contents

3.1. Test concept

The over-arching concept of the experimental campaign is to conduct a limited number of (static) bulge tests to acquire an extensive dataset from a diverse range of sensor systems. It is envisioned that the multi-sensor test series sheds experimental insights into element-level testing conducted. The expected objectives of the test campaign shall be specified in subsection 3.1.1. As the present focus is on an optimal test specimen design (as explained in chapter 2), subsection 3.1.2 describes the variables that have to be constrained to derive the reduced test matrix presented in subsection 3.1.3.

3.1.1. Objectives

It is necessary that the CFRP bulge test specimen truly behaves in a representative manner to that of a cryogenic tank. Namely, the region of bi-axial strain in the middle of the bulge test specimen is considered characteristic of the strain state in the tank's spherical end-caps. It is desired that the bi-axial zone is as large as possible. For scientific research, it is required that the specimen fails in this bi-axial zone as a direct consequence of the applied thermo-mechanical load, and not due to the indirect or direct effects of the boundary conditions of the bulge test setup.

This experimental campaign explore different CFRP specimen design, with varied geometry (detailed in section 3.1). While experimental data can be acquired for different test designs of the specimen, the costly, time-intensive nature of (cryogenic) experiments makes it impractical to conduct parametric design studies. Only a simulation-driven-design approach can fine tune an optimal specimen. With that said, one aim of the experimental campaign is to provide validation data for FEM simulations.

Specifically, linear-elastic (strain) data of undamaged CFRP specimen is identified as a priority. As numerical simulation can predict strain over the entire specimen, as many strain sensors as possible are used to maximise the spatial regions of data acquisition. This in turn maximises the number of comparison not only between FEM-experiment but also between different sensors. Cross-referencing various sensors sheds light into erroneous measurements. In particular, a cryogenic environment is known to amplify temperature-induced errors and uncertainties in sensors.

Other data may help in further scientific work. For example, temperature readings may help validate a transient thermal/thermo-mechanical model. The onset of leakage can be traced back to the formation of through-the-thickness microcrack networks, thanks to the progression of damage in the laminate. [24], [30], [43]

Finally, the multi-sensor campaign shall help enrich the experimental know-how in integrating different sensors and setting up different configurations of the bulge test bench for future work.

3.1.2. Specimen constraints

The number of specimen parameters had to be constrained to isolate key variables of interest. The pre-preg material, (some) geometric parameters and stacking sequence of the specimen and the design of the reinforcement remain unchanged. These constrained specimen parameters are provided in Table 3.1.

It will later be seen in subsection 3.2.4 that the positioning of the sensors was also varied as little as possible across different test configurations to maintain comparable results. Other control variables pertaining to the test procedure shall also be described later in section 3.5.

Material

Hexcel® IM7/8552 unidirectional pre-preg is selected for the test campaign. This pre-preg system is the typically used for studying the behaviour of composites under a cryogenic environment. [16], [28],[46]. Pre-preg with intermediate modulus (IM) fibres, presumably due to their high tensile modulus, are widely used in development studies of linerless cryogenic tanks. [22], [60], [24], [68] The toughened 8552 epoxy resin system resists microcracks, thus rendering it a promising design choice against leakage. Thinner plies too are proven to resist mirco-cracking and delamination (and by extension leakage). [40] Thus, plies with a cured thickness of 0.131 $[\text{mm}]$ are used. [32]

Laminate

A cross-ply laminate is selected. It uses 8-plies, totalling a thickness of 1 $[\text{mm}]$. The same laminate design was used in preliminary bulge tests conducted by Hauser [28], making it a practical choice for comparing future test results.

It should be noted that a symmetric and balanced laminate is selected, to decouple bending/membrane and in-plane shear/axial behaviour. This may lead to an unanticipated strain (or even initiate unanticipated failure modes) at cryogenic temperature and/or pressure load. [39] In short, the additional influence of an unbalanced/asymmetric laminate is beyond the scope of the current experimental investigation. However, in future studies, a validated numerical model of the bulge specimen can help predict the performance of different laminates.

While stacks of same ply orientation are avoided to limit the propagation of transverse matrix cracks [39], such a laminate design may induce intra-laminar crack formation and lead to the detection of leakage at lower pressure loads. At the same time, it should be cautioned that such a laminate is only of scientific interest rather than a sound design choice for engineering a real-world hydrogen tank.

From experience, the 1 $[\text{mm}]$ thick laminate seems to be adequately thick to not be susceptible to damage during processing/handling but also thin enough to result in large strain amplitudes.

Geometry

The diameter and curvature of the test specimen were constrained. These parameters were derived from the anticipated geometry of the tank dome section.

The diameter of all specimen are practically determined by the dimensions of the bulge setup's test housing. It is therefore not possible to vary the diameter of the specimen without completely re-milling new clamps for the test bench.

Considering the curvature, it will be later seen in Figure 3.6 that the layup of the double curved specimen takes place on a positive mould. This mould is machined with a predefined curvature, that is not possible to modify.

Table 3.1: Overview of specimen constraints

Material [-]	Laminate [-]	Thickness [mm]	Diameter [mm]	Curvature [mm]
IM7/8552 UD Pre-preg	$[0/90/0/90]_s$	1.0	160	1000

Reinforcement design

One of the objectives of the experiment campaign is to understand the influence of a reinforcement ring. However, it is beyond the scope of the current test series to study the effectiveness of various reinforcement configurations. Therefore, the material and geometry of the reinforcement were kept constant. A metal ring (over a composite one) allowed for easier processing by machining the ring separately and then bonding it to the specimen. Aluminium was preferred (over steel) to better match the compliance of the CFRP specimen. The ring is 20 $[\text{mm}]$ wide and 1.5 $[\text{mm}]$ thick. The ring is only bonded to the outer side of the laminate. [46]

3.1.3. Reduced test matrix

After constraining parameters beyond the scope of the test series, a reduced test matrix was derived to focus on achieving the main objectives of the project. To re-iterate, these aims included quantifying the effect of: specimen geometry (F-Flat, C-Curved), presence of reinforcement (R-Reinforced, U-Unreinforced) and test temperature (RT-Room Temperature, CT-Cryogenic Temperature). CT is taken as the boiling point of LN_2 (-196 $[^\circ\text{C}]$). With that said, 5 tests were planned, as summarised by the test matrix in Table 3.2.

Table 3.2: Test matrix of the multi-sensor experimental campaign

ID	Reinforcement	Geometry	Test Temperature [°C]
U-F-RT	✗	Flat	20 ± 5
U-C-RT	✗	Curved	20 ± 5
R-C-RT	✓	Curved	20 ± 5
U-C-CT	✗	Curved	-196
R-C-CT	✓	Curved	-196

3.2. Sensors

The multi-sensor test series makes use of a large number of instruments that are part of the standard bulge test rig or have been integrated onto the specimen. Unless otherwise stated, a measurement frequency of 10 $[\text{Hz}]$ is used.

3.2.1. Standard sensors of the bulge test setup

The bulge test stand comprises of the following measurement systems: Pfeiffer ASM 340 leak detector, Thyracont VSR vacuum transducer, and Aventics pressure sensor. It can be assumed that these standard sensors will always acquire and record data during the test.

The Pfeiffer ASM 340 leak detector [64] measures the helium leak-rate on the gas analysis side. The device contains a turbo-molecular pump to create high-vacuum, as well as a mass spectrometer to measure the molecular flow of helium through it. It has a precision of 5.0×10^{-12} [mbar l s^{-1}]. A sudden increase in the leak-rate, during testing, may imply leakage in the specimen [28].

3.2.2. Thermocouples

Thermocouples are used for temperature measurement. Type T thermocouples to ensure cryogenic compatibility. PT-1000 sensors, with tolerance class F-01, are selected [6]. Up to 6 thermocouples can be connected to the data acquisition system of the bulge setup. However, at least 1 thermocouple must be mounted on the test setup itself. As a result, up to 5 thermocouples can be bonded to the bulge specimen, at measurement points of interest.

3.2.3. Integrated strain sensors

On top of thermocouples and pressure/vacuum gauges, strain sensors need to be integrated onto the bulge element. Strain-gauges, digital image correlation and fibre-optic strain sensors are available options for use. An overview is provided in Table 3.3.

Table 3.3: Comparison of Strain Measurement Techniques. Note that ϵ_{11}, ϵ_{22} refers to local strains, relative to the integrated sensor's co-ordinate system; ϵ_{xx}, ϵ_{yy} refer to global strains, relative to the coordinate system of the specimen

	Strain Gauges	**Digital Image Correlation (DIC)**	**Fibre Optic Strain Sensor (FOSS)**
Test Temperature	RT + CT	RT	RT + CT
Strain Components	ϵ_{11}, ϵ_{22}	ϵ_{xx}, ϵ_{yy}	ϵ_{11}
Dimensionality of Measurement	0D (point)	2D (surface)	1D (line)
Spatial Resolution	Up to 8 points [28]	Up to 20 [μm]	0.65 mm [7], [62]
Feasible Sensor Integration Location	Free surface of outer-most ply (gas analysis side only)	Free surface of outer-most ply (gas analysis side only)	Free surface of outer-most plies + Multiple inner ply-interfaces
Disruption to Standard Sensors	None	Vacuum Transducer and Leak Detector* cannot be connected	None

*While it is not possible to connect the ASM 340 leak detector for room temperature tests, coarse (helium) leakage measurements are taken using a hand-held sniffer. As the sniffer is as sensitive as the leak-detector (5.0×10^{-12} [mbar l s^{-1}]), the leakage measurement is easily affected by the ambient concentration of helium gas, that usually increases over the duration of the experiment. Therefore, only the presence of a leak can reliably be extracted by means of a helium sniffer. The corresponding leak-rates should be interpreted with caution.

Strain gauges (DMS)

Strain gauges compute strain by measuring the change of resistance of a conductor wire. The change of resistance is associated with the deformation of the wire seen by the strain gauge.

A number of different types of strain gauges are used. For example, a combination of uni-axial and bi-axial strain gauges are to be used for any given specimen configuration. This ensures that all eight channels of the experimental setup are always used, whilst gathering strain data for the largest number of points of interest. Cryogenic tests use special, self-compensated strain gauges.

Another point about the location of the strain gauge measurement has to be addressed. Strictly speaking, strain is measured over a grid area. uni-axial ones have a measurement grid of 3.0×1.6 [mm] while bi-axial ones cover an area of 3.0×3.2 [mm]. While comparing strain gauge data with numerical results, it is important to compare the strain over the entire measurement grid.

Digital Image Correlation (DIC)

DIC tracks the movement of an applied pattern during an experiment. Highly random and high contrast, black & white, speckle patterns are used.

The 12 MPixel ARAMIS system by GOM is used. Photographs are taken with a consumer full frame mirrorless camera with a resolution of 42 mega pixel. This achieves an estimated resolution of 20 [μm]. Two triangulating cameras must be used to conduct 3D DIC.

Moreover, a bright, blue light is used to click the DIC photographs, thus ensuring good brightness and reducing the dependency of ambient light.

It should be further noted that DIC is only possible if there is direct access to one side of the specimen. That means that the compartment on the side of gas analysis will be left open during DIC. Submerging a half-open specimen into a cryogenic bath may lead to complications in the experimental procedure. Therefore, it is assumed that DIC is only possible at room temperature.

Fibre Optic Strain Sensors (FOSS)

A polyimide coated optical fibre (with core) measures 1D strain over the length of the fibre, by using the principle of Reyleigh back-scattering. An acrylate coated coreless fibre is used for sensor termination, that will be shown in Figure 3.4. FOSS fibres can be embedded into the specimen during the manufacturing process, enabling the characterisation of strain along ply interfaces.

3.2.4. Positioning of temperature and strain sensors

Figure 3.1 illustrates the positioning of strain gauges and thermocouples. All 8 available strain channels in the software of the bulge setup are used by three bi-axial and two uni-axial strain gauges.The strain gauges are placed along two orthogonal lines, that coincide with the theoretical position of the embedded FOSS sensors. This is supposed to help make different sensor measurements spatially comparable. The position of strain gauges in the cryogenic and room temperature specimen configuration are the same, again to make different measurements easily comparable.

The difference in the cryogenic configuration is the presence of more than one thermocouple, at radially different points. Some thermocouples are placed along the fibre while other transverse to it. It is hoped that doing so can better help understanding the thermal anisotropic of CFRP during cryogenic cooling.

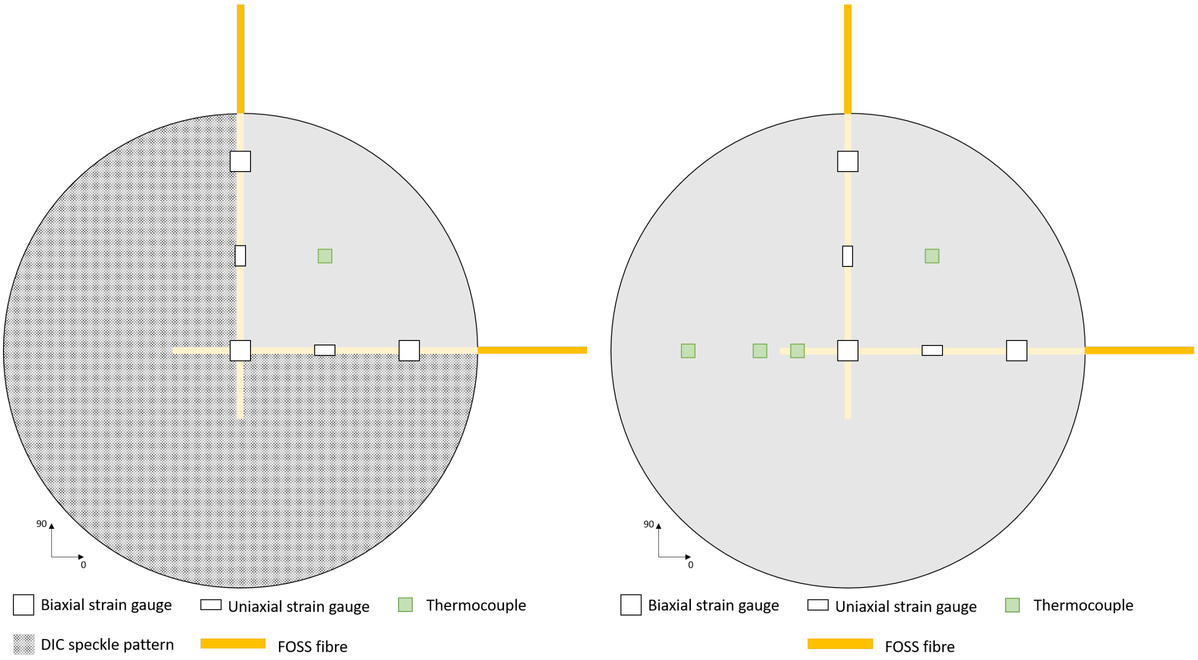

(a) Room temperature configuration

(b) Cryogenic temperature configuration

Figure 3.1: Illustration of the specimen showing the position of the strain sensors and thermocouples

Detailed technical drawings showing the exact position of the strain gauges and thermocouples in all 5 specimen are provided in chapter 4.

A cross-section illustration showing the through-the-thickness position of the FOSS fibres embedded in the laminate is given by Figure 3.6a. While four FOSS fibres can be connected to the data acquisition system, only two are used (per specimen) due to practical constraints.

3.3. Damage assessment

Thus far, strain and temperature measurements were outlined. However, it is difficult to directly assess damage in the specimen. Therefore, some damage assessments must be qualitatively performed on the bulge specimen before (if possible) and after testing, to provide insight into the existence of damage.

Acoustic emissions and optical microscopy are commonly used methods at the DLR. A note about X-ray Computed Tomography. The X-ray at the DLR does not offer a sufficiently high resolution to detect microcracks.

An overview of the two structural integrity assessments are provided in Table 3.4

Table 3.4: Summary of qualitative damage assessment techniques

	Acoustic Emissions (AE)	Optical Microscopy
Type	Non-Destructive	Destructive
Applicability	Pre-/Post-test	Post-test only
Output	Ultrasound C-Scans	2D Optical Micrographs
Damage Assessment	Delamination	Matrix Cracking/Delamination/Fibre Failure

3.3.1. Acoustic Emissions (AE)

Ultrasound examination can be performed on the specimen before and after the bulge test. Pulse-echo is used at a frequency of 5 $[\text{MHz}]$ or 10 $[\text{MHz}]$, at an interval of 0.25 $[\text{mm}]$ to obtain a C-scan [28].

These C-scans can be used to detect delamination. As a result, there is potential in comparing the results of acoustic emissions with the output of the inter-laminar damage model. However, one must be careful about interpreting results in highly curved regions. In the pulse-echo method, the ultrasonic wave relies on being reflected back towards the transducer. Strong curvature of the specimen surface can cause the wave to scatter or be deflected away, reducing the return signal and thereby introducing uncertainty or false negatives in the detection of damage.

3.3.2. Optical microscopy

Optical micro-graphs can be obtained after the bulge test. Cross-section of the specimen, at the regions of interest, need to be cut with a diamond saw. Unfortunately, that means that the specimen will be destroyed.

These micro-graphs have the potential to help identify leakage paths, that may arise due to a combination of matrix cracking and delamination.

3.4. Specimen preparation

A number of experimental activities and quality checks were conducted in order to integrate multiple sensors into the CFRP bulge specimen. These processes are summarised in Figure 3.2.

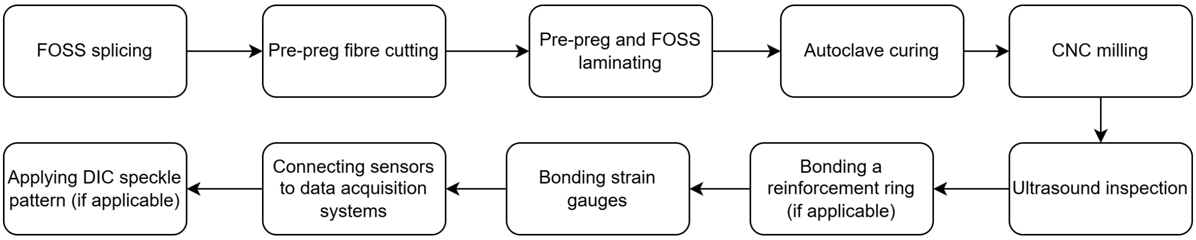

Figure 3.2: Overview of multi-sensor specimen preparation, prior to bulge testing.

In this section, the steps depicted in Figure 3.2 shall be described in a sufficient level of detail to ensure reproducibility of the experimental work.

3.4.1. FOSS Splicing

In the context of FOSS, a 'splice' refers to a permanent joint between different lengths of fibre. At the DLR, a fusion splicer, as shown in Figure 3.3b, is used to join two optical fibre by melting them with an electric arc. Prior to splicing, the cross-section faces of both fibres are prepared. A precise 'cleaver' (Figure 3.3a) finely cuts the ends of the fibre, thus leaving behind a smooth, flat face that is ready to be fused. A smooth end-face ensures low signal losses across a splice as well as improves mechanical integrity of the weld. [21]

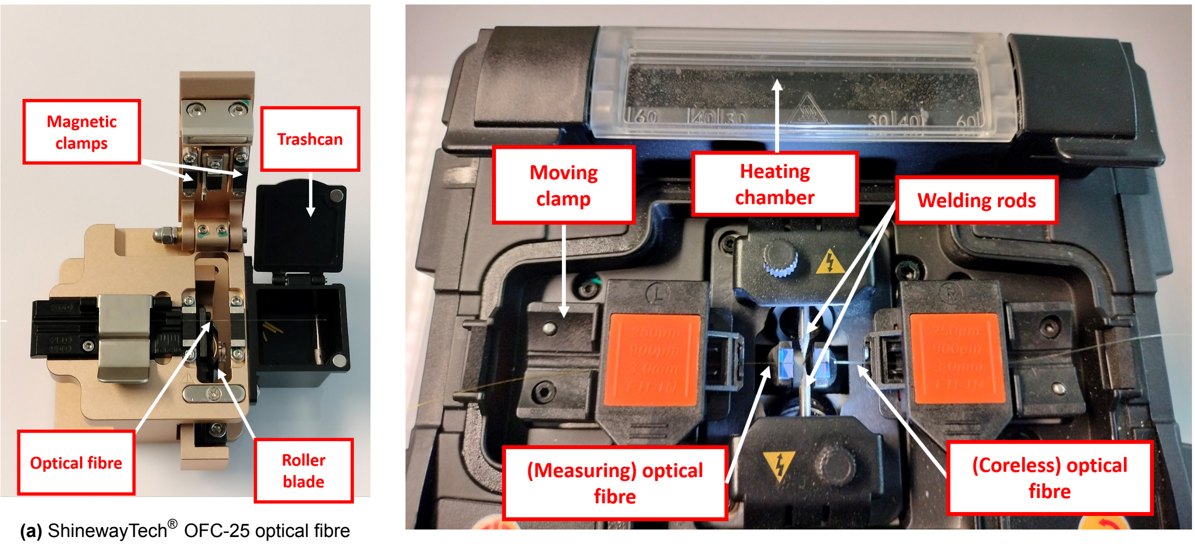

(a) ShinewayTech® OFC-25 optical fibre cleaver. Two clamps fix the fibre in place. A sharp roller blade cuts the rough ends of the optical fibre to leave behind a flat surface for welding.

(b) ShinewayTech® OFS-95 S optical fibre splicer. Two moving clamps bring two optical fibres into contact, prior to fusion. An electric arc heats the ends of the optical fibres above their melting point to create a seamless weld. Due to the fragile nature of the splice, it is covered with a protective shrink tubing in the heating chamber.

Figure 3.3: FOSS splicing system used at the DLR

Specifically, a splice has to be created between the measuring optical fibre and core-less fibre. As the name suggests, coreless fibre do not have any optical fibre (only a protective coat) that do not allow for signal transmission. This causes light to be dispersed into the core-less fibre, instead of being reflected back into the measuring segment. This ensures that the signal terminates correctly, without interfering with the measurement signal. Figure 3.4 shows a termination splice.

It is to be noted that the fibres must be decoated before splicing. Wire strippers are used to remove the coating of the coreless fibre. The measuring fibre is burned at the edges with a lighter, and the coating dissolved in water.

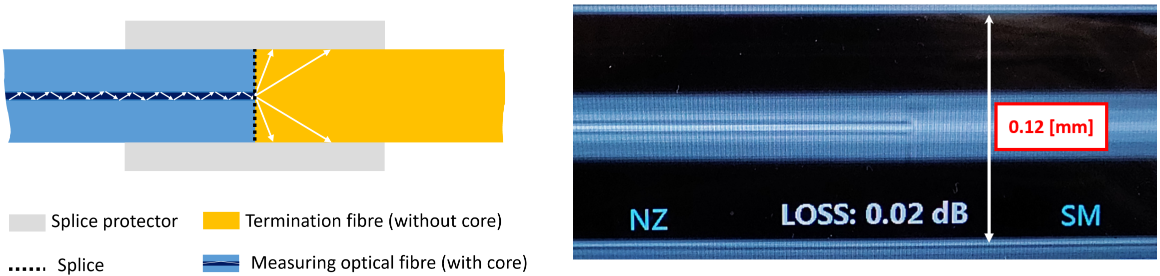

(a) (Not-to-scale) schematic of fibre termination. The measuring fibre is spliced with a shorter coreless segment, to disperse the travelling light wave. While it is recommended to use the splice protector to fortify the fragile weld, it cannot be used if the fibre terminates inside the specimen itself. This is because the $1 - 2$ [mm] thick walls of the tubing would create an unevenly thick laminate and possily introduce void defects. The diagram is adapted from Herget's work [31].

(b) Photograph of an exemplary termination splice, between measuring optical fibre (left) and coreless fibre (right). The coreless fibre can be visually identified by the absence of a sharp white line in the middle. In this splice, a signal loss of 0.02 [dB] is achieved. All fibres were spliced with a signal loss of $0.01 - 0.03$ [dB]. The splice was redone if the signal loss was higher than 0.05 [dB] or if defects at the weld were visible.

Figure 3.4: FOSS termination splice

In Figure 3.4a, it can be seen that the fibre terminates inside the specimen. This was necessary to preserve the structural integrity of the FOSS. Specifically, from experience, it was determined that the delicate measuring fibre would not be able to withstand the compressive clamping force from the housing of the bulge rig. Therefore, it was necessary to connect the measuring fibre to its core-less counterpart prior to the start of the clamping zone of the bulge rig. Consequently, strain data from the FOSS is not available for the entire length of the bulge specimen, but it is ensured that the measurement range encompasses at least the radius.

Further practical details of the splicing procedure are provided by Herget [31].

3.4.2. Pre-preg fibre cutting

A CNC fibre-cutting is used to cut the pre-preg to the required dimensions. Effectively, a 400×400 [mm] template is cut. Four specimen can later be CNC milled from the cured laminate. Doing so reduces the laminating time and ensures that the test specimen are away from the high defect edge regions.

The exact dimensions of the pre-preg template is shown in Figure 3.5a, which in turn is derived from the positioning of the FOSS fibres and the positioning of the specimen (Figure 3.5b). The size of the template is constrained by the area of the milling bed.

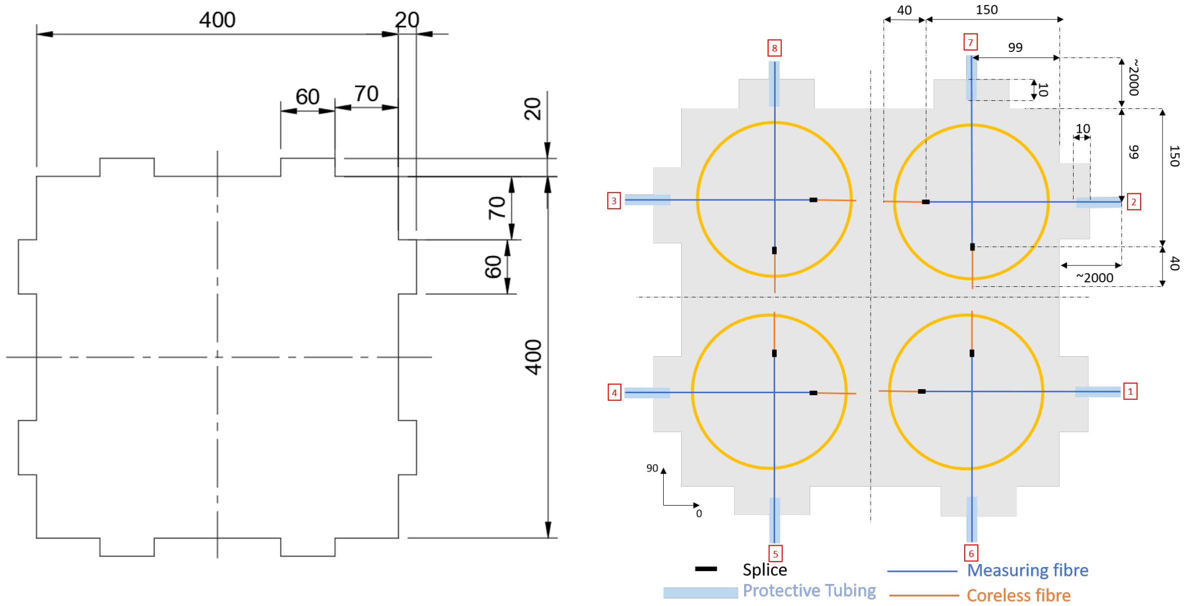

(a) Technical drawing of the pre-preg that was cut. The protruding edges provide a pathway for one end of the embedded FOSS fibre to leave the specimen when it is clamped inside the bulge test setup. It was not possible to make the plate bigger, due to limited clearance on the bulge milling tool.

(b) (Not-to-scale) illustration showing the position of the four bulge specimen and dimensions of different segments of the FOSS fibre.

Figure 3.5: Pre-preg template

Consider the layout of the FOSS fibre in the specimen (Figure 3.5b). Two orthogonal optical measuring fibres were placed at least from the edge of the specimen to its centre. This ensured that strain measurement took place along two perpendicular radii of the specimen. It should be noted that two FOSS fibres are placed at different ply interfaces, as later clarified by Figure 3.6a.

3.4.3. Pre-preg and FOSS laminating

A 1 [mm] symmetric, balance cross-ply laminate with two orthogonal FOSS fibres was selected. The laminate stacking sequence is illustrated by Figure 3.6a. An example of the FOSS placement during the laminate build-up is photographed in Figure 3.6b.

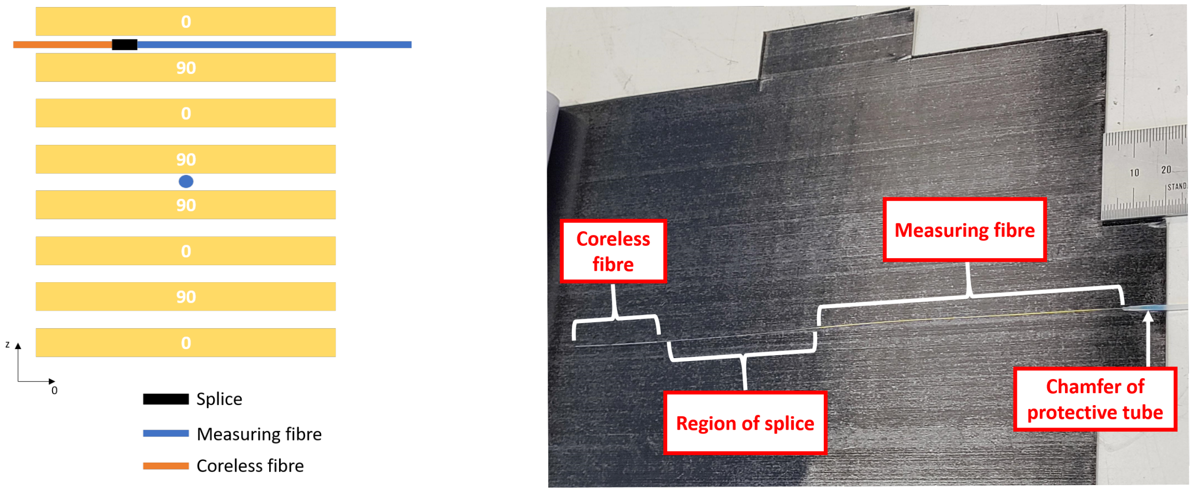

(a) Illustration of cross-ply specimen, depicting the position of the FOSS fibres (90° FOSS at the midplane; 0° FOSS one ply below the topmost layer).

(b) Photograph of a FOSS fibre. The termination of the measuring fibre with the shorter coreless segment is visible inside the laminate

Figure 3.6: Laminating pre-preg and integrating FOSS fibres, for the flat plate

Figure 3.6b can revealed insightful details about the laminating procedure of the optical fibres.

In order to securely bond the protective tubing to the laminate (during the cure cycle), 10 $[\text{mm}]$ of the tube has to be introduced into the plate. Furthermore, a shallow chamfer is cut into the protective tubing to allow a smooth transition in the stiffness of the tube as it is introduced to the laminate.

Unfortunately, the hand placement of the optical fibres means that they will never be perfectly straight. This is despite the use of multiple rulers for alignment. Some distortion is caused when tapping the fibres into the pre-preg. The position of each fibre can be captured via a T-scan, using the Hawk 2 scanner. In fact, the dotted black reference points for this system are visible in Figure 3.8. With the use of these T-scans, it is determined that there is a deviation of $0-6$ $[\text{mm}]$ of the fibre from the target path. The path deviation of all fibres is visualised in Figure 3.7. The index of the fibres shown in Figure 3.7a-3.7d are referenced from Figure 3.5b.

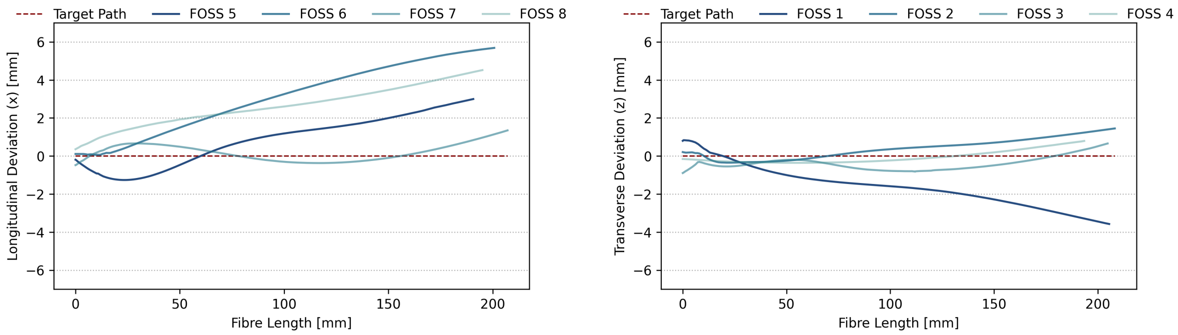

(a) Curved plate, ”Transverse” fibre between ply 4 and 5

(b) Curved plate, ”Longitudinal” fibre between ply 7 and 8

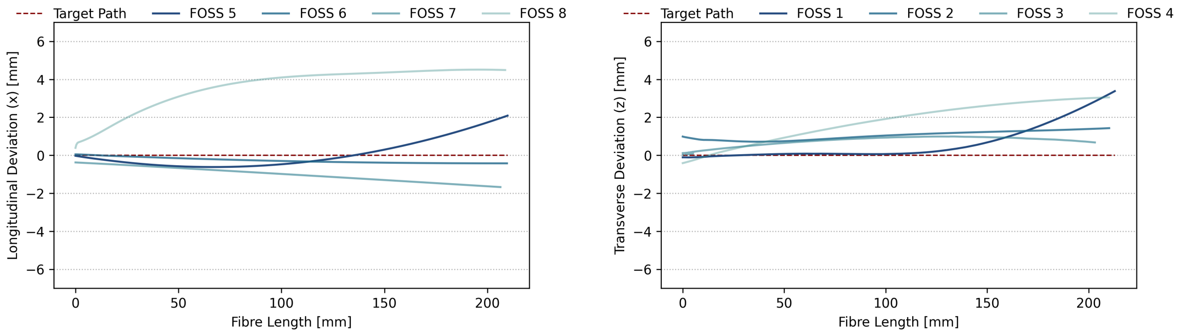

(c) Flat plate, ”Transverse” fibre between ply 4 and 5

(d) Flat plate, ”Longitudinal” fibre between ply 7 and 8

Figure 3.7: Deviation of FOSS fibres from the target path, based on T-Scan images.

Over and above that, there is uncertainty in the exact termination location of the measurement optical fibre. Prior to splicing, the protective sheath of both optical/coreless fibres must be removed with wire-strippers. The splice is then created in the region of ’naked wire’ (without protective coating). It is not possible to visually identify the exact location of the splice, but it is said to exist in this region of ’naked wire’ (easily identifiable where the fibre becomes thinner). This explains why ’a region of splice’ is labelled in Figure 3.6b.

Finally, snapshots of the plate buildup is shown in Figure 3.8.

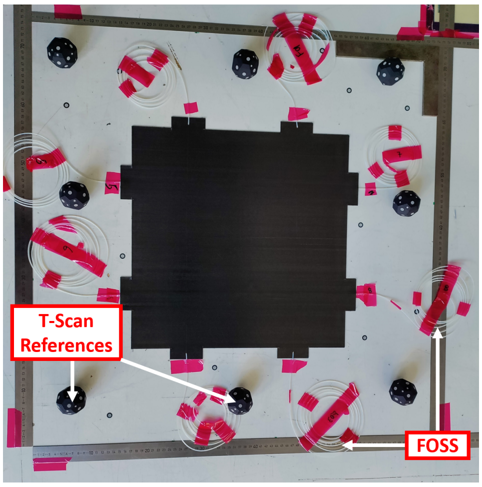

Figure 3.8: Pre-preg layup of the flat plate

3.4.4. Vacuum build-up and autoclave curing

After laminating the FOSS and prepreg, vacuum build-up takes place. Cork is applied around the edges of the uncured laminate, to allow an even exit passage of trapped air through the side edges. Unperforated release film is placed on the plies, to prevent excessive loss of the resin. Peel-ply is placed on top of the release film, and breather on top of the peel-ply.

Upon ensuring leak-tightness of the vacuum build-up, both the flat and curved plates were cured inside an autoclave. The manufacturer's recommended cure cycle is shown in Figure 3.9

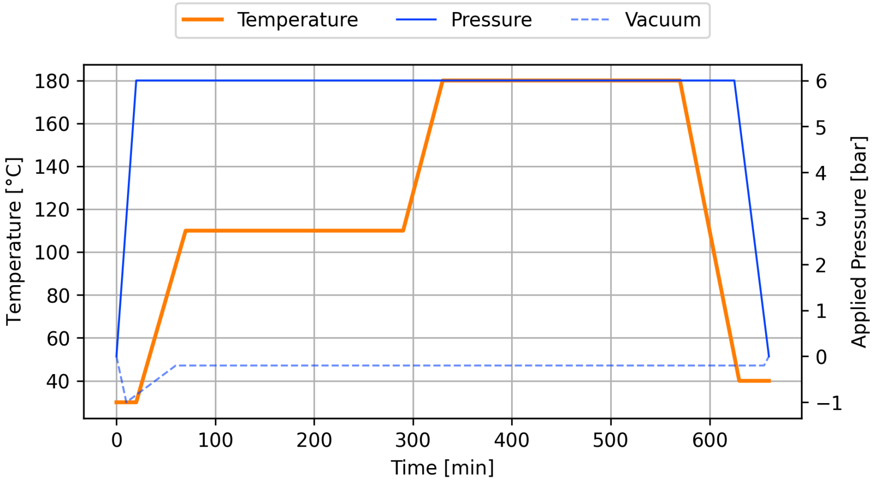

Figure 3.9: IM7/8552 cure cycle

After curing, the thickness of each plate was measured at 10 different locations. The mean thickness and the range (difference between thickest and thinnest point) is reported to be 1.04 ± 0.05 [mm] and 1.02 ± 0.10 [mm] for the flat and curved plate respectively.

3.4.5. CNC milling

The cured laminates were CNC milled. Supporting the curved plate during milling requires a positive aluminium mandrel. This mandrel was machined to match the inner radius of curvature of the plate. Pockets were created along the milling route, to allow adequate clearance for the end mill-bit during processing.

(a) Cured flat plate before milling.

(b) Curved plate after milling. Each cured plate yields four (circular) bulge specimen, and four small (rectangular) passenger samples. The edges of the bulge specimen provided an exit route for the embedded FOSS fibres. These edges were subsequently removed using a dremel.

Figure 3.10: Cured laminate: before and after milling

3.4.6. Ultrasound inspection

The hand layup of the pre-preg and milling may cause defects in the specimen. The presence of voids and delamination especially may alter the leakage performance of the CFRP laminates [24]. Therefore, an ultrasound emission was conducted to identify the onset of any (inter-laminar) damage. No visible damage/delamination could be seen in the C-scans of the specimen after manufacturing.

A second ultrasound inspection shall be conducted after the bulge test- to assess any damage that occurred during testing. Selected scans will be presented in chapter 5.

3.4.7. Bonding the reinforcement ring

The influence of a reinforcement ring was subject to investigation in this test campaign. Therefore, a machined aluminium ring was adhesively bonded to the CFRP specimen. The surfaces were prepared by solvent cleaning with isopropanol and hand sanding to improve roughness.

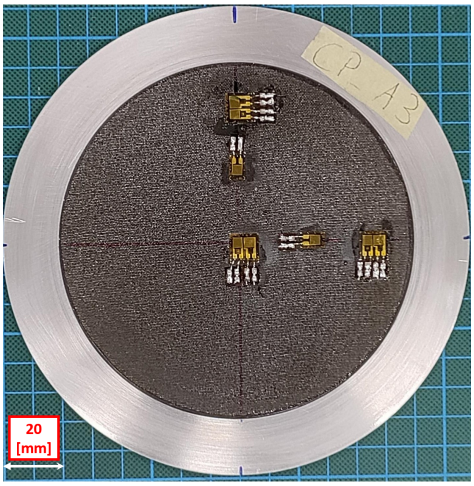

Figure 3.11: CFRP specimen with reinforcement ring and strain gauges

3.4.8. Bonding the strain gauges

Several steps are required for the precise adhesion of the strain gauges. 3D printed alignment jigs are used to keep the specimen (especially the curved one) in place during markings, sanding and glueing.[28] Specifically, a stencil aids the marking of the positioning of the strain gauges, as measured from the centre of the specimen. Figure 3.11 shows an exemplary specimen with bonded strain gauges.

3.4.9. Connecting sensors to data acquisition systems

Strain gauges and FOSS fibres have to be connected to their data acquisition systems. All strain gauges need to be soldered while FOSS fibres need to be keyed.

FOSS keying

The FOSS fibres are connected to the LUNA Odisi 6 interrogator. Prior to doing so, the measuring optical fibres are spliced to pigtails. Each pigtail has a sensor key, to uniquely identify the FOSS fibre and characterise the sensor's strain state. [47]

Connecting the sensor to the data acquisition system for the first time verifies the sensor health. For example, the strength of the return signal is measured. The loss of the return signal must be in the range of -75 [dB] to -55 [dB]. It is possible to make the signal loss more negative by cleaning the sensor plugs; alternatively, the signal loss can be made more positive by making the connectors more 'dirty' (eg: by gently rubbing against the skin). Often, a non-zero strain signal is shown. This can be due to the spooling of the fibre or residual strains from the autoclave processing. In any case, the strain sensor has to be tared. Following on, the gauge length inside the specimen should be indicated. This is because one is only interested in the strain values inside the specimen, and not over the length of the measuring fibre that is outside of it. The starting point is recognised as the ends of the specimen's protrusions. By pressing the fibre at this point, a sharp peak in the signal is created at that location, thus helping identify the starting point of the measurement.

Soldering the strain gauges

Strain gauges are soldered to be connected to the bulge test stand. Three-wire technique is used to cancel out cable/lead effects. [28], [29] What is more is that the cables of the strain gauges have a snagging risk, that may debond the already delicate sensors from the specimen. To reduce that, the sensors are first soldered onto the specimen, before being connected to the test bench. This is visible in Figure 3.12.

Upon the completion of that, thermocouples are finally attached using adhesive strips. 24 [h] of room temperature curing is needed.

3.4.10. DIC speckle pattern application

It is to be re-iterated that DIC is only applicable for room temperature tests. A black and white, dense, random, high contrast speckle pattern is applied to the surface of the specimen. An example image is shown in Figure 3.12. The speckle pattern is only applied to three-quadrants of the specimen. One quadrant is left free of the DIC, to allow room for routing the soldered wires of the strain gauges and thermocouples.

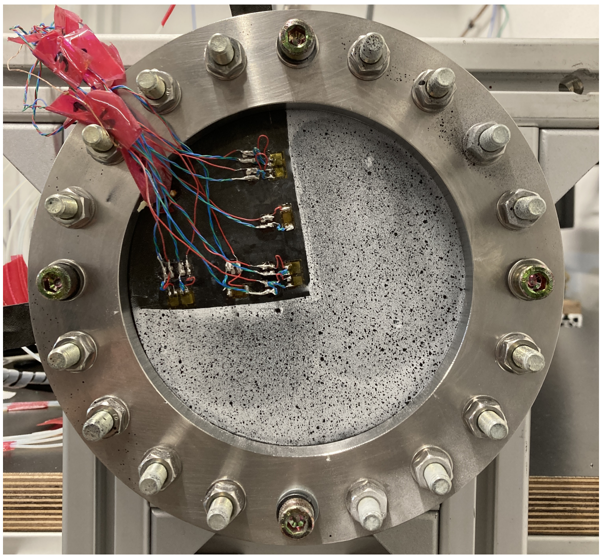

Figure 3.12: Clamped specimen with DIC speckle pattern and strain gauges/thermocouples attached.

3.5. Bulge test procedure

The complexity of the bulge test procedure can be simplified to controlling two independent variables: helium pressure and temperature. Raw test data of the input variables is visualised in Figure 3.13.

The amount of helium pressure is precisely controlled on the supply side (inner surface of the specimen) with a PID controller, comprising of pressure sensors and valves. In the multi-sensor test series, a pressure step of 1 $[\text{bar}]$ is used until the maximum allowable pressure of 20 $[\text{bar}]$ is reached. At every pressure step, data is collected over a measurement period of at least 5 $[\text{min}]$ - with the expectation that the specimen has enough time to stabilise to a higher load level.

For room temperature tests, the measurement interval involves clicking a DIC photo three times during the measurement interval (at $0,\ 2.5,\ 5$ $[\text{min}]$) and performing two handheld sniffer tests during that time. Concerning cryogenic tests, the valve connecting the gas analysis side (outer side of the specimen) is connected to the leak-detector if and only if an adequately low ($< 1.0^{-2}$ $[\text{mbar}]$) pressure is achieved with a rough vacuum pump. Doing so avoids polluting the highly sensitive mass spectrometer of the ASM 340.

The test temperature is coarsely controlled. Either the test is conducted at room temperature (RT), 20 ± 5 $[°\text{C}]$ or at cryogenic temperature -196 $[°\text{C}]$ by submerging the setup in LN_2.

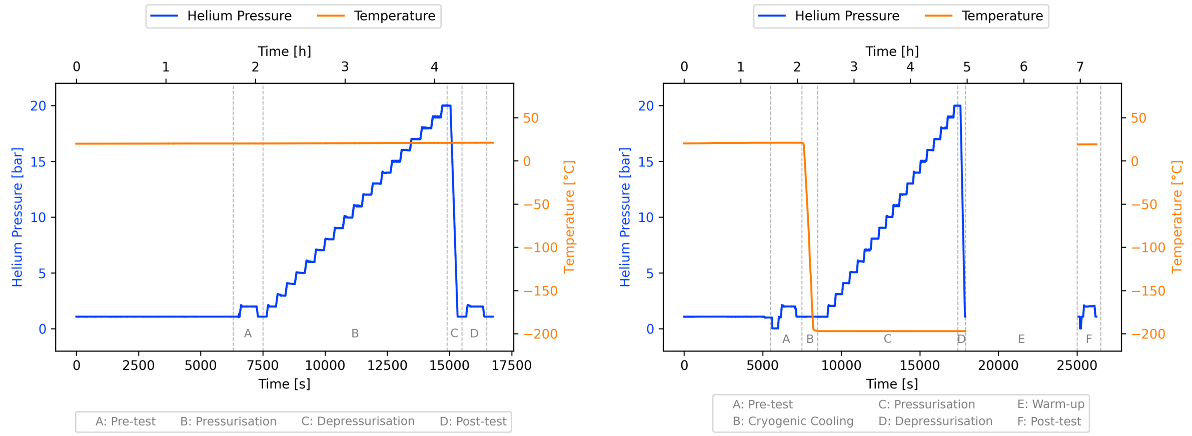

(a) Room temperature test. Data extracted from R-C-RT.

(b) Cryogenic temperature test. Data extracted from U-C-CT.

Figure 3.13: Bulge test procedure. Helium pressure and temperature are the two main independent variables of the experiment.

It can be seen from Figure 3.13 that the majority of testing time is dedicated to the pressurisation stage, where the pressure is ramped by 1 [bar]. A linear ramp rate of 1 [bar/min] is used. The majority of leakage, strain and temperature measurements are acquired during pressurisation. On top of that, a room temperature pre and post tests at $1,\ 2$ [bar] are conducted. These tests help quantify the difference in measurement due to a change in the condition of the specimen or the setup. For example, a specimen that gets damaged during the test may show higher strains/significant leakage in the post-test than the pre-test. Similarly, a polluted leak-detector may show higher apparent helium leak-rate in the post-test.

For cryogenic tests, at least 2 [h] of warm-up is needed. During this period, sensors are turned off to avoid excessive memory usage.

Over and above that, sensors are started $1 - 2$ [h] before the pre-test to record the strain response of the specimen during clamping.

Finally, there is one exception to the test procedure described so far. If the leak-rate exceeds 1×10^{-4} [mbar l s^{-1}], the test is stopped by de-pressurising the supply side chamber. Leakage before complete pressurisation is visualised using real test-data in Figure 3.14.

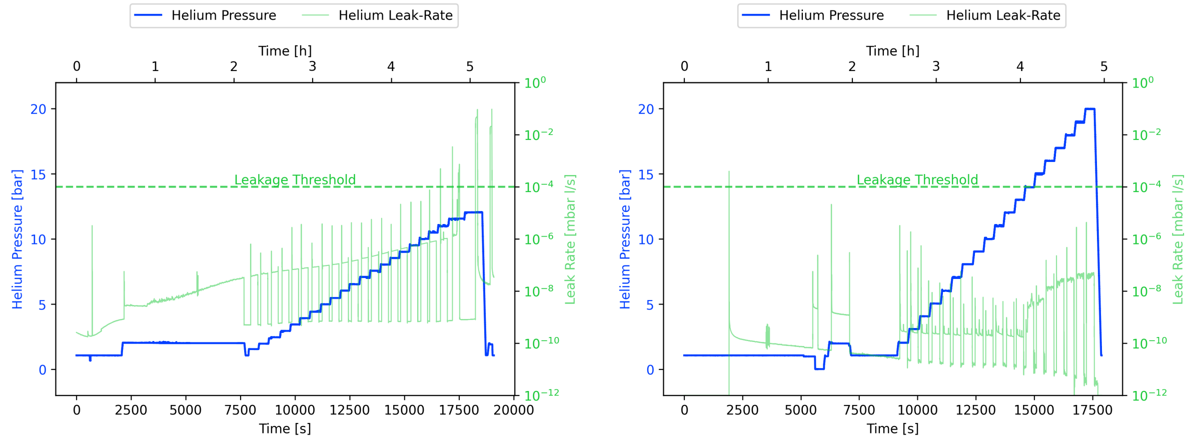

(a) Test stopped at 11 [bar] due to leakage. Data extracted from Hauser's U-C-RT test [28].

(b) Test continued till 20 [bar] due to absence of leakage. Data extracted from U-C-CT.

Figure 3.14: Exception to the bulge test procedure - leakage before 20 [bar]

Sharp peaks in the leak-rate are visible in Figure 3.14. These sharp peaks are attributed to the rapid pressurisation of fluid in the pipes of the gas analysis side of the specimen, due to the opening of valves connecting the specimen to the leak-detector. Usually, this transient response tends to steady-state within $5 - 15$ [s].

3.6. Outlook

The experimental methodology of the multi-sensor experimental campaign has been described. A total of 5 bulge tests, with different configurations are planned. Extensive data can be acquired for each tests. This data includes strains from DIC, FOSS and strain gauges (DMS). The dataset is augmented by the use of standard sensors from the bulge test- such as various thermocouples, pressure sensors and the leak detector. The raw results from these tests are reported in detail in chapter 4. Some of the experimental data is further post-processed to quantify the validity of the numerical model (chapter 5).

4

Experimental Results and Discussion

The objective of this chapter is to present the raw results of the multi-sensor experimental campaign. Five specimen configurations were tested, as previously described in chapter 3.

Each section reports the experimental results of one test. The structure of each section is the same:

- A post-test photograph of the bulge specimen is shown. A side-by-side technical drawing shows the exact position of various strain and temperature sensors.
- Test overview plots are extracted from the standard sensors of the bulge test setup. These include pressure/vacuum gauges and leak detectors/sniffers. In addition, signals from strain gauge and thermocouple are plotted. No corrections are made to the sensor signals in this chapter.
- Strain measurements from FOSS, DIC and DMS are compared, at select locations of each specimen.

The reader is provided with an overview of the test campaign. The failure (if any) load and mode for each specimen configuration is reported. Faulty sensors are identified. Data from faulty sensors is excluded from further analysis. All in all, an in-depth familiarisation of experimental results is an important prerequisite in interpreting the data that are subsequently compared with numerical predictions (chapter 5).

Contents

4.1. Un-reinforced, flat specimen at room temperature (U-F-RT)

The flat specimen offers a scientifically valuable control point. It helps quantify the effect of curvature. Differences in specimen behaviour, especially leakage, due to differences in processing (eg: less wrinkles created during pre-preg layup of flat specimen, in contrast to double curved ones) can potentially be explained by the test results of the flat sample. This test also produces an additional validation dataset for numerical simulations.

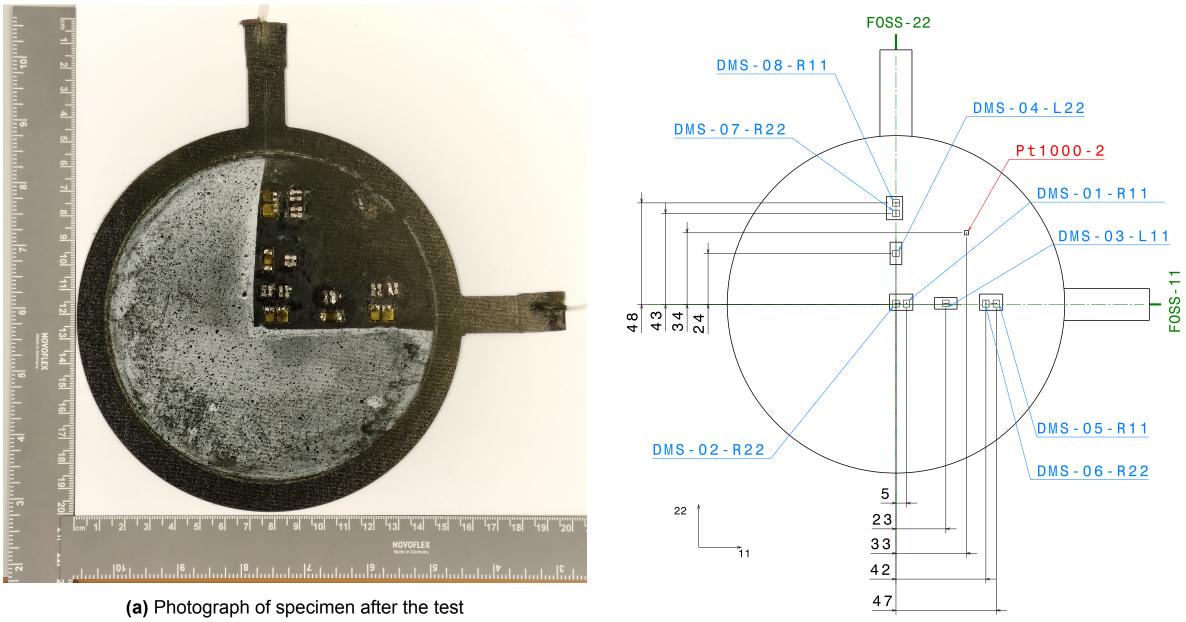

(a) Photograph of specimen after the test

(b) Technical drawing showing the position of sensors

Figure 4.1: U-F-RT specimen

Figure 4.1 shows the actual location of the sensors, as measured directly from the specimen that was manufactured and tested (Figure 4.1a). The exact position of strain gauges (DMS) and thermocouples (PT1000) is shown. The dimensions are referenced from the centroidal axes of the circular part of the specimen, and extend up to the midpoint of the measuring grids of the sensors. ”L” and ”R” refer to uni-axial and bi-axial strain gauges. ”11” and ”22” are parallel and perpendicular to the fibre direction of the outer-most ply.

4.1.1. Test overview

An overview of leakage and strain is presented for U-F-RT. The progression of strain corresponds to the strain gauges (DMS) shown in Figure 4.1. The reader is reminded that the leak-detector cannot be connected for room temperature tests. Therefore, an external hand-held sniffer is used. ”Average” values of the leak-rate at each pressure steps are noted down discretely.

It is known a priori that there are several caveats in the design of flat specimen for representative element-level testing. Trivially, the geometry of the tank dome is not matched. The absence of curvature is expected to amplify the stress concentration at the clamp. Unlike curved specimen, there is no taper angle near the clamp to minimise the rotational strain of the specimen due to a pressure load. [61] As a consequence, the physical boundary conditions of the test rig are anticipated to have the biggest influence on the flat specimen. From prior testing experience, it was assumed that there can be damage near the clamps and the specimen will leak before maximum loading. It was also assumed that leakage will likely be present near the clamp and not at the central bi-axial strain zone.

Indeed, the test overview (Figure 4.2a verifies the leakage before maximum loading expectation). The test was stopped at a helium pressure of 11 [bar]. Figure 4.2a shows that the leakage threshold of 1×10^{-4} [mbar l/s] was exceeded. Figure 4.2b shows the strain overview corresponding to the position of sensors in Figure 4.1b.

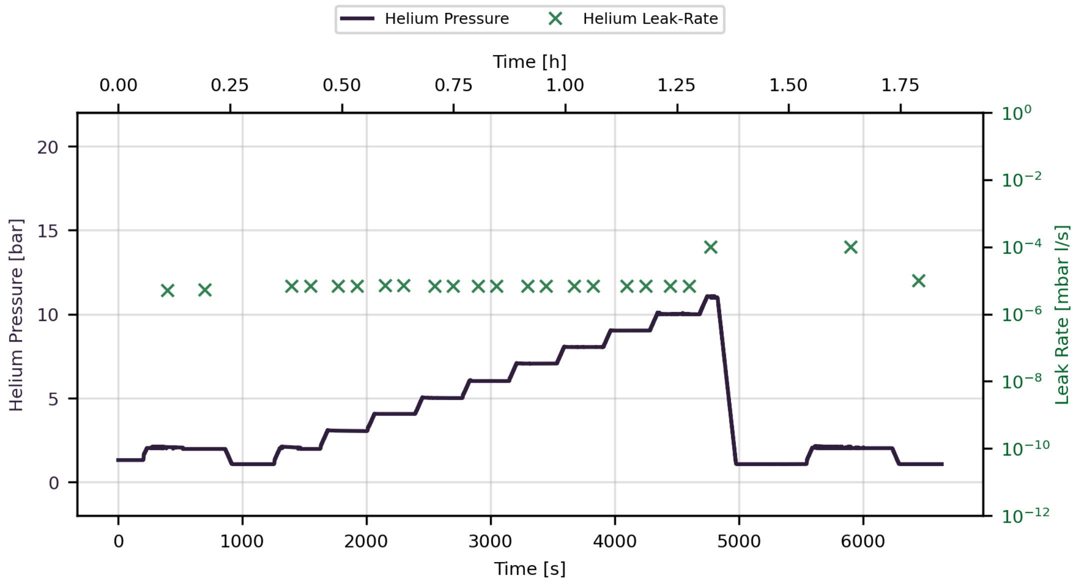

(a) Leakage overview

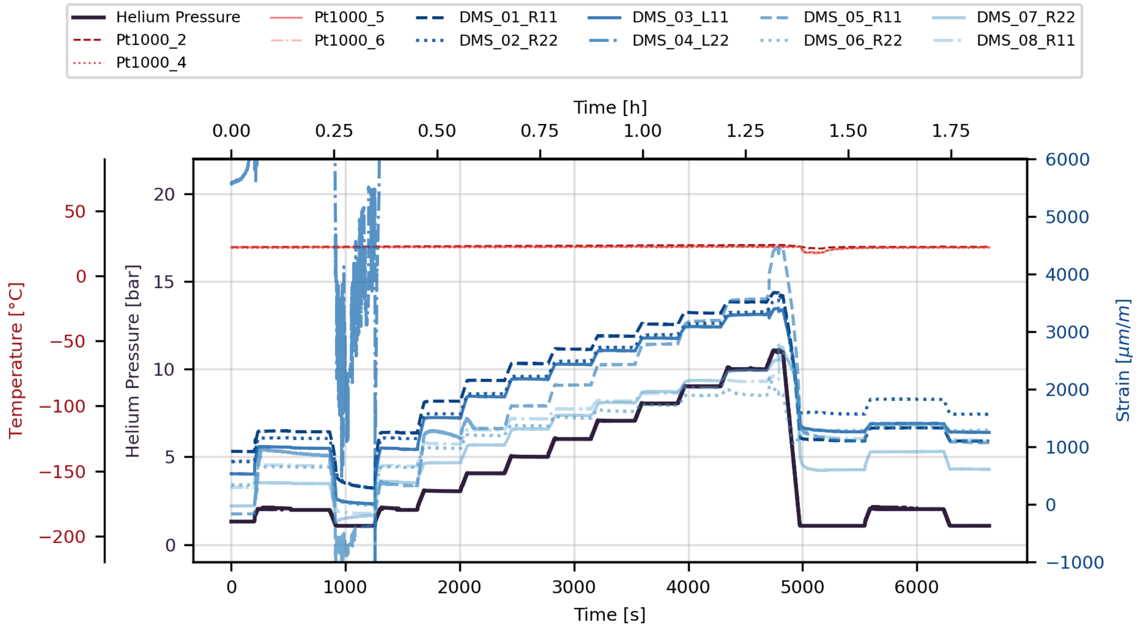

(b) Strain overview

Figure 4.2: U-F-RT specimen: Progression of strain, leakage, temperature and pressure through pre-, main, and post- test

Consider Figure 4.2b. DMS-04-L22 loses signal after the pre-test; it shall be excluded from later analyses. Most notably, it is seen that DMS-05-L22 reaches a higher strain value than other sensors near the leakage pressure. A higher local strain value is plausibly caused by local stiffness degradation due to damage. As DMS-05-L22 is the closest to the clamp, it can anticipated that the specimen failed there. Interestingly, other strains gauges near the clamps (DMS-06-R22, DMS-07-R11, DMS-08-R22) exhibit significantly lower strains that their DMS-05-L22 counterpart. Bulging of the specimen during pressurisation may cause delamination of the strain gauges. However, no visible de-bonding of the strain gauges (DMS-06-R22, DMS-07-R11, DMS-08-R22) are be identified from specimen photograph (Figure 4.1a). Uneven adhesive thickness between the strain gauge and specimen can lead to different strain gauge compliance. However, this claim is difficult to verify and practically unlikely because the strain gauges are pressed in position during mounting. All in all, the difference in the strain response at point symmetric clamp locations cannot be explained with confidence without further analyses (eg: comparing with other sensors).

The strain gauges at the centre of the specimen shows the presence of a bi-axial zone. DMS-02-R11 and DMS-02-R22 exhibit similar strain, offset by $100 - 200$ $[\mu\text{m}]$. The offset can be explained by the grids of the strain gauges being averaged at different positions (location of the grids in a bi-axial strain gauge differ by $3 - 4$ [mm]. Finally, The strain at an intermediate location (DMS-03-L11) follows closely with that of the centre (DMS-02-R22).

Overall, the strain response appears to be higher at 1 [bar] after the test, yet again hinting at the hypothesis of laminate stiffness degradation.

4.1.2. Temporal strain: DMS, FOSS, & DIC

The strain measurements from DMS, FOSS & DIC are qualitatively compared in Figure 4.3. The progression of strain is shown over time, for six fixed points on the specimen. These points correspond to the location of the strain gauges (DMS). The location of the strain gauges are referenced from Figure 4.1b. The FOSS fibres are embedded underneath the surface of the laminate. A point on the FOSS fibre is selected such that it matches the position of the strain gauge, bonded to the surface of the specimen. No DIC speckle pattern is applied in the upper right quadrant of the specimen. This is the same quadrant that contains the DMS and FOSS sensors. Therefore, the DIC strain data is extracted from a point that is rotated $180°$ from the location of the strain gauge.

Finally, it should be noted that all sensors have been time-synchronised. t $=$ 0 [s] refers to the start of the pre-test. Data before that point in time is truncated. The DMS and FOSS readings are initially non-zero. This is because both sensors were switched on before clamping the specimen. In other words, the DMS and FOSS record a tensile strain caused by the clamping force. On the contrary, the start of the pre-test is treated as the reference point for the DIC measurement. Three DIC readings are shown per pressure level.

In Figure 4.3d, the strain gauge (DMS) reading is not shown. In subsection 4.1.1, the strain gauge at this location was identified to have lost its signal.

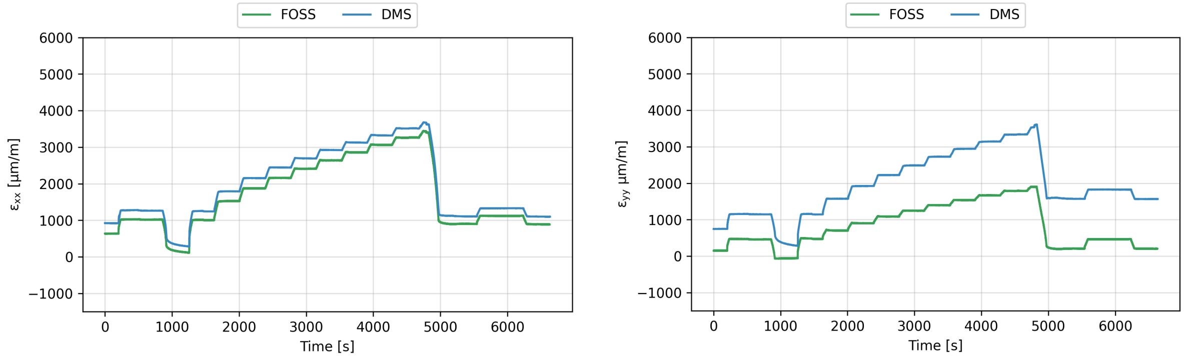

(a) Longitudinal in-plane strain (ϵ_{xx}) at $(x, y) = (5, 0)$ [mm] **(b)** Transverse in-plane strain (ϵ_{yy}) at $(x, y) = (0, 0)$ [mm]

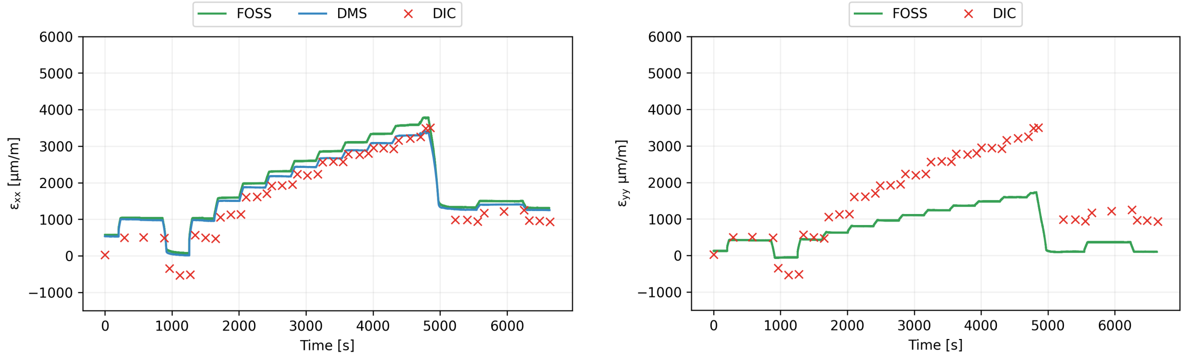

(c) Longitudinal in-plane strain (ϵ_{xx}) at $(x, y) = (23, 0)$ [mm] **(d)** Transverse in-plane strain (ϵ_{yy}) at $(x, y) = (0, 24)$ [mm]

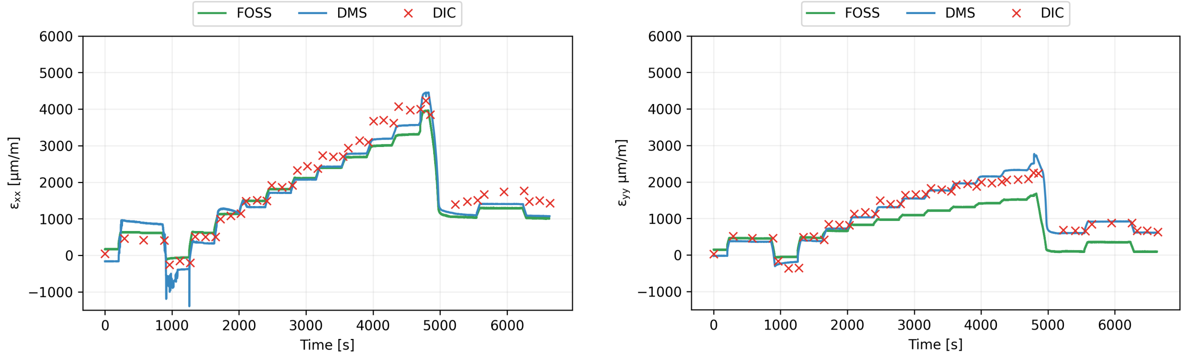

(e) Longitudinal in-plane strain (ϵ_{xx}) at $(x, y) = (47, 0)$ [mm] **(f)** Transverse in-plane strain (ϵ_{yy}) at $(x, y) = (0, 43)$ [mm]

Figure 4.3: U-F-RT specimen: Progression of strain (DIC, Strain Gauges, FOSS) over time, for pre-, main and post-test, (x, y) coordinates are taken from the centre of the specimen, as shown in Figure 4.1b. The laminate's global coordinates (x, y) are aligned with the local coordinates $(11, 22)$ of the outer-most ply.

Looking at Figure 4.3, a qualitative good agreement is seen between DMS, FOSS and DIC for the longitudinal strains $(\pm 500\ [\mu\text{m/m}])$. The absolute difference of $\pm 500\ [\mu\text{m/m}]$ translates to a relative difference of $10 - 15$% at higher load levels (≈ 10 [bar]). The magnitude of the absolute difference appears to remain unchanged during the loading step. This means that the relative difference between sensor readings is higher at lower load levels. To reduce the relative differences between sensors in further analysis, data is extracted from higher load levels.

However, for the transverse strains, the FOSS readings are significantly lower. This can be explained by the simple fact that the transverse FOSS fibre is located at the mid-plane. That is four plies underneath the surface of the laminate. The lack of strain uniformity through the thickness of the laminate is explained by the bending of the laminate, caused by the application of a pressure load. Strains on the outer-most surface are the most tensile. The strains nearer the mid-plane are closer to the neutral axis of bending, thus resulting in lower magnitude of tensile strain.

In subsection 4.1.1, leakage was reported at 11 [bar] of helium pressure. Leakage implies damage in the laminate. Figure 4.3 shows an unusual change in strain at the last pressure level, at ≈ 4750 [s]. For example, Figure 4.3e shows that strain increases by 800 [μm/m] from 10 to 11 [bar]. That is almost double the increase in strain/bar as lower pressure levels. This implies that the laminate does not exhibit linear, elastic behaviour when leakage/damage is observed.

4.2. Un-reinforced, curved specimen at room temperature (U-C-RT)

The un-reinforced, curved element has been the default bulge specimen so far. Conducting the test at room temperature is a stepping stone isn understanding the thermo-mechanical loading. This is because in the absence of a cryogenic environment, the loading becomes purely mechanical.

A similar test configuration (without FOSS/DIC) was previously investigated by Hauser [28]. The specimen leaked before maximum loading, and delamination was identified in post-mortem C-scans. Thus, it is expected that the U-C-RT multi-sensor specimen provides extensive strain data showcasing not only linearly elastic behaviour but also progressive damage. Such data is crucial for validating numerical simulation for the 3D bulge specimen, with a higher geometrical complexity than a flat coupon. It should be noted that only room temperature simulation (absence of any cryogenic cooling thermal step) can be validated using the data from U-C-RT.

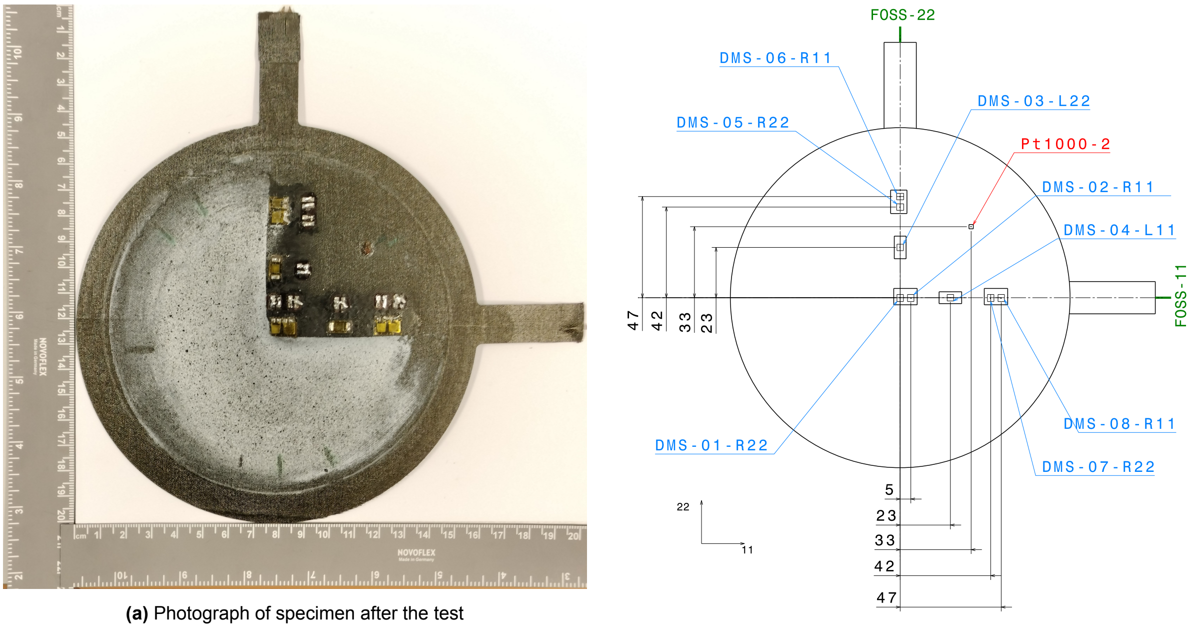

(a) Photograph of specimen after the test

(b) Technical drawing showing the position of sensors

Figure 4.4: U-C-RT specimen

Figure 4.4 shows the actual location of the sensors, as measured directly from the specimen that was manufactured and tested (Figure 4.4a). The exact position of strain gauges (DMS) and thermocouples (PT1000) is shown. The dimensions are referenced from the centroidal axes of the circular part of the specimen, and extend up to the midpoint of the measuring grids of the sensors. ”L” and ”R” refer to uni-axial and bi-axial strain gauges. ”11” and ”22” are parallel and perpendicular to the fibre direction of the outer-most ply.

4.2.1. Test overview

An overview of leakage and strain is presented for U-F-RT. The progression of strain corresponds to the strain gauges (DMS) shown in Figure 4.4. The reader is reminded that the leak-detector cannot be connected for room temperature tests. Therefore, an external hand-held sniffer is used. ”Average” values of the leak-rate at each pressure steps are noted down discretely.

Figure 4.5a shows that the test was stopped at a helium pressure of 12 $[\text{bar}]$, due to leakage. Cracking of the laminate was also heard at this pressure level. Taking 1 $[\text{bar}]$ as ambient pressure on the outer side of the specimen, the applied pressure at failure is considered to be 11 $[\text{bar}]$. This is consistent with the previous test conducted by Hauser [28], who reported a helium pressure of 11 $[\text{bar}]$ as the failure load. It should be noted that the setup used previously by Hauser had vacuum $(< 1 \times 10^{-2}$ $[\text{mbar}])$ on the outer side of the specimen. This means that the applied pressure was treated as equal to the helium pressure.

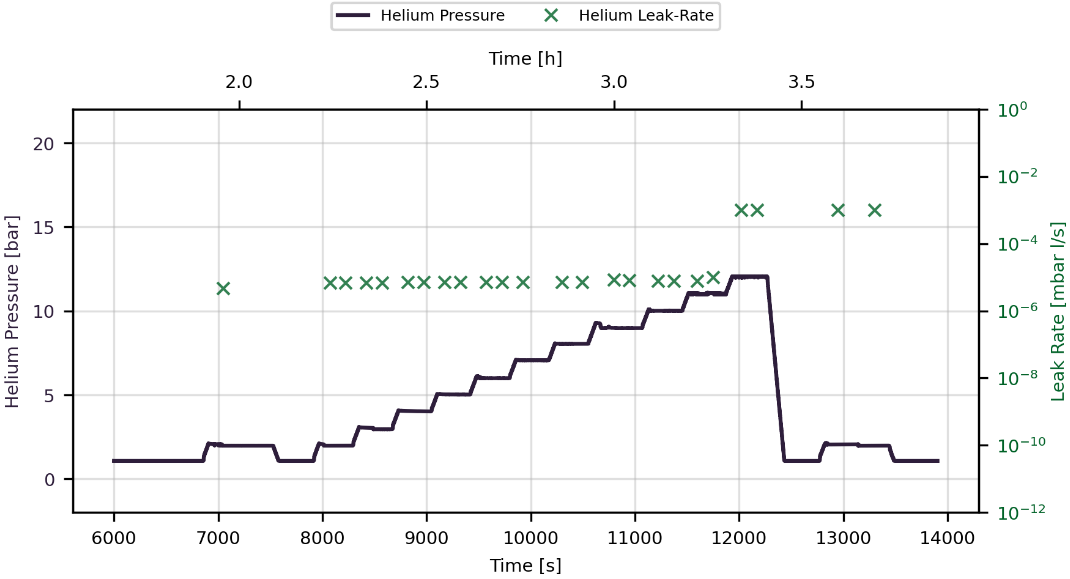

(a) Leakage overview

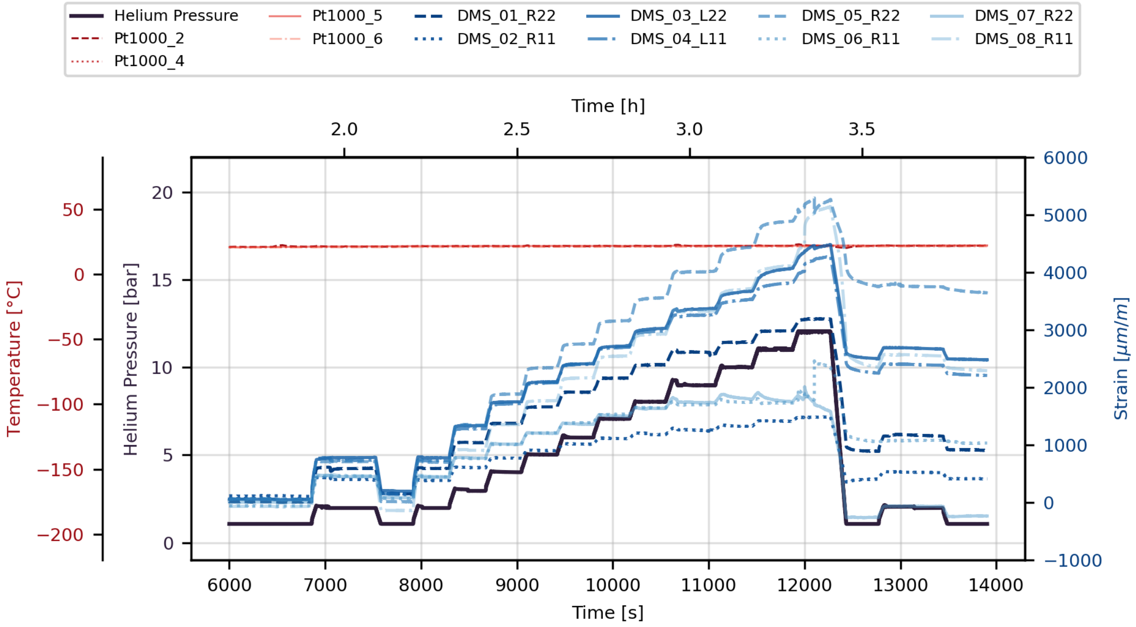

(b) Strain overview

Figure 4.5: U-C-RT specimen: Progression of strain, leakage, temperature and pressure through pre-, main, and post- test

In Figure 4.5, it should be noted that the start time is around 6000 $[\text{s}]$. This is because data from the preparation phase (such as clamping of the specimen) before the pre-test is not shown. However, the effect of clamping is seen in Figure 4.5b, as a small non-zero strain response from all strain gauges at the start of the pre-test (at 6000 $[\text{s}]$).

No obvious erroneous signal is observed from any strain gauge. At the same time, it should be noted that the in-plane components of strain at the centre of the specimen are significantly different. This can be seen with a significantly lower value from DMS-02-R11 as compared to DMS-01-R22. Generally, the centre of the specimen is well inside the bi-axial strain zone. Thus, a similar strain response would have been expected from DMS-01-R22 and DMS-02-R11. A careful post-test inspection of the specimen revealed that the measuring grid of DMS-02-R11 was partially de-bonded. It is difficult to assess whether DMS-02-R11 was improperly bonded during specimen manufacturing or the adhesive bond was damaged during the test. Therefore, the results from DMS-02-R11 should not be used for further analysis.

Consider DMS-03-L22 and DMS-04-L11. Both these uni-axial strain gauges are positioned at the same distance away from the centre of the specimen. No visible difference is observed in their strain response until 8 $[\text{bar}]$. At higher helium pressure, the strain from DMS-03-L22 is higher than DMS-04-L11 by up to 200 $[\mu\text{m}]$- a small relative difference compared to the maximum strain. Consequently, a preliminary comment can be made about the size of the bi-axial strain zone, for the U-C-RT configuration. It appears to extend to at least 23 $[\text{mm}]$ (coincident to the location of DMS-03-L22 and DMS-04-L11) from the centre. In any case, more detailed analysis of the bi-axial zone will follow in later sections.

Clearly, DMS-05-R22 exhibits the highest strain. Its longitudinal counterpart, DMS-08-R11, has a lower strain offset by $500 - 750$ $[\mu\text{m}]$. DMS-06-R11 and DMS-07-R22 show similar strains. It is interesting to note that during the last pressure step (12 $[\text{bar}]$), the strain from DMS-06-R11 increases while that from DMS-07-R22 decreases. All in all, during failure, the outer-most ply has increasing strain along the fibre direction nearer the clamping area.

The post-test shows a larger distribution of strain than the pre-test. As the magnitude of strain is also higher after the main test, the specimen is likely to be damaged due to a reduction in laminate stiffness.

4.2.2. Temporal strain: DMS, FOSS, & DIC

The strain measurements from DMS, FOSS & DIC are qualitatively compared in Figure 4.6. The progression of strain is shown over time, for six fixed points on the specimen. These points correspond to the location of the strain gauges (DMS). The location of the strain gauges are referenced from Figure 4.4b. The FOSS fibres are embedded underneath the surface of the laminate. A point on the FOSS fibre is selected such that it matches the position of the strain gauge, bonded to the surface of the specimen. No DIC speckle pattern is applied in the upper right quadrant of the specimen. This is the same quadrant that contains the DMS and FOSS sensors. Therefore, the DIC strain data is extracted from a point that is rotated 180° from the location of the strain gauge.

The strain gauge measurement is omitted from Figure 4.6a. In subsection 4.2.1, this strain gauge (DMS-02-R22) was confirmed to be debonded. The longitudinal strain signals of the FOSS (Figure 4.6a, 4.6c and 4.6e) are incomplete. The signal is lost after $2500 - 3500$ $[\text{s}]$. A conclusive reason for the sensor failure cannot be established. Nevertheless, possible explanations include kinking of the optical fibre, and/or failure at the welded joints along the wire. In the absence of information explaining the sensor failure, it was decided to exclude the longitudinal strain data from the FOSS sensor in further analysis.

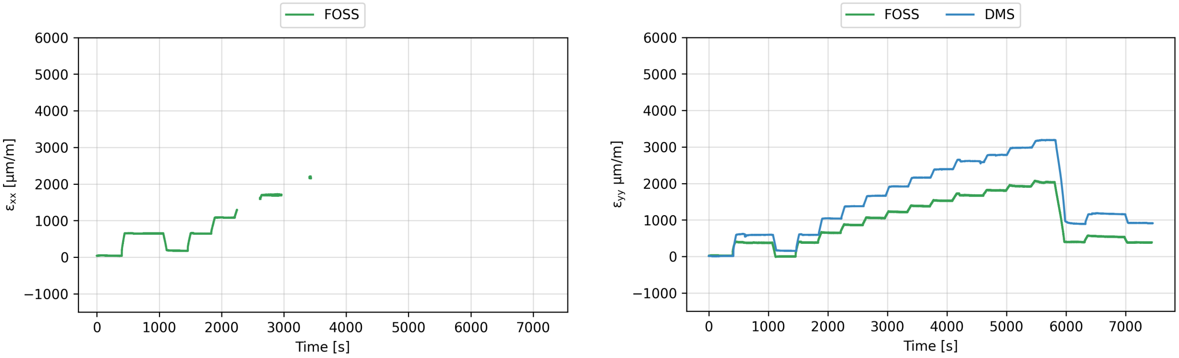

(a) Longitudinal in-plane strain (ϵ_{xx}) at $(x, y) = (5, 0)$ [mm]

(b) Transverse in-plane strain (ϵ_{yy}) at $(x, y) = (0, 0)$ [mm]

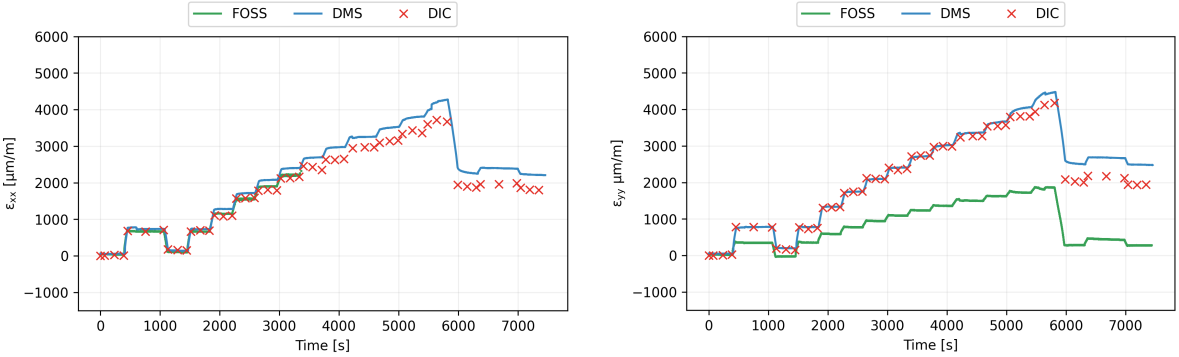

(c) Longitudinal in-plane strain (ϵ_{xx}) at $(x, y) = (23, 0)$ [mm]

(d) Transverse in-plane strain (ϵ_{yy}) at $(x, y) = (0, 23)$ [mm]

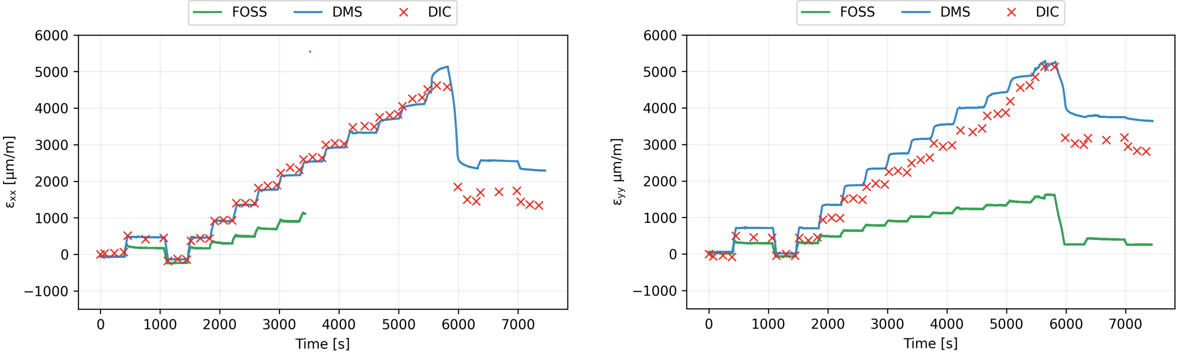

(e) Longitudinal in-plane strain (ϵ_{xx}) at $(x, y) = (47, 0)$ [mm]

(f) Transverse in-plane strain (ϵ_{yy}) at $(x, y) = (0, 42)$ [mm]

Figure 4.6: U-C-RT specimen: Progression of strain (DIC, Strain Gauges, FOSS) over time, for pre-, main and post-test. (x, y) coordinates are taken from the centre of the specimen, as shown in Figure 4.4b. The laminate's global coordinates (x, y) are aligned with the local coordinates $(11, 22)$ of the outer-most ply.

Interestingly, the strain gauges do not return to their initial strain value after deloading. Figure 4.6 shows that the post-test strains are higher than the pre-test ones by up to $500\ [\mu\text{m}/\text{m}]$ at the centre (Figure 4.6b), $1500\ [\mu\text{m}/\text{m}]$ in the transition zone (Figure 4.6c-4.6d) and $3000\ [\mu\text{m}/\text{m}]$ near the clamping zone (Figure 4.6e-4.6f). These differences may be explained by the considering the material behaviour of strain gauge and the specimen. A scenario could be the plastic yielding of the metal wires of the strain gauges. This may explain why a tensile strain remains in the strain gauges even after de-pressurisation. Another possibility is the permanent deformation of the specimen itself. Plastic deformation of a toughened thermoset (epoxy) resin is limited, and has to be ruled out as an unlikely possibility. Delamination, especially buckled delamination, could mean that the individual plies remained strained even after the load is removed. However, if there was significant permanent deformation in the specimen, it would have been reflected in the strain measured by the FOSS fibres. This was not the case. The pre- and post-test strain from the FOSS system are in agreement (within a tolerance of $250\ [\mu\text{m}/\text{m}]$. With that being said, two possible causes of non-zero strains in the strain gauge after unloading are identified:

permanent deformation of the specimen and/or permanent deformation of the strain gauge. Additional investigation is needed to establish causality.

4.3. Reinforced, curved specimen at room temperature (R-C-RT)

Thus far, the bulge specimen were not reinforced. Both the specimen (U-F-RT and U-C-RT) leaked before the maximum loading of 20 [bar]. Pre-mature leakage is likely to be caused by damage at the clamps.[46], [28] To reduce the effects of the clamping boundary conditions of the bulge rig, it is desired to locally increase the stiffness of the specimen near the clamps by adding an aluminum reinforcement ring. This test aims to quantify the effect of the reinforcement on the strain field, purely due to a mechanical bi-axial load at room temperature. By extension, this test aims to validate numerical models of the reinforced bulge specimen. After sufficient validation, it may be possible to optimise the reinforcement design, by parametric numerical studies.

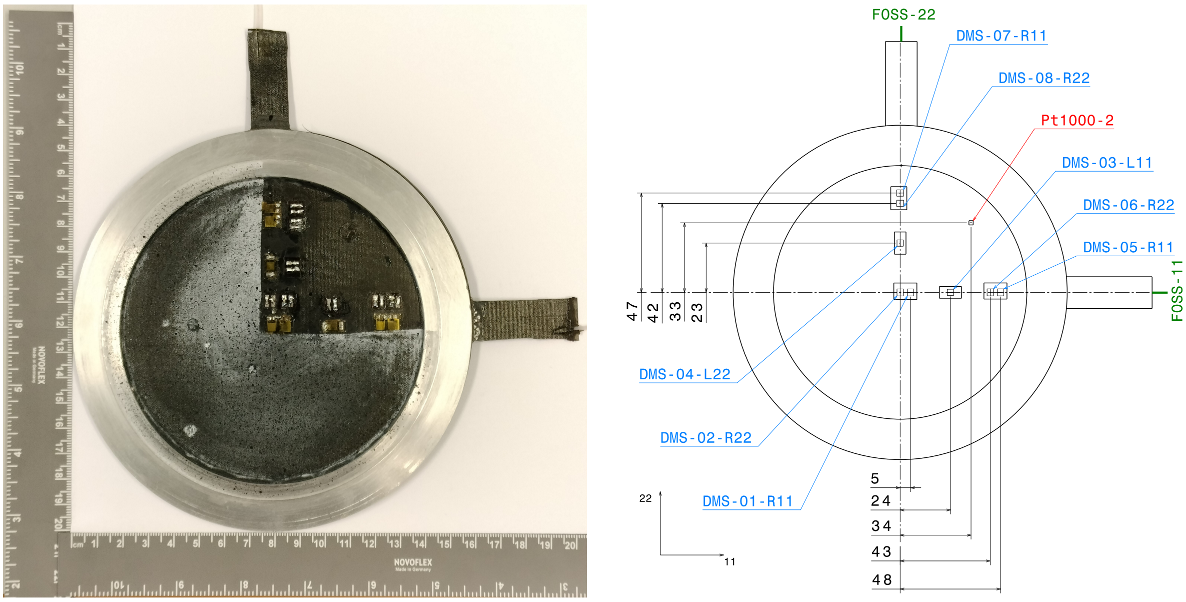

(a) Photograph of specimen after the test

(b) Technical drawing showing the position of sensors

Figure 4.7: R-C-RT specimen

Figure 4.7 shows the actual location of the sensors, as measured directly from the specimen that was manufactured and tested (Figure 4.7a). The exact position of strain gauges (DMS) and thermocouples (PT1000) is shown. The dimensions are referenced from the centroidal axes of the circular part of the specimen, and extend up to the midpoint of the measuring grids of the sensors. ”L” and ”R” refer to uni-axial and bi-axial strain gauges. ”11” and ”22” are parallel and perpendicular to the fibre direction of the outer-most ply.

4.3.1. Test overview

An overview of leakage and strain is presented for R-C-RT. The progression of strain corresponds to the strain gauges (DMS) shown in Figure 4.7. The reader is reminded that the leak-detector cannot be connected for room temperature tests. Therefore, an external hand-held sniffer is used. ”Average” values of the leak-rate at each pressure steps are noted down discretely.

In short, the specimen was loaded to 20 [bar] without leakage, as substantiated by the helium leak rate remaining below the 1×10^{-4} [mbar l/s] in Figure 4.8a.

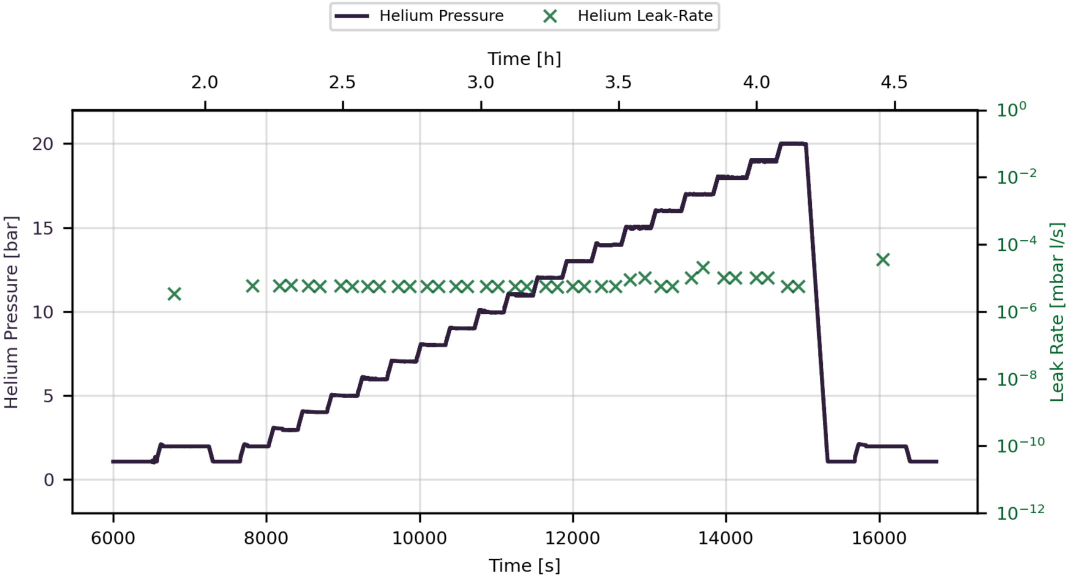

(a) Leakage overview

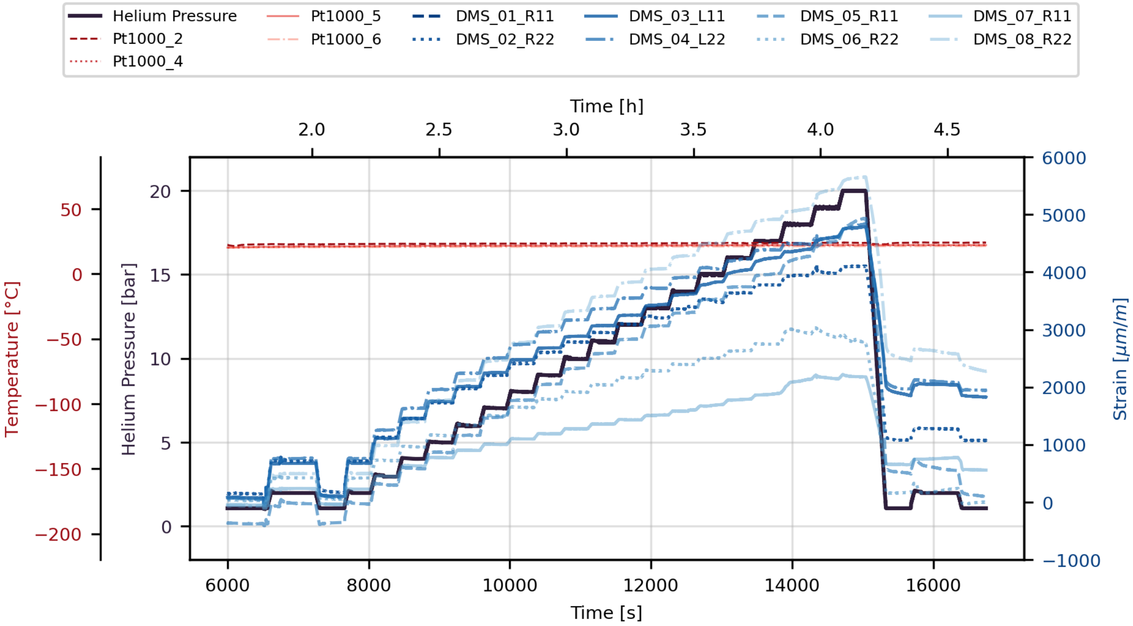

(b) Strain overview

Figure 4.8: R-C-RT specimen: Progression of strain, leakage, temperature and pressure through pre-, main, and post- test

Unfortunately, no data is available for DMS-01-R11.

It can be seen in Figure 4.8b that the distribution of the strain magnitude is lower than that of the tests without a reinforcement ring. Nevertheless, the highest strain still occurs near the clamping region, as shown by DMS-08-R22. Its longitudinal counterpart, DMS-05-R11, has an offset of $-1000~[\mu\text{m}]$. The reason for this offset is not clear yet, but it may be attributed to (a combination of) DMS-05-R11 being $5~[\text{mm}]$ closer to the reinforcement ring and/or the outer-most lamina straining more transverse to the fibre direction. The former claim demands further analysis, using DIC. The latter hypothesis seems to apply to DMS-06-R22 and DMS-07-R11 as well. Namely, the strain measured by DMS-07-R11 is offset by up to -750 $[\mu\text{m}]$, from that of DMS-06-R22. A (slightly) lower strain, by an offset of around -300 $[\mu\text{m}]$, is also recorded by DMS-03-L11 as compared to DMS-04-L22.

In summary, the addition of the reinforcement ring appears to create a more uniform strain distribution. However, a marginally anisotropic strain response is observed. Specifically, strain gauges show less deformation in the longitudinal direction (at least of the outer-most ply). The cause of the anisotropic is not clear, but it can be attributed to the reinforcement ring reducing the cross-section area of the un-reinforced part of the specimen. Quantifying any such anisotropy will be treated in upcoming discussions.

4.3.2. Temporal strain: DMS, FOSS, & DIC

The strain measurements from DMS, FOSS & DIC are qualitatively compared in Figure 4.9. The progression of strain is shown over time, for six fixed points on the specimen. These points correspond to the location of the strain gauges (DMS). The location of the strain gauges are referenced from Figure 4.7b. The FOSS fibres are embedded underneath the surface of the laminate. A point on the FOSS fibre is selected such that it matches the position of the strain gauge, bonded to the surface of the specimen. No DIC speckle pattern is applied in the upper right quadrant of the specimen. This is the same quadrant that contains the DMS and FOSS sensors. Therefore, the DIC strain data is extracted from a point that is rotated 180° *from the location of the strain gauge.*

The strain gauge (DMS) is omitted from Figure 4.9a.

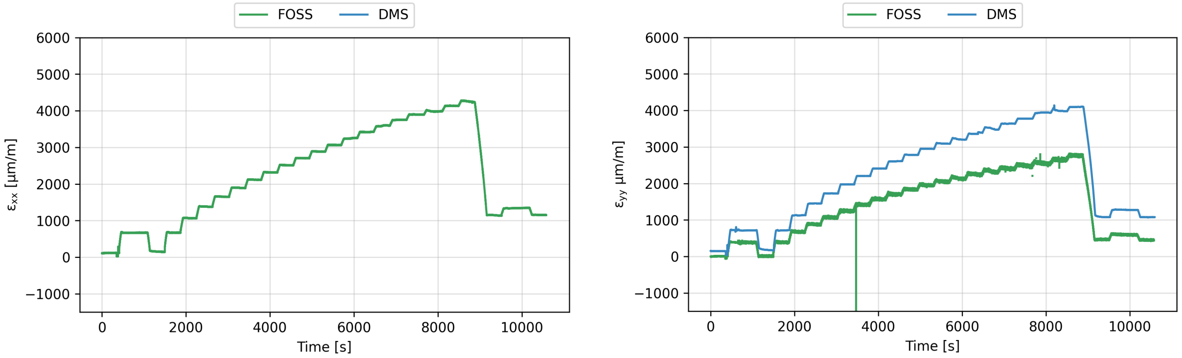

(a) Longitudinal in-plane strain (ϵ_{xx}) at $(x, y) = (5, 0)$ [mm]

(b) Transverse in-plane strain (ϵ_{yy}) at $(x, y) = (0, 0)$ [mm]

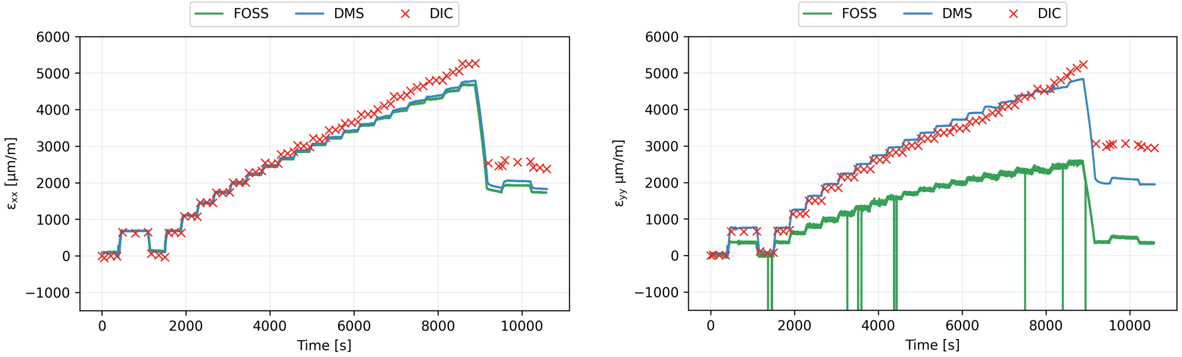

(c) Longitudinal in-plane strain (ϵ_{xx}) at $(x, y) = (24, 0)$ [mm]

(d) Transverse in-plane strain (ϵ_{yy}) at $(x, y) = (0, 23)$ [mm]

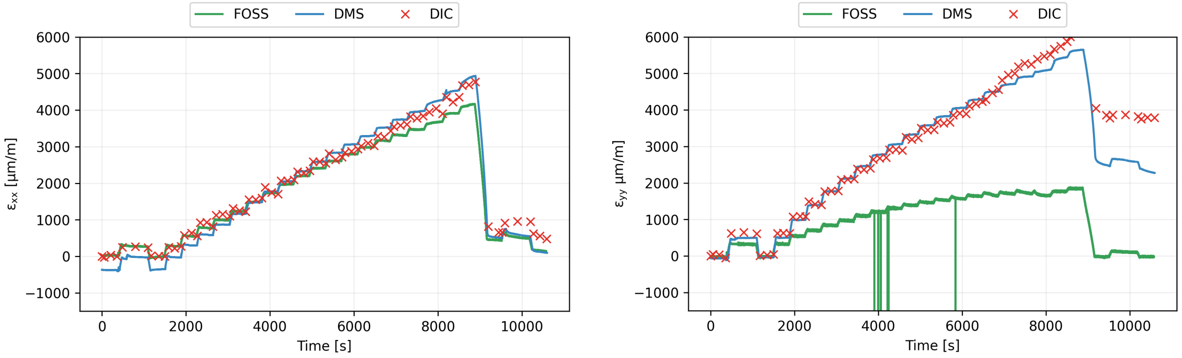

(e) Longitudinal in-plane strain (ϵ_{xx}) at $(x, y) = (48, 0)$ [mm]

(f) Transverse in-plane strain (ϵ_{yy}) at $(x, y) = (0, 42)$ [mm]

Figure 4.9: R-C-RT specimen: Progression of strain (DIC, Strain Gauges, FOSS) over time, for pre-, main and post-test. (x, y) coordinates are taken from the centre of the specimen, as shown in Figure 4.7b. The laminate's global coordinates (x, y) are aligned with the local coordinates $(11, 22)$ of the outer-most ply.

Figure 4.9c and 4.9e shows excellent $(< 5\%)$ qualitative agreement between DIC, DMS, and FOSS until ≈ 6000 [s]. The strain measured by DIC is higher than the one from the strain gauge by $\approx 500[\mu\text{m}/\text{m}]$ $(\approx +10\%)$ at 8000 [s] (Figure 4.9e, 4.9d, 4.9f). This behaviour has not been observed in previous tests (Figure 4.3-4.6). Therefore, out-of-plane displacement of the specimen resulting in apparent tensile strain is an unlikely explanation (especially in the case of 3D/stereo DIC). No alternative reason can be suggested with confidence. With that being said, a difference of up to $10 - 15$% between strain measurements from multiple sensors is still useful as preliminary validation data.

The transverse FOSS fibre (Figure 4.15b, 4.15d and 4.15f) measures a lower strain than other sensors. The lack of strain uniformity is attributed to the bending of the laminate, as described previously in subsection 4.2.2. Unfortunately, the transverse FOSS signal appears to be more noisy than the longitudinal one. Fibre optic noise has not been observed in other room temperature tests. Thus, a systematic error seems unlikely. A more random error, such as a manufacturing defect in the sensor, may explain why noise is only observed for one fibre.

4.4. Un-reinforced, curved specimen at cryogenic temperature (U-C-CT)

Thus far, experimental results from room temperature tests is presented. Room temperature test configurations are subjected to a purely mechanical load. This helps gain not only a valuable dataset for validating numerical models but also verify the behaviour of the test setup. However, room temperature testing alone does not mimic the thermo-mechanical stress state of a cryogenic tank element. In the U-C-CT test, a a thermo-mechanical stress state is created. Namely, the specimen is clamped at room temperature, cryogenically cooled and pressurised.

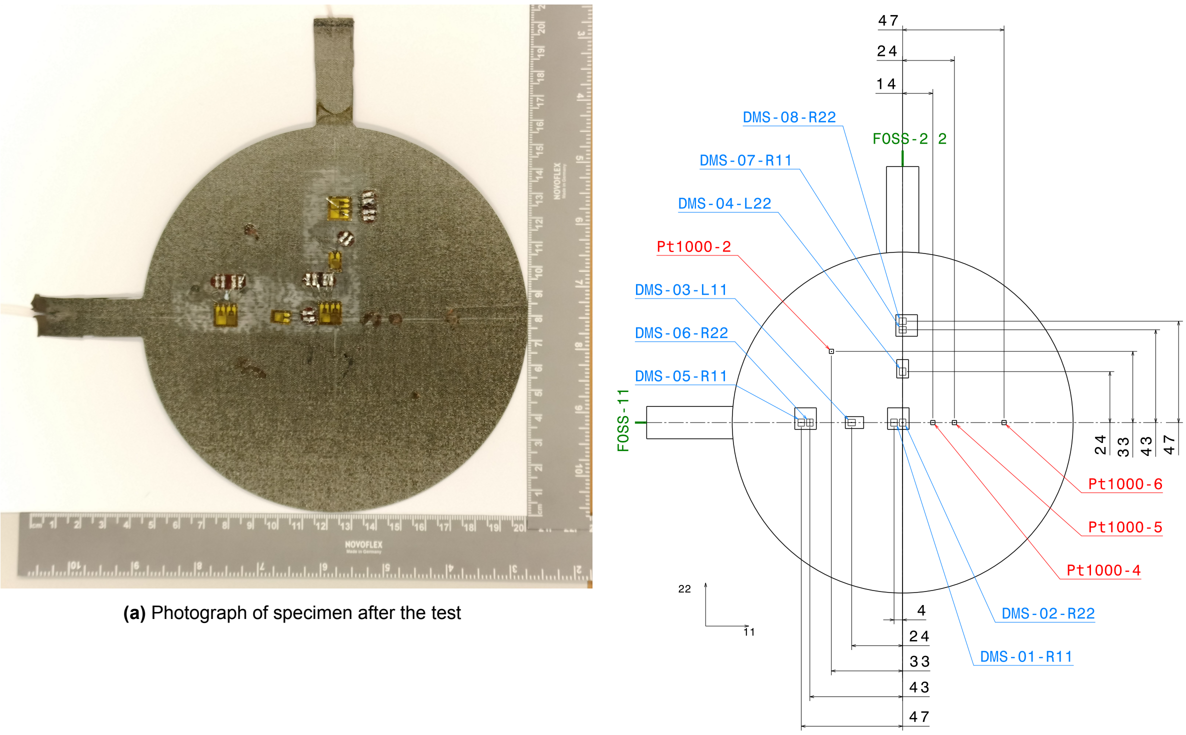

(a) Photograph of specimen after the test

(b) Technical drawing showing the position of sensors

Figure 4.10: U-C-CT specimen

Figure 4.10 shows the actual location of the sensors, as measured directly from the specimen that was manufactured and tested (Figure 4.10a). The exact position of strain gauges (DMS) and thermocouples (PT1000) is shown. The dimensions are referenced from the centroidal axes of the circular part of the specimen, and extend up to the midpoint of the measuring grids of the sensors. ”L” and ”R” refer to uni-axial and bi-axial strain gauges. ”11” and ”22” are parallel and perpendicular to the fibre direction of the outer-most ply.

4.4.1. Test overview

An overview of leakage and strain is presented for U-C-CT. The progression of strain corresponds to the strain gauges (DMS) shown in Figure 4.10. The leak-detector is connected for cryogenic tests. Therefore, leak-rate can be measured continuously over time.

Figure 4.11a shows that the specimen was loaded to the maximum helium pressure of 20 $[\text{bar}]$ without (significant) leakage. It is important to note that the specimen was exposed to vacuum on one side, and not ambient air like the previously presented room temperature tests. Figure 4.11a shows the vacuum pressure, ie the pressure on the gas analysis side of the specimen. The vacuum pressure always remained below 1×10^{-1} $[\text{mbar}]$, the maximum acceptable threshold to connect the specimen to the leak-detector. Exposing the sensitive leak-detector of the leak-detector to higher gas pressure and/or higher helium concentration may cause damage and/or pollution. To monitor the gas pressure inside the detector, its inlet pressure is also plotted in Figure 4.11a. It is seen that the inlet pressure maintains an order of magnitude of 10^{-3} [mbar] until 13 [bar], before increasing to around 10^{-1} [mbar] during the remainder of the main-test. A similar shape is followed by the helium leak-rate, which confirms that the gas pressure was purely due to (trace amounts of helium). In other words, it is verified that the gas analysis side is hermetically tight. The steady state leak rate is in the range of $10^{-10} - 10^{-9}$ [mbar l/s] from $1 - 13$ [bar]. The leak-rate then increases to about $10^{-8} - 10^{-7}$ [mbar l/s]. Diffusion-driven permeation can be ruled out, as experiments have shown that a lot more time (in days, not hours) is needed to detect it at cryogenic temperature [16], [51]. While the increase in helium flow rate is noticeable, it is still 3-5 orders of magnitude lower to confidently conclude on the existence of extensive leak-paths in the laminate [24], [26]. Thus, the increase in helium leak-rate can neither be conclusively attributed to leakage nor permeation. However, the possibility of (some) leak-paths must still not be ruled out. These leak-paths may only be observed during post-test analysis, using microscopy and/or computed tomography scans.

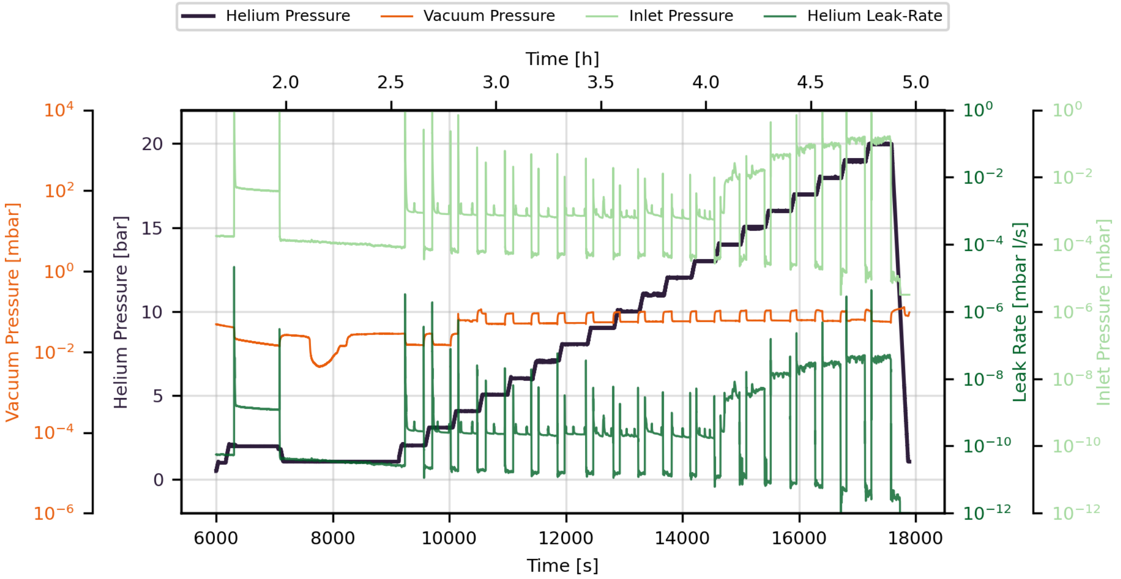

(a) Leakage overview

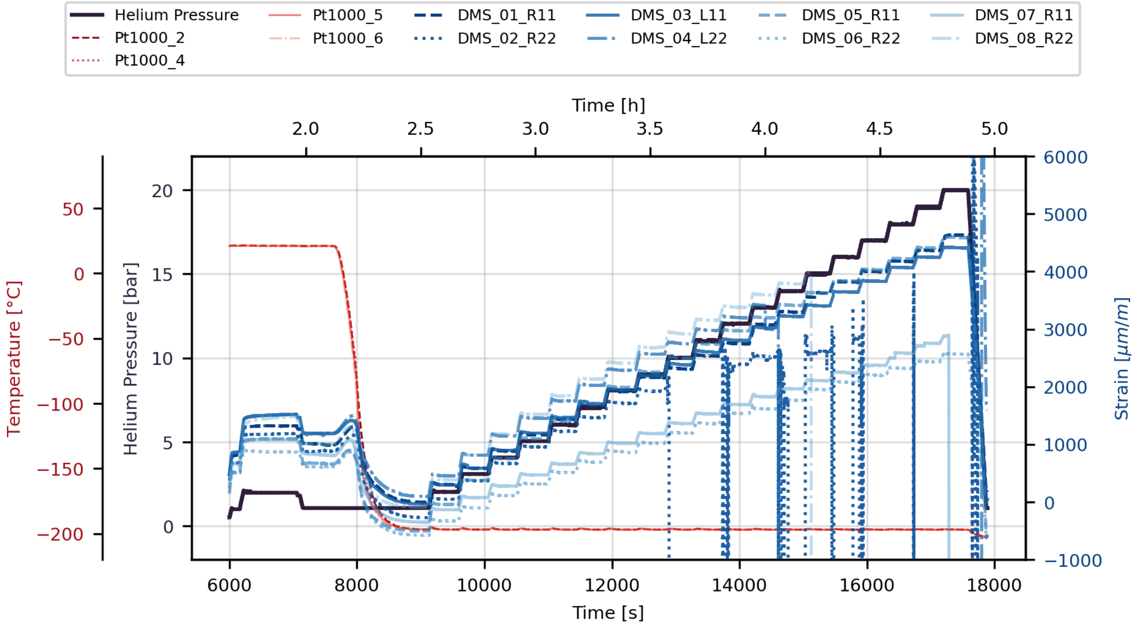

(b) Strain overview

Figure 4.11: U-C-CT specimen: Progression of strain, leakage, temperature and pressure through pre-, and main test

Cryogenic immersion takes place at 6000 [s]. All thermocouples (red) show a sharp decrease in temperature from ≈ 20 [°C] to ≈ -196 [°C]. One would expect that the thermocouple at the centre of the specimen (Pt1000-4) cools down the last. However, the time-lag $60 - 90$ [s] between all thermocouples is negligible compared to the total duration of the test. From an experimental point of view, the specimen can be considered to cool down homogeneously.

The response from the strain gauges during cryogenic cooling can also be observed from Figure 4.11b. Interestingly, the strain signal in all strain gauges increases immediately after the cryogenic immersion. The measured strains increase by $\approx 200 - 300$ $[\mu\text{m/m}]$. A definite reason for such behaviour cannot be established. Nevertheless, all strain gauges reach a steady-state measurement. At cryogenic temperature, the strains are ≈ 1000 μm/m lower than at room temperature. It is tempting to attribute the decrease in strain to the thermal contraction of the laminate. However, the specimen remains mechanically clamped. In the case of a perfect clamp and in the absence of thermal residual stresses, the total strain of the laminate should be zero. In other words, the thermal contraction should be equal to an opposing mechanical elongation. Further analysis is required to understand to verify whether the total strain of the laminate during cryogenic cooling is equal to zero. A completing explanation for the negative strain after cryogenic immersion could be the mismatch of thermal expansion between the strain gauge and specimen. Specifically, the strain gauge may contract more than the specimen. Subsequently in chapter 5, a correction shall be proposed to account for the mismatch in the thermal expansion coefficient of the strain gauge and specimen. However, the reader is reminded that only the raw sensor data is presented in this chapter.

No strain gauge signal was lost during the cooling phase. However, DMS-02-R22, DMS-07-R11 and DMS-08-R22 shows erroneous measurements after $9,\ 14,$, and 19 [bar] respectively.

4.4.2. Temporal strain: DMS, & FOSS

The strain measurements from DMS, & FOSS are presented in Figure 4.12. No temperature compensation is applied to the signal. The progression of strain is shown over time, for six fixed points on the specimen. These points correspond to the location of the strain gauges (DMS). The location of the strain gauges are referenced from Figure 4.10b. The FOSS fibres are embedded underneath the surface of the laminate. A point on the FOSS fibre is selected such that it matches the position of the strain gauge, bonded to the surface of the specimen.

Erroneous strain gauge signals are identified in subsection 4.4.1. These are excluded from Figure 4.12f. However, the complete FOSS measurement is presented. Doing so helps understand the behaviour of the fibre optic system at cryogenic temperature.

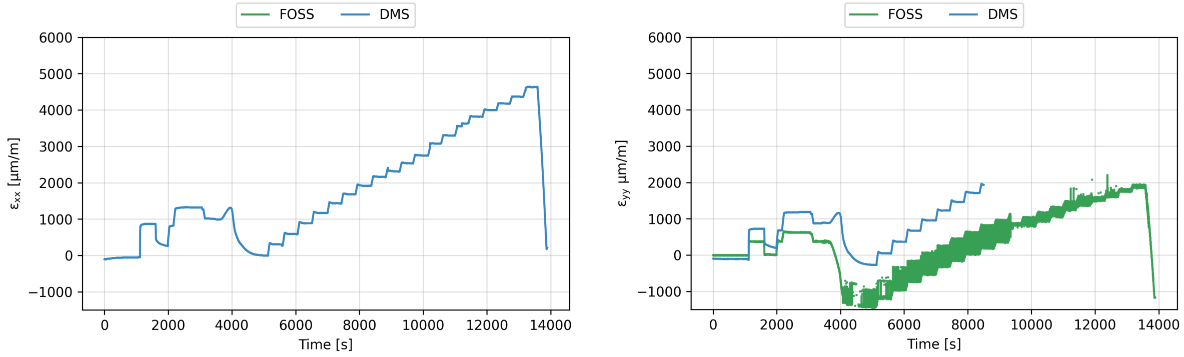

(a) Longitudinal in-plane strain (ϵ_{xx}) at $(x, y) = (-5, 0)$ [mm]

(b) Transverse in-plane strain (ϵ_{yy}) at $(x, y) = (0, 0)$ [mm]

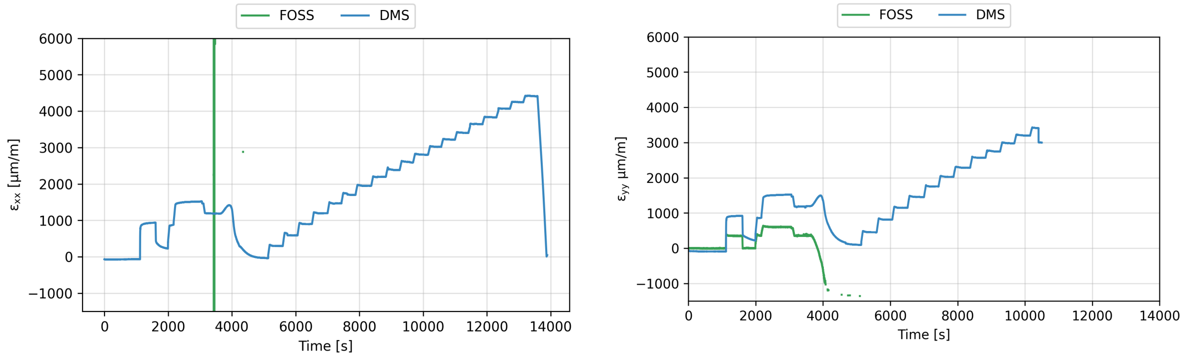

(c) Longitudinal in-plane strain (ϵ_{xx}) at $(x, y) = (-24, 0)$ [mm]

(d) Transverse in-plane strain (ϵ_{yy}) at $(x, y) = (0, 24)$ [mm]

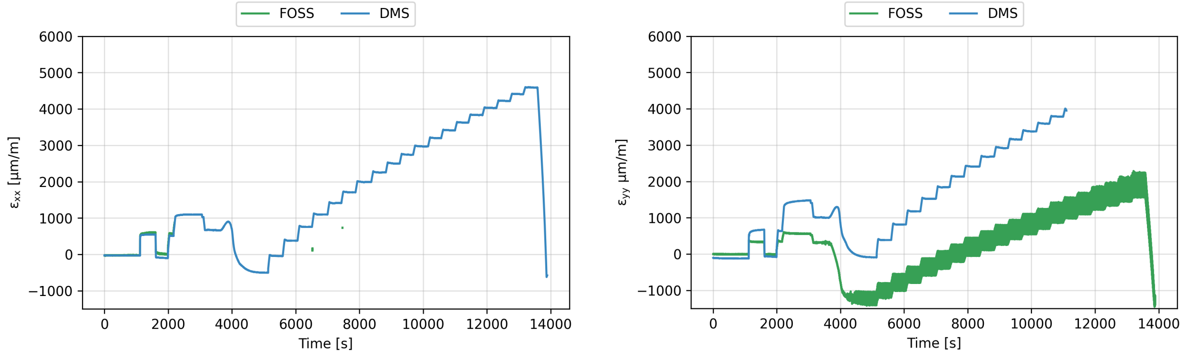

(e) Longitudinal in-plane strain (ϵ_{xx}) at $(x, y) = (-47, 0)$ [mm]

(f) Transverse in-plane strain (ϵ_{yy}) at $(x, y) = (0, 47)$ [mm]

Figure 4.12: U-C-CT specimen: Progression of strain (DIC, Strain Gauges, FOSS) over time, for pre-, main and post-test. (x, y) coordinates are taken from the centre of the specimen, as shown in Figure 4.10b. The laminate's global coordinates (x, y) are aligned with the local coordinates $(11, 22)$ of the outer-most ply.

The longitudinal FOSS fibre (Figure 4.12a, 4.15c, 4.12e) malfunction prior to cryogenic immersion. The transverse FOSS fibre (Figure 4.12b, 4.12d, 4.12f) transmitted a signal throughout the test. However, Figure 4.12b, 4.12f shows significant noise $(500 - 1000\ [\mu m/m])$. The low signal-to-noise ratio of the back-scattered signal may be explained by reduced phonon activity at cryogenic temperature [17]. The electronic noise may remain unchanged, because the data acquisition system is maintained at room temperature. Yet, such a hypothesis cannot be verified. Further investigations are needed to deeply understand the cause of signal noise in the FOSS. An independent study of the FOSS system in a cryogenic environment is well beyond the scope of this thesis.

4.5. Reinforced, curved specimen at cryogenic temperature (R-C-CT)

The U-C-RT configuration should represent the thermo-mechanical stress state of a cryogenic pressure vessel. Nevertheless, in element-level bulge testing, the absence of a reinforcement increases the risk of damage induced by the boundary conditions of the setup. The benefit of a reinforcement is already mentioned in chapter 2. From the room temperature tests, one learned that the reinforced specimen did not prematurely leak near the clamping region. It is hypothesised that the R-C-CT configuration reduces the damage due to the setup's clamps, while creating representative multi-axial, thermo-mechanical loading conditions as U-C-CT.

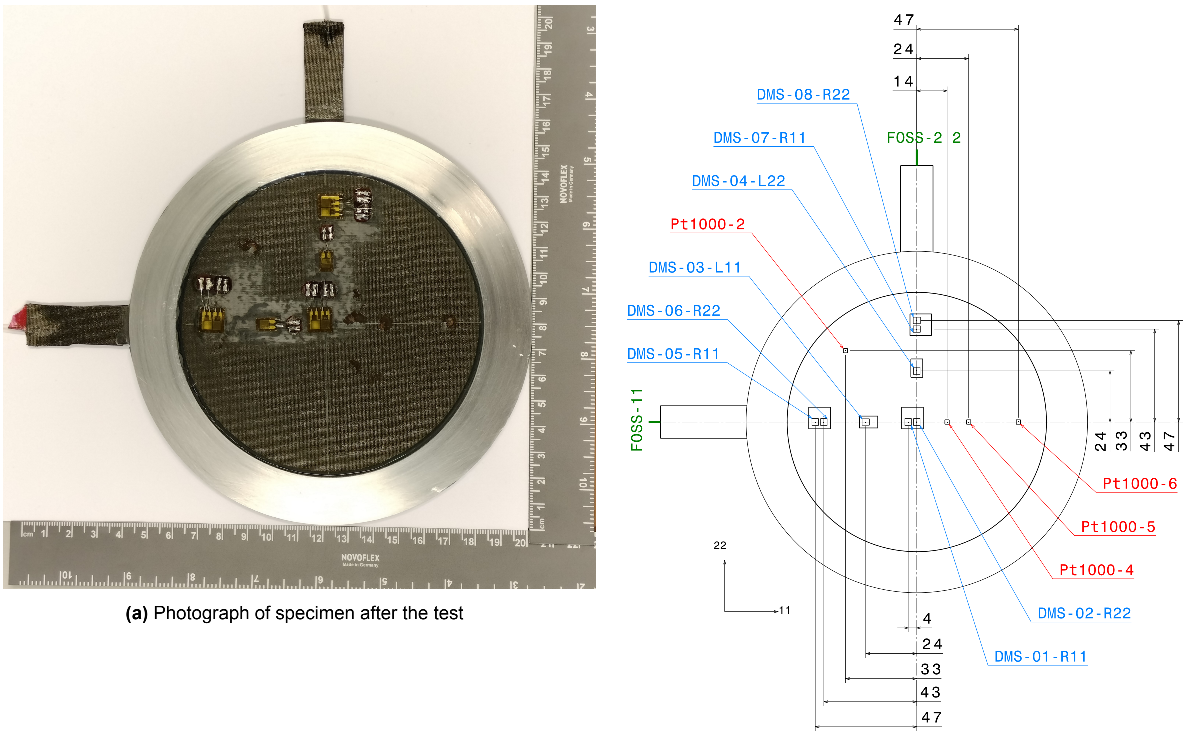

(a) Photograph of specimen after the test

(b) Technical drawing showing the position of sensors

Figure 4.13: R-C-CT specimen

Figure 4.13 shows the actual location of the sensors, as measured directly from the specimen that was manufactured and tested (Figure 4.13a). The exact position of strain gauges (DMS) and thermocouples (PT1000) is shown. The dimensions are referenced from the centroidal axes of the circular part of the specimen, and extend up to the midpoint of the measuring grids of the sensors. "L" and "R" refer to uni-axial and bi-axial strain gauges. "11" and "22" are parallel and perpendicular to the fibre direction of the outer-most ply.

4.5.1. Test overview

An overview of leakage and strain is presented for R-C-CT. The progression of strain corresponds to the strain gauges (DMS) shown in Figure 4.13. The leak-detector is connected for cryogenic tests. Therefore, leak-rate can be measured continuously over time.

The specimen was loaded to the maximum helium pressure of 20 [bar]. No leakage was detected. Figure 4.14a shows that the leak-rate remained at $\approx 10^{-9}$ [mbar l/s]. In fact, a small decrease in leak-rate can be observed. This is likely due to the leak-detector removing traces of helium from previous tests.

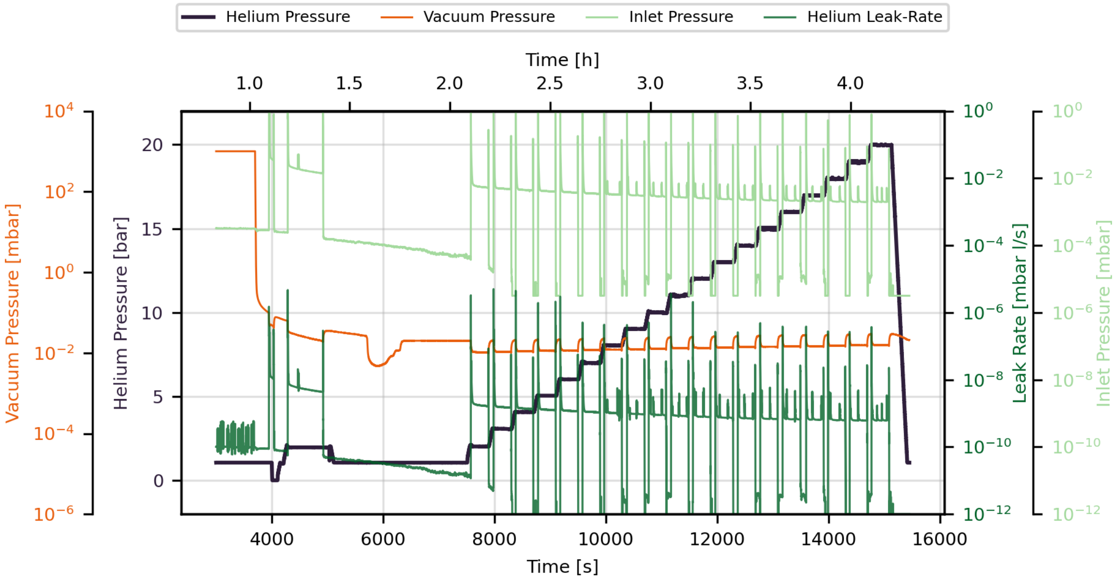

(a) Leakage overview

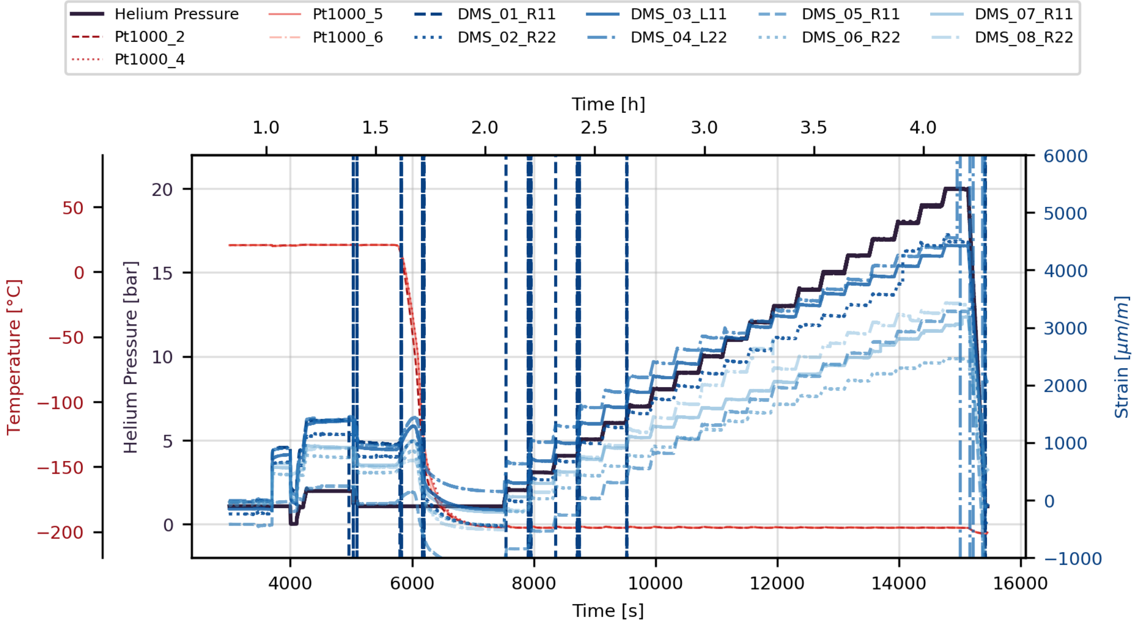

(b) Strain overview

Figure 4.14: R-C-CT specimen: Progression of strain, leakage, temperature and pressure through pre-, and main test

Cryogenic immersion took place at 5500 [s]. Similar observations as U-C-CT can be made about the behaviour of thermocouples and strain gauges.

DMS-01-R11 has a faulty signal. DMS-02-R22 sees a sharp increase in strain signal at 17 [bar]. The magnitude of the increase in strain is larger than expected for a 1 [bar] increase in the pressure load. A physical explanation cannot be found. However, the measurement from DMS-02-R22 shall be excluded after 17 [bar]. On the other hand, DMS-08-R22 sees a decrease in the strain at 12 [bar]. A likely explanation is the partial debonding of the strain gauge. In any case, the measurement from DMS-08-R22 should be excluded after 12 [bar].

4.5.2. Temporal strain: DMS, & FOSS

The strain measurements from DMS, & FOSS are presented in Figure 4.15. No temperature compensation is applied to the signal. The progression of strain is shown over time, for six fixed points on the specimen. These points correspond to the location of the strain gauges (DMS). The location of the strain gauges are referenced from Figure 4.13b. The FOSS fibres are embedded underneath the surface of the laminate. A point on the FOSS fibre is selected such that it matches the position of the strain gauge, bonded to the surface of the specimen.

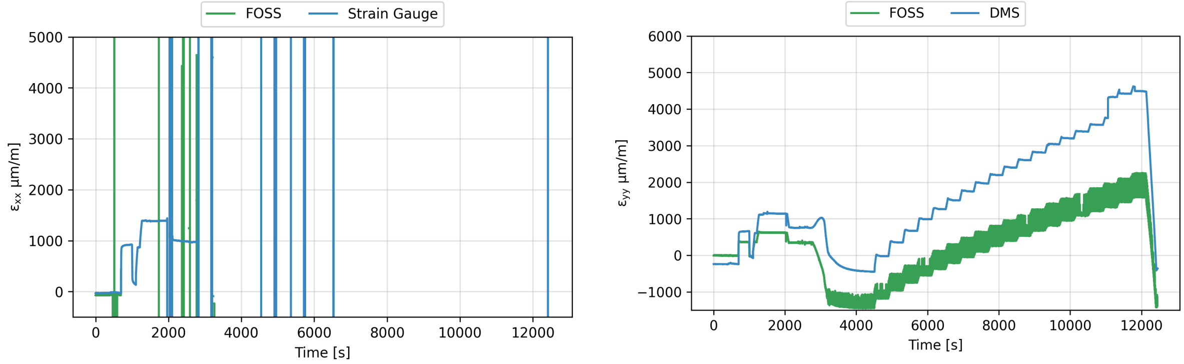

(a) Longitudinal in-plane strain (ϵ_{xx}) at $(x, y) = (-5, 0)$ [mm]

(b) Transverse in-plane strain (ϵ_{yy}) at $(x, y) = (0, 0)$ [mm]

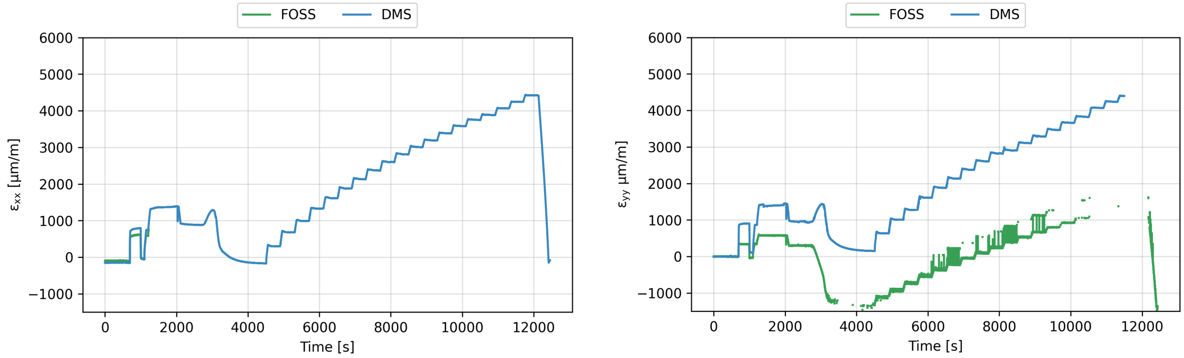

(c) Longitudinal in-plane strain (ϵ_{xx}) at $(x, y) = (-24, 0)$ [mm]

(d) Transverse in-plane strain (ϵ_{yy}) at $(x, y) = (0, 24)$ [mm]

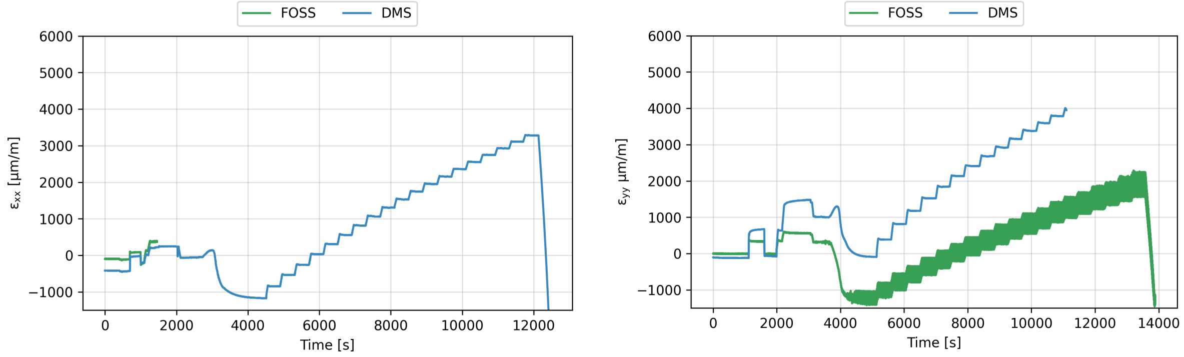

(e) Longitudinal in-plane strain (ϵ_{xx}) at $(x, y) = (-47, 0)$ [mm]

(f) Transverse in-plane strain (ϵ_{yy}) at $(x, y) = (0, 47)$ [mm]

Figure 4.15: R-C-CT specimen: Progression of strain (DIC, Strain Gauges, FOSS) over time, for pre-, main and post-test. (x, y) coordinates are taken from the centre of the specimen, as shown in Figure 4.13b. The laminate's global coordinates (x, y) are aligned with the local coordinates $(11, 22)$ of the outer-most ply.

The behaviour of the FOSS is similar to that observed in subsection 4.4.2. Once again, the longitudinal fibre fails prior to cryogenic immersion. The transverse fibre records data. However, the data is incomplete and noisy. A mitigation strategy for the noise (such as low-pass filtering) is beyond the scope of the thesis.

4.6. Outlook

Experimental results from five bulge tests have been presented. Two room temperature tests were terminated prior to maximum loading, due to significant leakage. The leakage was localised near the clamping zone. This means that leakage cannot be attributed to the thermo-mechanical stress state at the centre of the specimen.

Reinforcement was also used in some tests. No leakage could be observed in tests involving reinforced specimen. The reinforcement ring led to a more uniform distribution of strain throughout the specimen. It further appears to reduce the damage induced by the boundary conditions of the test setup. Post-test damage assessment will be discussed in more detail in chapter 5.

There appears to be good qualitative agreement between different strain sensors at room temperature $(< 10 - 15\%)$. Such an agreement is considered sufficient for preliminary numerical validation. It should, however, be noted that strain uniformity through the thickness of the specimen is absent. The transverse FOSS fibres integrated at the mid-plane of the laminate exhibit lower strains than other sensors. Through-the-thickness bending of the laminate explains the lack of strain uniformity. Hence, strains must always be referenced on a ply-by-ply basis. The concept of a global ”laminate strain” is not valid for the bulge specimen.

Sensors that malfunctioned should be excluded from further analysis. Detailed sensor failure has been reported in this chapter. Several strain gauges and fibre optic cables lost signal during testing. At cryogenic temperature, fibre optic signals have significant noise and missing data points. Thus, FOSS data at CT cannot be used to compare with numerical models. This means that only strain gauge (DMS) data is available at CT. To improve the accuracy of strain gauge data, temperature compensation will be used in chapter 5.

All in all, majority of the experimentally obtained strain results can be used to quantify the validity of numerical models in chapter 5.

5

Numerical-Experimental Results and Discussion

Until now, a numerical model has been set up and experimental bulge test data has been presented. In this chapter, numerical results shall be presented in-tandem with the experimental measurements. Firstly, experimentally obtained displacement fields shall be used to tune the parameters of the non-linear contact model. Following on, the validity of the numerical strains shall be evaluated using experimental data, acquired through three different sensor systems: strain gauges, fibre optics and digital image correlation. In addition, qualitative damage assessment is conducted. Optical micro-graphs and ultrasound C-scans are analysed. At the same time, damage initiation results from the numerical model help localise areas prone to damage.

Contents

5.1. Tuning the contact model using DIC

A contact model has been established to study the interaction between the test specimen and test setup. It has been explained in section 2.4 that the tangential contact behaviour is governed by the clamping force (F) and the coefficient of static friction (μ_s). The clamping force at room temperature (F_{RT}) and cryogenic temperature (F_{CT}) can be estimated analytically. The friction coefficient between the specimen and indium seal is not well known.

The use of experimental data can help infer μ_s. Specifically, displacements from DIC are compared with the ones from FEM. A simple post-hoc method is proposed. The maximum components of displacements are extracted from DIC. The contact model is simulated for a range of μ_s; all other parameters (such as F_{RT}) are kept constant. A range of maximum components of displacements, corresponding to the different values of μ_s, are extracted from FEM. Comparing the maximum values from DIC and FEM is justified because they always take place at the same location. In particular, the maximum out-of-plane displacement occurs at the centre of the specimen. The absolute maximum in-plane displacement occurs near the clamping region. The μ_s that minimises the difference between DIC and

FEM is selected. Once a suitable μ_s is selected, the displacement fields over the entire specimen are compared. The error between the results of the DIC and the tuned FEM model is quantified.

One limitation of such model tuning is that it cannot be mathematically proven that the selected μ_s is truly the optimal parameter. Implementing more advanced optimisation algorithms (such as kriging [11] or iFEM [19]) is beyond the scope of this thesis. However, as only 1-2 parameters need to be tuned, this approach is considered to be sufficient for a preliminary engineering assessment.

A second limitation of the selected method is that only one load level is considered. It could be possible that μ_s that minimises the difference between experimental and numerical result varies with the load level. Although, such a scenario is physically unlikely because μ_s is a material parameter. It is assumed that μ_s remains invariant for quasi-static loading. Furthermore, a high load level is selected. This ensures large strain/displacement amplitudes, thus reducing the relative error between FEM/DIC. At the same time, one must ensure that the specimen remains linearly elastic. Summarising from chapter 4, 10 $[\text{bar}]$ of helium pressure is the lowest load level that led to leakage (Figure 4.2a). This translates to an applied pressure of $10 - 1 = 9$ $[\text{bar}]$. The 1 $[\text{bar}]$ offset must be accounted for as the ambient pressure present in room temperature tests. To keep results comparable, a load level of 9 $[\text{bar}]$ is used throughout this chapter. Any exceptions are stated explicitly.

With that being said, data from two different room temperature tests is used for contact tuning. The interface conditions in these tests are different. The difference arises from the fact that one of the tests employed a metal reinforcement ring. This means that the μ_s has to be determined for aluminium and indium, which may differ from that of CFRP and indium. Finally, a sensitivity study on the clamping force is conducted.

5.1.1. Friction coefficient between CFRP and indium

μ_s between CFRP and indium can be deduced from the DIC data of the un-reinforced, curved specimen at room temperature (U-C-RT, as described in section 4.2). For the U-C-RT configuration, both sides of the CFRP laminate are in direct contact with the indium seal.

Figure 5.1 visualises the maximum/minimum components of displacement, from DIC and FEM. The FEM model is simulated for a range of static frictional coefficients (μ_s) between the CFRP specimen and indium seal. The stick/slip region is determined by analysing the ”Contact STATUS” (CSTATUS) output variable in Abaqus. The specimen is assumed to transition from stick to slip, when the area of ”slipping” elements appears to match the area of ”sticking” elements. As this assessment is made visually, the minimum static friction coefficient to prevent slippage is also an estimate. It should be noted that Figure 5.1 is only valid at a load level of 9 $[\text{bar}]$, and for a clamping force of 126 $[\text{kN}]$.

FEM$^+$/DIC$^+$ and FEM$^-$/DIC$^-$ refer to the maximum (most positive) and minimum (most negative) values of displacement in Figure 5.1a-5.1b. The superscript is dropped in Figure 5.1c because the out-of-plane displacement is always positive.

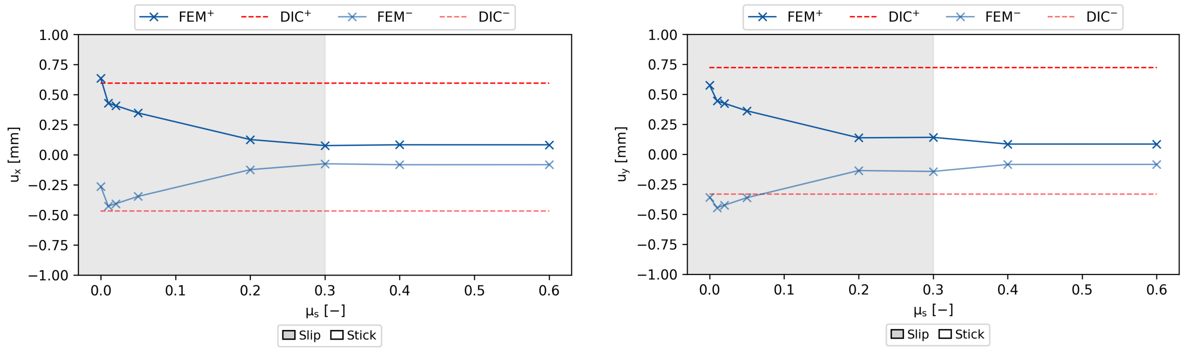

(a) Maximum/minimum longitudinal in-plane displacement

(b) Maximum/minimum transverse in-plane displacement

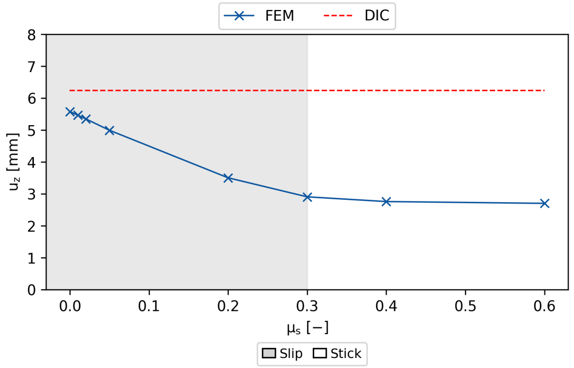

(c) Maximum out-of-plane displacement

Figure 5.1: Contact model tuning: CFRP-Indium interface

Figure 5.1 demonstrates that displacement depends on μ_s used in the contact model. For sticking specimen $(\mu_s > 0.3)$, the FEM model under-predicts all three components of displacement. This is because the stick behaviour in the contact model fully constraints the specimen. For example, u_z is 2.7 [mm] for $\mu_s = 0.4$, which is only 43% of the experimental value of 6.3 [mm] (Figure 5.1c). This is an acceptably large difference between numerical and experimental results.

However, the agreement is improved for lower values of μ_s. For $\mu_s = 0.01$, the difference in u_z between experiment and simulation is 13%. The simulation still under-predicts the out-of-plane, but by a smaller amount. A possible source of modelling error could lie in the force-controlled clamping. As described in section 2.2, the line of action of the clamping force is moved inwards. In the model, the clamping force acts directly on the specimen. In reality, the underside of each bolt results in a pre-load that is offset from the edges of the specimen. The effect of such a modelling assumption could result in reduced compliance of the test specimen, thus explaining the consistent under-prediction of out-of-plane displacement. In subsequent iterations of the numerical model, an investigation into sensitivity of the line of action of the clamping force is recommended. For this thesis, it is sufficient to know the contact model best mimics the experiment at low values of the static friction coefficient. In other words, the CFRP-indium interface appears to be nearly-frictionless.

Subsequent simulations with the contact model will use $\mu_s = 0.01$, unless otherwise stated. A frictionless interface is not used to avoid asymmetric displacement predictions, as observed in Figure 5.1a-5.1b for $\mu_s = 0.00$.

It should now be acknowledged that model tuning was based on a small number of points in space. Therefore, the entire surface displacement field is shown in Figure 5.2. The results for DIC, FEM and absolute error (DIC-FEM) are visualised for all three components of displacement. Tuned contact model parameters are used to generate Figure 5.2.

The DIC speckle pattern is applied to only three quadrants (Figure 3.12). The upper right quadrant is kept free to route the wires from other sensors. Hence, one quarter of the circle is omitted from Figure 5.2.

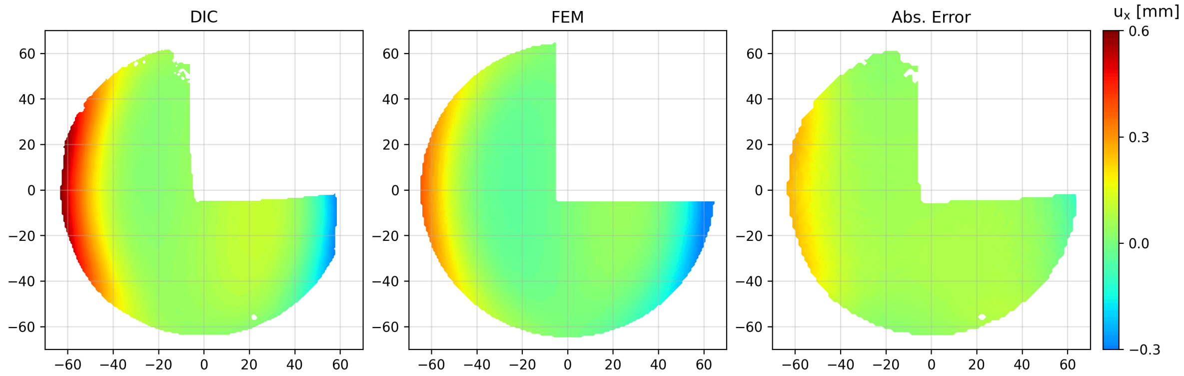

(a) Longitudinal in-plane displacement

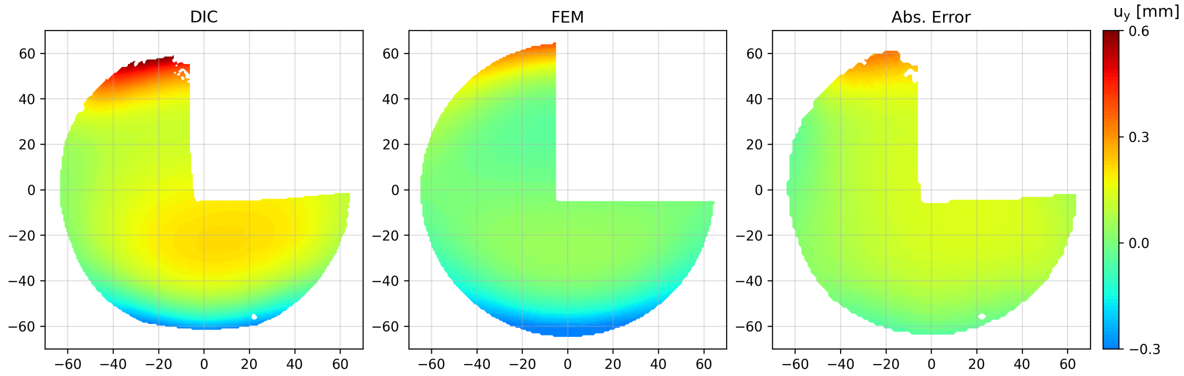

(b) Transverse in-plane displacement

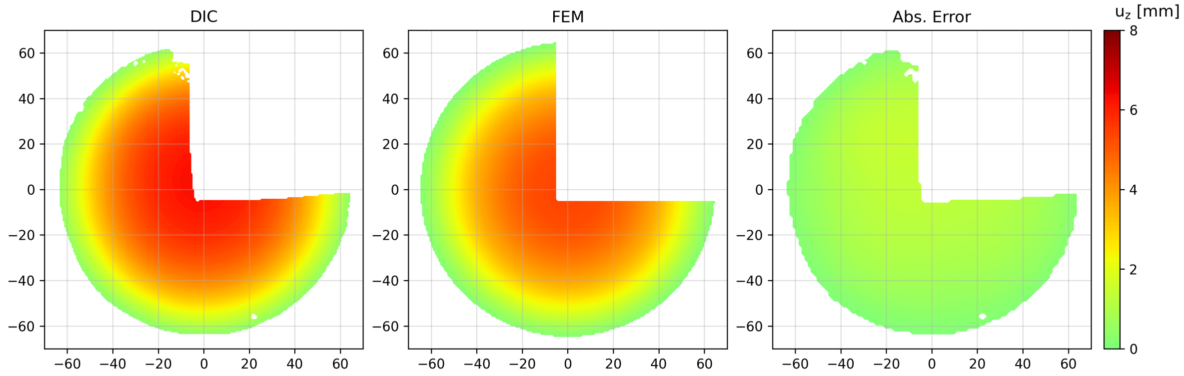

(c) Out-of-plane displacement

Figure 5.2: Comparison of surface displacement field for the entire specimen.

Figure 5.6 verifies that the tuned contact model qualitatively agrees with the DIC results.

5.1.2. Friction coefficient between aluminium and indium

Strictly speaking, the results of the previous section are only valid for CFRP-indium interfaces. Reinforced specimen have at least one aluminium-indium interface. It is possible that μ_s varies for CFRP-indium and aluminium-indium surfaces. As there is DIC data available for a reinforced room temperature test (R-C-RT, section 4.3), it is possible to derive μ_s.

A similar procedure to subsection 5.1.1 is employed. One key difference is that μ_s only needs to be varied on one side of the specimen. This is because only a one-sided reinforcement ring is used in the R-C-RT experiment. The other contact interface remains CFRP-indium. The coefficient of static friction between CFRP-indium has already been derived in subsection 5.1.1.

With that in mind, Figure 5.3 visualises the maximum/minimum components of displacement, from DIC and FEM. The FEM model is simulated for a range of static frictional coefficients (μ_s) between the aluminium reinforcement ring and indium seal. The stick/slip region is determined by analysing the ”Contact STATUS” (CSTATUS) output variable in Abaqus. The specimen is assumed to transition from stick to slip, when the area of ”slipping” elements appears to match the area of ”sticking” elements. The values in Figure 5.3 are only valid at a load level of 9 $[$bar$]$, and for a clamping force of 126 $[$kN$]$.

FEM$^+$/DIC$^+$ and FEM$^-$/DIC$^-$ refer to the maximum (most positive) and minimum (most negative) values of displacement in Figure 5.3a-5.3b. The superscript is dropped in Figure 5.3c because the out-of-plane displacement is always positive.

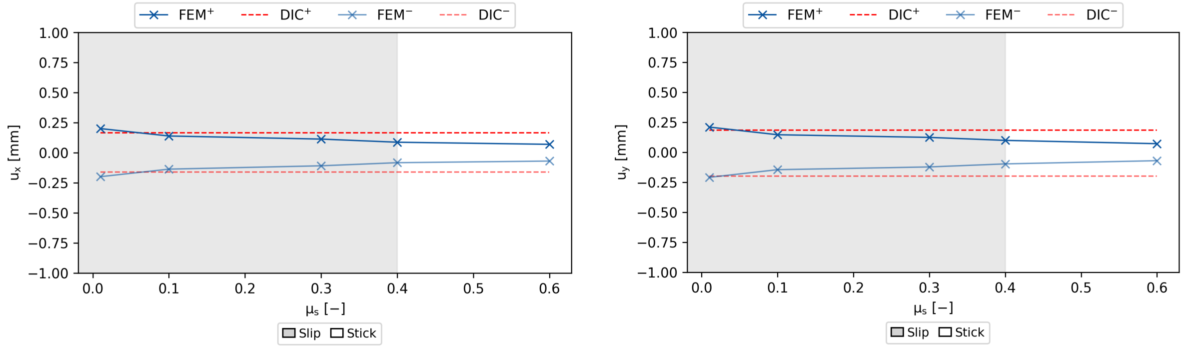

(a) Maximum/minimum longitudinal in-plane displacement

(b) Maximum/minimum transverse in-plane displacement

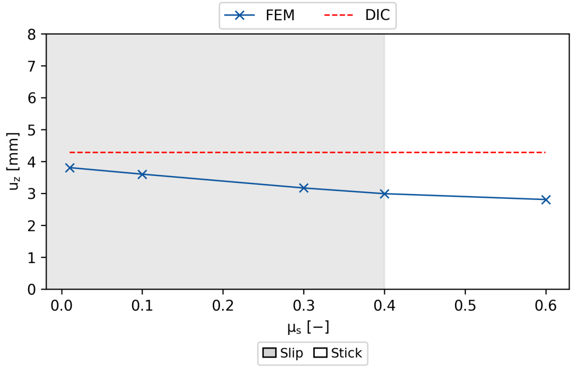

(c) Maximum out-of-plane displacement

Figure 5.3: Contact model tuning: aluminium-Indium interface

Figure 5.3c shows that the difference in out-of-plane displacement is minimised for a near-zero static friction coefficient. A near-frictionless interface also leads to excellent agreement of the in-plane displacements (Figure 5.3a-5.3b). This implies that the aluminium-indium interface is smooth, similar to the CFRP-indium one. As a result, $\mu_s = 0.01$ shall be used for all contact surfaces from now on. No distinction between CFRP-indium and aluminium-indium needs to be made when specifying the tangential contact behaviour in FEM.

The surface displacement field is visualised in Figure 5.4. This helps verify that the tuned contact model parameters are valid for the entire specimen, and not just a small number of selected points.

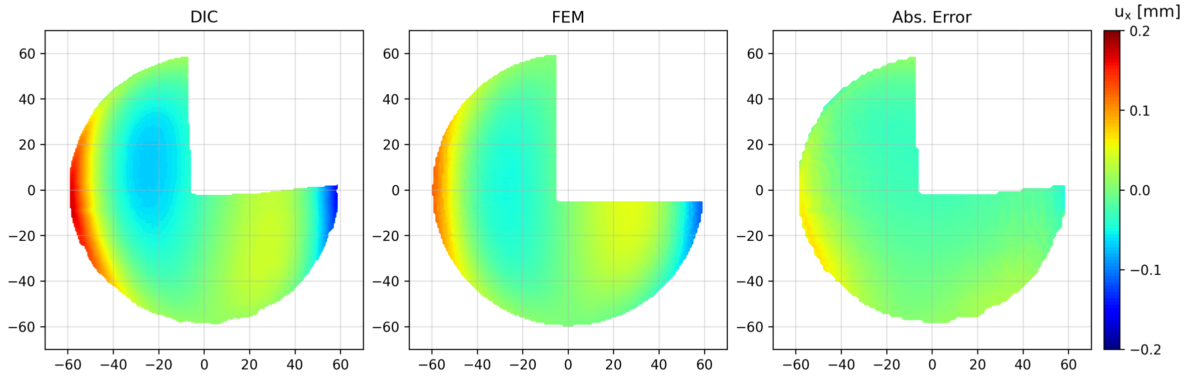

(a) Longitudinal in-plane displacement

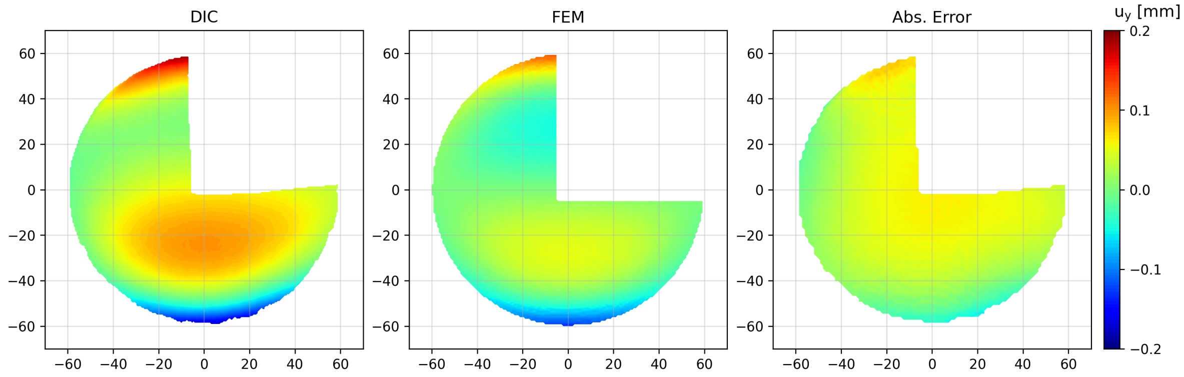

(b) Transverse in-plane displacement

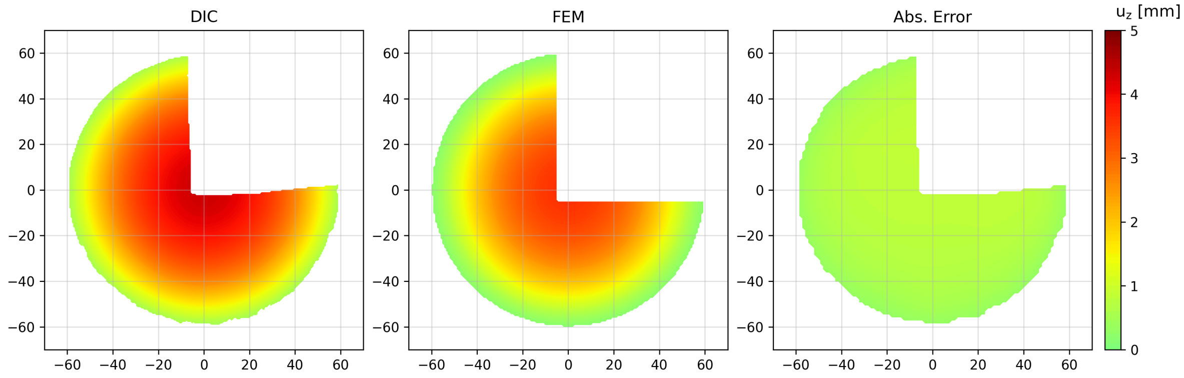

(c) Out-of-plane displacement

Figure 5.4: R-C-RT specimen: Comparison of surface displacement field obtained from DIC and FEM, at an applied pressure of 9 $[\text{bar}]$, for $\mu = 0.01$ (between both CFRP-indium and aluminium-indium surfaces) and $F_{\text{CLAMP}} = 126$ $[\text{kN}]$

Figure 5.4 verifies that the tuned contact model agrees with the DIC results.

5.1.3. Sensitivity of the clamping force

μ_s was determined in subsection 5.1.1-5.1.2, for a constant magnitude of the clamping force at room temperature (F_{RT}). Nevertheless, the F_{RT} was based on an a priori analytical estimate (subsection 2.4.2). Quantifying the error in the analytical calculation may involve precise numerical submodelling of the bolt assembly or separate experiments to measure the bolt pre-load. An alternative, pragmatic approach is to numerically understand the sensitivity of the contact model to a change in F_{RT}. This helps determine if more accurate modelling of the bolt is necessary, or if the analytical estimate is sufficient.

Similar to subsection 5.1.1-5.1.2, the maximum/minimum components of displacement, from DIC and

FEM, are extracted. The results are comparatively visualised in Figure 5.5. Multiple simulations are executed with varying values of F_{RT}. The results are valid at a load level of 9 $[\text{bar}]$, and for a static friction coefficient of 0.01.

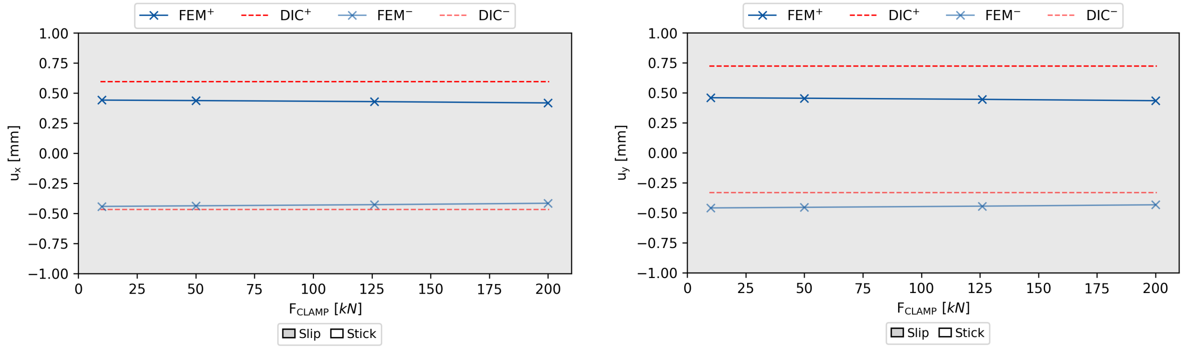

(a) Maximum/minimum longitudinal in-plane displacement

(b) Maximum/minimum transverse in-plane displacement

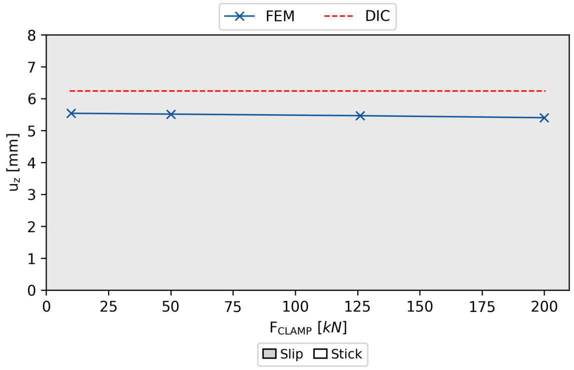

(c) Maximum out-of-plane displacement

Figure 5.5: Clamping force sensitivity study

Figure 5.5 indicates that the clamping force is less sensitive than the friction coefficient (Figure 5.1). The displacement values vary by less than 5% over a range of $10 - 200$ $[\text{kN}]$. The specimen keeps slipping despite an increase in clamping force. On a practical note, it is not recommended to keep increasing the clamping force either. This may increase the out-of-plane compressive stresses in the laminate, and potentially amplify the damage induced by the clamps.

5.2. Further processing of strain sensor data

Thus far, the contact model has been experimentally tuned. Only DIC displacement fields, acquired at room temperature, were used. No correction to the raw sensor signal was conducted. Moving forward, the strain data has to be interpreted cautiously. To improve accuracy, several considerations and corrections to the strain data are suggested in this section.

5.2.1. DIC

Room temperature

The DIC software internally computes the strains using displacement fields. True strains, as compared to engineering strains, are extracted. True strains from DIC make for a fair comparison with the logarithmic strains derived from FEM.

In addition, a note is required on filtering. No temporal or spatial filtering is used in this study. It is desired to preserve the exact strain data. Possible risks of signal filtering are over-smoothing and cut-off.[42] These risks are considered unacceptable for the bulge specimen. Significant strain gradients are expected from the centre of the specimen to the clamping region. It is possible that over-smoothing may under-predict the magnitude of the sharp strain gradients. Any cut-offs may falsely reduce the magnitude of the strain peaks as well. The drawback of using unfiltered data is noise. Noise in the DIC strain data will become apparent in section 5.3. The presence of noise is considered acceptable, if the risks of over-smoothing/cut-off are mitigated. As noise is inherently random, it does not forbid us from identifying major trends in the strain field (eg: regions of high strain, strain gradients, etc). Furthermore, in this chapter, the DIC results are always plotted in tandem with those from FEM. Strains from FEM are smoother.

Other settings are not modified. The manufacturer's default values of subset size and step size were used. [75] No user-defined interpolation was specified either.

Cryogenic temperature

It was not possible to set up the DIC for cryogenic tests, as explained in chapter 3.

5.2.2. FOSS

Room temperature

No corrections were made to the FOSS data obtained at room temperature. Room temperature FOSS data, as previously shown in chapter 4, is used for further analysis. Low signal noise was observed at room temperature too.

Cryogenic temperature

A sound interpretation of the cryogenic FOSS data requires temperature compensation [17]. FOSS temperature compensation is recommended for future studies for several reasons. To begin with, raw strain data acquired from the FOSS at cryogenic temperature is of low quality. section 4.4-4.5 mentions that FOSS signals are incomplete and highly noisy at cryogenic temperature. Simply reconstructing the signal may require significant filtering and interpolation. Such numerical techniques risk generating data that may not even be physically accurate. Even if the strain signal could be regenerated, further experiments are needed to derive the temperature compensation curve of the FOSS. These experiments are only planned to take place at the DLR after the completion of thesis. As a result, the data from these tests cannot be used for thesis. With that being said, the data from FOSS sensors at cryogenic temperature are not used for further analysis. In fact, this is not considered a major loss of data because only 4 out of 10 FOSS fibres were embedded in specimen that were tested cryogenically. 2 out of those 4 optical fibres malfunctioned even before the main part of the test. That means that data from only 2 out of 10 fibres is lost.

5.2.3. Strain gauges (DMS)

Room temperature

Only the gauge factor correction is applied at room temperature. The gauge factor of a strain gauge correlates the change in resistance of the measuring grid to the strain applied to it. A normalised gauge factor value of 2 $(\kappa_{\text{norm}} = 2.00)$ is used for all bulge tests. This is practically convenient because it eliminates the need to manually set the gauge factor for different types of strain gauges. However, the gauge factor must be corrected for the actual strain gauge during post-processing. This gauge factor is stated on the manufacturer's datasheet $(\kappa_{\text{datasheet}})$. The gauge or k-factor correction at room temperature is given by Equation 5.1. $\kappa_{\text{datasheet}}$ of (room-temperature) uni-axial and bi-axial strain gauges are 2.07 and 2.06 respectively.

$$\epsilon_{\text{c}} = \epsilon \cdot \frac{\kappa_{\text{norm}}}{\kappa_{\text{datasheet}}} \tag{5.1}$$

ϵ is the measured strain signal, and ϵ_{c} is the strain corrected for the k-factor. ϵ_{c} is used for all comparisons in this chapter.

Cryogenic temperature

Temperature compensation can be applied to correct for the low temperature environment. Several thermal effects must be taken into account and corrected for. [29]

To start with, the gauge factor has a temperature dependence. The manufacturer proposes a linear relationship, using a temperature coefficient (α_{k}), to correct for the gauge factor at the test temperature: $\kappa_{\mathsf{datasheet}}(T)$. This relationship is given in Equation 5.2. $\kappa_{\mathsf{datasheet}}$ is defined for the reference temperature (T_{ref}).

$$\kappa_{\mathsf{datasheet}}(T) = \kappa_{\mathsf{datasheet}} \cdot (1 + \alpha_{\mathsf{k}} \cdot \Delta T), \quad \Delta T = T - T_{\mathsf{ref}} \tag{5.2}$$

In addition, the resistivity of the measuring grid changes with temperature. This leads to a change of the measured resistance, even without the presence of any physical strain on the specimen. [52] Such apparent thermal strain ϵ_{s} (Equation 5.3) is typically measured by the manufacturer of the strain gauge over a range of operating temperatures. The manufacturer then curve-fits a polynomial, with coefficients a_i.

$$\epsilon_{\mathsf{s}} = a_0 + a_1 \cdot T + a_2 \cdot T^2 + a_3 \cdot T^3 + a_4 \cdot T^4 \tag{5.3}$$

To avoid repeating these tests for different types of strain gauges, the manufacturer usually only measures ϵ_{s} for one value of the gauge factor. Precisely, $\kappa_{\mathsf{polynomial}}$ is the gauge factor used to derive the polynomial. This term appears in Equation 5.5.

Over and above that, the substrate and strain gauges contract by different amounts during cryogenic cooling. This is because they have a different coefficient of thermal expansion (CTE). In other words, $(\alpha_{\mathsf{substrate}} \neq \alpha_{\mathsf{strain-gauge}})$. One important point must be noted. Even though ”self-compensating” strain gauges are used, they are designed to match the expansion coefficient of steel. This means that if steel was used as the substrate, there will be no CTE mismatch. Unfortunately, the CTE of CFRP is lower than that of steel. This means that the strain gauge experiences more contraction than the substrate. The strain caused by the mismatch of CTE (ϵ_{f}) is given by Equation 5.4.

$$\epsilon_{\mathsf{f}} = (\alpha_{\mathsf{substrate}} - \alpha_{\mathsf{strain-gauge}}) \cdot \Delta T \tag{5.4}$$

Combining the effect of the temperature dependent gauge factor, changing electrical resistivity of the measuring grid and CTE mismatch yields Equation 5.5.

$$\epsilon_{\mathsf{c}} = \epsilon \cdot \frac{\kappa_{\mathsf{datasheet}}}{\kappa_{\mathsf{datasheet}}(T)} \cdot \frac{\kappa_{\mathsf{norm}}}{\kappa_{\mathsf{datasheet}}} - \epsilon_{\mathsf{s}} \cdot \frac{\kappa_{\mathsf{polynomial}}}{\kappa_{\mathsf{datasheet}}(T)} - \epsilon_{\mathsf{f}} \tag{5.5}$$

ϵ_{c} is the temperature compensated strain, that should represent the true physical thermo-mechanical strain. From now on, ϵ_{c} shall be computed from the raw measurement signal ϵ. The parameters required in Equation 5.2-5.5 are tabulated in Table C.1.

*An alternative method, and corresponding raw data for correcting the cryogenic strain gauge data is presented in section C.2. However, this method is not used in this thesis. An explanation of this choice is detailed in section C.2, but it is not relevant to the remainder of this chapter.

5.3. Experimental-numerical comparison of the strain field

The simulated strain fields are extensively compared with the experimental ones. Two main objectives can be achieved by doing this. Firstly, the error between numerical and experimental results can be quantified. Secondly, analysing strains helps understand the influence of design/test configuration variables.

Table 5.1 proposes a ”funnel” analysis. Three-stages of strain comparison, with increasing spatial resolution but decreasing field of view, are used in this section. In other words, strain is first visualised over the entire surface of the specimen before zooming into lines or points of interest.

Experimental strain data has been acquired using multiple sensors, as tabulated in Table 3.3 and as initially plotted in chapter 4. Sensor data is available at different locations (as conceptualised in Figure 3.1). Numerical results are extracted for the corresponding sensor locations.

In this section, strains are compared for a selection of bulge tests. The remainder of the results can be found in Appendix D. The test IDs for each stage of comparison are mentioned in Table 5.1. Test IDs follow the notation tabulated in Table 3.2. The overarching motivation behind the selection of tests is the availability of (high-quality) sensor data. chapter 4 concludes that not all test data should be used for numerical validation because some sensors return erroneous signals. Over and above that, comparing data from different test configurations sheds light on the effect of the varied parameter.

Finally, to reduce visual clutter, 2D and 1D strains are shown at one load level only. 9 [bar] of applied pressure is selected, as all bulge specimen remain in the linear, elastic regime. For the 0D strain, the full load history of the pressurisation test step is used. A description of the steps of the bulge test has been included in Figure 3.13.

Table 5.1: Proposed numerical-experimental strain comparison

	2D surface strain	**1D path strain**	**0D point strain**
Spatial field of view	High	Medium	Low
Spatial resolution	Low	Medium	High
Sources of data	DIC, FEM	FOSS, DMS, DIC, FEM	FOSS, DMS, DIC, FEM
Test ID	U-C-RT, R-C-RT	U-F-RT, U-C-RT, R-C-RT	R-C-RT, R-C-CT
Variables	Reinforcement	Reinforcement, curvature	Temperature

5.3.1. 2D surface strain

DIC displacements have been used to tune the contact model. The true DIC strains are compared with the numerical strain predictions. This helps gain an oversight into the accuracy of the tuned numerical model. The strains from DIC and FEM are plotted side by side in Figure 5.6-5.7. The absolute error is taken as the difference between the DIC and FEM values, ie, Abs. Error $=$ DIC $-$ FEM. In other words, a negative absolute error implies that the FEM over-predicts the strain while a positive absolute error implies that the FEM under-predicts the strain. For ease of comparison, the absolute error is plotted on the same scale. Finally, only three quarters of the specimen is shown no speckle pattern was applied to the top right quadrant (see Figure 3.12).

Only the axial strains (ϵ_{xx}, ϵ_{yy}) are plotted. The in-plane shear strain, γ_{xy} is left out because it is nearly zero.

Results from two room temperature bulge tests, with and without the reinforcement, are compared. Despite repeated attempts, it was unfortunately not possible to extract the 2D strain data from the native DIC software for the flat specimen tested at room temperature (U-F-RT). The reader is also reminded that it is not possible to take DIC measurements for cryogenic bulge tests.

Un-reinforced specimen

The 2D strain comparison for the un-reinforced specimen is visualised in Figure 5.6.

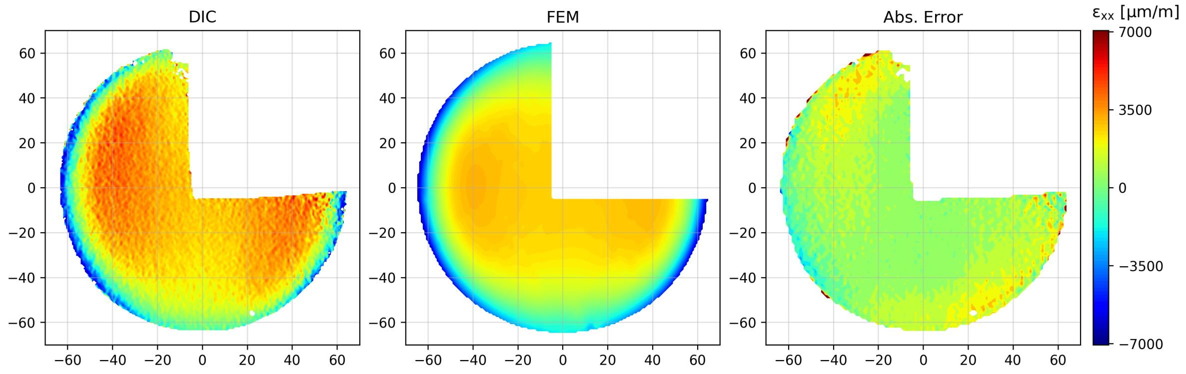

(a) Longitudinal strain

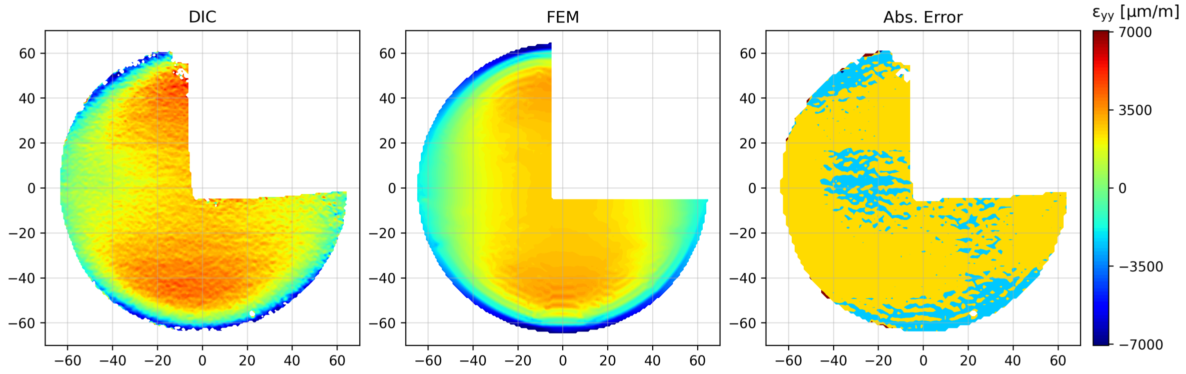

(b) Transverse strain

Figure 5.6: U-C-RT specimen: Comparison of surface strains obtained from DIC and FEM, at an applied pressure of 9 [bar]

Figure 5.6 indicates a qualitative agreement in the strain field between DIC and FEM. Both the experimental and numerical results show a "circular band" of large compressive strain (blue) towards the edges of the specimen. This compressive strain arises at the boundary of the clamping zone. Following on, the maximum tensile strains are localised between the circumference and the centre of the specimen. It should particularly be noted that the maximum tensile strains are not located at the centre of the (unreinforced) specimen.

However, the FEM appears to under-predict the size and magnitude of the maximum tensile strain. Looking at the absolute error in Figure 5.6a, the relative error can be approximated to be $-(15-20)\%$.

The absolute error plot in Figure 5.6b must be addressed. The blue and orange regions refer to a large absolute error (up to $\approx 50\%$ relative error). It appears unphysical that the numerical model both under-predicts and over-predicts the strain. A possible explanation for such sharp oscillations can be given by the noise of the DIC strain field.

Reinforced specimen

The 2D strain comparison for the reinforced specimen is visualised in Figure 5.7.

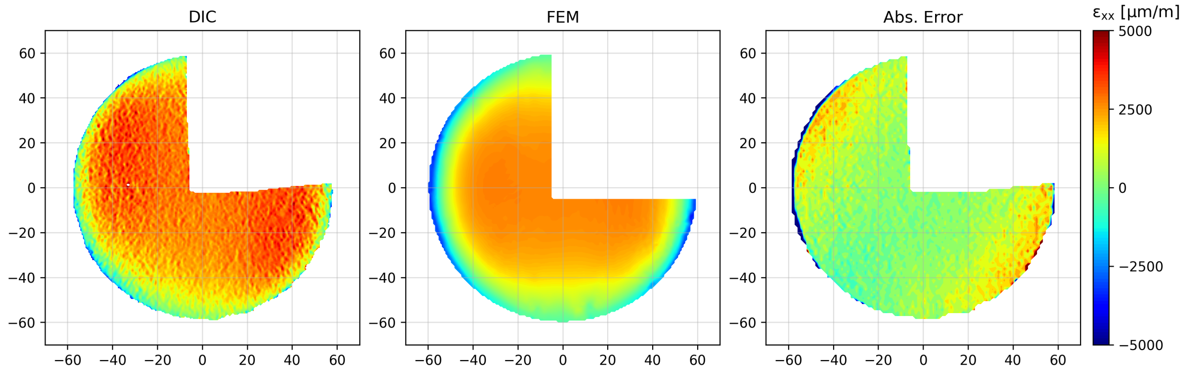

(a) Longitudinal strain

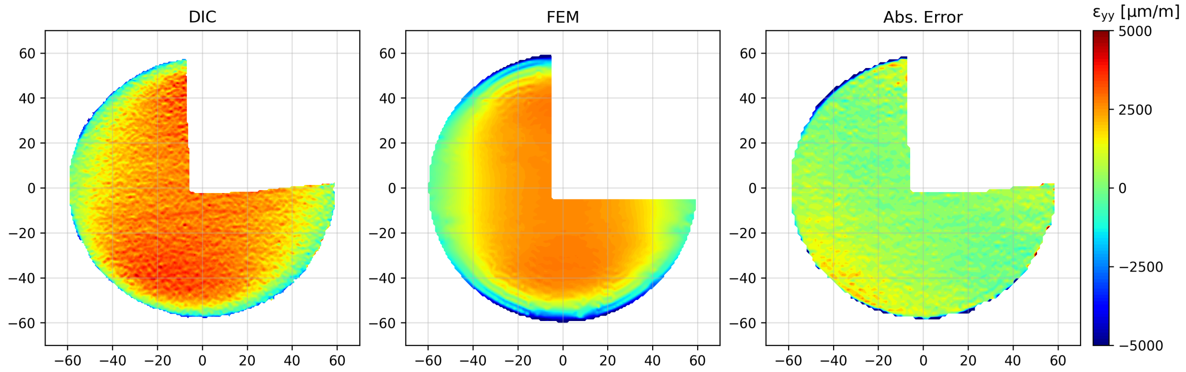

(b) Transverse strain

Figure 5.7: R-C-RT specimen: Comparison of surface strains obtained from DIC and FEM, at an applied pressure of 9 [bar]

Figure 5.7 shows that the addition of a reinforcement results in a more uniform distribution of the surface strain. The relative difference between the strain at the centre and at the transition region of the specimen is lower, compared to the un-reinforced case.

There is a good qualitative agreement between the DIC and FEM, as shown by the absolute error plots in Figure 5.7. The relative error appears to be within $\pm 10\%$ at the centre of the specimen. The difference between DIC and FEM is larger towards the edges of the specimen. This may be explained by the poor application of the DIC speckle pattern near the edges (eg: some paint was sprayed on the clamp) can explain this.

One final observation is the "misalignment" of the DIC strain. For example, the maximum ϵ_{xx} in Figure 5.7a is not perfectly aligned with the x-axis. This is not the case for the FEM, nor was it observed previously in Figure 5.6. A plausible, but unconfirmed, reason could be the metal reinforcement reducing the anisotropy of the cross-ply specimen.

5.3.2. 1D path strain

The experimental and numerical strain along various 1D paths are compared. Several paths are selected to assess if the bulge specimen preserves its radial symmetry despite of the non-linear contact boundary condition. In addition, comparing several paths maximally utilises the available multi-sensor strain data.

Figure 5.8 shows the four paths that are compared for the outer-most ply. It should be clarified that the DIC data is only available at the surface. The FEM strains are extracted at the integration points of the outer-most ply, which coincides with the ply's mid-point in the thickness direction. The FOSS fibre is underneath the outer-most ply. Previous optical micro-graphs show that the FOSS sensor tends to embed into the ply whose fibres are parallel to it [12]. In this case, the FOSS sensor is aligned with the outer-most ply. Therefore, the FOSS is likely to measure the strain of the outer-most ply- than the sub-surface ply or the ply interface. This means that, all sensors/model measure strains that are within one ply thickness of one another: an acceptable comparison.

On another note, the paths shown in Figure 5.8–5.9 extend into the clamping zone. Strain data within this region is available from the FEM, and to a lesser extent, from the FOSS.

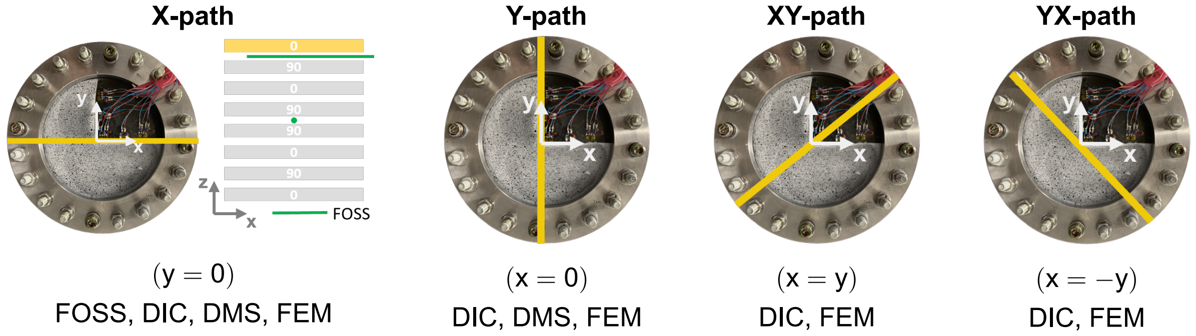
X-path | Y-path | XY-path | YX-path

(y = 0) FOSS, DIC, DMS, FEM | (x = 0) DIC, DMS, FEM | (x = y) DIC, FEM | (x = −y) DIC, FEM

Figure 5.8: Radial paths drawn on the surface of the outer-most ply

Figure 5.9 shows the selected paths to compare the laminate's mid-plane strain. The mid-plane is chosen because one FOSS sensor is integrated there. As the laminate is symmetric, the plies adjacent to the mid-plane are both aligned with the direction of the FOSS fibre. This means that is it not possible to know a prior if the sensor will mimic the behaviour of the inner-adjacent or outer-adjacent ply. Therefore, the FEM results from both the mid-plane adjacent plies are visualised.

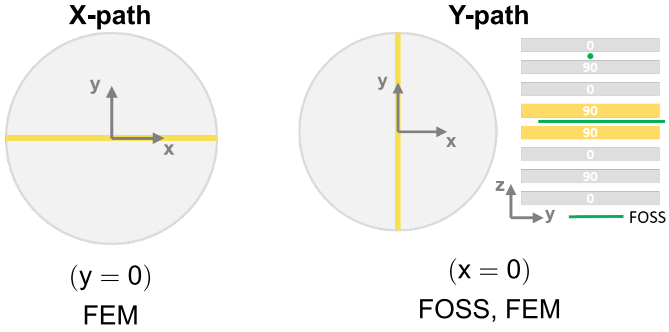
X-path | Y-path

(y = 0) FEM | (x = 0) FOSS, FEM

Figure 5.9: Radial paths drawn at the laminate's mid-plane

On top of quantifying the validity of the FEM, 1D experimental-numerical 1D strains help understand the influence of geometry: curvature and reinforcement. To that end, sensor-rich results from all room temperature tests are displayed. Plots for the cryogenic tests are moved to Appendix D.

Flat specimen

The flat specimen serves as the control configuration, as it has no curvature and no reinforcement.

Outer-most ply Figure 5.10 shows the numerical/experimental strains for the outer-most ply. Four different 1D paths as specified in Figure 5.8, are selected for the comparison.

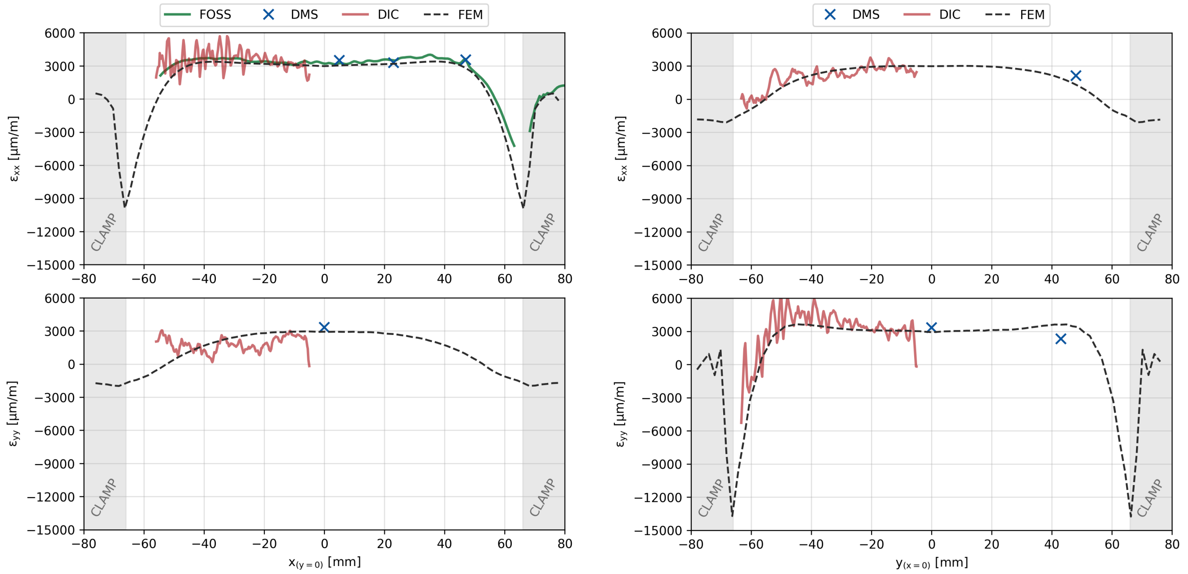

(a) Longitudinal (ϵ_{xx}) and transverse (ϵ_{yy}) in-plane strain components along X-path ($y = 0$)

(b) Longitudinal (ϵ_{xx}) and transverse (ϵ_{yy}) in-plane strain components along Y-path ($x = 0$)

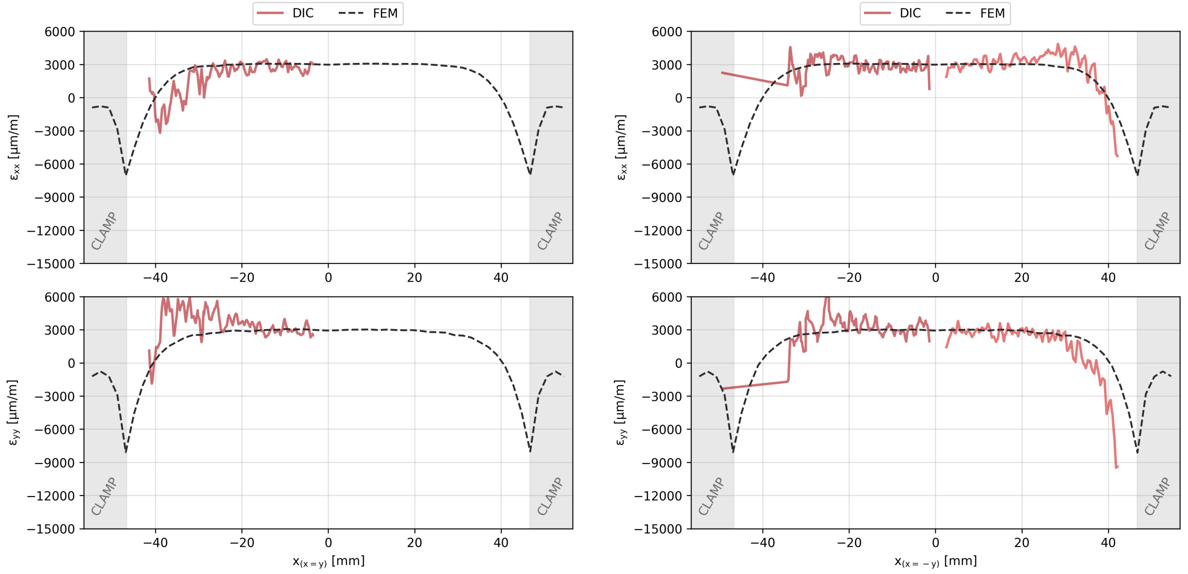

(c) Longitudinal (ϵ_{xx}) and transverse (ϵ_{yy}) in-plane strain components along diagonal XY-path ($x = y$)

(d) Longitudinal (ϵ_{xx}) and transverse (ϵ_{yy}) in-plane strain components along diagonal YX-path ($x = -y$)

Figure 5.10: U-F-RT specimen: 1D strain paths, at an applied pressure of 9 [bar]

Overall, the results in Figure 5.10 demonstrate good agreement between the measurement techniques and the numerical model. For example, consider the X-path results in Figure 5.10a. Experimental and computational longitudinal strains are within 10-15% within the central region of interest ($|x| < 20$ [mm]). Such a relative comparison excludes the random error present in the DIC measurements. The noise in the DIC strains is a consequence of using the raw unfiltered data, as explained previously in subsection 5.2.1. Unfortunately, the magnitude of the strain peak cannot be experimentally verified for this case. This is because the FOSS data in Figure 5.10a is missing at the location of the clamp edge. Near the clamping zone, it is possible that the optical sensor experienced excessive fibre kinking due to the adverse strain gradient. In any case, the strain gradients predicted by FEM appear to qualitatively agree with the ones from FOSS in Figure 5.10a.

Mid-plane Figure 5.11 shows the numerical/experimental strains for the plies adjacent to the mid-plane. Two different 1D paths as specified in Figure 5.9, are selected for the comparison.

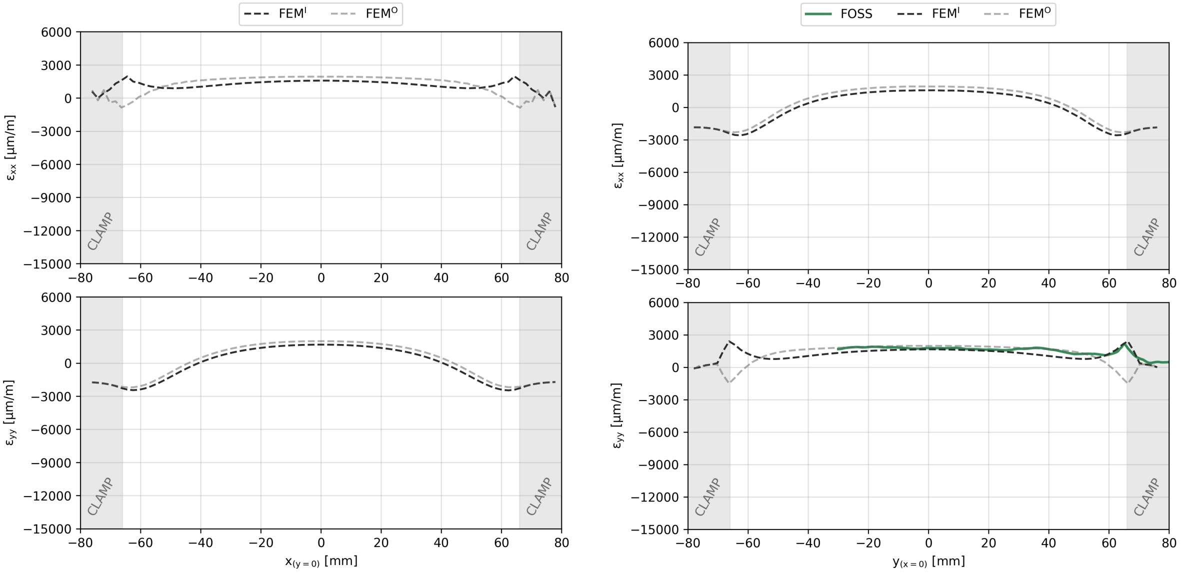

(a) Longitudinal (ϵ_{xx}) and transverse (ϵ_{yy}) in-plane strain components along X-path $(\mathrm{y} = 0)$

(b) Longitudinal (ϵ_{xx}) and transverse (ϵ_{yy}) in-plane strain components along Y-path $(\mathrm{x} = 0)$

Figure 5.11: U-F-RT specimen: 1D strain paths, at an applied pressure of 9 [bar]

Figure 5.11b shows that the FOSS strain matches closely with the one of the inner mid-plane ply (FEM$^{\mathrm{I}}$). Both the numerical and experimental data show a strain peak of 3000 $[\mu\mathrm{m}/\mathrm{m}]$ at the end of the clamp.

There are also several differences between the strain paths observed at mid-plane, compared to the outer-most ply. Figure 5.11a shows that the magnitude of strain in the plies adjacent to the mid-plane is considerably lower, only half as much as the ones predicted in the outer-most ply. This is because of the fact there the mid-plane is closer to the laminate's neutral axis of bending. This in turns demonstrates that the use of the classical laminate theory is not sufficient in predicting the strains within a laminate, as it assumes a uniform strain distribution through all plies.

Curved specimen

Outermost ply Figure 5.12 shows the numerical/experimental strains for the outer-most ply. Four different 1D paths as specified in Figure 5.8, are selected for the comparison.

Unfortunately, no FOSS data is available due to a malfunctioned sensor.

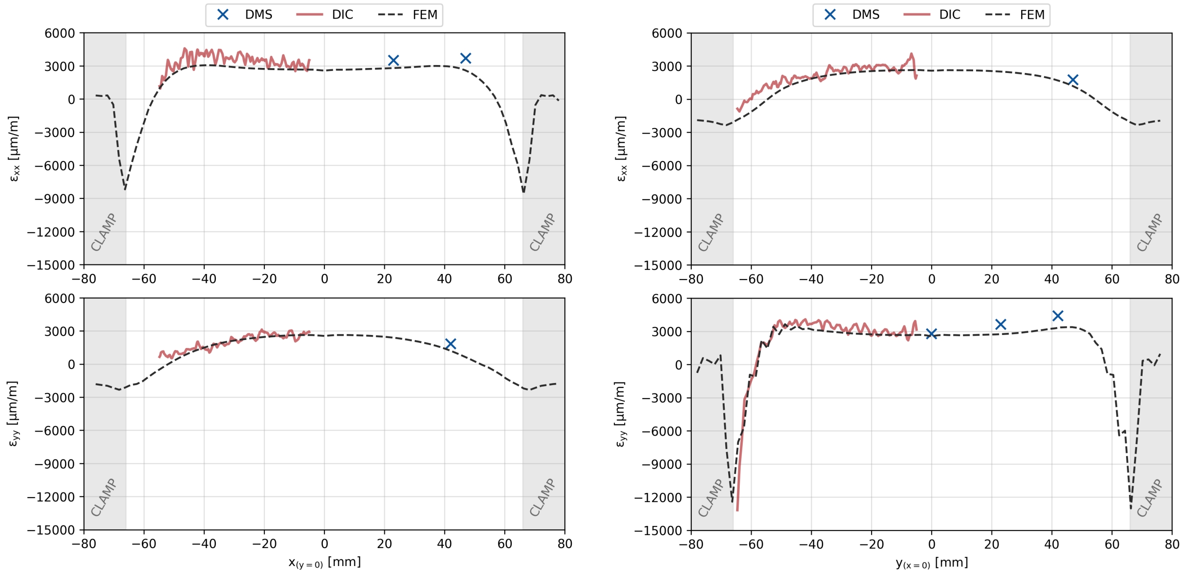

(a) Longitudinal (ϵ_{xx}) and transverse (ϵ_{yy}) in-plane strain components along X-path (y = 0)

(b) Longitudinal (ϵ_{xx}) and transverse (ϵ_{yy}) in-plane strain components along Y-path (x = 0)

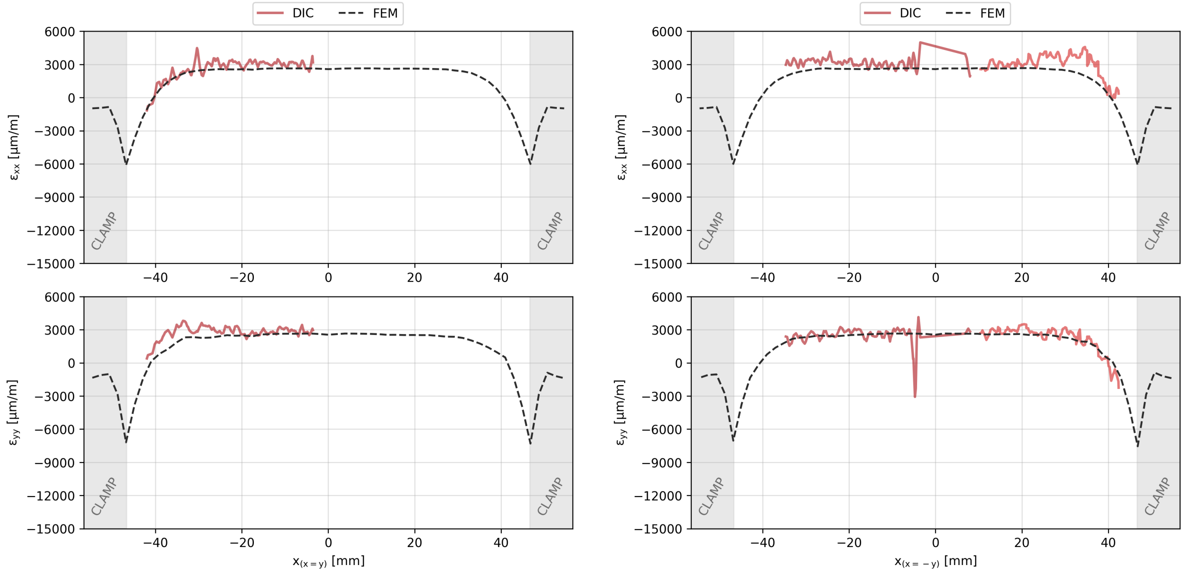

(c) Longitudinal (ϵ_{xx}) and transverse (ϵ_{yy}) in-plane strain components along diagonal XY-path (x = y)

(d) Longitudinal (ϵ_{xx}) and transverse (ϵ_{yy}) in-plane strain components along diagonal YX-path (x = −y)

Figure 5.12: U-C-RT specimen: 1D strain paths, at an applied pressure of 9 [bar]

Figure 5.12 helps assess the agreement between the experimental and numerical data. Firstly, there appears to be qualitative agreement between the DIC and FEM ($\approx \pm 10\%$). This relative error cannot be quantified accurately, due to the inherent noise present in DIC measurements. However, it appears that the FEM path is a (smoothened) curve-fit of the DIC data. Concerning the strain gauges (DMS), the FEM under-predicts the strain. The difference between the DMS and FEM increases for points nearer the clamping zone. For example, the DMS transverse strain in Figure 5.12b is 35% higher than that of the FEM. At the same time, there only appears to be a small difference in strain (absolute: ≈ 200 $[\mu m/m]$, relative: $\approx 6\%$) for the DMS point located at the centre (y = 0). As the bi-axial strain zone is located at the centre of the specimen, it is more important that the strain there is predicted accurately than near the edges. Therefore, the relative differences between DMS and FEM are considered to be acceptable for preliminary numerical analysis.

One other observation should be addressed. The DIC data exhibits strain peaks near the centre of the specimen along the YX-path (Figure 5.12d). These peaks are not associated with a physical phenomenon. As shown in Figure 5.8, the YX-path passes through the specimen's centre, which coincides with the edges of the DIC speckle pattern. The poor quality of the speckle pattern in this region accounts for the spurious peaks and discontinuities observed in the DIC measurements in Figure 5.12d.

A statement can also be made about the influence of curvature. To do so, the results of the curved specimen (Figure 5.12) are compared with the ones from the flat specimen (Figure 5.10). The most observable difference is in the magnitude of the strain peaks at the clamp location. The curved specimen marginally reduces the magnitude of this strain peak, by approximately 20% for Figure 5.12a, 12% for Figure 5.12b, and 14% for Figure 5.12c-5.12d. The reduced magnitude of the strain peak can be explained by considering the interaction between the specimen and the clamp. Special adapter plates, that match the curvature of the specimen, are used to clamp the curved specimen. These plates could marginally reduce the rotation of the curved specimen, thus leading to a marginally reduced strain peak.

Mid-plane Figure 5.13 shows the numerical/experimental strains for the plies adjacent to the mid-plane. Two different 1D paths as specified in Figure 5.9, are selected for the comparison.

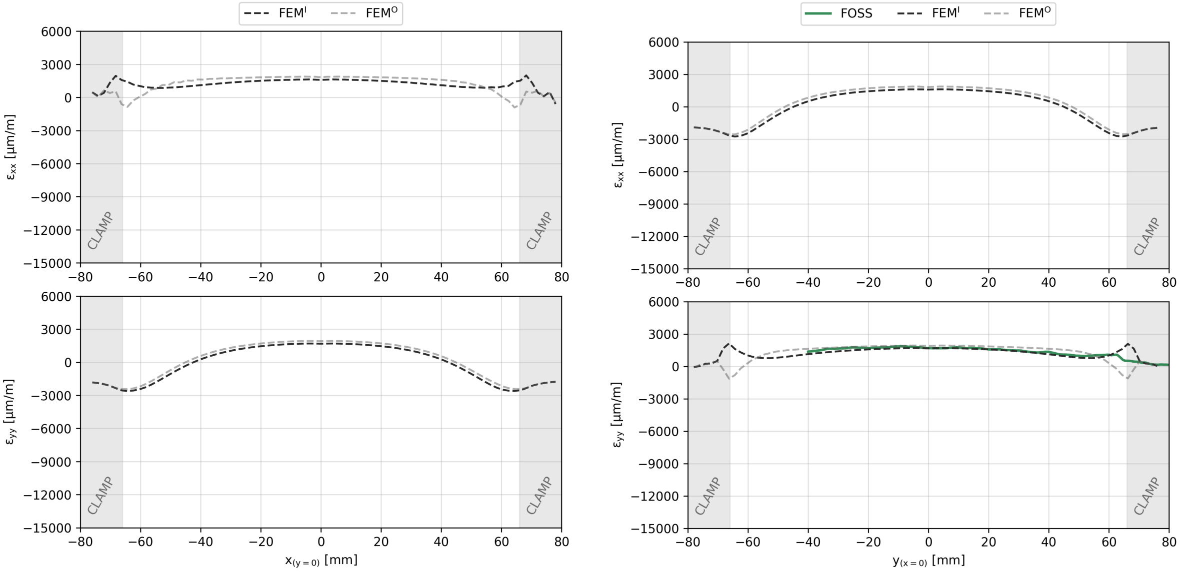

(a) Longitudinal (ϵ_{xx}) and transverse (ϵ_{yy}) in-plane strain components along X-path ($y = 0$)

(b) Longitudinal (ϵ_{xx}) and transverse (ϵ_{yy}) in-plane strain components along Y-path ($x = 0$)

Figure 5.13: U-C-RT specimen: 1D strain paths, at an applied pressure of 9 [bar]

Figure 5.13b shows that the FOSS strain matches closely with the one of the inner mid-plane ply (FEM$^{\text{I}}$). Both the numerical and experimental data show a strain peak of 2000 [μm/m] at the end of the clamp.

Similar to the observations made for the flat specimen, there is no strain uniformity through the thickness of the specimen. The strains for the outer-most ply are generally double that of the ones near the mid-plane.

Curved, reinforced specimen

Outer-most ply Figure 5.14 shows the numerical/experimental strains for the outer-most ply. Four different 1D paths as specified in Figure 5.8, are selected for the comparison.

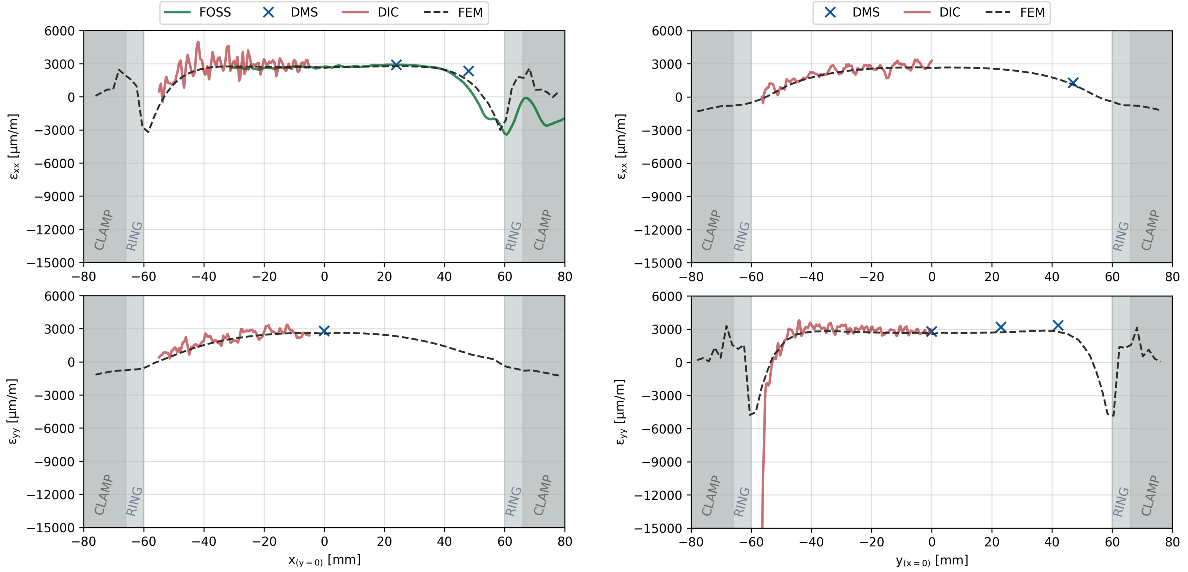

(a) Longitudinal (ϵ_{xx}) and transverse (ϵ_{yy}) in-plane strain components along X-path (y = 0)

(b) Longitudinal (ϵ_{xx}) and transverse (ϵ_{yy}) in-plane strain components along Y-path (x = 0)

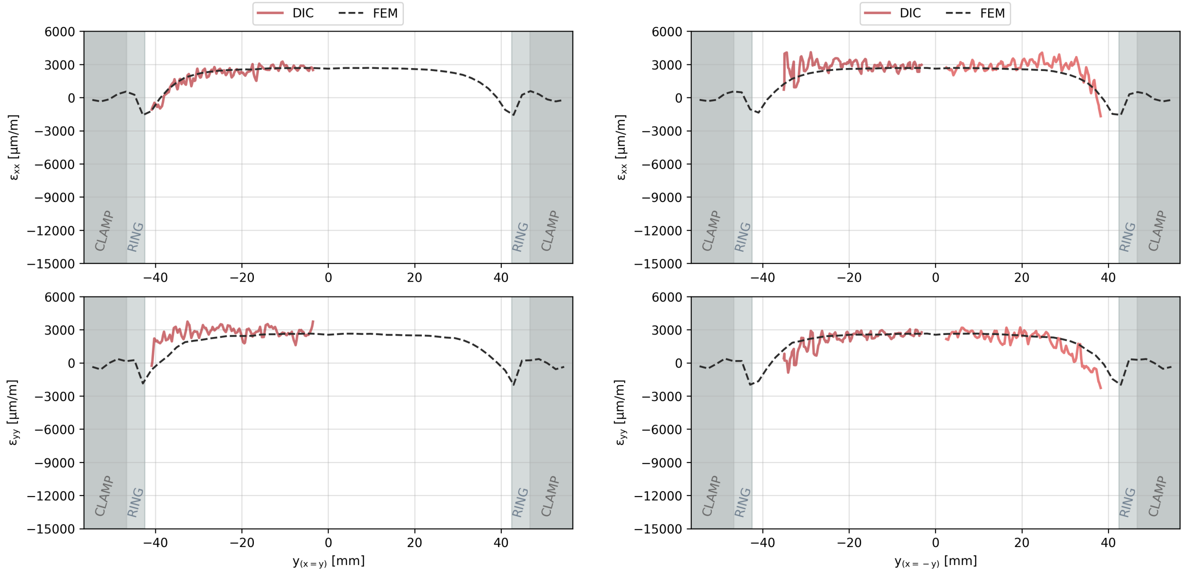

(c) Longitudinal (ϵ_{xx}) and transverse (ϵ_{yy}) in-plane strain components along diagonal XY-path (x = y)

(d) Longitudinal (ϵ_{xx}) and transverse (ϵ_{yy}) in-plane strain components along diagonal YX-path (x = −y)

Figure 5.14: R-C-RT specimen: 1D strain paths, at an applied pressure of 9 [bar]

The strain sensor and the model yield similar results. Some DIC measurements in Figure 5.14 are able to capture the strain gradient near the region of reinforcement. As explained previously in Figure 5.3.2, the DMS measurements are higher than the FEM predictions, especially for points away from the centre of the specimen. Moreover, FOSS data is available for the entire strain path in Figure 5.14a. This means that a comparison can be made for the strain gradients and peaks. Both the FEM and FOSS show a compressive strain peak of -3000 [μm/m] at x = 60 in Figure 5.14a. However, a notable discrepancy is observed in the second peak at x = 68 in Figure 5.14a, where the FOSS records a near-zero strain while the FEM predicts $+3000$ [μm/m]. It is not completely clear whether the true strain peak of the specimen is represented more accurately by the FEM or the FOSS. For example, kinking of the optical fibre can induce compressive strains within the sensor, potentially (and erroneously) offsetting any tensile strains present in the specimen. Consequently, the FOSS measurements should be interpreted with caution, as they may not reliably represent the actual specimen behaviour. From a pragmatic standpoint, it would be reasonable to adopt the (conservative) FEM-predicted strain for further analysis, thereby minimising the risk of underestimating strain—particularly within the clamping zone.

A statement can also be made about the influence of reinforcement. To do so, the results of the curved specimen (Figure 5.14) are compared with the ones from the flat specimen (Figure 5.12). Firstly, there are two stiffness jumps in the reinforced configuration. This results in an additional strain peak. Furthermore, the reinforcement reduces the magnitude of these strain peaks by a factor of 2. This is a promising outcome, as it suggests an increased tolerance of the specimen to damage induced by the clamping process.

Mid-plane Figure 5.15 shows the numerical/experimental strains for the plies adjacent to the mid-plane. Two different 1D paths as specified in Figure 5.9, are selected for the comparison.

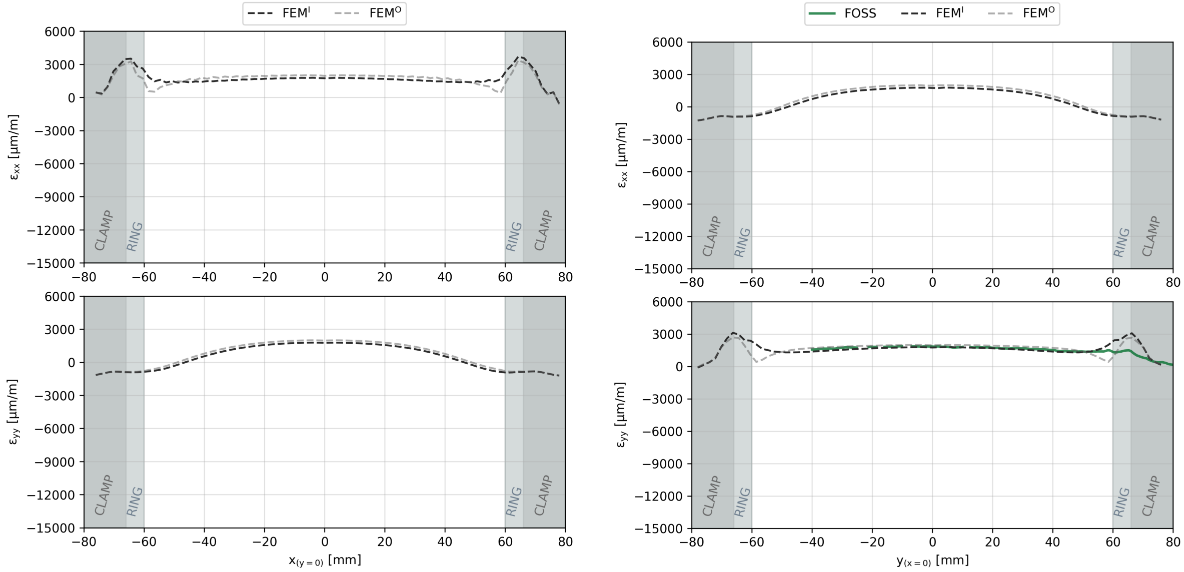

(a) Longitudinal (ϵ_{xx}) and transverse (ϵ_{yy}) in-plane strain components along X-path (y = 0)

(b) Longitudinal (ϵ_{xx}) and transverse (ϵ_{yy}) in-plane strain components along Y-path (x = 0)

Figure 5.15: R-C-RT specimen: 1D strain paths, at an applied pressure of 9 [bar]

Figure 5.15b shows that the strain measured by the FOSS matches well with that of the plies adjacent to the mid-plane. Unlike the model, the FOSS is not able to capture the $+3000$ $[\mu\mathrm{m/m}]$ strain peak at the boundary of the ring and clamp.

To avoid repeated discussion, the difference in the strains at the mid-plane vs surface plies shall not be covered here. A more interesting question is the influence of the reinforcement on the strains at the mid-plane. An observable difference arises in the magnitude of the strain peak. Specifically, the FEM shows that the tensile strain peak at the clamp–ring boundary is approximately 30% higher than the corresponding peak at the clamp–specimen boundary in the un-reinforced specimen. This increase is not considered critical, as the absolute strain of this peak is 3000 $[\mu\mathrm{m/m}]$, which is significantly lower than the strain peak observed in the outer-most ply.

5.3.3. 0D point strain

Thus far, 2D and 1D strains were compared. A limitation of these comparisons is that the strain data could only be plotted at one load level. It is possible to plot the entire load history by selecting specific points on the specimen. In order to include as much sensor data as possible, the points of comparison were taken to be the locations of the strain gauges (DMS). A point was selected on the FOSS fibre to best match the position of the strain gauge. Note that the FOSS fibre embedded at the mid-plane of the laminate is excluded from this analysis, because it has been established in chapter 4 and subsection 5.3.2 that there is a non-uniform strain distribution through the laminate's thickness. Thus, for a fair comparison, only surface strains or strains of the outer-most ply are compared. With that in mind, the DIC data is picked for a point corresponding to that of the strain gauge. An axially symmetric point, strictly speaking, had to be used as the DIC speckle pattern is not sprayed on top of the strain gauges. Finally, the strains from the FEM are extracted from the outer-most ply. The true/logarithmic strains are selected at the integration points of four, neighbouring mesh elements. The total area of these mesh elements approximately matches the area of the measuring grids of the strain gauges. These strains are averaged to yield a mean value that coincides with the location of the physical strain gauge.

The goal of this analysis is both quantifying the validity of the model for various load levels and understanding the influence of temperature. To keep the discussion focused on temperature, the effect of geometry is not analysed again here. For ease of comparison, data for the same specimen design, but tested at different temperatures, is visualised. Specifically, the data from the reinforced specimen is selected, because it did not fail even at the maximum pressure level (as shown by the test overview plots in chapter 4). This means that the strain data is available for more load levels than other un-reinforced specimen, allowing for a more extensive comparison. Strain vs pressure data for all other tests are provided in Appendix D.

Room temperature

Figure 5.16 shows the numerical and experimental strains extracted at selected points on the specimen. The location of each point is provided. The coordinates of these points can be referenced from Figure 4.7b.

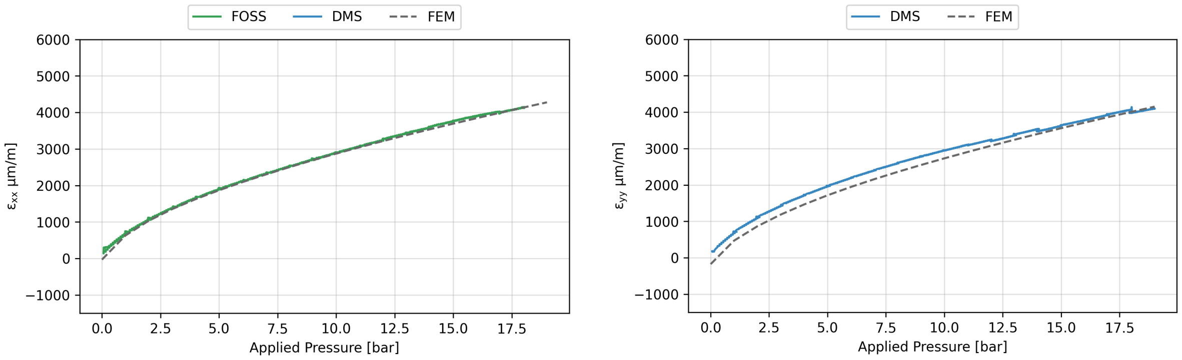

(a) Longitudinal in-plane strain (ϵ_{xx}) at $(x, y) = (5, 0)$ [mm]

(b) Transverse in-plane strain (ϵ_{yy}) at $(x, y) = (0, 0)$ [mm]

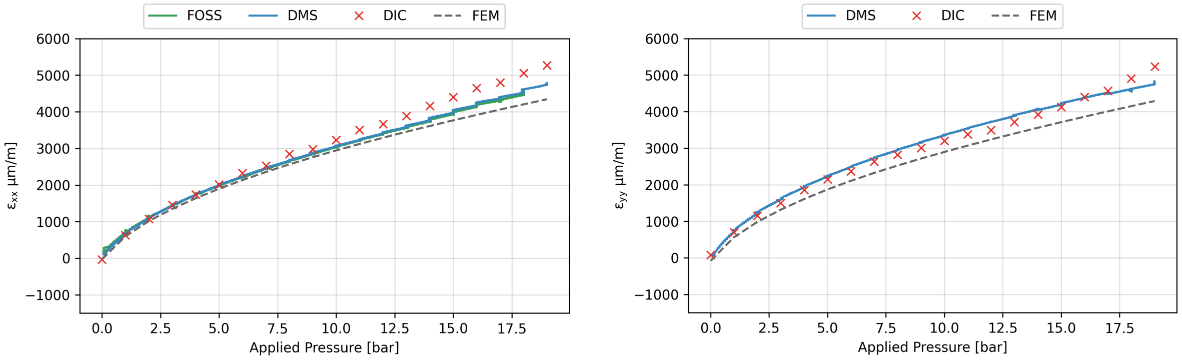

(c) Longitudinal in-plane strain (ϵ_{xx}) at $(x, y) = (24, 0)$ [mm]

(d) Transverse in-plane strain (ϵ_{yy}) at $(x, y) = (0, 23)$ [mm]

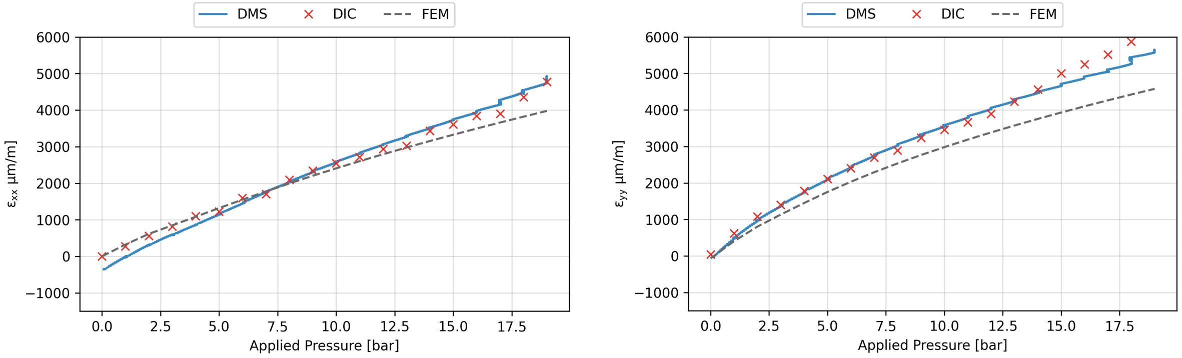

(e) Longitudinal in-plane strain (ϵ_{xx}) at $(x, y) = (48, 0)$ [mm]

(f) Transverse in-plane strain (ϵ_{yy}) at $(x, y) = (0, 42)$ [mm]

Figure 5.16: R-C-RT specimen: Strain vs pressure at selected points

The availability of strain data from multiple sensors allows Figure 5.16 to be used for comparison with the numerical model. The experimental strain dataset is nearly complete, with the exception of a missing strain gauge in Figure 5.16a and a missing FOSS point in Figure 5.16e. Several observations can be made. For example, excellent agreement between FEM and DMS is observed at the centre of the specimen (Figure 5.16a–5.17b), particularly at higher load levels. However, the agreement worsens in the intermediate region (Figure 5.17c–5.17d). In Figure 5.17c, the sensors record noticeably higher strains beyond 10 [bar], resulting in a difference of up to 20% between the experiment (specifically, DIC) and the model at the highest load level of 19 [bar]. The largest discrepancy is observed in Figure 5.17d, where the experimental strains are offset by approximately $+15$% relative to the numerical predictions.

Cryogenic temperature

Figure 5.17 shows the numerical and experimental strains extracted at selected points on the specimen. The location of each point is provided. The coordinates of these points can be referenced from Figure 4.13b.

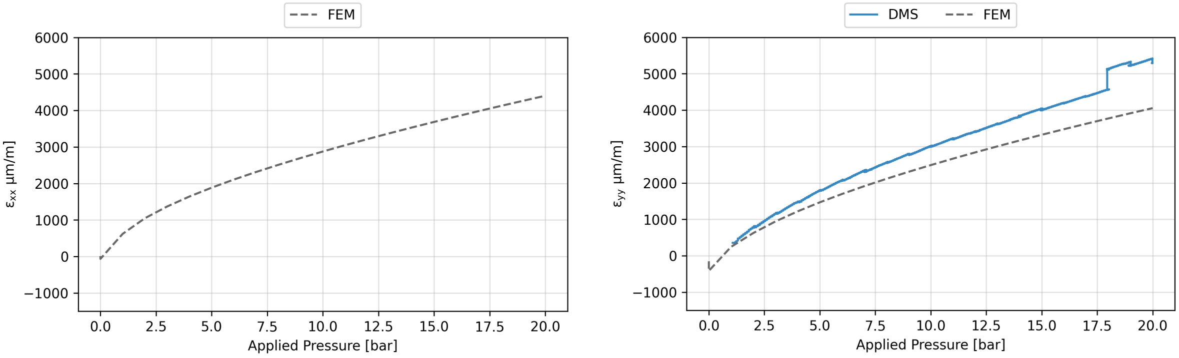

(a) Longitudinal in-plane strain (ϵ_{xx}) at $(x, y) = (-5, 0)$ [mm]

(b) Transverse in-plane strain (ϵ_{yy}) at $(x, y) = (0, 0)$ [mm]

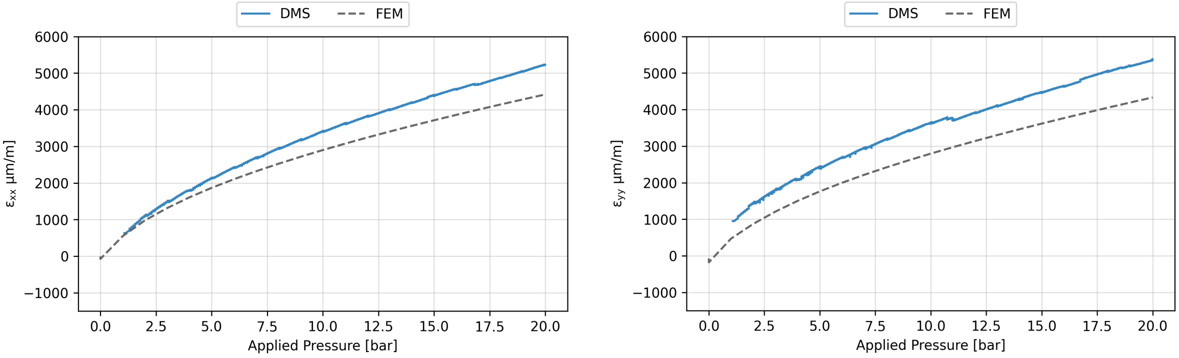

(c) Longitudinal in-plane strain (ϵ_{xx}) at $(x, y) = (-24, 0)$ [mm]

(d) Transverse in-plane strain (ϵ_{yy}) at $(x, y) = (0, 24)$ [mm]

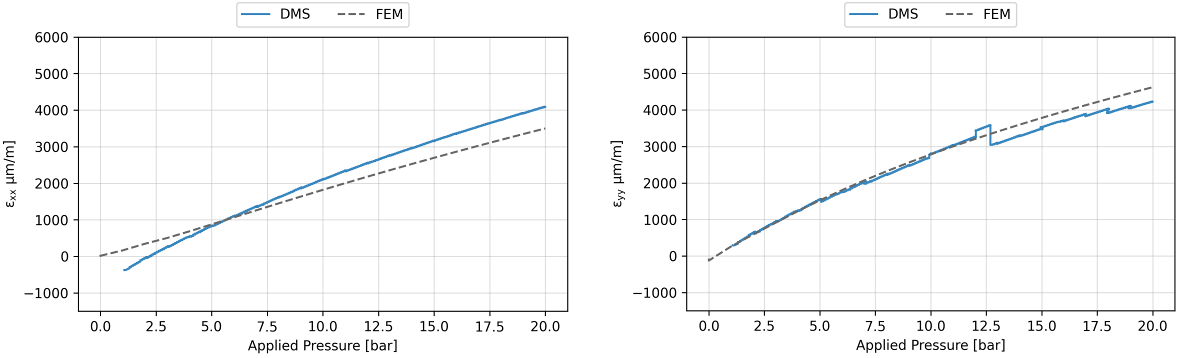

(e) Longitudinal in-plane strain (ϵ_{xx}) at $(x, y) = (-47, 0)$ [mm]

(f) Transverse in-plane strain (ϵ_{yy}) at $(x, y) = (0, 47)$ [mm]

Figure 5.17: R-C-CT specimen: Strain vs pressure at selected points

The cryogenic FEM strains are very similar to the room-temperature results shown in Figure 5.16. The key differences in the cryogenic numerical model are the inclusion of a cooling step prior to pressurisation and the temperature dependence of the material properties. As the specimen is restrained during cooling, the total thermal and mechanical strains remain close to zero during this stage. However, because a contact boundary condition is applied, there is some unrestrained movement at the clamps. This may result in a small amount of thermal contraction, which could explain why the numerical strains in Figure 5.17 are 200–300 $[\mu\text{m}/\text{m}]$ lower than those in Figure 5.16.

The agreement between FEM and DMS is noticeably worse at cryogenic temperature. For example, Figure 5.17b shows that the experimental strains at the centre of the specimen exceed the numerical predictions by up to 1300 $[\mu\text{m}/\text{m}]$. This is unexpected, given the near-perfect agreement between numerical and experimental strains at room temperature. Furthermore, offsets of up to 1000 $[\mu\text{m}/\text{m}]$ are observed at other locations (Figure 5.17c–5.17d), corresponding to a relative difference of almost 20% between FEM and DMS. Such discrepancies could plausibly be attributed to temperature-induced errors in the strain gauges. Although the strain gauges were temperature-compensated, as described in subsection 5.2.3, there is no guarantee that the inputs to the compensation equation are fully accurate. This is particularly relevant for the apparent strain caused by the mismatch in thermal contraction between the strain gauge and the substrate. Specifically, there is uncertainty in the coefficients of thermal expansion listed in Table C.1 used to correct for this CTE mismatch. These uncertainties may explain why the experimental strains deviate from the numerical predictions at cryogenic temperature.

5.4. Damage Assessment

The inter and intra-laminar damage, as observed in post-mortem test specimen and as predicted by the numerical model, is assessed in subsection 5.4.1 and subsection 5.4.2 respectively.

5.4.1. Inter-laminar: Comparing QDC damage initiation with ultrasound C-scans

This sub-section compares the extent of inter-laminar damage predicted by the numerical model with that detected experimentally. The Quadratic Damage Criterion (QDC), described in subsection 2.6.1, is evaluated at each interface in the model. To provide a conservative assessment, only the interface exhibiting the largest area of predicted delamination (defined as QDC > 1) is presented. The experimental measurements are obtained from ultrasonic C-scan imaging, as described in section 3.3.

The un-reinforced specimen tested at room temperature (RT) exhibited leakage, as reported in chapter 4, with the leakage localised near the clamping region. These RT specimens are therefore selected for analysis, as they maximise the likelihood of identifying damage. Additionally, results for the un-reinforced specimen tested at cryogenic temperature (CT) are included to assess the influence of temperature on delamination behaviour. Results for the reinforced specimen are provided separately in subsection D.3.1.

Damaged un-reinforced specimen at room temperature

Damage is observed in both the flat and curved un-reinforced specimen that were tested at room temperature. For a fair comparison, the results from the numerical model are extracted at the experimentally determined failure load.

Flat

Figure 5.18 reports the inter-laminar results for the flat specimen.

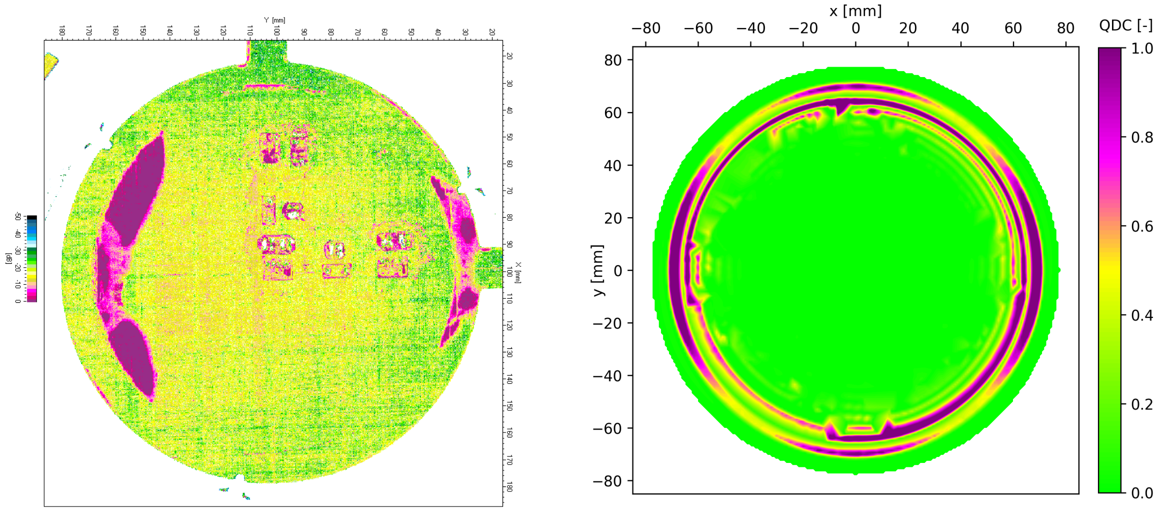

(a) Post-test pulse-echo ultrasound C-Scan at 10 [MHz]

(b) Estimation of delamination onset using the QDC at the applied (failure) pressure of (10 [bar]). The QDC plot is selected for the ply interface that exhibits the largest area of delamination initiation.

Figure 5.18: U-R-RT specimen inter-laminar damage

The ultrasound inspection (Figure 5.18a) clearly reveals two delamination zones, visualised as pink regions that correspond to areas with a low signal-to-noise ratio in the reflected ultrasound signal. The attenuation of the signal is caused by trapped pockets of air, indicating the presence of buckled delaminations within the specimen. These delamination zones are located near the clamping region of the specimen, coinciding with the leakage location.

In the numerical results (Figure 5.18b), delamination is also initiated towards the specimen edges. However, unlike the C-scan, the predicted damage onset extends along the entire circular path. This difference arises because the model reports the area of delamination initiation at a single interface, whereas the ultrasound captures the propagation of delamination through the specimen thickness. Achieving closer agreement between model and experiment would require modelling inter-laminar damage progression—using, for example, VCCT, XFEM, or CZM—which was beyond the scope of this work, as explained in chapter 2. Nevertheless, the QDC results from the model can be useful in a preliminary localisation of inter-laminar damage.

Curved

Figure 5.19 reports the inter-laminar results for the curved specimen.

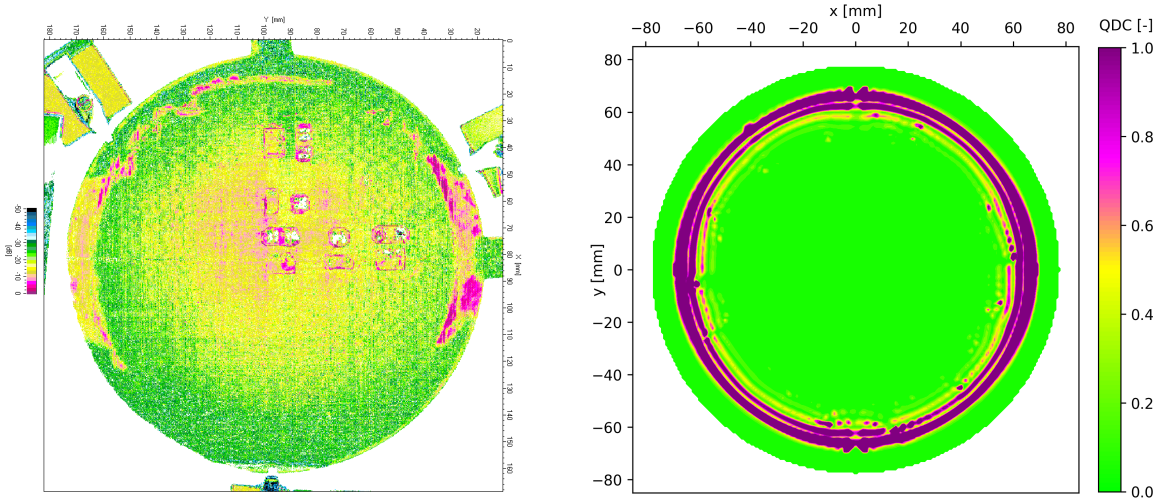

(a) Post-test pulse-echo ultrasound C-Scan at 10 [MHz]

(b) Estimation of delamination onset using the QDC at the applied (failure) pressure of $(11$ [bar]$)$. The QDC plot is selected for the ply interface that exhibits the largest area of delamination initiation.

Figure 5.19: U-C-RT specimen inter-laminar damage

Figure 5.19a indicates one delamination zone. This is seen by the pink area on the right side of the specimen. Comparing the size of the delamination zone with Figure 5.18a, it qualitatively appears that curvature reduces the total area of delamination.

Undamaged, un-reinforced specimen at cryogenic temperature

Figure 5.20 reports the results for the curved, un-reinforced specimen tested at cryogenic temperature.

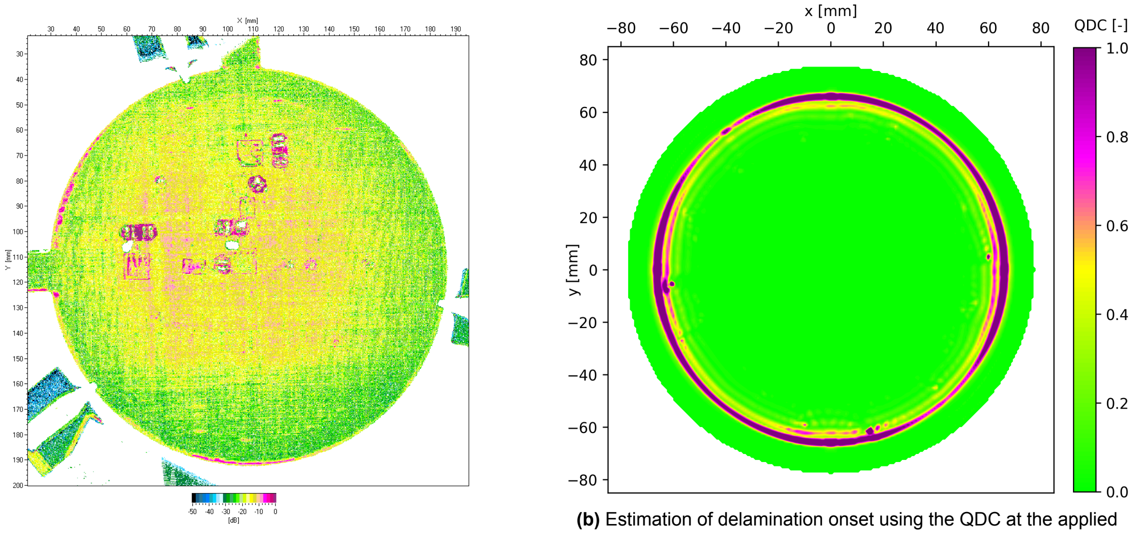

(a) Post-test pulse-echo ultrasound C-Scan at 10 [MHz]

(b) Estimation of delamination onset using the QDC at the applied (maximum) pressure of $(20$ [bar]$)$. The QDC plot is selected for the ply interface that exhibits the largest area of delamination initiation.

Figure 5.20: U-C-CT specimen inter-laminar damage

Figure 5.20a does not show any signs of delamination. Some small pink areas remain at the location of the strain gauges, and partly on the circumference where the specimen was milled from the plate. However, these cannot be attributed to the delamination of the specimen during the test.

The model does show delamination initiation in a thin circular band, that coincides with the edge of the clamp. However, it is visually seen that delamination is initiated in a smaller area, despite the results being taken at a higher load level. This means that even the numerical model predicts a delayed onset of delamination at cryogenic temperature. This is explained by the fact that interface strength increases with decreasing temperature, thus increasing the laminate's tolerance to inter-laminar damage at CT.

5.4.2. Intra-laminar: Comparing LARC05 damage initiation with optical micro-graphs

In chapter 2, it was identified that damage in the specimen can occur in two distinct regions due to two different reasons. Firstly, damage that is observed in the central bi-axial strain zone is likely to be a result of thermo-mechanical stress state. However, a second, undesired location of damage is near the clamp that is introduced because of the test setup's boundary condition. The aim here is to distinguish between these two categories of damage. To do so, the LARC05 damage initiation criterion is first used to localise the damage. As the model is not able to capture progressive damage, optical microscopy is needed to analyse the damage state in more detail. Micro-graphs of sections cut at the centre and near the clamping region of the specimen are provided.

The scope of intra-laminar damage assessment is limited to one specimen only. Specifically, the flat specimen at room temperature is selected. This is because the ultrasound C-scan in Figure 5.18a shows distinct damaged and undamaged regions at the clamping region and centre region respectively. Such a sharp distinction was not observed in other specimen. Therefore, the flat specimen can best illustrate the difference in damage states seen in different parts of the specimen.

Localisation of damage initiation using LARC05

Figure 5.21 shows the damage initiation variables at the end of the simulation. It should be noted that these variables are only valid in the range of 0 (no damage) and 1 (damage initiation). Four damage modes are shown: fibre splitting (LARCFSCRT), matrix cracking (LARCMCCRT), fibre kinking (LARCFKCRT) and tensile fibre failure (LARCFTCRT)

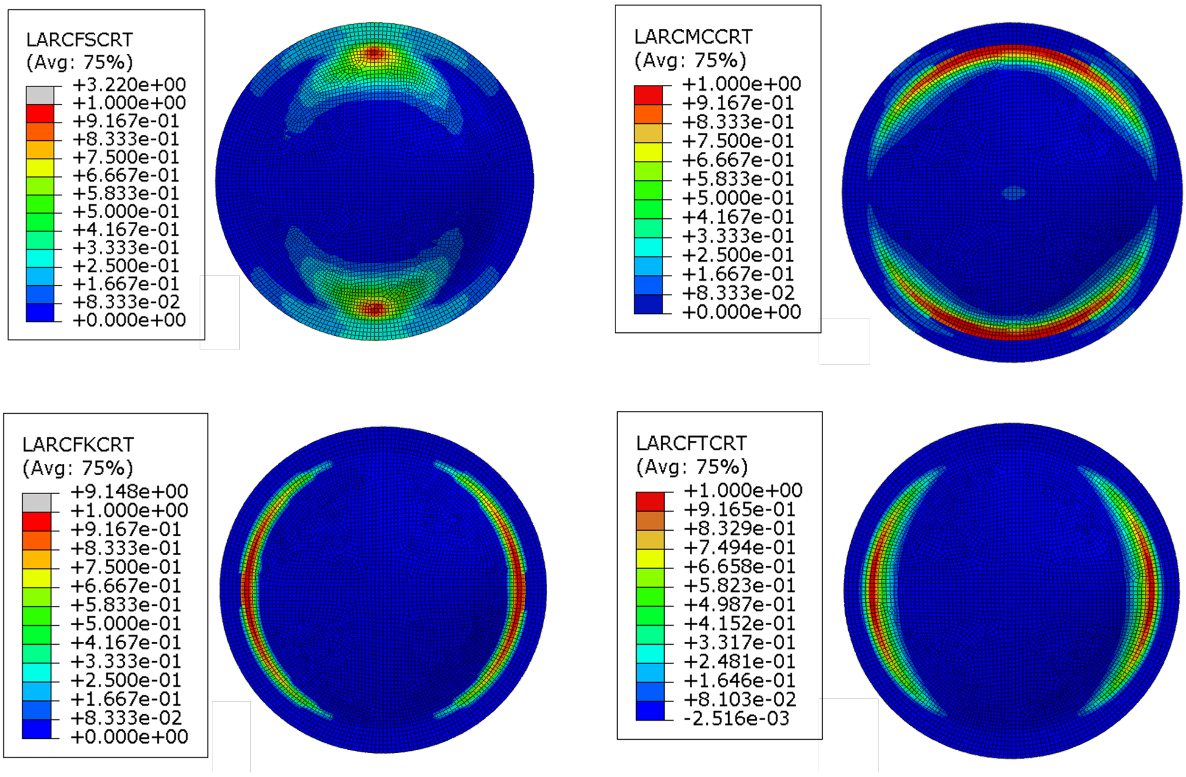

Figure 5.21: U-F-RT specimen: LARC05 damage initiation

Figure 5.21 clearly shows that all intra-laminar damage modes are localised towards the edges of the specimen, coinciding with the location of the stiffness jump caused by the end of the clamp. Significantly less damage occurs at the centre of the specimen.

Optical micro-graphs near the clamping region

Selected optical micro-graphs of the damaged region are shown in Figure 5.22. The sections were cut near the clamping region of the flat specimen. The global coordinates of the section cuts are captioned for each micrograph, and referenced from the technical drawing shown in Figure 4.1b.

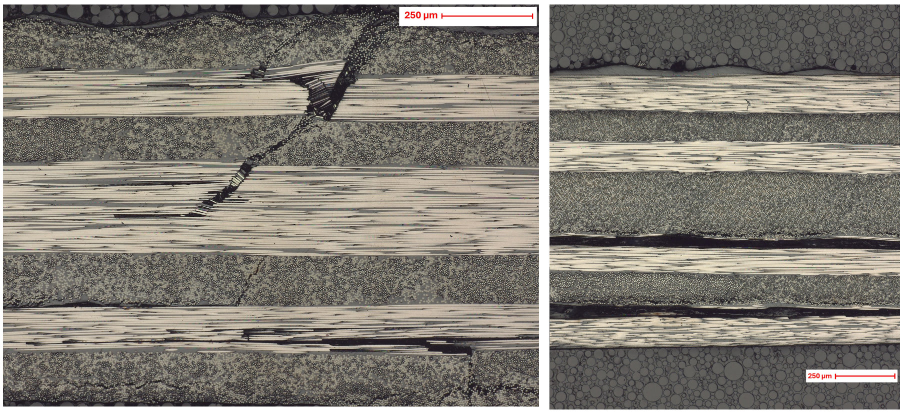

(a) Crack network: Section cut at $(x, y) = (0, 60)$ [mm]

(b) Delamination: Section cut at $(x, y) = (-60, 0)$ [mm]

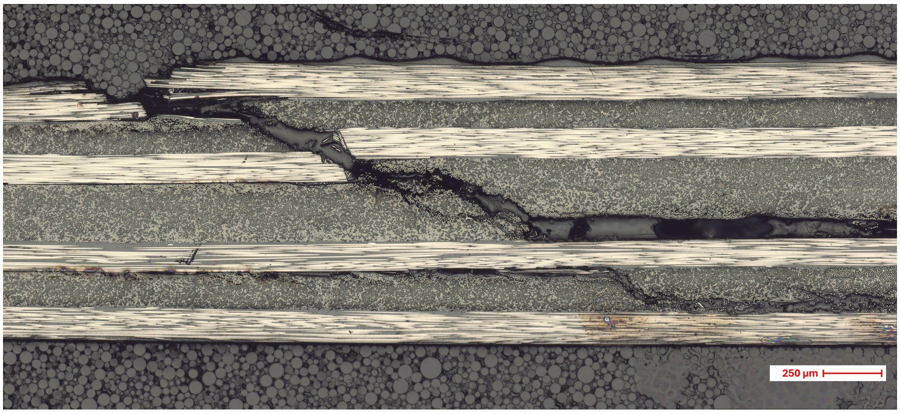

(c) Crack network: Section cut at $(x, y) = (-60, 0)$ [mm]

Figure 5.22: U-F-RT specimen: Optical micro-graphs of damaged sections in the clamping region

Multiple damage modes are visible in Figure 5.22. Observing Figure 5.22a, matrix cracks can be seen in top two $90°$ plies. Fibre failure is also visible. Similarly, an extensive crack network is present in Figure 5.22c. This crack network results from both intra (tensile fibre failure and matrix cracks in ply) and inter (delamination between plies) laminar damage modes. Leakage detected experimentally in subsection 4.1.1 is a likely result of these crack paths. Furthermore, two distinct delaminations are evident in Figure 5.22b. The location of these delaminations are in agreement with the specimen's C-scan (Figure 5.18a).

Optical micro-graphs at the centre of the specimen

Some cut-sections at the centre of the specimen are shown in Figure 5.23. The global coordinates of the section cuts are captioned for each micrograph, and referenced from the technical drawing shown in Figure 4.1b.

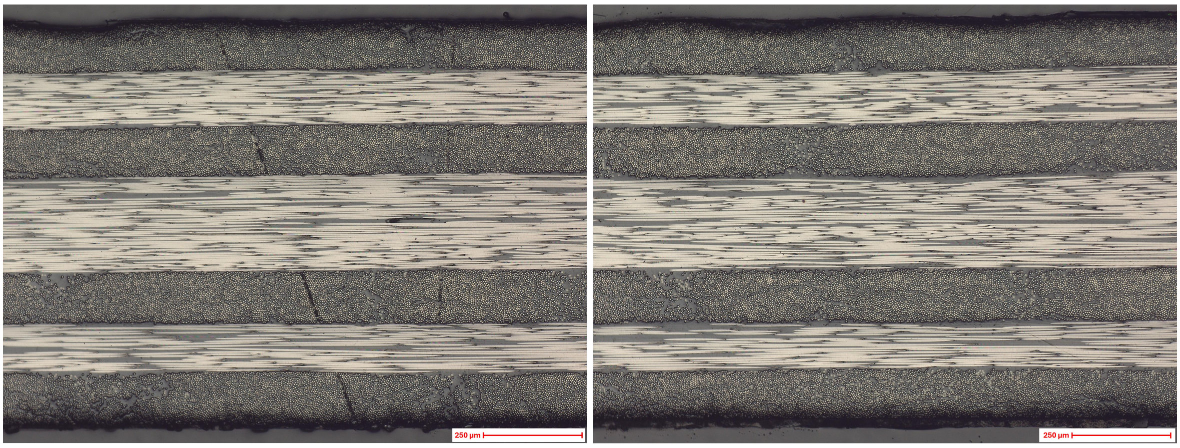

(a) Two isolated transverse matrix cracks: Section cut at $(x, y) = (0, 10)$ [mm]

(b) Undamaged laminate: Section cut at $(x, y) = (0, 10)$ [mm]

Figure 5.23: U-F-RT specimen: Optical micro-graphs at the centre of the specimen

Compared to the clamping zone, the centre region remains largely undamaged. In Figure 5.22b, no damage can be recognised. Two separate matrix cracks can be detected in Figure 5.23a. These occurs only in the 90° plies. No fibre damage or delamination is observed in Figure 5.23b. Therefore, the existence of through-the-thickness leak paths, at the centre of the specimen, cannot be confirmed.

5.5. Outlook

Numerical-experimental results were compared in this chapter. The contact model was tuned based on the DIC displacement field at room temperature, resulting in a static friction coefficient of 0.01 between the specimen and indium seal. It was shown that once the specimen started slipping, the magnitude of the clamping force of the contact model was insensitive to the displacement results. The validity of the tuned model was subsequently quantified. The numerically predicted strains were evaluated against the experimentally measured ones. The agreement between the simulation and the experiment varies, depending on the load level, position on the specimen, temperature and sensor. The results may differ by up to 20%. Such an upper limit is considered to be adequate for a preliminary numerical design study that will be conducted in (chapter 6). Finally, the model's intra and inter laminar damage initiation criteria can coarsely localise damage. Both optical microscopy and ultrasound reveal that damage is present in the clamping region of some specimen.

6

Numerical Design Study

The validated numerical model can be used to aid the preliminary design of bulge test specimen. In order to do so, parametric studies are conducted using the numerical model. The objective of these parametric simulations is to identify the design variables that may improve the representativeness of the bulge test.

The setup of the design study is described, including an explanation of the post-processing of the simulation results. A default configuration is simulated, which serves as a basis for further comparisons. Subsequent simulations explore the effect of other design variables. The motivation, results and discussion of each design variable is provided (locally) in its respective section.

Contents

6.1. Setup of the parametric design study

The parametric design study utilises the numerical model that was validated in chapter 5, as per the methodology outlined in chapter 2. For the design study, a post-processing workflow was augmented to the numerical model. Several python scripts were written to directly access the .odb files of the simulation, thus bypassing the need for the Abaqus GUI. This meant that it was necessary to decide on how the simulation data should be universally processed and visualised in the design study. Thus, multiple analyses were derived based on the objectives of the parametric study.

6.1.1. Coordinate system

First and foremost, the coordinate system that is referenced in the remainder of the chapter is given by Figure 6.1.

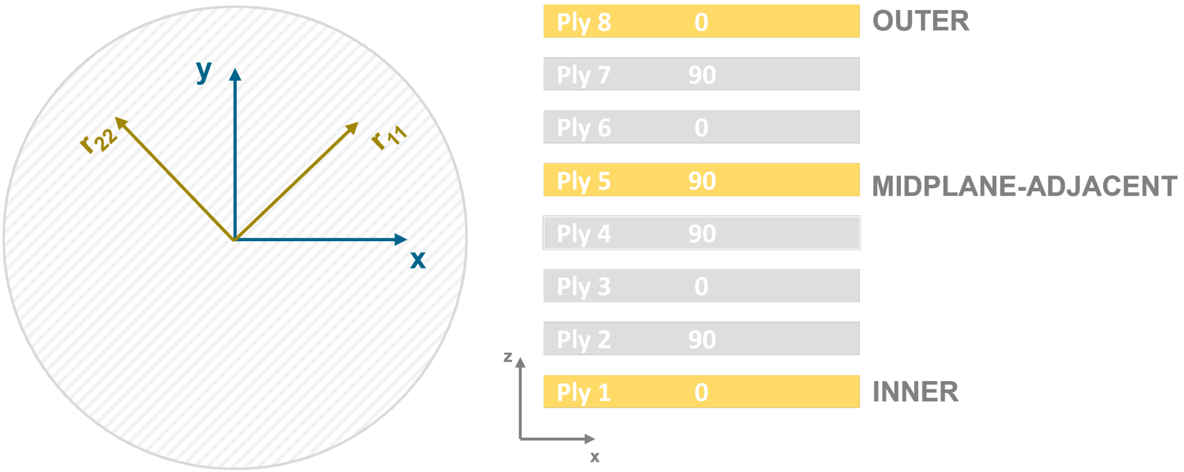

(a) Global/laminate (x, y), and local/ply (r_{11}, r_{22}) paths

(b) Ply index of a standard 8-ply, symmetric balanced cross-ply laminate

Figure 6.1: Coordinate system used in the parametric design study

It must be explicitly noted that the coordinate system of the ply is not always aligned with that of the laminate (Figure 6.1a). In Figure 6.1b, plies highlighted in yellow are given names. Generally, results are provided for only these plies. Strictly speaking, the stress-strain values are extracted from the integration points of these plies, which coincide with the mid-plane of the ply. As there is no integration point on the mid-plane of the laminate, stress-strain results are not directly available at the mid-plane of the laminate. Consequently, results are provided for the ply adjacent to the mid-plane. The inner-ply in Figure 6.1b corresponds to the side of the laminate to which the pressure load was applied.

6.1.2. Strain bi-axiality

The strain bi-axiality in the specimen's region of interest is analysed. The region of interest of the bulge specimen is assumed to be a central, circular area. The in-plane components of strain should be equal to each other to correctly represent the equal bi-axial strain state of a tank dome. Therefore, to quantify bi-axiality, the ratio of in-plane strains[1] $\varepsilon_{22}/\varepsilon_{11}$ are plotted only inside a (small) circular region of radius 30 [mm]. Preliminary visualisations showed that the bi-axiality ratio significantly deviated from the ideal value of 1 ($\varepsilon_{22}/\varepsilon_{11} > 1.2$, or $\varepsilon_{22}/\varepsilon_{11} < 0.8$) outside of the 30 [mm] zone. Hence, for a standard 160 [mm] specimen, it can already be said that the upper limit of the equal bi-axial zone is 30 [mm], for a 20% tolerance on bi-axiality. In this study, it is of interest to determine the size of the equal bi-axial zone for a lower tolerance. This means that it is unnecessary to plot $\epsilon_{22}/\epsilon_{11}$ outside the 30 [mm] zone. Additionally, the magnitude of in-plane strain[2] $\left(\sqrt{\varepsilon_{11}^2 + \varepsilon_{22}^2}\right)$ is computed in tandem with the bi-axiality ratio. It is of interest to maximise the strain magnitude in the central region of interest of the specimen, to observe potential leakage/damage in the equal bi-axial zone. As strain uniformity through the thickness of the bulge specimen does not exist (discussed in chapter 4-5), it is useful to analyse the bi-axiality state for multiple plies of the laminate. Three plies are selected, as shown in Figure 6.1b.

6.1.3. Stress-strain path

The longitudinal stress-strain $(\sigma_{11} - \varepsilon_{11})$ along the fibre path (r_{11}) is extracted. ε_{11} along r_{11} is comparable in magnitude to ε_{22} along r_{22}. However, it was marginally beneficial to plot ε_{11} to allow for the visualisation of σ_{11} in the same plot.

r_{11} is drawn from the centre to the edge of the specimen, as shown in Figure 6.1a. This visualises not only the region of (nearly) constant strain in the middle of the specimen, but also identify any peaks

---

[1] The out-of-plane axial strain, ε_{33}, is non-zero due to the large out-of-plane displacement of the laminate. It is of a similar order of magnitude to the in-plane strains. However, the scope of this study will be similar to the analysis of bi-axiality only.

[2] Shear strains are neglected, because they are zero at the centre of the specimen.

inside the clamping zone. For design purposes, it is considered sufficient to only show one half-path, due to the near-perfect radial symmetry demonstrated by the bulge specimen in Figure 5.3.2-5.3.2.

6.1.4. Fibre tensile (FT) failure

The fibre tensile initiation helps quickly assess the existence and location of first-ply failure (if any). This is a useful piece of information to a designer, as one should ensure that that tensile fibre failure does not occur prematurely at an undesired location. To do so, the LARC05 damage initiation variable for fibre tensile failure is shown, for one quarter of a ply. Figure 5.21 and results from Lentner [46] reveal a near-perfect four-way radial symmetry. Results for the ply with the highest value of the damage initiation variable is shown.

6.1.5. Quadratic delamination criterion (QDC)

The QDC helps assess the existence and location of delamination (if any). A designer should try to reduce the onset of delamination due to clamping. Simultaneously, the presence of delamination in the bi-axial area may indicate leak-paths in the desired region of interest. The QDC is computed for all interfaces of the laminate. Only results for the interface with the highest value of the QDC variable is shown. One quarter specimen is displayed, due to the nearly symmetric radial distribution of QDC observed in subsection 5.4.1.

6.2. Default design

Motivation

The R-C-CT configuration was selected as the default design configuration, where:

- R - (Reinforcement) tests indicated a reduction in the peak stress/strain magnitude.
- C - (Curvature) accounts for the geometric effects of the tank wall.
- CT - (Cryogenic Temperature) is representative of the operational environment of an LH_2 tank.

Numerical and experimental results for this configuration have showed good agreement (see chapter 5). The same numerical model as the validated R-C-CT case will be employed in the present study, with one modification concerning the tangential boundary condition between the specimen and the clamp. Instead of prescribing a static friction coefficient, a rough friction formulation will be applied. This enforces a full stick condition throughout the simulation, eliminating the effect of slippage on the measured response and enabling a more direct investigation of the parameter of interest.

It is acknowledged that enforcing a stick condition does not fully represent the current experimental reality, in which measurable slippage occurs. Nevertheless, this assumption is considered justifiable given the expectation that slippage will be mitigated in the near future through practical measures, such as increasing the surface roughness of the specimen-ring interface via processing techniques like sand-blasting.

Results

The quantification of strain bi-axiality at the specimen centre is shown in Figure 6.2a, while Figure 6.2b illustrates the onset of maximum delamination (QDC) between plies 7 and 8. The local longitudinal stress–strain response along the fibre path is presented in Figure 6.2c, and Figure 6.2d highlights the maximum fibre tensile (FT) damage initiation for the inner ply.

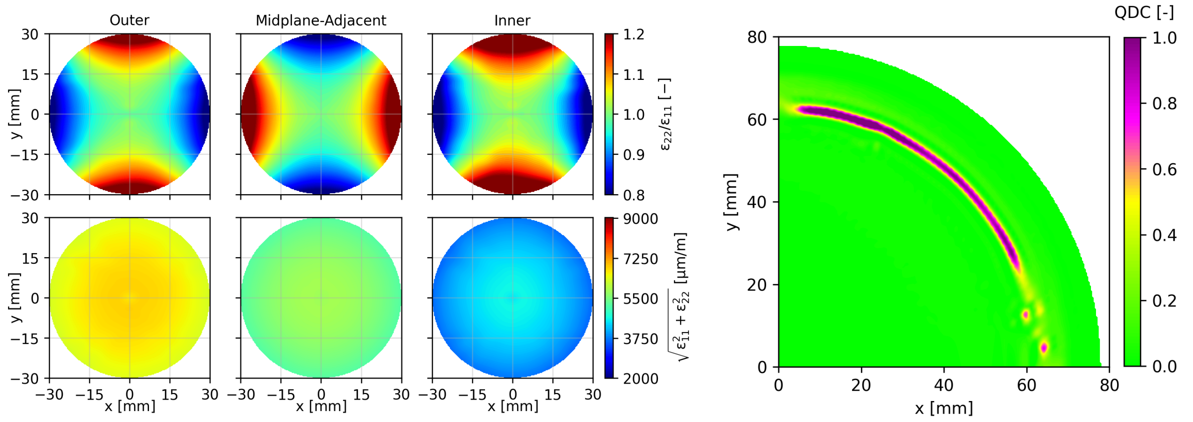

(a) Strain biaxiality at specimen centre

(b) Max. delamination (QDC), ply 7/8

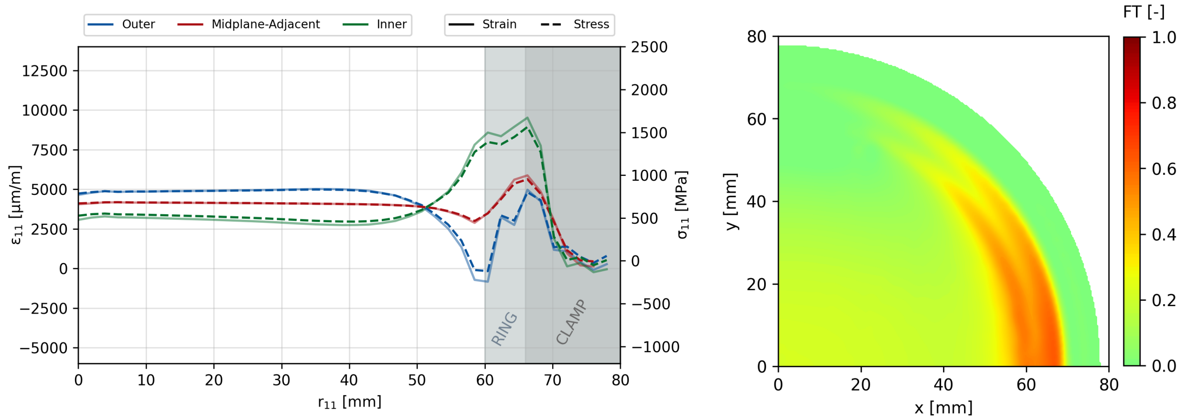

(c) Longitudinal stress–strain along fibre path

(d) Max. fibre tensile (FT) damage, ply 1

Figure 6.2: Strain biaxiality and damage initiation for the default specimen at 20 bar (CT).

Discussion

Several observations can be made from Figure 6.2. According to Figure 6.2a, the shape of the bi-axialzone appears to be hyperbolic. The magnitude of the bi-axial (tensile) strain also decreases, from the outer ply to the inner ply of the laminate. This can be explained by the fact that the contribution of the bending strain is compressive below its neutral axis. As a result, the magnitude of tensile strain of the inner ply is lower. Interestingly, this theory does not hold true for $r_{11} > 50$ $[\mathrm{mm}]$ (Figure 6.2c). As one reaches closer to the clamping region of the laminate, the highest tensile strain occurs on the inner-most ply. A possible reason could be the larger local radius of bending as the laminate leaves the reinforcement ring. In addition, there are two strain peaks corresponding to the two stiffness jumps. This is visible in the strain path of the inner ply in Figure 6.2c, as well as the two red ”bands” of fibre tensile failure in Figure 6.2d. Finally, Figure 6.2b shows that a radial strip of delamination may initiate at the location of the stiffness jump.

6.3. Influence of slippage

Motivation

chapter 4 demonstrated the occurrence of slippage under the current experimental conditions. Given that this reflects the present operational reality, it is important to quantify the influence of slippage on the measured response. From a practical standpoint, such quantification enables an assessment of the severity of the slippage. This, in turn, informs whether the associated decrease in strain justifies the allocation of additional experimental effort toward its mitigation.

Results

The effect of specimen slippage on strain distribution and damage initiation is illustrated in Figure 6.3. The strain biaxiality at the specimen centre is quantified in Figure 6.3a, while Figure 6.3b shows the predicted maximum delamination (QDC) initiation at the ply 7/8 interface. The local longitudinal stress–strain response along the fibre path is given in Figure 6.3c, and Figure 6.3d presents the maximum fibre tensile (FT) damage initiation in the inner ply.

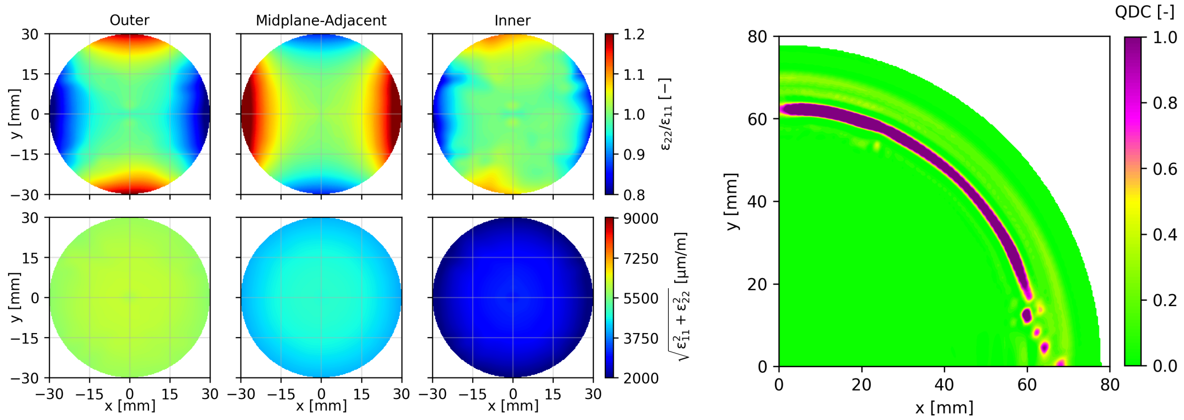

(a) Strain biaxiality at specimen centre

(b) Max. delamination (QDC), ply 7/8

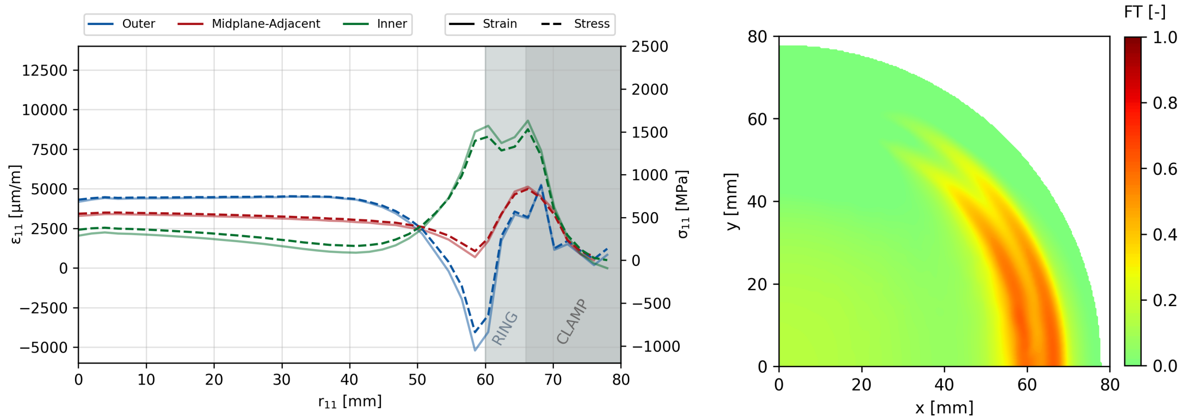

(c) Longitudinal stress–strain along fibre path

(d) Max. fibre tensile (FT) damage, ply 1

Figure 6.3: Strain biaxiality and damage initiation for a slipping specimen at 20 bar (CT).

To understand the influence of slippage, key results of the slipping specimen are compared with the default configuration in Table 6.1. Specifically, the average magnitude of the in-plane strain within the 30 [mm] radius is tabulated, for multiple plies. Then, the maximum fibre-tensile failure initiation is reported. Finally, the delaminated area, where QDC > 1, as a percentage of the total specimen area is reported.

Table 6.1: Strain metrics and damage indicators for each slippage configuration, at 20 [bar] (CT)

Configuration	$\left(\sqrt{\varepsilon_{11}^2+\varepsilon_{22}^2}\right)\Big\vert_{r\leq 30\,\text{mm}}^{\text{avg}}$ [µm]			FT$_{\text{max}}$ [-]	QDC > 1 [%]
	Outer	Mid.-Adj.	Inner		
Stick (Default)	6556	5517	4121	0.621	1.24
Slip	5924	4483	2545	0.630	3.38

Discussion

In the event of slippage, Figure 6.3a shows that the strain distribution through the laminate thickness is non-uniform. In particular, the inner ply exhibits a square-like biaxiality distribution, reflecting a heterogeneous strain state. This is in contrast to the highly regular bi-axialstrain zone observed in Figure 6.2a.

Quantitatively, the strain magnitude within the region of interest is reduced compared to the baseline, as summarised in Table 6.1. The relative difference in strain is -10 to -39%, for the outer and inner ply respectively.

Additionally, during slippage, a compressive strain peak is observed in the outermost ply at $r_{11} = 60$ mm (Figure 6.3c). This compressive peak may contribute to undesired, localised fibre kinking.

6.4. Influence of laminate thickness

Motivation

In the current experimental configuration, no leakage or damage is observed within the region of interest. While this outcome is favorable from an engineering perspective, it limits the ability to investigate the leakage phenomenon from a scientific standpoint. It is therefore hypothesised that a thinner specimen, which would experience higher strains, could induce damage in the centre of the specimen. At the same time, it is recognised that increased stress and strain can still be tolerated at the clamping region without causing fibre failure, due to the presence of the reinforcement ring. Consequently, the design objective can be simplified to determining the maximum allowable specimen thickness that ensures a positive, yet minimal, safety margin against fibre failure at the clamp.

The simulation results presented here correspond to a symmetric, balanced 4-ply cross-ply laminate. Specimens thicker than the default 8-ply configuration (i.e., > 1 mm) are not simulated, as the current assembly is already sufficiently stiff and does not exhibit failure under the applied loading.

Results

Figure 6.4 presents the strain biaxiality and damage initiation results for a thin laminate at 20 bar (CT). The strain biaxiality at the specimen centre is quantified in Figure 6.4a, while Figure 6.4b shows the maximum delamination (QDC) initiation at the ply 2/3 interface. The local longitudinal stress–strain response along the fibre path is given in Figure 6.4c, and Figure 6.4d presents the maximum fibre tensile (FT) damage initiation in the inner ply.

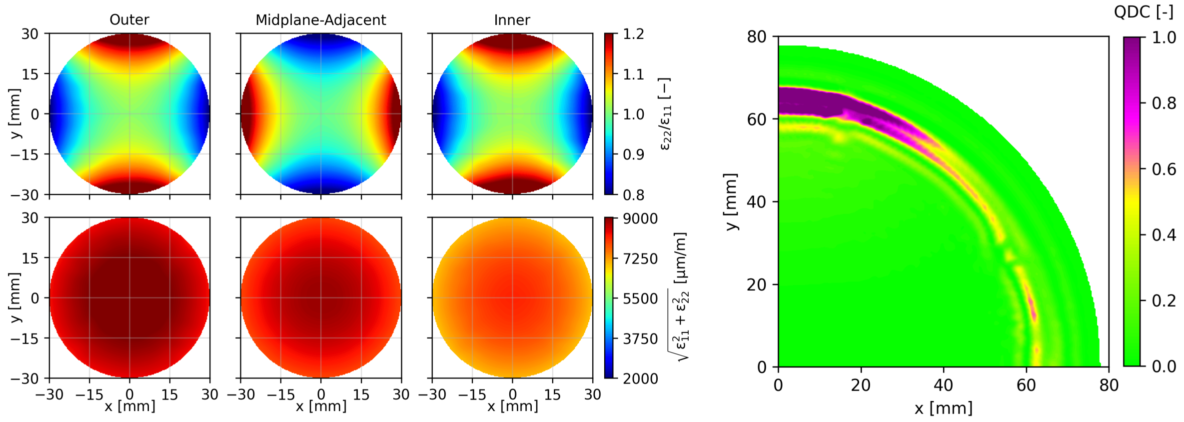

(a) Strain biaxiality at specimen centre

(b) Max. delamination (QDC), ply 2/3

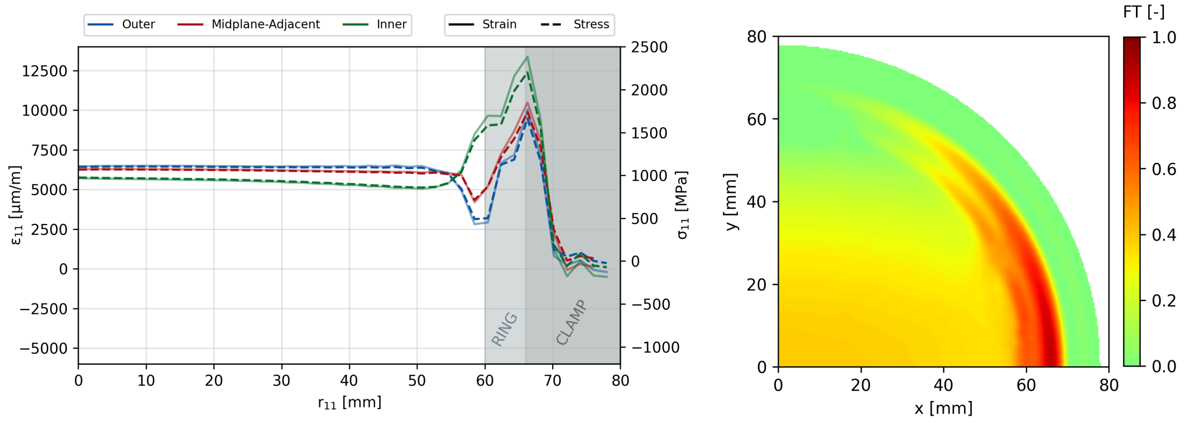

(c) Longitudinal stress–strain along fibre path

(d) Max. fibre tensile (FT) damage, ply 1

Figure 6.4: Strain biaxiality and damage initiation for a thin laminate at 20 bar (CT).

To understand the influence of laminate, key results of the thinner specimen are compared with the default, thicker one in Table 6.2. Specifically, the average magnitude of the in-plane strain within the 30 [mm] radius is tabulated, for multiple plies. Then, the maximum fibre-tensile failure initiation is reported. Finally, the delaminated area, where QDC > 1, as a percentage of the total specimen area is reported.

Table 6.2: Strain metrics and damage indicators for different laminate thicknesses, at 20 [bar] (CT)

Laminate Thickness	$\left(\sqrt{\varepsilon_{11}^2+\varepsilon_{22}^2}\right)\Big\rvert^{\text{avg}}_{r\leq 30\,\text{mm}}$ [µm]			FT$_{\text{max}}$ [-]	QDC > 1 [%]
	Outer	Mid.-Adj.	Inner		
1.0 [mm] (Default)	6556	5517	4121	0.621	1.24
0.5 [mm] - Thin	8754	8348	7535	0.885	2.04

Discussion

Reducing the thickness of the (cross-ply) laminate leads to a significant increase in strain at the centre of the specimen, with magnitudes rising by approximately 30-70% for the outer and inner plies respectively (Table 6.2). Concurrently, the strain peaks at the clamping region also increase, by 25-35% (Figure 6.4c). Despite these elevated strain levels, the laminate remains below the fibre failure threshold, with a safety margin of 0.885/1.00 (Table 6.2). Despite the reduced safety margin to fibre failure,

Figure 6.4d shows that the relative difference between the stress at the centre and at the clamps is lower. This means that the thinner specimen is more equally loaded than the thicker one.

6.5. Influence of material

Motivation

The default material, IM7/8552, is excessively strong for the current study. IM7 fibres exhibit high elastic and strength moduli, while the toughened 8552 epoxy resin provides high shear resistance. As a result, matrix cracking and delamination are not observed within the region of interest, limiting the ability to investigate the relevant damage and leakage phenomena.

A less stiff pre-preg system is selected, namely M21/T700GC. This choice is motivated by the availability of experimental data at both room temperature (RT) and low temperature (LT, $-55°$C) [41]. In this analysis, the LT properties are assumed to be representative of cryogenic temperature (CT), as data at CT are not available due to the experimental challenges of material characterisation at such low temperatures. This assumption is conservative, since the LT strength properties are likely lower than the actual CT values, yet it allows capturing the most significant changes in material response, particularly the increase in strength with decreasing temperature.

Table 6.3: Temperature dependent elastic properties of M21/700GC [41]

Temperature [K]	**E_1 [GPa]**	**$E_2 = E_3$ [GPa]**	**$\nu_{12} = \nu_{13}$ [-]**	**ν_{23} [-]**	**$G_{12} = G_{13}$ [GPa]**	**G_{23} [GPa]**
77 (CT)	102.4	10	0.287	0.622	5.8	3.1
293 (RT)	103.4	8.3	0.291	0.609	4.6	2.6

Table 6.4: Temperature dependent thermal properties of M21/700GC [41]

Temperature [K]	**α_{11} [K^{-1}]**	**$\alpha_{22} = \alpha_{33}$ [K^{-1}]**
77 (CT)	-1.94×10^{-5}	2.97×10^{-5}
293 (RT)	-3.74×10^{-5}	3.85×10^{-5}

Table 6.5: Temperature dependent strength properties of M21/700GC [41]

Temperature [K]	**$R_{\parallel}^{T}/X_T$ [MPa]**	**$R_{\parallel}^{C}/X_C$ [MPa]**	**$R_{\perp}^{T}/Y_T$ [MPa]**	**$R_{\perp}^{C}/Y_C$ [MPa]**	**$R_{\parallel\perp}/S$ [MPa]**
77 (CT)	2230	1593	93	344	106
293 (RT)	2214	1521	86	207	80

Results

Figure 6.5 presents the strain biaxiality and damage initiation results for the M21/T700GC laminate at 20 bar (CT). The strain biaxiality at the specimen centre is quantified in Figure 6.5a, while Figure 6.5b shows the maximum delamination (QDC) initiation at the ply 2/3 interface. The local longitudinal stress–strain response along the fibre path is given in Figure 6.5c, and Figure 6.5d presents the maximum fibre tensile (FT) damage initiation in the inner ply.

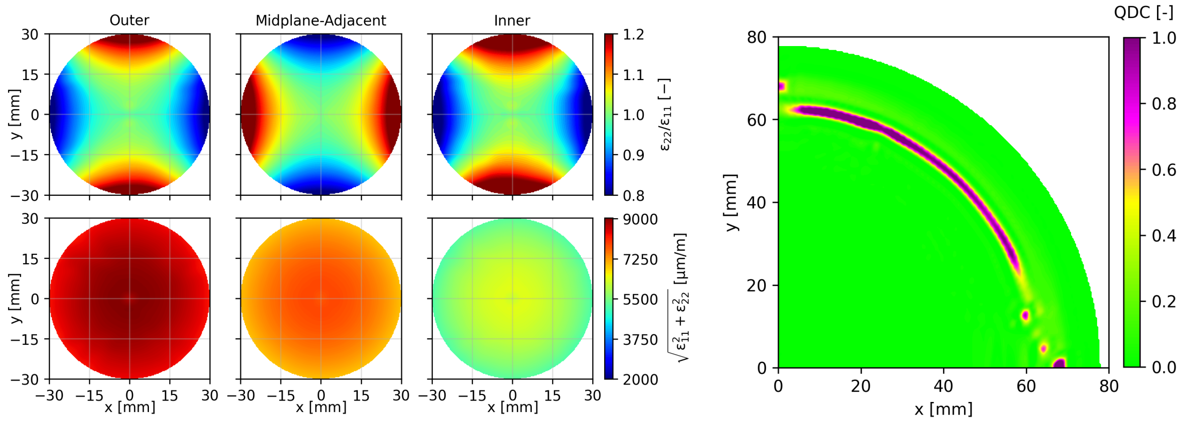

(a) Strain biaxiality at specimen centre

(b) Max. delamination (QDC), ply 2/3

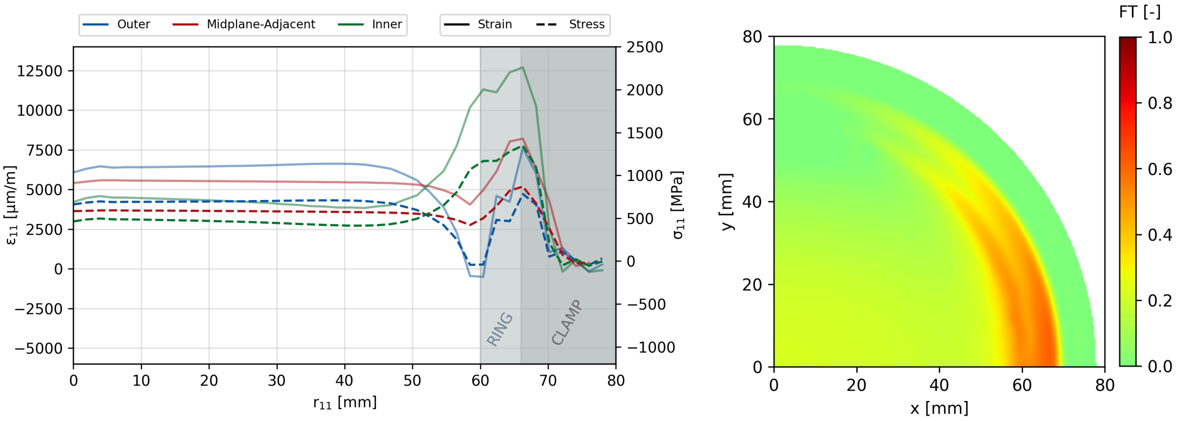

(c) Longitudinal stress–strain along fibre path

(d) Max. fibre tensile (FT) damage, ply 1

Figure 6.5: Strain biaxiality and damage initiation for M21/T700GC at 20 bar (CT).

To understand the influence of the material, key results of the M21/T700GC pre-preg system are compared with the default IM7/8552 one in Table 6.6. Specifically, the average magnitude of the in-plane strain within the 30 [mm] radius is tabulated, for multiple plies. Then, the maximum fibre-tensile failure initiation is reported. Finally, the delaminated area, where QDC > 1, as a percentage of the total specimen area is reported.

Table 6.6: Strain metrics and damage indicators for different UD-prepreg CFRP material system, at 20 [bar] (CT)

Material	$\left(\sqrt{\varepsilon_{11}^2+\varepsilon_{22}^2}\right)\Big\rvert^{\text{avg}}_{r\leq 30\,\text{mm}}$ [µm]			FT$_{\text{max}}$ [-]	QDC > 1 [%]
	Outer	Mid.-Adj.	Inner		
IM7/8552 (Default)	6556	5517	4121	0.621	1.24
M21/T700GC	8626	7406	5765	0.606	1.57

Discussion

The M21/T700GC laminate exhibits higher strains throughout the specimen, as quantified by Figure 6.5c. Table-6.6 shows that the central outer and inner regions of M21/T700GC are strain by 32-39% more, compared to the default IM7/8552 pre-preg. Despite these higher strains, no fibre tensile (FT) failure is observed, with a maximum FT indicator of 0.606 (relative to 1.0 for failure). Delamination initiation remains low and comparable between the two materials, confirming the suitability of M21/T700GC for achieving larger central strains without compromising structural integrity.

6.6. Influence of reinforcement design

Motivation

Chapter 4-5 demonstrate the clear benefits of reinforcing the specimen. In brief, stress concentrations arising from the stiffness discontinuity at the clamp are substantially reduced. The question is therefore not whether a reinforcement should be used, but whether its design can be optimised. Indeed, for the thin specimen, the maximum fibre tensile (FT) indicator was already $0.9/1.0$. From a design perspective, a greater margin of safety against fibre tensile failure is desirable.

6.6.1. Double-sided reinforcement

Motivation

Thus far, only single-sided reinforcement has been considered. Lentner [46] demonstrated that double-sided reinforcement can delay the onset of tensile fibre failure. Experimental observations, including optical micrography and damage initiation analysis, have shown that fibre failure does not occur for the R-C-CT configuration. Nevertheless, delaying the onset of fibre failure improves the margin of safety against damage induced by clamping.

Beyond this, double-sided reinforcement may also help mitigate specimen slippage. In many cases, surface treatment is required to overcome slippage. However, certain surface treatments cannot be directly applied to the specimen—for example, knurling, which requires a machining step that could damage the specimen. In such situations, it is practically advantageous to modify the contact surfaces of the reinforcement rings before they are bonded to the CFRP specimen. Assuming the same surface texturing is desired on both contact surfaces, using a double reinforcement ring allows precise *a priori* control of the anti-slip surface treatment.

Results

Figure 6.6 presents the strain biaxiality and damage initiation results for a specimen with a double-sided reinforcement ring at 20 bar (CT). The strain biaxiality at the specimen centre is quantified in Figure 6.6a, while Figure 6.6b shows the maximum delamination (QDC) initiation at the ply 1/2 interface. The local longitudinal stress–strain response along the fibre path is given in Figure 6.6c, and Figure 6.6d presents the maximum fibre tensile (FT) damage initiation in the inner ply.

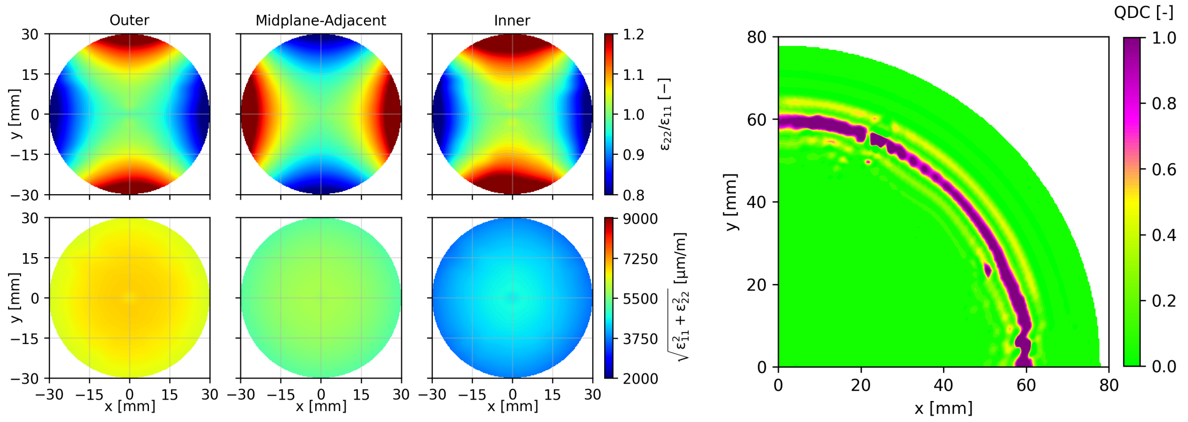

(a) Strain biaxiality at specimen centre

(b) Max. delamination (QDC), ply 1/2

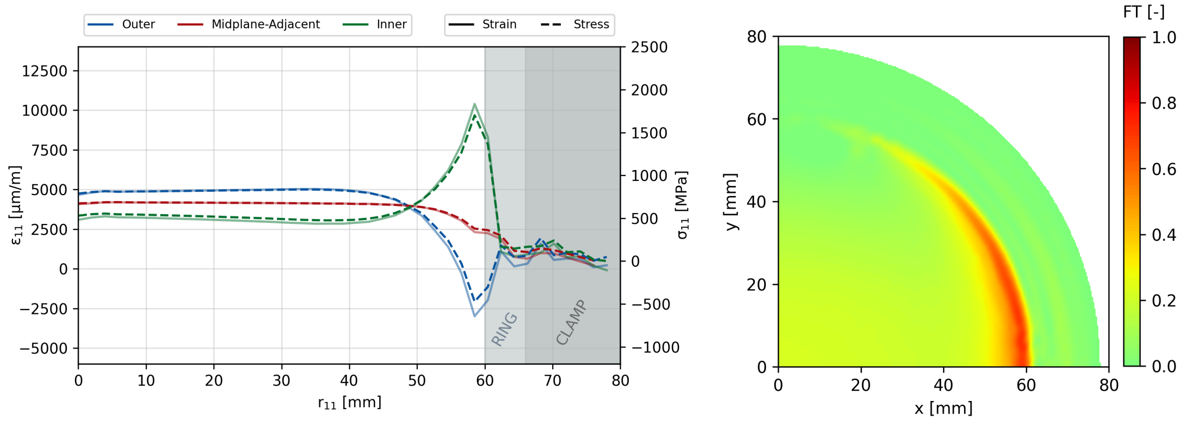

(c) Longitudinal stress–strain along fibre path

(d) Max. fibre tensile (FT) damage, ply 1

Figure 6.6: Strain biaxiality and damage initiation for a double-sided reinforcement ring at 20 bar (CT).

Discussion

The introduction of the modified reinforcement configuration did not yield the expected improvement in first-ply failure (FPF) resistance. On the contrary, FPF onset occurred slightly earlier (as seen by a sharp peak in Figure 6.6d). This is because of a more pronounced stiffness jump at the end of the doubly-reinforced ring. The location of the highest stress peak no longer occurs at the boundary of the reinforcement and clamp, as seen in Figure 6.6c. According to Figure 6.6b, the delamination initiation shifted from the outer-most interface (7/8) to the inner-most interface (1/2), with an overall increase in the delaminated area. The biaxiality and size of the equal-bi-axialstrain zone (Figure 6.6a) remained essentially unaffected, suggesting that the observed damage evolution is primarily governed by local stiffness gradients rather than changes in global deformation patterns.

6.6.2. Chamfered reinforcement

Motivation

Introducing a chamfer leads to a gradual transition in the stiffness of the laminate. As a consequence, it is hypothesised that the stresses will be distributed more evenly, over a larger area.

Results

Figure 6.7 presents the strain biaxiality and damage initiation results for a specimen with a chamfered reinforcement ring at 20 bar (CT). The strain biaxiality at the specimen centre is quantified in Figure 6.7a, while Figure 6.7b shows the maximum delamination (QDC) initiation at the ply 4/5 interface. The local longitudinal stress–strain response along the fibre path is given in Figure 6.7c, and Figure 6.7d presents the maximum fibre tensile (FT) damage initiation in the inner ply.

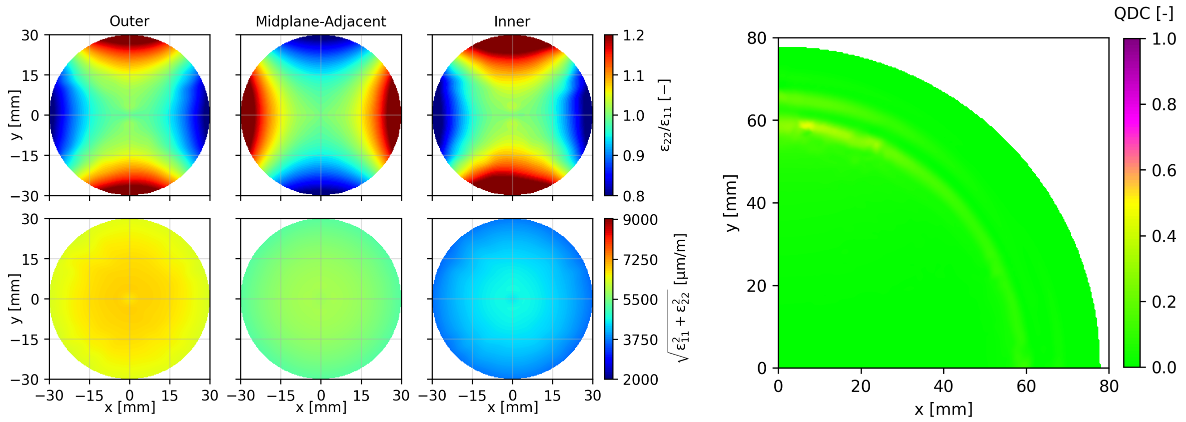

(a) Strain biaxiality at specimen centre

(b) Max. delamination (QDC), ply 4/5

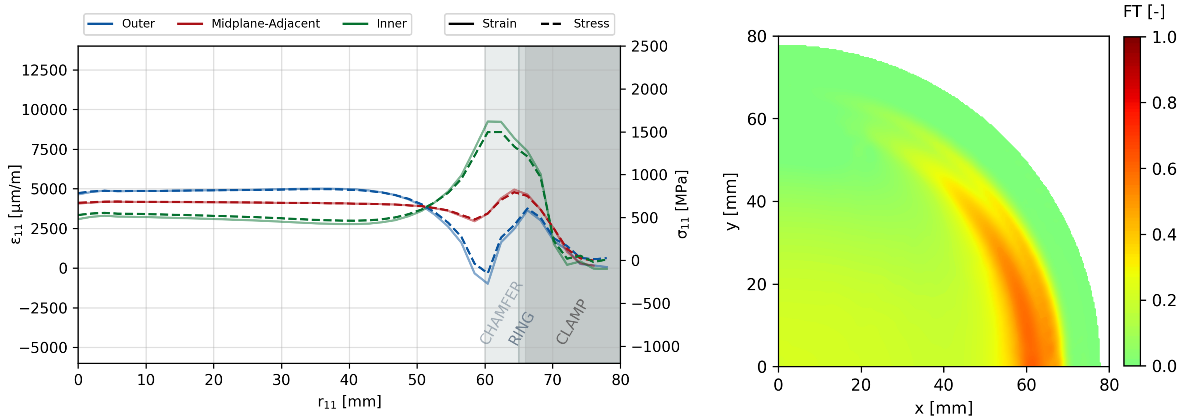

(c) Longitudinal stress–strain along fibre path

(d) Max. fibre tensile (FT) damage, ply 1

Figure 6.7: Strain biaxiality and damage initiation for a chamfered reinforcement ring at 20 bar (CT).

Discussion

The introduction of the chamfer produced a modest but positive effect. Most notably, no delamination initiation was observed in Figure 6.7b, representing an improvement in the inter-laminar damage tolerance. Although the first-ply failure (FPF) load decreased slightly, the biaxiality and size of the equal-bi-axialstrain zone remained unchanged. Overall, the chamfer can be considered a small improvement, primarily in mitigating inter-laminar damage, without compromising the bi-axialstrain distribution.

6.6.3. Wider reinforcement

Motivation

The use of a wider reinforcement is considered to potentially reduce the magnitude of stress concentration at the point where the ring leaves the specimen, as observed in Figure 6.2c, which shows the two distinct stress jumps. Moreover, a wider reinforcement redistributes the clamping stress over a larger area and increases the overall stiffness of the specimen. It is therefore of interest to assess whether this modification can lower the strain in the central region of the specimen, which is critical for improving the margin of safety.

Results

Figure 6.8 presents the strain biaxiality and damage initiation results for a specimen with a wider reinforcement ring at 20 bar (CT). The strain biaxiality at the specimen centre is quantified in Figure 6.8a, while Figure 6.8b shows the maximum delamination (QDC) initiation at the ply 4/5 interface. The local longitudinal stress–strain response along the fibre path is given in Figure 6.8c, and Figure 6.8d presents the maximum fibre tensile (FT) damage initiation in the inner ply.

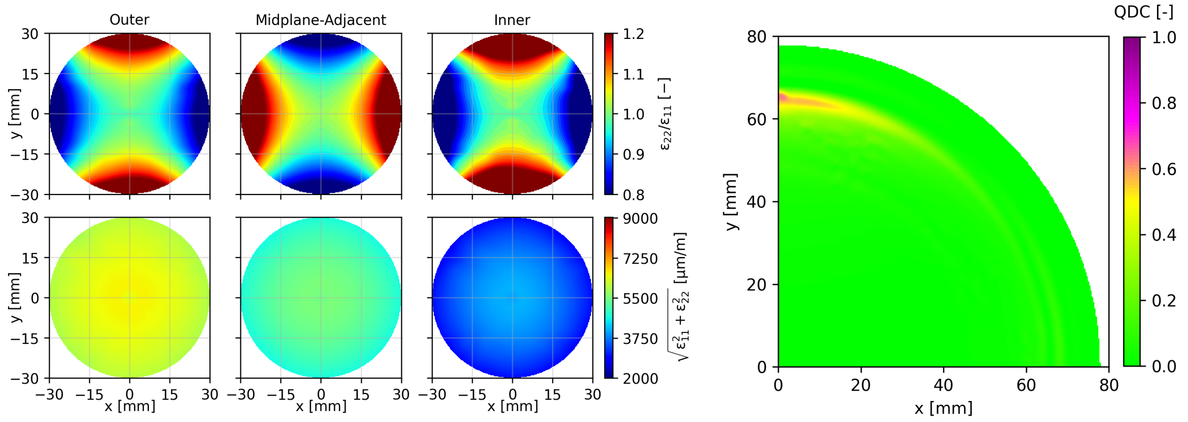

(a) Strain biaxiality at specimen centre

(b) Max. delamination (QDC), ply 4/5

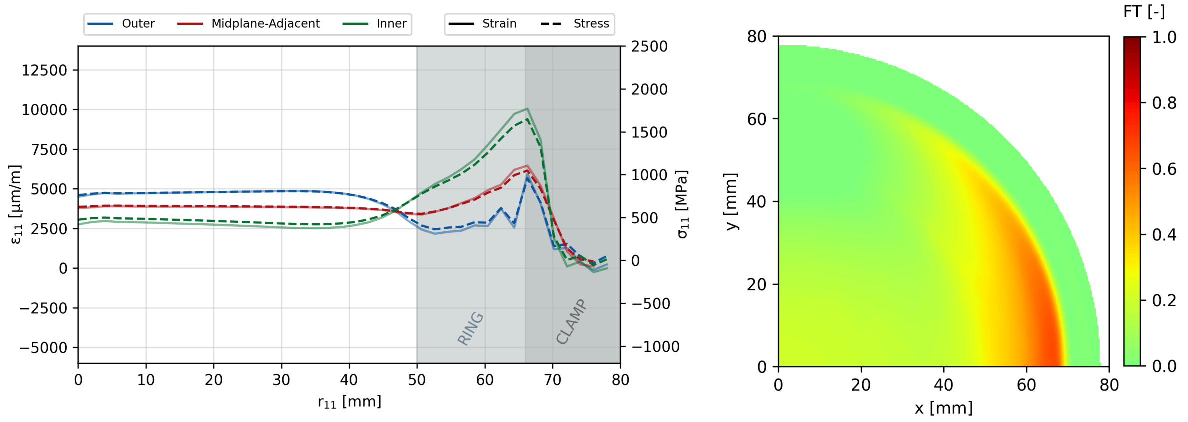

(c) Longitudinal stress–strain along fibre path

(d) Max. fibre tensile (FT) damage, ply 1

Figure 6.8: Strain biaxiality and damage initiation for a wider reinforcement ring at 20 bar (CT).

Discussion

A wider reinforcement effectively reduced clamp-induced damage by lowering the strain peaks at the edges of the ring. This translated into a delay in fibre tensile failure initiation and an increased margin of safety. However, the increased stiffness of the specimen also led to a slight reduction in the magnitude of in-plane strains in the bi-axialzone, while its size remained largely unaffected. Overall, the wider reinforcement offers a beneficial trade-off when clamp-induced failure is the primary concern.

6.6.4. GFRP reinforcement

Motivation

A GFRP tab was selected, based on the recommendations for tensile testing of composites [3]. CFRP was not chosen because it is more expensive and less compliant, which would again lead to high stress concentrations in the clamping region.

The tab is made from G-10 CR, a plain weave material, oriented in a $\pm 45°$ layup according to the design guidelines [3]. A quasi-isotropic configuration is selected as a starting point because the reinforcement is subjected to pressure loading from multiple directions; the laminate can be tailored in the future if this configuration proves promising.

The material properties were obtained as follows:

- Thermal expansion: estimated from NIST [56].
- Mechanical properties (E_1, E_2, Poisson's ratio): obtained from Kasan [38].
- Out-of-plane modulus (E_3) at room temperature: obtained from Adams [3], with an assumed 20% increase at cryogenic temperature.
- Shear modulus at room temperature: from Shindo [74], assuming a 20% increase at cryogenic temperature. Poisson's ratio is considered invariant.

Results

Figure 6.9 presents the strain biaxiality and damage initiation results for a specimen reinforced with a $\pm 45°$ GFRP ring at 20 bar (CT). The strain biaxiality at the specimen centre is shown in Figure 6.9a, while Figure 6.9b shows the maximum delamination (QDC) initiation at the ply 4/5 interface. The local longitudinal stress–strain along the fibre path is given in Figure 6.9c, and Figure 6.9d presents the maximum fibre tensile (FT) damage initiation in the inner ply.

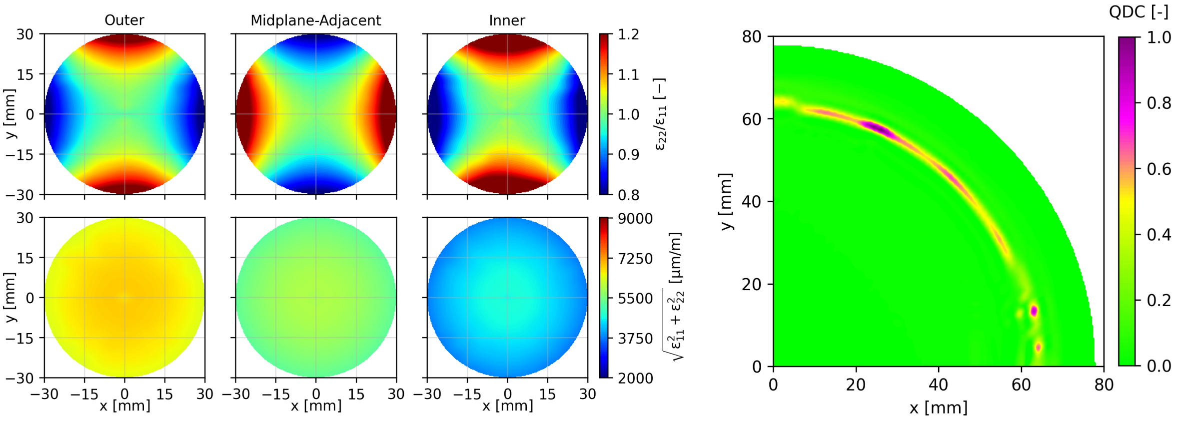

(a) Strain biaxiality at specimen centre

(b) Max. delamination (QDC), ply 4/5

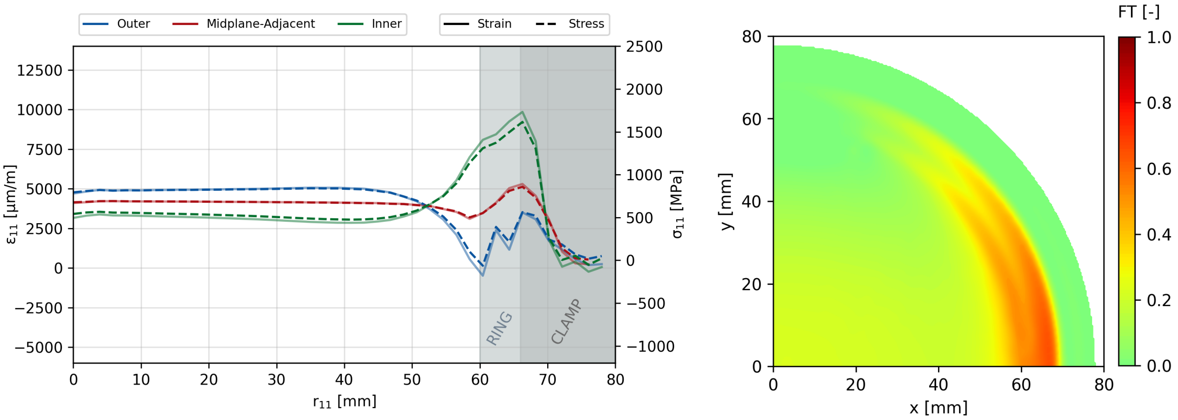

(c) Longitudinal stress–strain along fibre path

(d) Max. fibre tensile (FT) damage, ply 1

Figure 6.9: Strain biaxiality and damage initiation for a $\pm 45°$ GFRP reinforcement ring at 20 bar (CT).

Discussion

Replacing the metal reinforcement with GFRP provided slightly better resistance to delamination. However, the resistance to the fibre tensile failure is marginally worse. The size and quality of the bi-axialstrain zone remained essentially unchanged. Overall, the behaviour was comparable to the default configuration.

Summary of reinforcement design results

Key simulation results for various reinforcement design condigurations are tabulated in Table 6.7. Specifically, the average magnitude of the in-plane strain within the 30 [mm] radius is tabulated, for multiple plies. Then, the maximum fibre-tensile failure initiation is reported. Finally, the delaminated area, where QDC > 1, as a percentage of the total specimen area is reported.

Table 6.7: Strain metrics and damage indicators for each reinforcement configuration, at 20 [bar] (CT)

Configuration	$\left(\sqrt{\varepsilon_{11}^2+\varepsilon_{22}^2}\right)\Big\|_{\mathrm{r}\leq 30\,\mathrm{mm}}^{\mathrm{avg}}$ [µm]			$\mathrm{FT}_{\mathrm{max}}$ [-]	QDC > 1 [%]
	Outer	Mid.-Adj.	Inner		
Default	6556	5517	4121	0.621	1.24
Double	6569	5538	4152	0.721	2.44
Chamfer	6568	5534	4147	0.607	0.00
Wide	6266	5087	3503	0.661	0.00
GFRP	6613	5599	4237	0.642	0.16

6.7. Outlook

Overall, several design parameters were varied in this chapter. The primary objective was to identify the factors most worth adjusting in future experiments, with the aim of increasing the likelihood of observing leakage in the central bi-axialzone before damage is induced by the boundary conditions of the test set-up. Based on the findings, the following improvements are suggested:

- **Mitigate slippage:** A practical anti-slip solution is required to maintain a uniform bi-axialstrain zone through the thickness of the laminate. Slippage can reduce strain in the bi-axialzone by approximately 1500–2000 µm. This should be addressed first, as it does not require modifications to the laminate design. For the bulge test to serve as a reliable element test standard, slippage should be minimised as far as possible.
- **Use thinner specimens:** Consider 0.5 [mm] instead of 1.0 [mm]. With reinforcement, fibre failure should still be avoided, although the margin of safety is reduced. Limiting the thickness to 4 plies (assuming 0.125 mm each) restricts the possibility of testing thinner, balanced, symmetric QI specimens using UD plies. A potential compromise is an antisymmetric 6-ply UD laminate incorporating ± 45 plies: [0/90/45/-45/90/0], with the antisymmetric plies placed near the midplane to minimise bending–membrane coupling.
- **Use lower-grade CFRP material systems:** Replace IM7 with SM carbon fibre and the toughened 8552 epoxy with a more standard resin system. For example, simulations for the M21/T700GC system indicate significantly higher strain in the region of interest (≈ 2000 [µm]) while maintaining a positive margin of safety with respect to fibre failure at the clamp.
- **Optimise reinforcement ring design:** To compensate for the increased compliance of the laminate, the reinforcement ring geometry can be optimised. For instance, a chamfer can delay the onset of delamination by distributing stresses over a larger transition area.

One limitation of this study is that only one parameter was varied at a time. Before implementing any practical changes to the specimen design, further simulations should be performed to assess potential interactions between variables (for example, a thinner specimen combined with a wider, chamfered reinforcement).

7

Conclusion

The purpose of this work was to develop a validated numerical model of the bulge test, thus simulating CFRP specimen under multi-directional thermo-mechanical loading.

A detailed numerical model was built to mimic the bulge test as accurately as possible. This involved multi-stepped thermo-mechanical simulations, modelling both inter- and intra-laminar damage initiation, and accounting for the interaction between the specimen and the test setup. Notably, a non-linear contact model was implemented to capture specimen slippage. Through a comprehensive mesh study and selective use of numerical damping, computational efficiency was improved without compromising predictive accuracy.

In addition, experimental data were obtained from five bulge tests conducted at DLR. Various configurations were tested to study the influence of curvature, reinforcement and temperature. To summarise the main results of the test campaign, bulge experiments at cryogenic temperature mitigated premature leakage. The of reinforcement effectively reduced damage induced by the clamping. Post-test examination of the reinforced specimens showed no visible delamination, fibre failure, or matrix cracks in the clamping region.

An extensive validation dataset was collected using strain gauges, digital image correlation (DIC), and fibre optic strain sensors. The DIC displacement fields were used to calibrate the contact model, resulting in a low static friction coefficient of 0.01, between the CFRP specimen and the indium seal. This indicates that the specimen may slip by up to 1 mm during testing. Comparison of simulated and experimental strains showed the best agreement (<5%) at the centre of the reinforced specimen at room temperature. The model also correctly predicts the location of intra- and inter-laminar damage using the LARC05 and QDC criteria, consistent with ultrasound C-scan and optical micrograph observations.

The validated numerical model can be used to aid the design of more representative bulge specimen. For example, mitigating slippage is critical to achieving a uniform bi-axial strain zone at the specimen's centre; under no-slip conditions, in-plane strains may increase by 32–39% across different plies. Higher strain regions promote desired leak paths within the biaxial zone. Additionally, increasing laminate compliance, eg, using thinner 0.5 mm symmetric, balanced cross-ply laminates, can further enhance strains in the region of interest without inducing first-ply failure. The margin of safety against clamp-induced damage can potentially be improved through reinforcement design; for example, chamfered edges help distribute out-of-plane stresses more evenly, delaying delamination onset.

In summary, the combined experimental and numerical approach provides a robust framework to guide the design and testing of bulge specimens, ensuring reliable bi-axial strain fields while minimising boundary-induced damage.

8

Recommendations

A range of recommendations can be identified based on the numerical and experimental work conducted during this thesis. These recommendations are grouped into three main topics: sensor temperature compensation, design optimisation of the bulge test specimen, and further numerical modelling.

The topic of sensor temperature compensation must be addressed to ensure the validity of strain measurements acquired in a cryogenic environment. In this study, strain gauge measurements were corrected using an analytical equation provided by the manufacturer. However, accurately correcting for the thermal contraction mismatch between the specimen and the strain gauge requires precise knowledge of the temperature dependence of the respective coefficients of thermal expansion (CTE). The exact material composition of the strain gauges is not publicly disclosed, introducing uncertainty into the correction. It is therefore recommended to obtain a comprehensive in-house calibration dataset using passenger samples. In such tests, a thermocouple and strain gauge are bonded to the specimen, which is then submerged (without a restraint) into a cryogenic bath. These calibration tests should initially be conducted on isotropic reference materials, such as metals or standard resins, before validating the methodology on anisotropic CFRP laminates. Additionally, temperature compensation for fibre-optic sensors remains an open task. A thorough understanding of thermo-optical effects is likely required to correct measurements obtained at cryogenic temperatures. Furthermore, the increased noise in the optical fibre signals under these conditions should be addressed through appropriate signal processing techniques.

Several improvements can also be made to optimise the design of the bulge test specimen. The objective of this optimisation is to ensure that leakage occurs within the central bi-axial strain zone prior to the onset of clamp-induced damage, thereby allowing reliable characterisation of leakage. This can be translated as maximising the strain in the centre of the specimen whilst minimising stress-concentration peaks in the clamping zone. A multi-parameter study is recommended, extending the single-parameter investigations presented in chapter 6. For instance, the influence of specimen thickness and material was studied individually, but not in combination. Multi-parameter optimisation may require efficient sampling algorithms, such as Latin Hypercube sampling, to explore the design space effectively. The workflow can be further streamlined by scripting an Abaqus model generator to automate the creation of parametric models. It should be noted that the results presented in chapter 6 assume a no-slip condition, which relies on mitigation of specimen slippage. While reducing slippage has been shown to increase strain in the region of interest, complete elimination may not be achievable. In such cases, the parametric study could be repeated using the static friction coefficients determined in this thesis.

The scope of the current work was limited to a linearly elastic material model, allowing only the initiation of damage to be captured. Accurate numerical prediction of leakage, however, requires information such as crack-opening displacements, which can be obtained from a progressive damage model. If it can be demonstrated experimentally that leakage is driven solely by the thermo-mechanical stress state within the bi-axial strain zone, the predictions of a leakage model could be directly compared with experimental measurements. An appropriate progressive damage modelling strategy, that accounts for both intra-laminar (matrix cracking) and inter-laminar (delamination) damage modes, should be selected. The blended XFEM-SCZM discrete damage framework, for example, is considered to be the state-of-the-art for leakage modelling in CFRP

In this study, only undamaged, un-notched CFRP specimens have been modelled deterministically. The effects of manufacturing defects, such as voids or wrinkles, have not been considered, nor has the statistical distribution of material strength, particularly at cryogenic temperatures. Stochastic finite element modelling could be employed to account for these uncertainties. In practical tank structures, cut-outs are necessary to integrate feed-lines or other components, which may be welded or bonded to the tank walls. The influence of such joint components on strain, damage, and leakage remains an important research question and is a necessary consideration for the structural development of cryogenic CFRP hydrogen tanks.

A

Mesh Study

The complete raw results of the mesh study are provided in this section. The results follows from the discussion in subsection 2.5.4.

Mesh convergence study

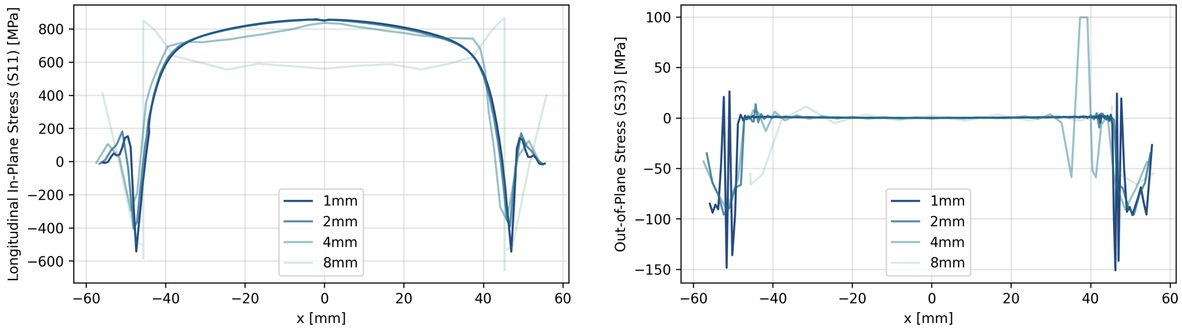

(a) Longitudinal in-plane stress (S11) against the global/laminate's x-ordinate

(b) Out-of-plane stress (S33) against the global/laminate's x-ordinate

Figure A.1: Components of stress along the global XY-path, for the outer/top-most ply

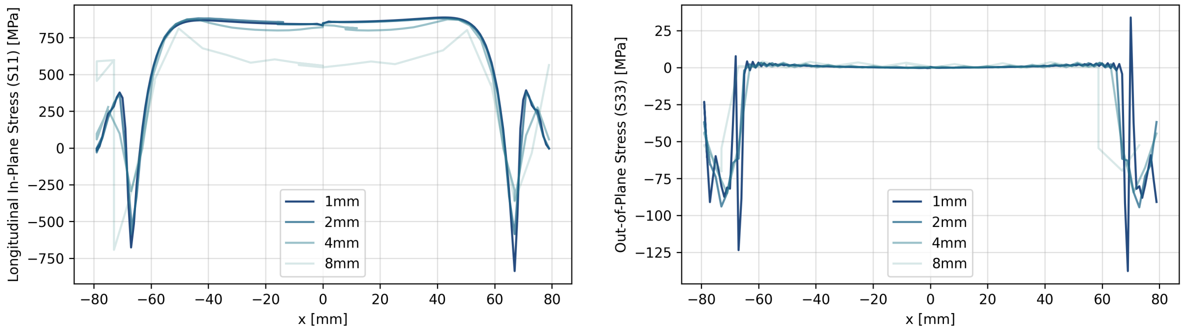

(a) Longitudinal in-plane stress (S11) against the global/laminate's x-ordinate

(b) Out-of-plane stress (S33) against the global/laminate's x-ordinate

Figure A.2: Components of stress along the global X-path, for the outer/top-most ply

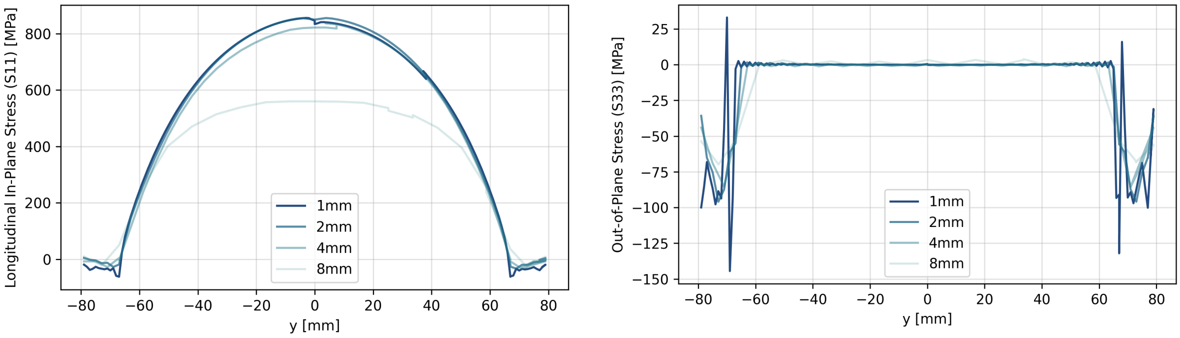

(a) Longitudinal in-plane stress (S11) against the global/laminate's y-ordinate

(b) Out-of-plane stress (S33) against the global/laminate's y-ordinate

Figure A.3: Components of stress along the global Y-path, for the outer/top-most ply

Partitioning strategy

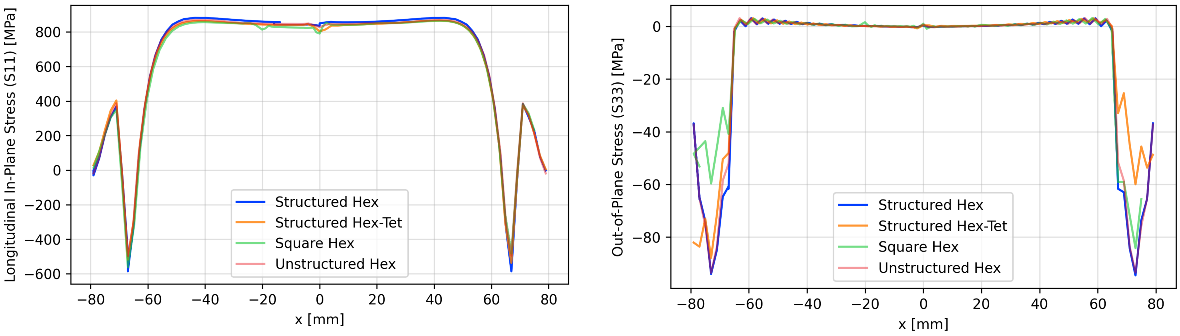

(a) Longitudinal in-plane stress (S11) against the global/laminate's x-ordinate

(b) Out-of-plane stress (S33) against the global/laminate's x-ordinate

Figure A.4: Components of stress along the global X-path, for the outer/top-most ply

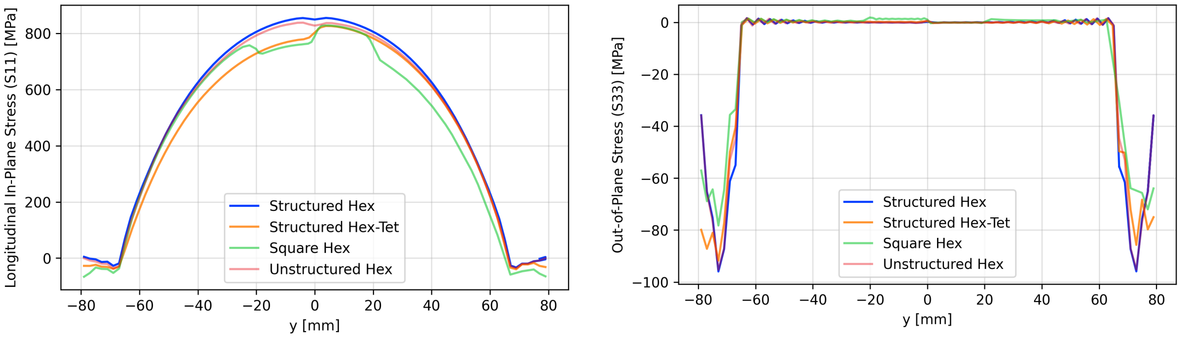

(a) Longitudinal in-plane stress (S11) against the global/laminate's y-ordinate

(b) Out-of-plane stress (S33) against the global/laminate's y-ordinate

Figure A.5: Components of stress along the global Y-path, for the outer/top-most ply

Influence of mesh element type

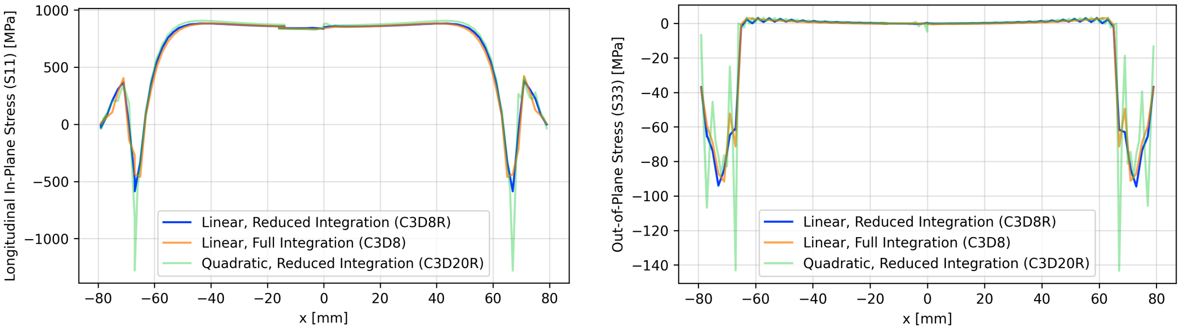

(a) Longitudinal in-plane stress (S11) against the global/laminate's x-ordinate

(b) Out-of-plane stress (S33) against the global/laminate's x-ordinate

Figure A.6: Components of stress along the global X-path, for the outer/top-most ply

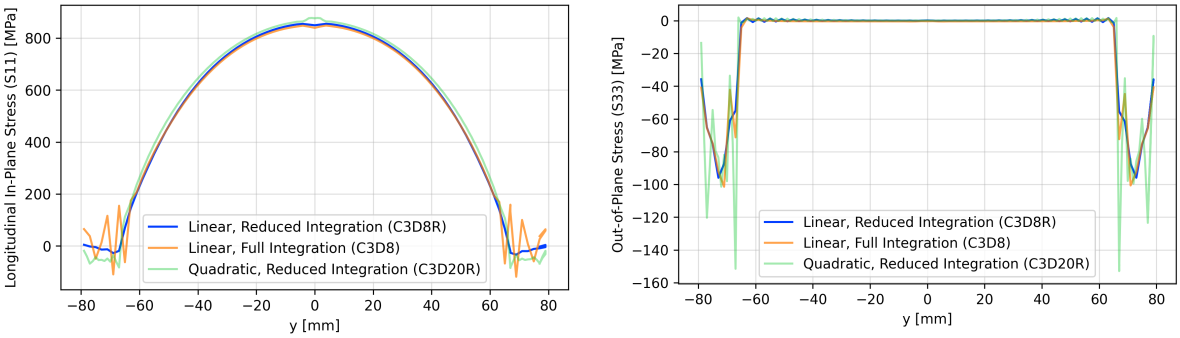

(a) Longitudinal in-plane stress (S11) against the global/laminate's y-ordinate

(b) Out-of-plane stress (S33) against the global/laminate's y-ordinate

Figure A.7: Components of stress along the global Y-path, for the outer/top-most ply

B

Post-tests

B.1. Cryogenic post-tests

This section shows the raw-data for the post-tests. It follows the results from chapter 4.

B.1.1. U-C-CT post-test

The post-test of U-C-CT specimen (raw data in section 4.4) is given by Figure B.1.

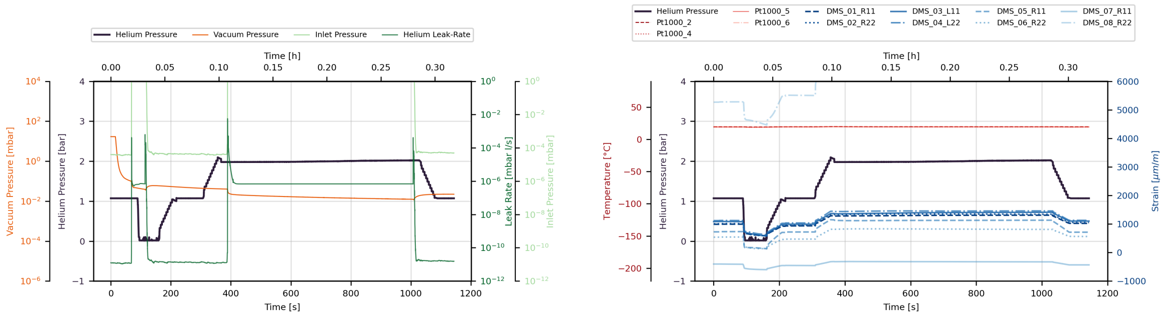

(a) Leakage overview

(b) Strain overview

Figure B.1: U-C-CT specimen: Progression of strain, leakage, temperature and pressure through the post-test

B.1.2. R-C-CT post-test

The post-test of R-C-CT specimen (raw data in section 4.5) is given by Figure B.2.

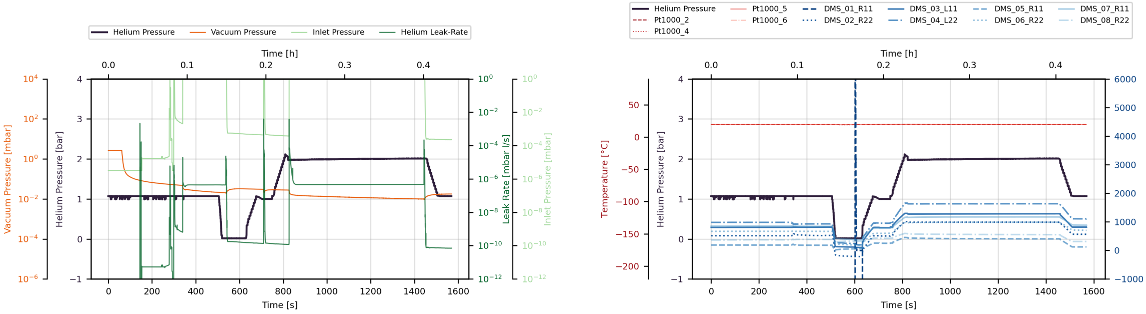

(a) Leakage overview

(b) Strain overview

Figure B.2: R-C-CT specimen: Progression of strain, leakage, temperature and pressure through the post-test

C

Temperature compensation

C.1. Strain gauge temperature compensation using correction curve

The manufacturer of strain-gauges provides a correction to apparent strains caused by a measurement temperature significantly different to ambient reference table. The corrective relationship was introduced in subsection 5.2.3. The empirical constants are tabulated in Table C.1. [28], [29]

Table C.1: Parameters needed for temperature compensation of strain gauges, at cryogenic temperature

a_0	-44.12	[-]
a_1	2.89	[-]
a_2	-3.86×10^{-2}	[-]
a_3	5.85×10^{-5}	[-]
a_4	-5.16×10^{-9}	[-]
T_{ref}	293	[K]
T	77	[K]
ΔT	-216	[K]
$\alpha_{\text{strain-gauge}}$	10.8×10^{-6}	[K^{-1}]
$\alpha_{\text{substrate-CP, 11}} =$ $\alpha_{\text{substrate-CP, 22}}$	2.03×10^{-6}	[K^{-1}]
$\kappa_{\text{polynomial}}$	2.00	[-]
$\kappa_{\text{datasheet}}$	2.34	[-]
α_{k}	2.85×10^{-4}	[K^{-1}]
$\kappa_{\text{datasheet}}(T)$	2.484	[-]

C.1.1. Thermal expansion coefficients

A note must be made on the coefficient of thermal expansion (CTE) used in Table C.1. The secant α must be used for both the substrate and the strain gauge. Secant, or the mean CTE, must be valid for the temperature range between T and T_{ref}. A brief description of the derivation of $\alpha_{\text{substrate-CP}}$ and $\alpha_{\text{strain-gauge}}$.

CFRP substrate

$\alpha_{\text{substrate}-\text{CP}-11}$ and $\alpha_{\text{substrate}-\text{CP}-22}$ represent the laminate (macroscopic) level coefficients of thermal expansion of a symmetric, balanced cross-ply laminate $[(0/90)_2]_s$. The classical laminate theory is used to obtain the laminate level CTE. The CLT uses the lamina level stiffness (E_{11}, E_{22}, G_{12}, ν_{12}) as well as the CTE for a unidirectional laminate. The secant CTE for IM7/8552 is -1×10^{-7} [K^{-1}] in the fibre direction and 3×10^{-5} [K^{-1}] in the matrix direction. These secant CTEs are obtained from internal sources. An open-source CTE calculator based on CLT, such as elamX2 [27], can be used.

Strain gauge

The strain gauges used for the cryogenic experiments have a Self-Temperature Compensation (STC) number of 11. This refers to the CTE of the strain gauge at reference temperature. To be precise, the manufacturer states that the strain gauges are compensated for a ferritic steel with a CTE of 10.8×10^{-6} [K^{-1}]. This does **not** necessarily mean that the material used in the measuring grids of the strain gauges is made up of steel. In fact, the manufacturer states that a ”special nickel-chromium” alloy is used. By considering the shape of the thermal output curves from other manufacturers [53], it can be inferred that the measuring grid is likely made of the (modified) Karma alloy. The exact alloy composition, of course, remains proprietary.

This means that extracting the secant CTE of the strain gauge between 77 K and 293 K is equivalent to obtaining the secant CTE of the (modified) Karma material. It is assumed that the effect of the plastic backing foil is negligible. Unfortunately, the author could not find the secant CTE of the required alloy in literature. It was also not possible to directly find the variation of the instantaneous CTE with temperature. The use of published thermal output curves to derive the instantaneous CTE of the strain gauge grid to subsequently estimate the secant CTE [53], [35] is riddled with assumptions and may lead to inaccuracies. The next best alternative is to simply use the room temperature value of CTE that is provided by the manufacturer. Observing the behaviour of other metals, the room temperature CTE is likely to be 20-30% larger than the mean CTE between room and cryogenic temperature.

C.2. Strain gauge temperature compensation using passenger samples

An alternative method of temperature compensation is using passenger samples. Passenger samples are milled out from the same plate as the bulge specimen. These are seen as the small rectangular cut-outs at the centre of the plate shown in Figure 3.10b.

The passenger samples are cryogenically cooled to 77 K inside the bulge compartment. No mechanical load is applied. This means that the deformation of the specimen is caused due to the thermal load only. In other words, the mechanical strain should be zero. If the true, physical (thermal) strain is accurately known a priori, it is possible to quantify the difference with the measurement signal.

Raw data of the passenger sample tests is available. Data from the thermocouples and bi-axial strain gauges of the passenger samples are shown in Figure C.1-C.4. All passenger samples are 8-ply symmetric, balanced 1 [mm] thick cross-ply IM7/8552 laminates. There are four flat and four curved specimen.

An important note: no correction is applied on the strain values in Figure C.1-C.4. The measurement strain signal, as it was recorded in the log file, is plotted. This signal was acquired for a k-factor of 2. The k-factor of the used strain gauge, or the temperature corrected k-factor is not applied here. No corrections have been made either for the CTE mismatch of the strain gauge/CFRP sample or for the apparent thermal strain in the strain gauge.

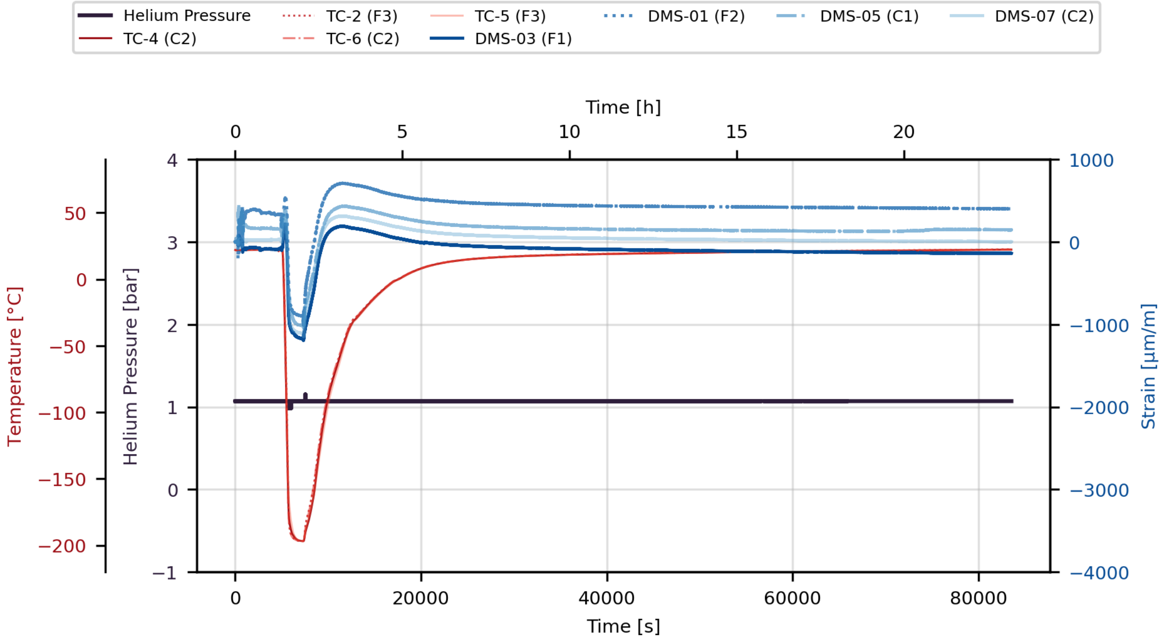

Figure C.1: Batch 01: Longitudinal (11) strain

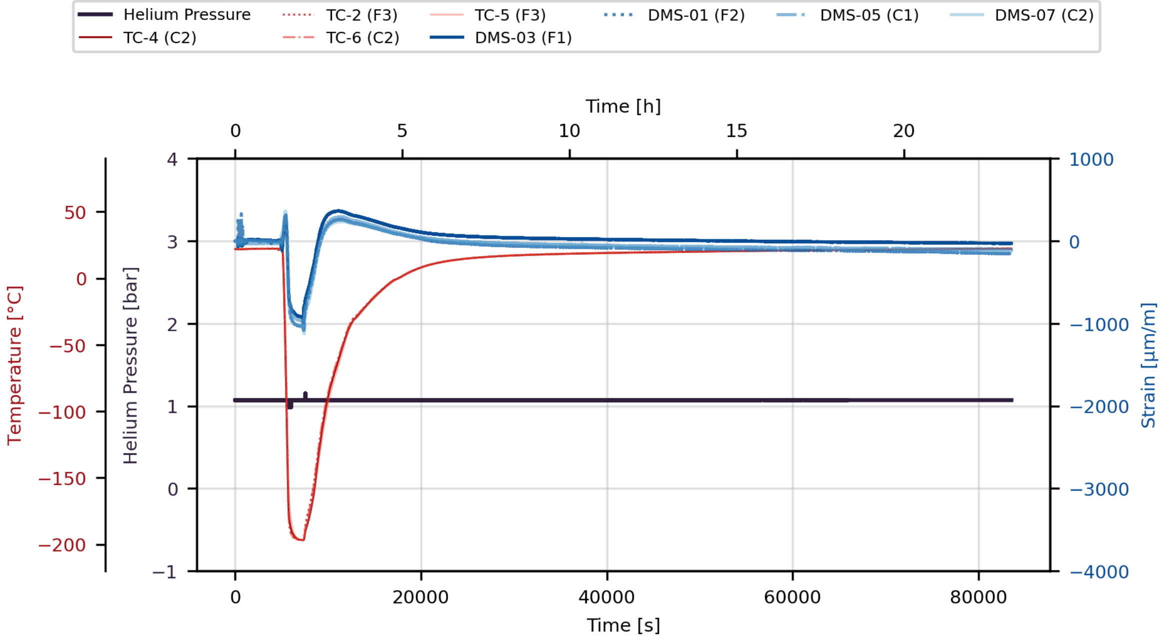

Figure C.2: Batch 01: Transverse (22) strain

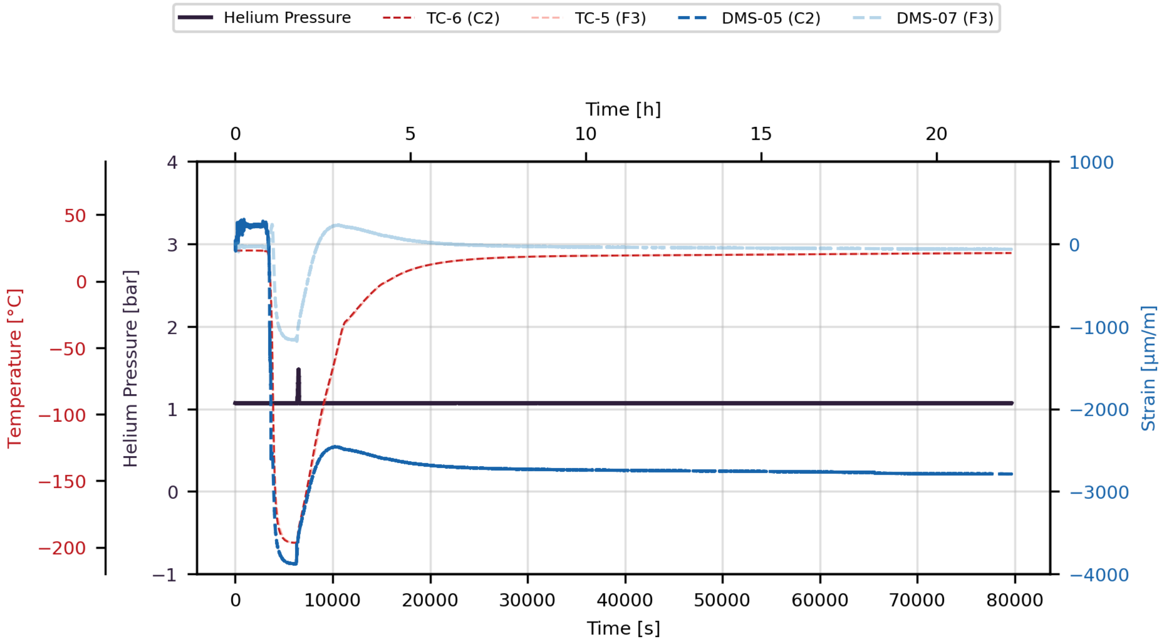

Figure C.3: Batch 02: Longitudinal (11) strain

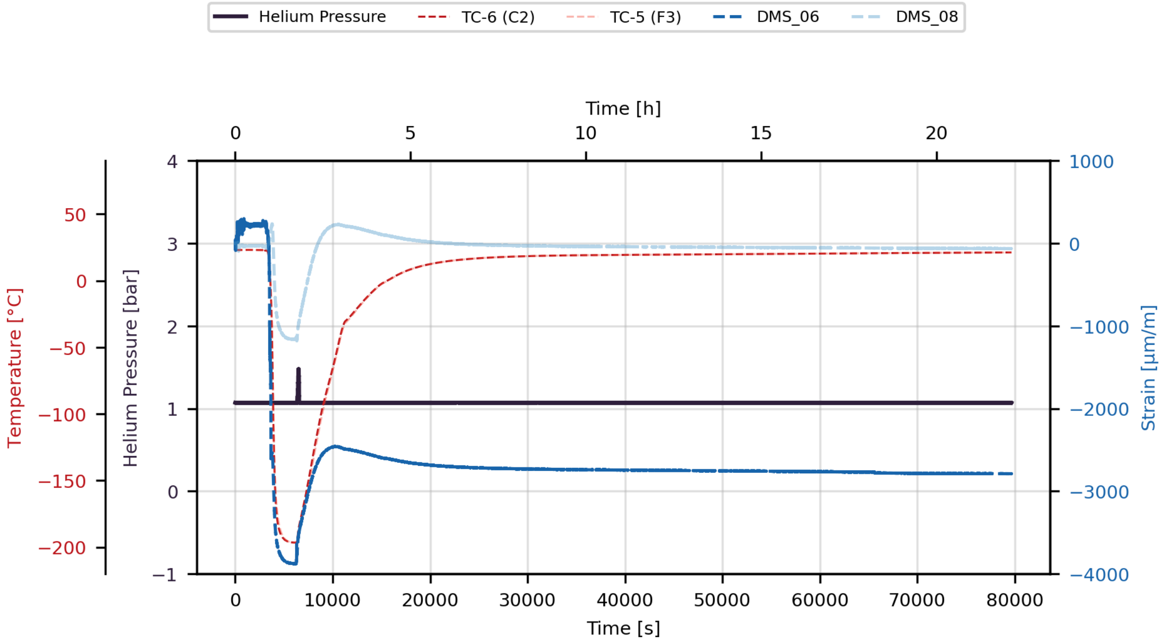

Figure C.4: Batch 02: Transverse (22) strain

Results from Figure C.1-C.4 are further processed. The results are grouped based on the principal direction: longitudinal/along fibre (11) and transverse/across fibre (22).

The mean, min, and max values are shown in Figure C.5. The strain gauges already read a non-zero value at room temperature. This room temperature value is subtracted from the cryognic reading to compute the temperature offset.

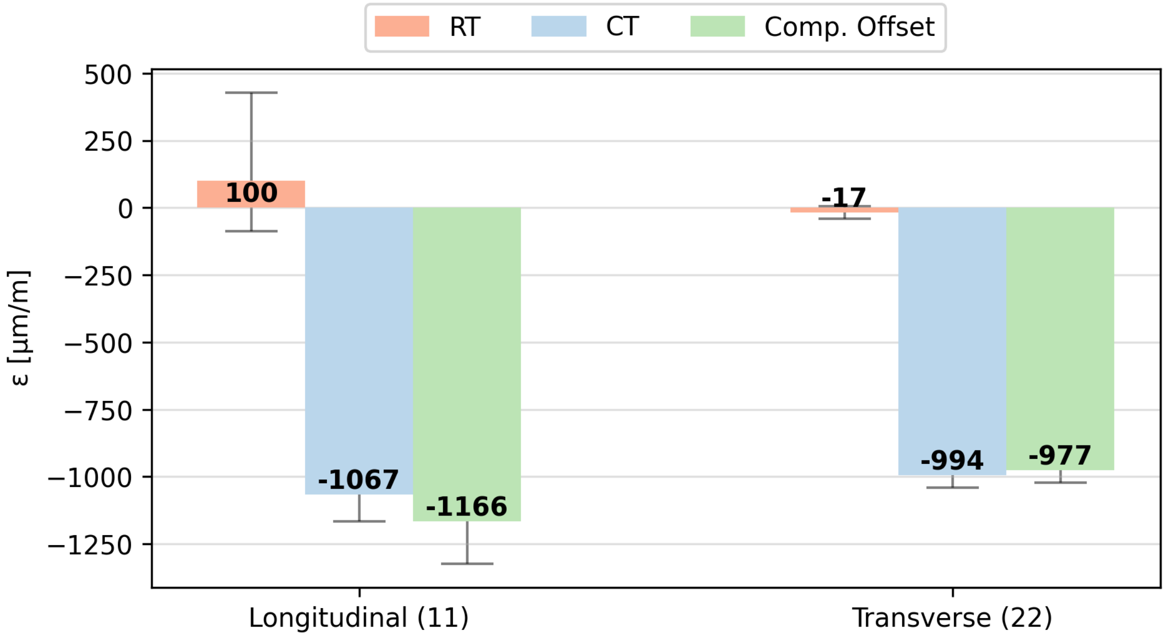

Figure C.5: Mean and distribution of the strains from passenger sample tests

The average values of strain can be considered as the measurement strain signals ϵ in Equation 5.5. It should still be noted that the passenger sample test is still like any other cryogenic test, in the sense that the measured strains need to be correct for thermal effects (CTE mismatch, k-factor, etc). By correcting for all these thermal effects, the temperature compensated strain ϵ_{c} should converge to the true physical strain experienced by the specimen. For the passenger sample, the physical strain can be computed analytically. As the passenger sample experiences no mechanical loads, no mechanical stress is developed in the laminate. This means that there is zero mechanical strain. Only thermal strain remains, that is: $\epsilon_{\text{th}} = \alpha_{\text{substrate-CP}} \cdot \Delta T$. However, it was observed that -440 $[\mu\text{m/m}] = \epsilon_{\text{th}} \neq \epsilon_{\text{c}} = -2400$ $[\mu\text{m/m}]$ (longitudinal direction - 11). Such a massive disagreement between the analytical correction and the passenger sample method is deemed unacceptable. The cause of this disagreement is not well known. However, there may be thermal residual stresses due to cryogenic cooling in a composite laminate. [33] This would mean that the mechanical stresses are non-zero, even in the absence of an obvious mechanical load. Therefore, the author has low confidence in using passenger sample data to temperature compensate the thermal effect of strain gauges.

*Further passenger sample tests, using an isotropic material with a well known temperature dependent CTE, can be potentially conducted to assess the suitable of passenger sample data for temperature compensation.

D

Numerical-experimental results

This appendix follows from chapter 5. Only a selected number of numerical-experimental comparisons are provided in the main text. For completeness, the remainder of data visualisation is provided in this appendix. The nomenclature of the tests follow from the test matrix stated in Table 3.2.

D.1. 1D path strain

D.1.1. Curved specimen at cryogenic temperature

Outermost ply

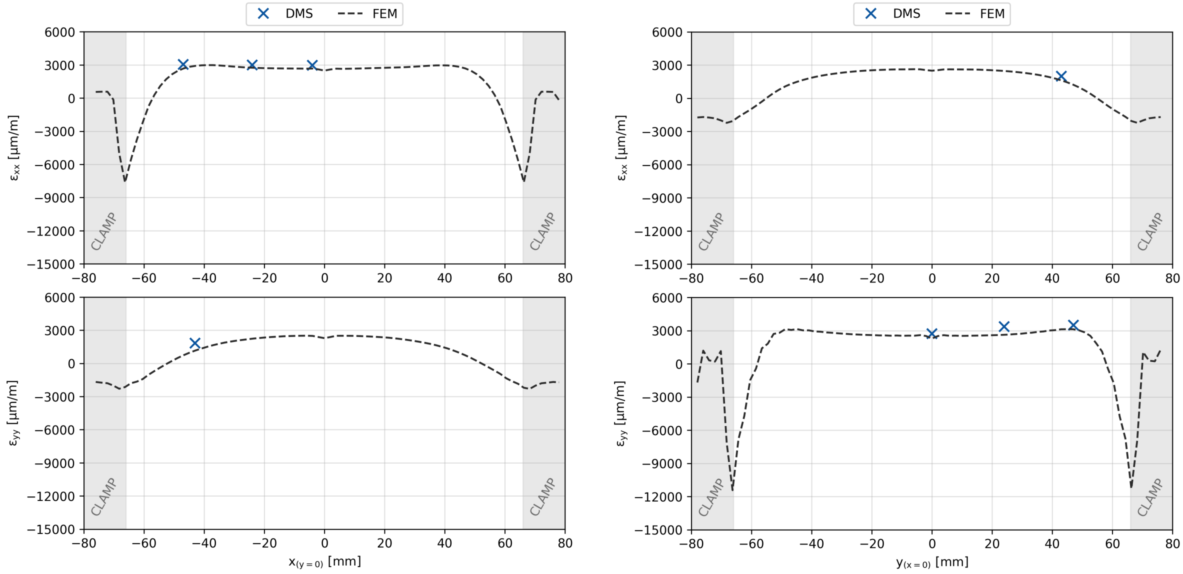

(a) Longitudinal (ϵ_{xx}) and transverse (ϵ_{yy}) in-plane strain components along X-path $(y = 0)$

(b) Longitudinal (ϵ_{xx}) and transverse (ϵ_{yy}) in-plane strain components along Y-path $(x = 0)$

Figure D.1: U-C-CT specimen: Experimental-numerical comparison of the biaxial strain zone, for the outer-most ply, at an applied pressure of 9 [bar]

Mid-plane

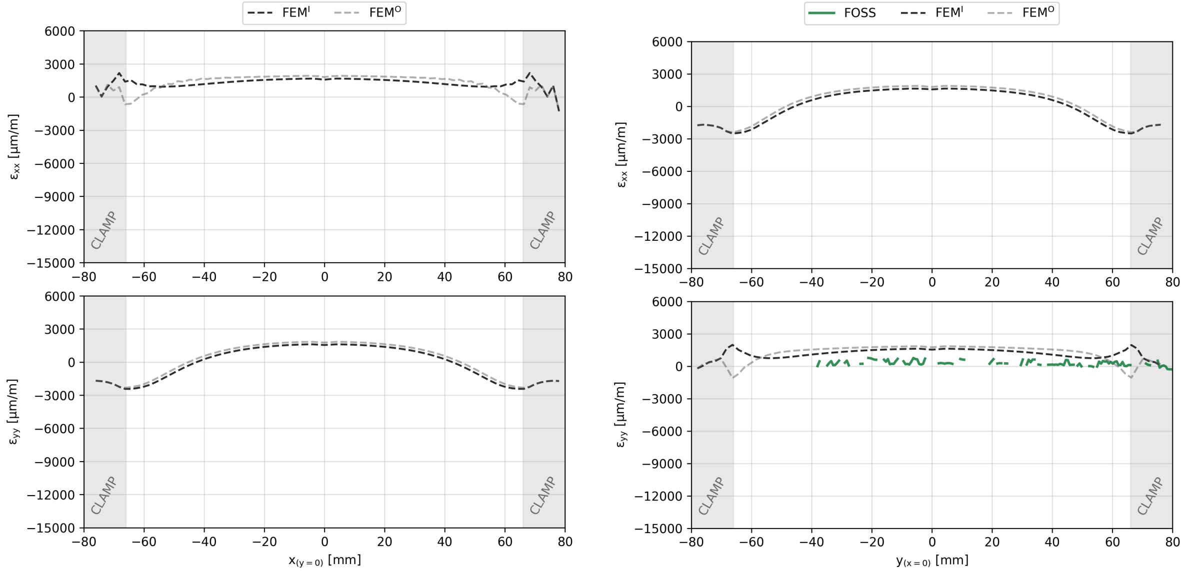

(a) Longitudinal (ϵ_{xx}) and transverse (ϵ_{yy}) in-plane strain components along X-path ($y = 0$)

(b) Longitudinal (ϵ_{xx}) and transverse (ϵ_{yy}) in-plane strain components along Y-path ($x = 0$)

Figure D.2: U-C-CT specimen: Experimental-numerical comparison of the biaxial strain zone, for plys adjacent to the laminate's mid-plane, at an applied pressure of 9 [bar]

D.1.2. Reinforced specimen at cryogenic temperature

Outermost ply

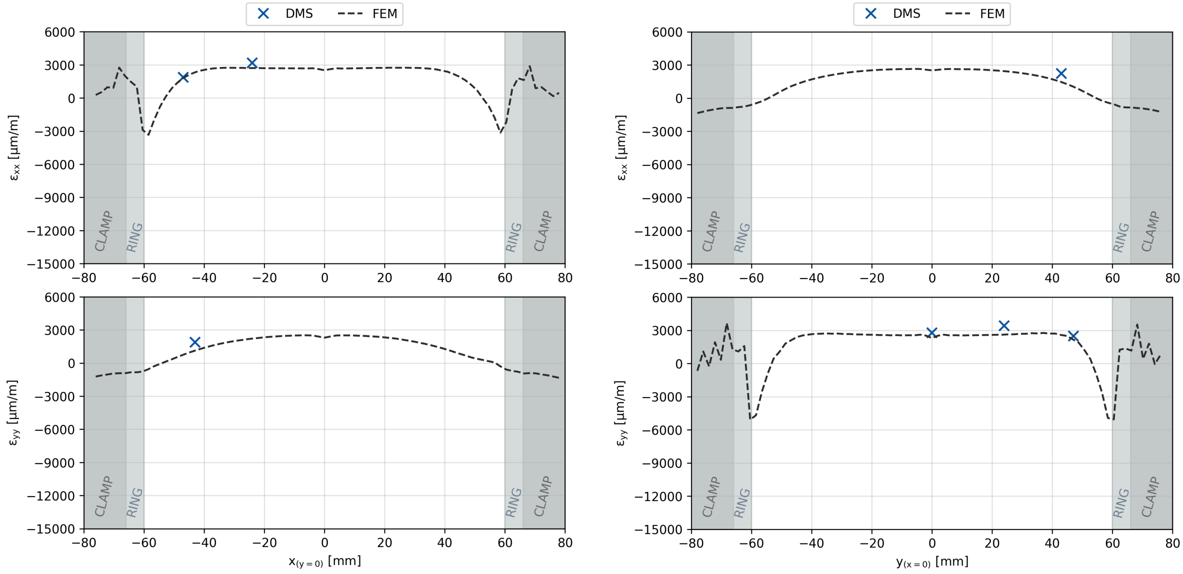

(a) Longitudinal (ϵ_{xx}) and transverse (ϵ_{yy}) in-plane strain components along X-path ($y = 0$)

(b) Longitudinal (ϵ_{xx}) and transverse (ϵ_{yy}) in-plane strain components along Y-path ($x = 0$)

Figure D.3: R-C-CT specimen: Experimental-numerical comparison of the biaxial strain zone, for the outer-most ply, at an applied pressure of 9 [bar]

Mid-plane

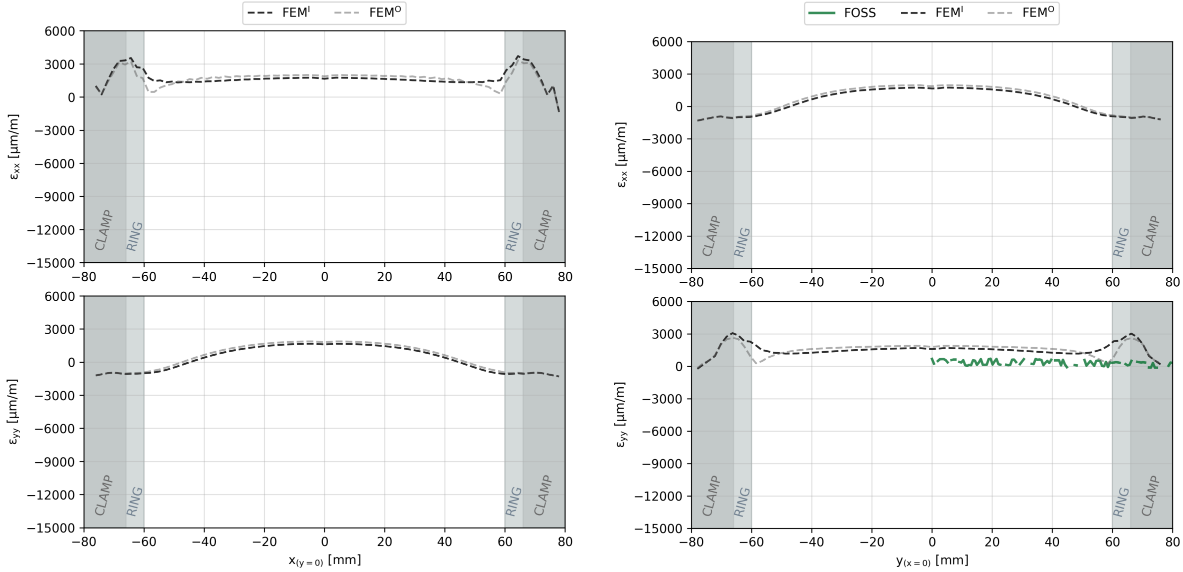

(a) Longitudinal (ϵ_{xx}) and transverse (ϵ_{yy}) in-plane strain components along X-path $(y = 0)$

(b) Longitudinal (ϵ_{xx}) and transverse (ϵ_{yy}) in-plane strain components along Y-path $(x = 0)$

Figure D.4: R-C-CT specimen: Experimental-numerical comparison of the biaxial strain zone, for plys adjacent to the laminate's mid-plane, at an applied pressure of 9 $[\text{bar}]$

D.2. 0D point strain

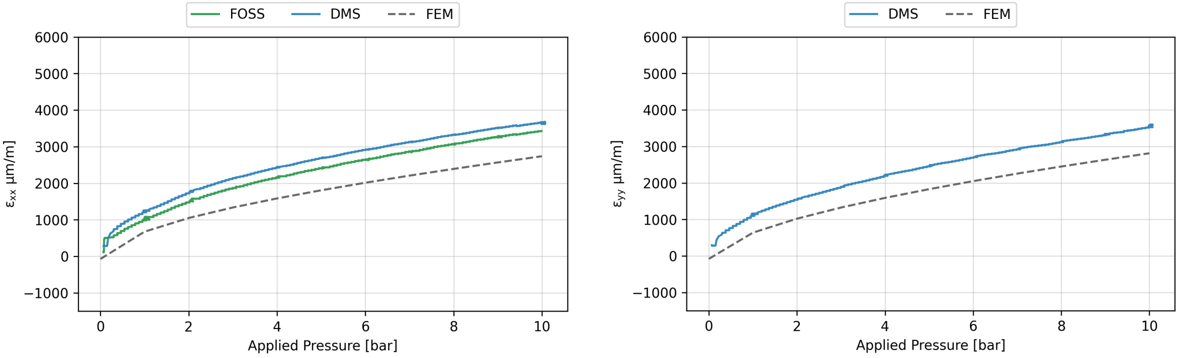

(a) Longitudinal in-plane strain (ϵ_{xx}) at $(x, y) = (5, 0)$ [mm]

(b) Transverse in-plane strain (ϵ_{yy}) at $(x, y) = (0, 0)$ [mm]

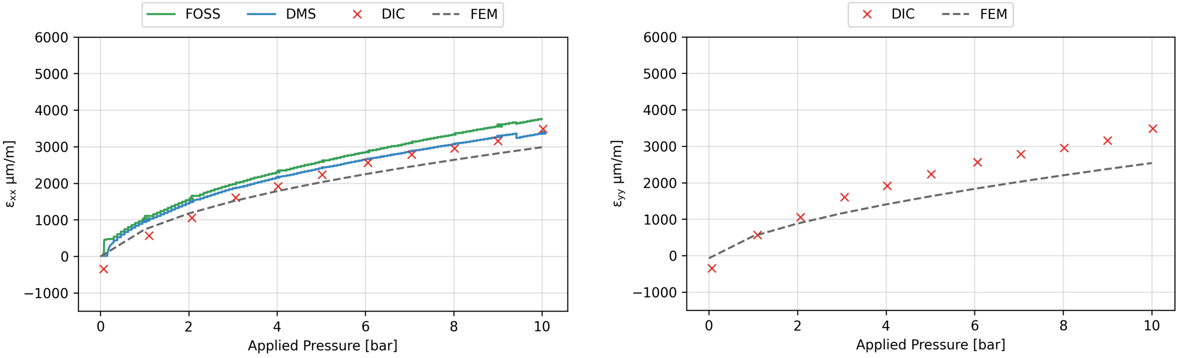

(c) Longitudinal in-plane strain (ϵ_{xx}) at $(x, y) = (23, 0)$ [mm]

(d) Transverse in-plane strain (ϵ_{yy}) at $(x, y) = (0, 24)$ [mm]

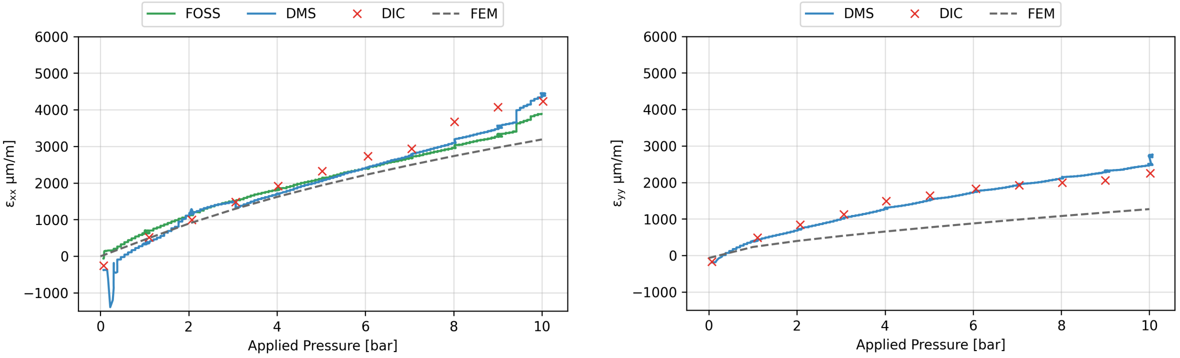

(e) Longitudinal in-plane strain (ϵ_{xx}) at $(x, y) = (47, 0)$ [mm]

(f) Transverse in-plane strain (ϵ_{yy}) at $(x, y) = (0, 43)$ [mm]

Figure D.5: U-F-RT specimen: Progression of strain (DIC, Strain Gauges, FOSS) over pressure, (x, y) coordinates are taken from the centre of the specimen, as shown in Figure 4.1b. The laminate's global coordinates (x, y) are aligned with the local coordinates $(11, 22)$ of the outer-most ply.

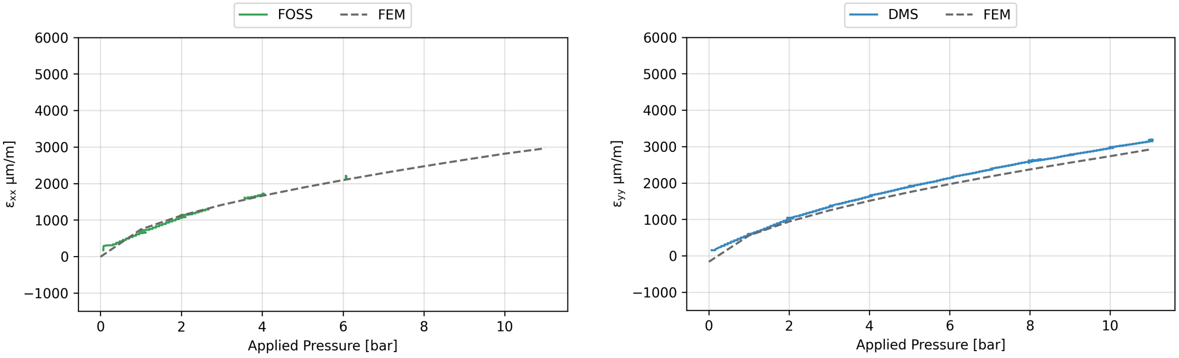

(a) Longitudinal in-plane strain (ϵ_{xx}) at $(x, y) = (5, 0)$ [mm] **(b)** Transverse in-plane strain (ϵ_{yy}) at $(x, y) = (0, 0)$ [mm]

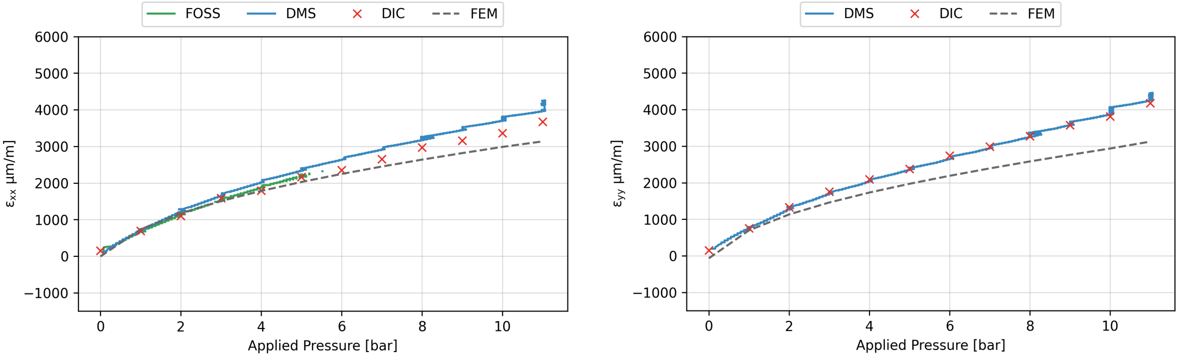

(c) Longitudinal in-plane strain (ϵ_{xx}) at $(x, y) = (23, 0)$ [mm] **(d)** Transverse in-plane strain (ϵ_{yy}) at $(x, y) = (0, 23)$ [mm]

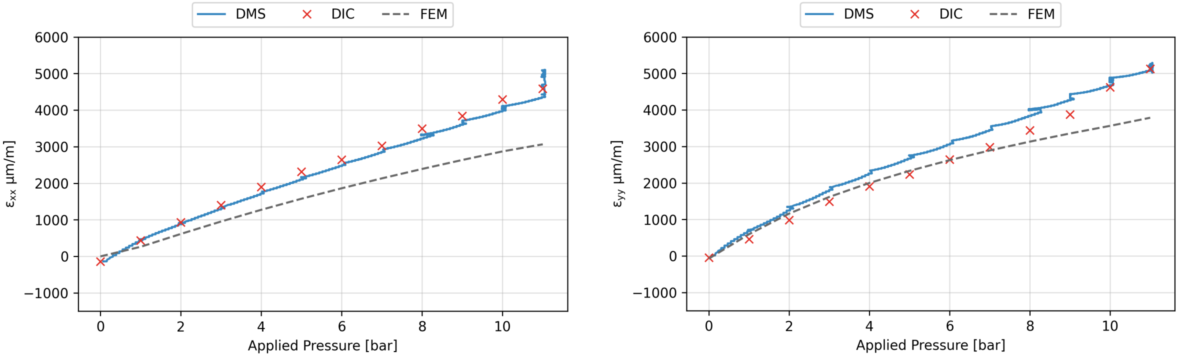

(e) Longitudinal in-plane strain (ϵ_{xx}) at $(x, y) = (47, 0)$ [mm] **(f)** Transverse in-plane strain (ϵ_{yy}) at $(x, y) = (0, 42)$ [mm]

Figure D.6: U-C-RT specimen: Progression of strain (DIC, Strain Gauges, FOSS) over pressure. (x, y) coordinates are taken from the centre of the specimen, as shown in Figure 4.4b. The laminate's global coordinates (x, y) are aligned with the local coordinates $(11, 22)$ of the outer-most ply.

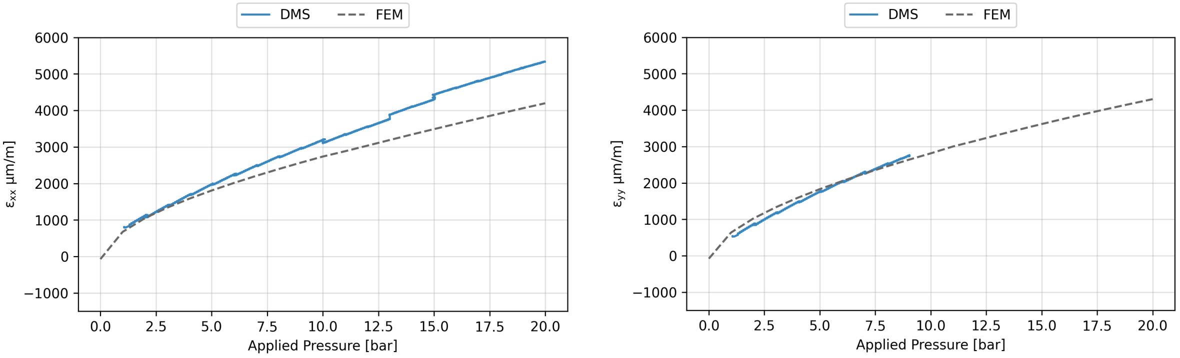

(a) Longitudinal in-plane strain (ϵ_{xx}) at $(x, y) = (-5, 0)$ [mm]

(b) Transverse in-plane strain (ϵ_{yy}) at $(x, y) = (0, 0)$ [mm]

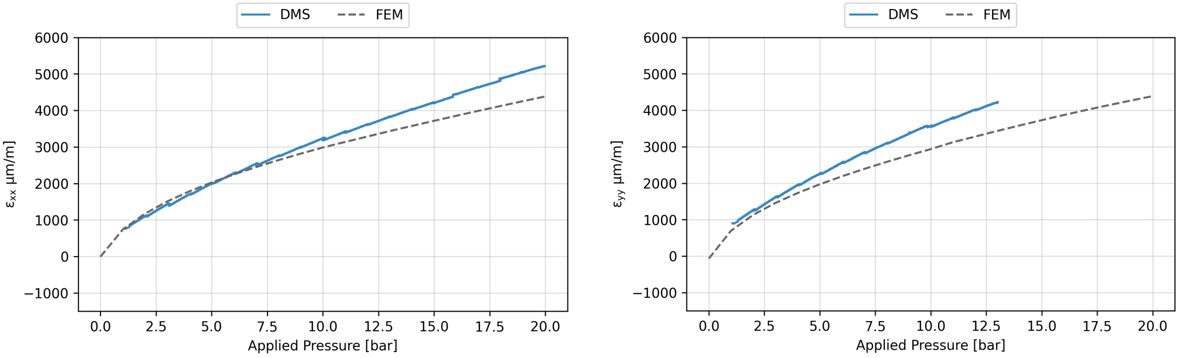

(c) Longitudinal in-plane strain (ϵ_{xx}) at $(x, y) = (-24, 0)$ [mm]

(d) Transverse in-plane strain (ϵ_{yy}) at $(x, y) = (0, 24)$ [mm]

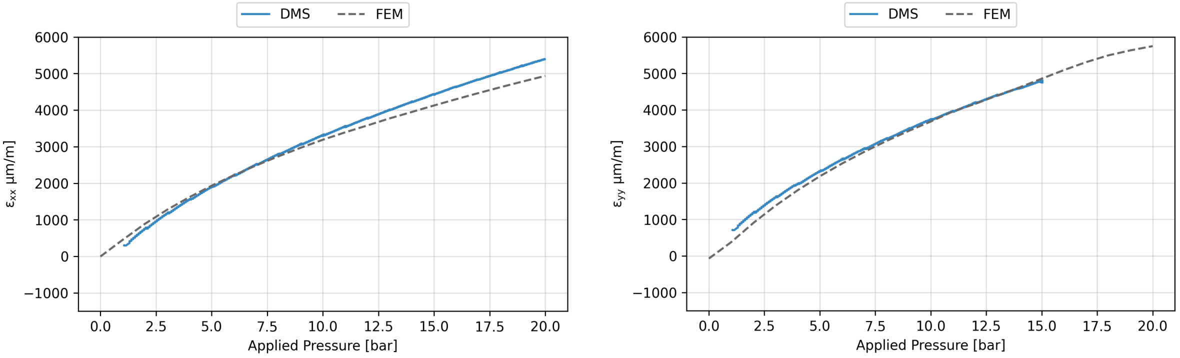

(e) Longitudinal in-plane strain (ϵ_{xx}) at $(x, y) = (-47, 0)$ [mm]

(f) Transverse in-plane strain (ϵ_{yy}) at $(x, y) = (0, 47)$ [mm]

Figure D.7: U-C-CT specimen: Progression of strain (DIC, Strain Gauges, FOSS) over time, for pre-, main and post-test. (x, y) coordinates are taken from the centre of the specimen, as shown in Figure 4.10b. The laminate's global coordinates (x, y) are aligned with the local coordinates $(11, 22)$ of the outer-most ply.

D.3. Damage assessment

D.3.1. Inter-laminar damage: Ultrasound and QDC

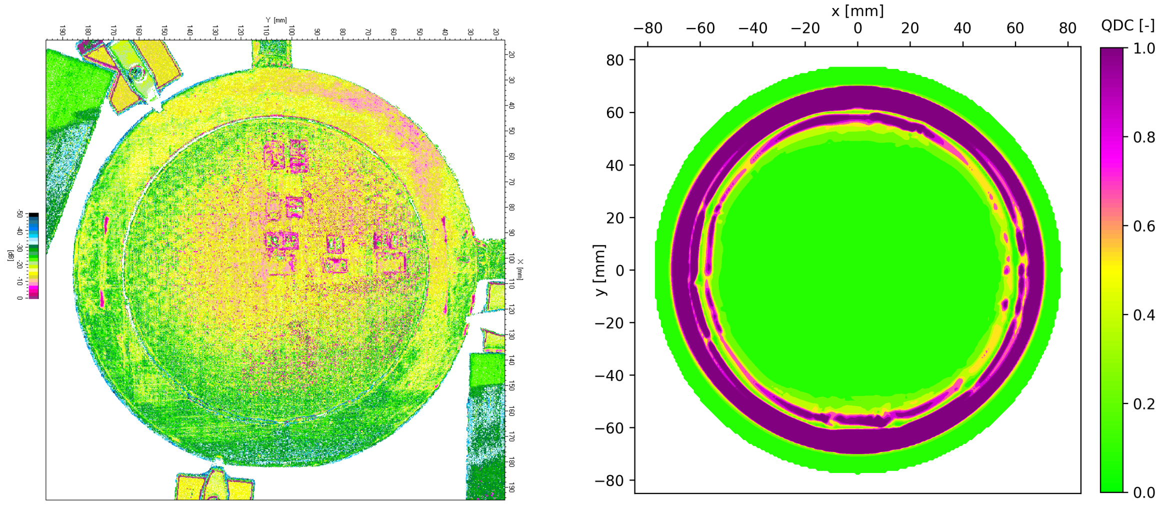

(a) Post-test pulse-echo ultrasound C-Scan at 10 [MHz]

(b) Estimation of delamination onset using the QDC at the applied (maximum) pressure of $(20$ [bar]$)$. The QDC values are shown for the interface between ply 4 and ply 5, which exhibited the largest area of delamination initiation.

Figure D.8: R-C-RT specimen inter-laminar damage

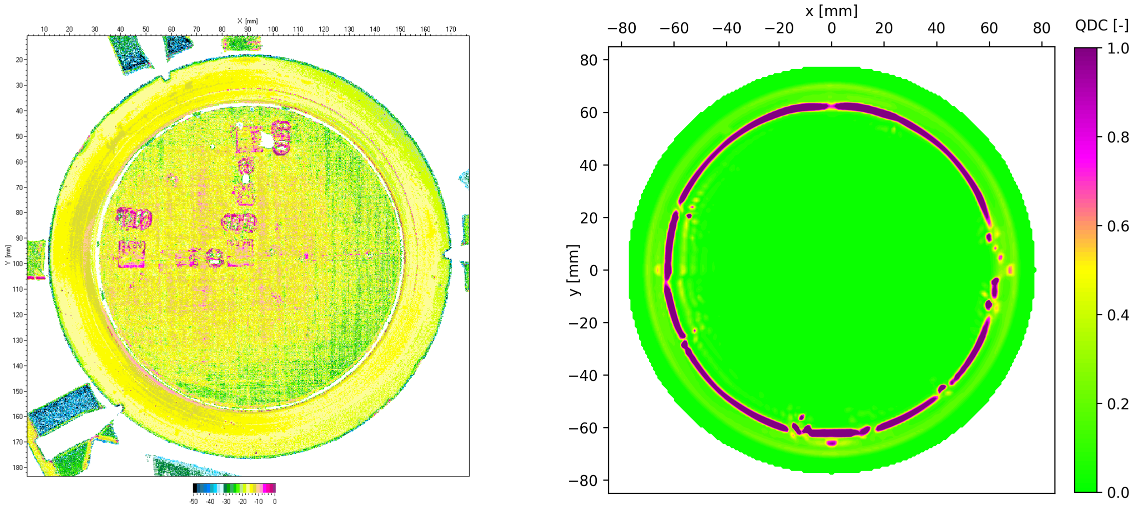

(a) Post-test pulse-echo ultrasound C-Scan at 10 [MHz]

(b) Estimation of delamination onset using the QDC at the applied (maximum) pressure of $(20$ [bar]$)$. The QDC values are shown for the interface between ply 7 and ply 8, which exhibited the largest area of delamination initiation.

Figure D.9: R-C-CT specimen inter-laminar damage

D.3.2. Optical micrograph

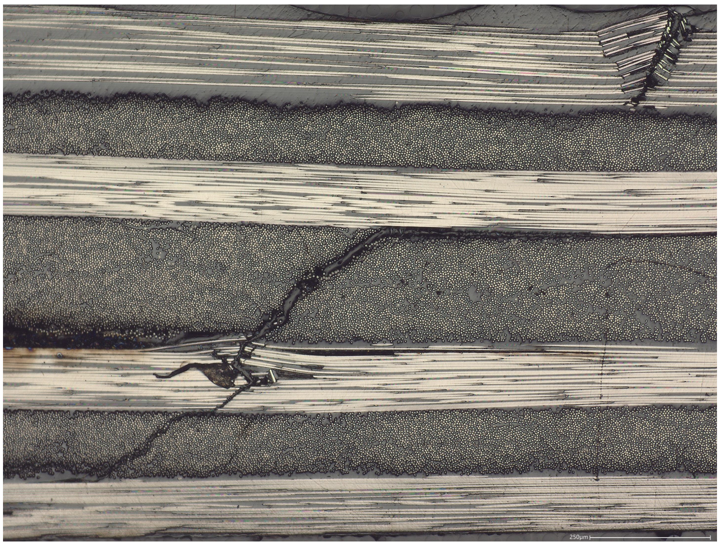

Figure D.10: U-C-RT specimen: optical micro-graphs in the clamping region. Crack propagation is visible. This damage is likely to have led to the leakage observed in section 4.1. Fibre kinking on top most ply at the clamp location. Fibre failure and transverse matrix cracks visible too.

E

Design Study

E.1. Influence of laminate design

In future bulge test campaigns, it may be desirable to test different laminate designs, not just cross-ply laminates. The validated numerical model can provide valuable insights before any physical testing is performed. Specifically, the model can quantify the size of the biaxial zone, which is expected to vary with different laminate designs. This information will help define the region of interest and can guide practical aspects such as sensor placement (e.g., placing strain gauges only where high-quality biaxiality is maintained).

In future test programs, leakage measurements are likely to be conducted on the region of interest, meaning that the remainder of the specimen (outside a $10–20$ $[\mathrm{mm}]$ radius) may be covered with an impermeable foil. It is also important to verify whether different laminates might suffer damage induced by the clamping.

For ease of comparison, 1 $[\mathrm{mm}]$ thick, 8-ply laminates shall be used.

E.1.1. Quasi-isotropic laminate

Motivation

Real-world composite structures should follow the ”10%” rule, to ensure stiffness in the four principle axes ($0,\ \pm45, 90$) to protect against secondary load cases [39]. Therefore, it is likely that future bulge test programs may use QI laminates, that better reflect the laminate designs used in practice. As a starting point, a balanced symmetric QI laminate is simulated.

Results

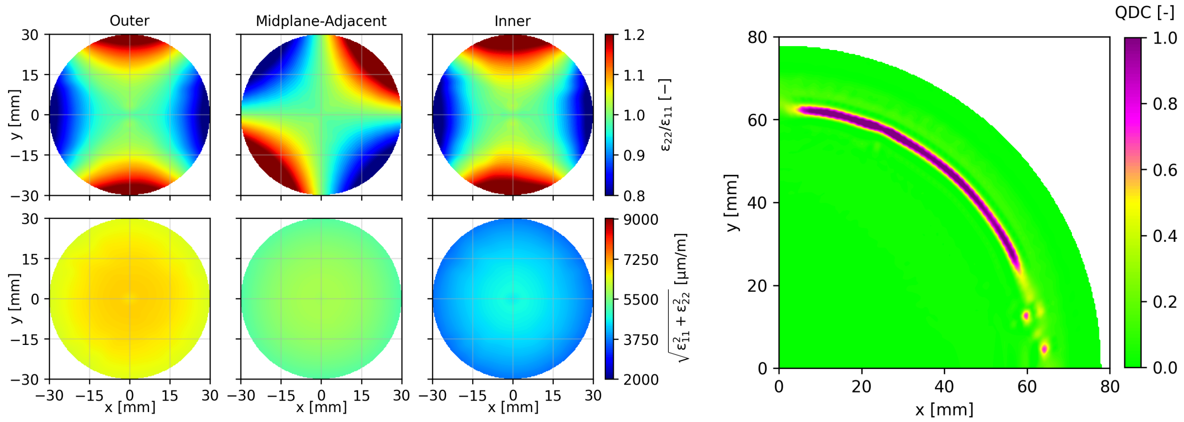

(a) Quantification of strain biaxiality at the centre of the specimen

(b) Maximum delamination (QDC) damage initiation, for interface between ply 7/8

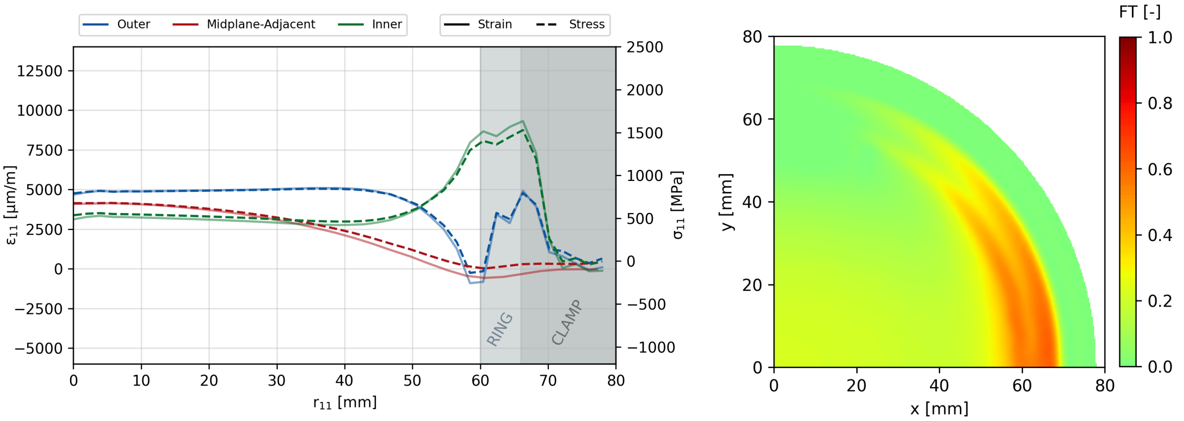

(c) Local longitudinal stress-strain along fibre path

(d) Maximum fibre tensile (FT) damage initiation, for ply 1 (inner ply)

Figure E.1: Strain biaxiality and damage initiation results for a symmetric, balanced quasi-isotropic laminate , at 20 [bar] (CT)

E.1.2. Asymmetric cross-ply laminate

Motivation

The asymmetric cross-ply laminate [0/0/90/90/0/0/90/90] is considered to investigate the effect of membrane-bending coupling under pressure loading. Unlike symmetric laminates, asymmetry can induce bending moments when the specimen is subjected to in-plane loads, potentially affecting the strain distribution and the size of the biaxial zone. Studying this configuration allows assessment of whether such coupling significantly influences the region of interest or damage initiation under the clamping and pressure conditions.

Results

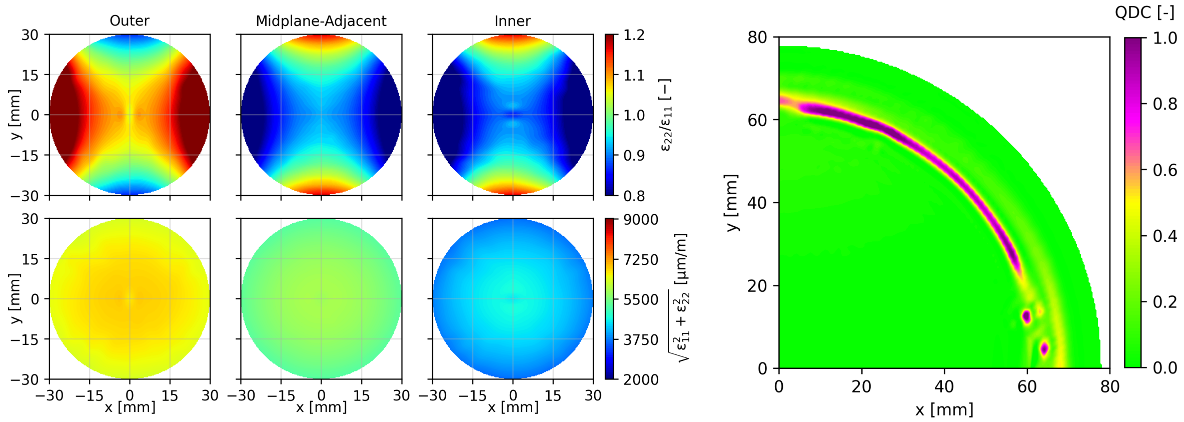

(a) Quantification of strain biaxiality at the centre of the specimen

(b) Maximum delamination (QDC) damage initiation, for interface between ply 7/8

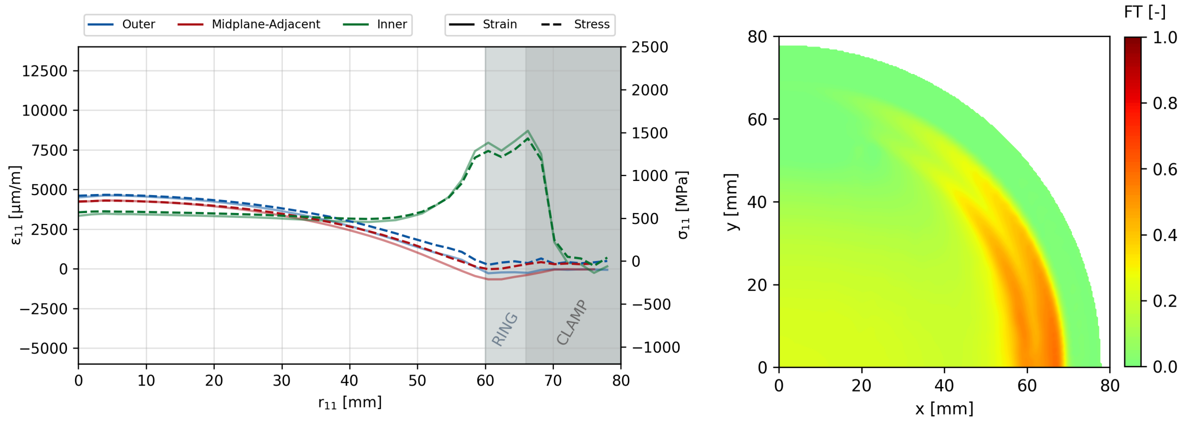

(c) Local longitudinal stress-strain along fibre path

(d) Maximum fibre tensile (FT) damage initiation, for ply 1 (inner ply)

Figure E.2: Strain biaxiality and damage initiation results for an asymmetric cross-ply laminate , at 20 $[\mathrm{bar}]$ (CT)

E.1.3. Highly directional cross-ply laminate

Motivation

The highly directional cross-ply laminate [0/0/0/90/90/0/0/0] is considered to investigate the influence of a predominantly longitudinal fibre direction, with only the mid-plane plies oriented at 90°. This configuration accentuates directional stiffness effects and may lead to localised differences in strain distribution under pressure loading. Studying this laminate helps evaluate the impact of fibre orientation on the biaxial zone and potential damage initiation, particularly in the centre region of interest.

Results

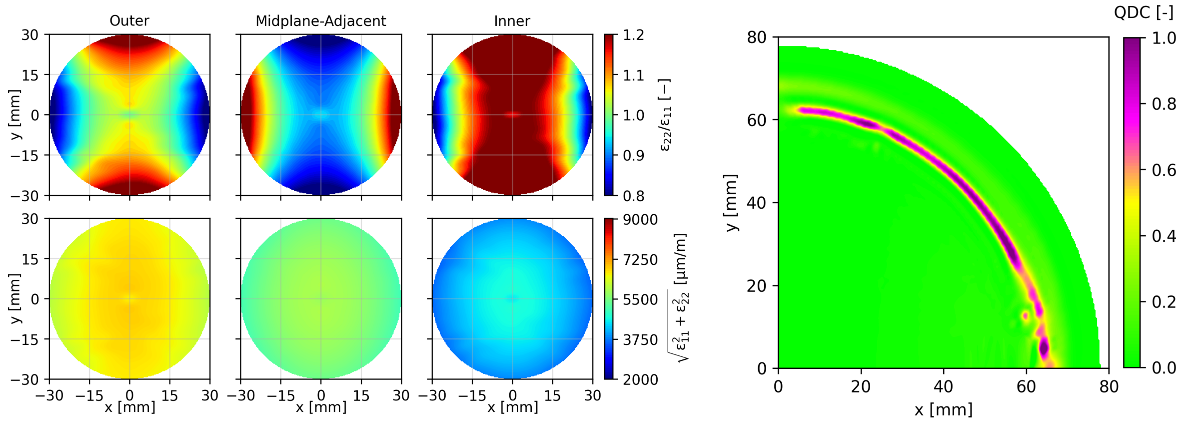

(a) Quantification of strain biaxiality at the centre of the specimen

(b) Maximum delamination (QDC) damage initiation, for interface between ply 7/8

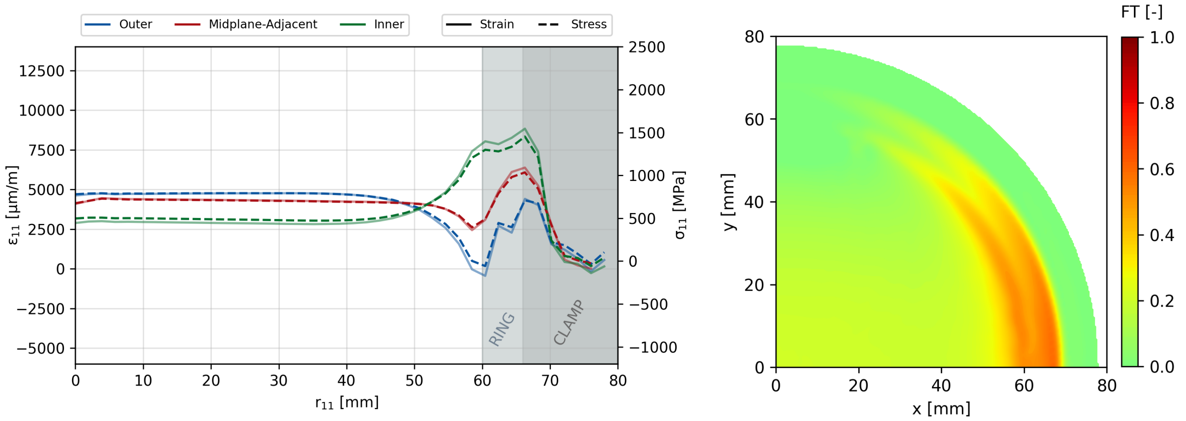

(c) Local longitudinal stress-strain along fibre path

(d) Maximum fibre tensile (FT) damage initiation, for ply 1 (inner ply)

Figure E.3: Strain biaxiality and damage initiation results for a highly directional (non-transversely isotropic), symmetric cross-ply laminate , at 20 [bar] (CT)

Summary of laminate design results

Table E.1: Strain metrics and damage indicators for each laminate design, at 20 [bar] (CT)

Laminate	$\left(\sqrt{\varepsilon_{11}^2+\varepsilon_{22}^2}\right)\Big\rvert_{r\leq 30\,\mathrm{mm}}^{\mathrm{avg}}$ [µm]			FT$_{\max}$ [-]	QDC > 1 [%]
	Outer	Mid.-Adj.	Inner		
$[(0/90)_2]_s$ (Default)	6556	5517	4121	0.621	1.24
$[0/90/45/-45]_s$	6572	5538	4146	0.620	1.71
$[(0)_2/(90)_2]_2$	6583	5552	4170	0.566	0.93
$[(0)_3/90]_s$	6547	5544	4205	0.572	0.75

References

[1] Abaqus. *Abaqus 6.11 Theory Manual*. Dassault Systèmes, 2011.

[2] Abaqus. *Abaqus 6.12 Analysis User's Manual, Volume V: Prescribed Conditions, Constraints and Interactions*. Dassault Systèmes, 2012.

[3] Daniel O. Adams and Daniel F. Adams. *Tabbing Guide for Composite Test Specimens*. Tech. rep. DOT/FAA/AR-02/106. Available from the FAA Office of Aviation Research. Federal Aviation Administration (FAA), Oct. 2002.

[4] Airbus. *ZEROe - Towards the world's first hydrogen-powered commercial aircraft*. `https://www.airbus.com/en/innovation/energy-transition/hydrogen/zeroe`. Accessed: 2024-07-23. 2024.

[5] ASTM International. *ASTM D3039 / D3039M – 14: Standard Test Method for Tensile Properties of Polymer Matrix Composite Materials*. `https://www.astm.org/d3039_d3039m-14.html`. West Conshohocken, PA. 2014.

[6] B+B Thermo-Technik GmbH. *Thermocouple Module THMOD-I2C-800 Datasheet*. 2022. URL: `https://shop.bb-sensors.com/out/media/Datasheet_thermocouple_module_THMOD-I2C-800.pdf`.

[7] Camille Barbier. "Internship Report". In: (Aug. 2024). Embargo date: 2027-08-23.

[8] Vernon T Bechel and Ran Y Kim. "Damage trends in cryogenically cycled carbon/polymer composites". In: *Composites Science and Technology* 64.12 (2004), pp. 1773–1784. ISSN: 0266-3538. DOI: `https://doi.org/10.1016/j.compscitech.2003.12.007`. URL: `https://www.sciencedirect.com/science/article/pii/S0266353804000156`.

[9] John H. Bickford. *An Introduction to the Design and Behavior of Bolted Joints*. 4th ed. CRC Press, 2007.

[10] Richard G. Budynas and J. Keith Nisbett. *Shigley's Mechanical Engineering Design*. 11th ed. McGraw-Hill Education, 2020. ISBN: 9781260573688.

[11] Ioana Ciobotia. "Incorporating Bird Strike Crashworthiness Requirements within an MDO Framework". Embargo date: 2026-01-12. Master's thesis. Delft, Netherlands: Delft University of Technology, Jan. 2024. URL: `http://resolver.tudelft.nl/uuid:d8d7f2a0-d1ba-46b6-affd-c2903a527fc1`.

[12] Joao Diniz. "Internship Report". In: (Feb. 2024). Embargo date: 2027-02-15.

[13] J. Ebadi-Rajoli et al. "Progressive damage modeling of composite materials subjected to mixed mode cyclic loading using cohesive zone model". In: *Mechanics of Materials* 143 (2020), p. 103322. ISSN: 0167-6636. DOI: `https://doi.org/10.1016/j.mechmat.2020.103322`. URL: `https://www.sciencedirect.com/science/article/pii/S0167663619309007`.

[14] Hector Estrada and Stanley S. Smeltzer III. *Design and Development of a Composite Dome for Experimental Characterization of Material Permeability*. Tech. rep. Work of the US Gov. Public Use Permitted. NASA Marshall Space Flight Center, 1999.

[15] European Commission. *Reducing Emissions from Aviation*. Accessed: 2025-02-25. 2025. URL: `https://climate.ec.europa.eu/eu-action/transport/reducing-emissions-aviation_en`.

[16] Manuel Fahjen. "Experimental investigation of the permeability of CFRP as a structural material for liquid hydrogen tanks". Master's thesis. Braunschweig, Germany: Braunschweig University of Technology, June 2024.

[17] Laurent Fouché. *Phonons and Rayleigh Scattering at Cryogenic Temperatures*. Conference presentation at DRTBT 2024, IN2P3, France. Accessed August 2025. June 2024. URL: `https://indico.in2p3.fr/event/30801/contributions/131359/attachments/83971/125137/Phonons_DRTBT2024.pdf`.

[18] Jordan French, Chris Dahlkamp, and Michael Czabaj. “Formation of cryobiaxial-induced damage in tape-laminate composites”. In: *Composite Structures* 235 (Dec. 2019), p. 111816. DOI: `10.1016/j.compstruct.2019.111816`.

[19] Nico Georghe. “A Feasibility Study of Using Inverse Finite Element Methods for Structural Health Monitoring of Offshore Access Systems”. Master’s thesis. Delft, Netherlands: Delft University of Technology, Feb. 2024. URL: `https://resolver.tudelft.nl/uuid:6537af5b-5d5d-4833-9598-b91e9076347a`.

[20] German Aerospace Center (DLR). *Exploration of Electric Aircraft Concepts and Technologies (EXACT)*. `https://www.dlr.de/de/tt/forschung-transfer/projekte/laufende-projekte/exact`. 2024.

[21] K. T. V. Grattan and B. T. Meggitt, eds. *Optical Fiber Sensor Technology: Fundamentals*. New York, NY: Springer, 2000. ISBN: 978-0-7923-7852-5. DOI: `10.1007/978-1-4757-6081-1`. URL: `https://link.springer.com/book/10.1007/978-1-4757-6081-1`.

[22] Ray W. Grenoble and Thomas S. Gates. *Hydrogen Permeability of Polymer Matrix Composites at Cryogenic Temperatures*. Tech. rep. NASA/TM—2005-213693. Accessed May 22, 2025. NASA Langley Research Center, 2005. URL: `https://ntrs.nasa.gov/archive/nasa/casi.ntrs.nasa.gov/20050199401.pdf`.

[23] D.M. Grogan et al. “Damage characterisation of cryogenically cycled carbon fibre/PEEK laminates”. In: *Composites Part A: Applied Science and Manufacturing* 66 (2014), pp. 237–250. ISSN: 1359-835X. DOI: `https://doi.org/10.1016/j.compositesa.2014.08.007`. URL: `https://www.sciencedirect.com/science/article/pii/S1359835X14002401`.

[24] David M. Grogan. “Damage and permeability in linerless composite cryogenic tanks”. PhD thesis. Galway, Ireland: National University of Ireland, Galway, Sept. 2015.

[25] H2FLY. *H2FLY Accelerates Progress Towards Zero-Emission Commercial Flight*. Accessed: 2025-02-25. 2023. URL: `https://www.h2fly.de/2023/04/05/h2fly-accelerates-progress-towards-zero-emission-commercial-flight-3/`.

[26] Hitoshi Hamori et al. “Numerical and experimental evaluation of the formation of leakage paths through CFRP cross-ply laminates with leak barrier layers”. In: *Composite Structures* 230 (Oct. 2019), p. 111530. DOI: `10.1016/j.compstruct.2019.111530`.

[27] Andreas Hauffe. *eLamX^2: expandable Laminate eXplorer – composite laminate analysis software*. Tech. rep. Open source Java application based on Classical Laminate Theory. Chair of Aircraft Engineering, Technische Universität Dresden, 2025. URL: `https://tu-dresden.de/ing/maschinenwesen/ilr/lft/elamx2/elamx`.

[28] Rebekka Hauser. “Experimental investigation of CFRP as a structural material for liquid hydrogen tanks”. Master’s thesis. Braunschweig, Germany: Braunschweig University of Technology, Dec. 2024.

[29] HBM. *Temperaturkompensation bei DMS-Viertelbrücken-Anwendungen*. 2024. URL: `https://www.hbm.com/de/10083/temperaturkompensation-bei-dms-viertelbruecken-anwendungen/`.

[30] J.J.M. van der Helm. “Limiting microcracks and hydrogen permeability in thermoplastic composites for LH2 storage”. Master thesis. MA thesis. Delft University of Technology: Aerospace Engineering, 2024. URL: `http://resolver.tudelft.nl/uuid:40c562f9-6d65-4a84-8bed-498ae828d8dd`.

[31] Thomas Herget. “Internship Report”. In: (Feb. 2025). Embargo date: 2028-02-11.

[32] Hexcel Corporation. *HexPly 8552 Epoxy Matrix Product Data Sheet*. `https://www.hexcel.com/user_area/content_media/raw/HexPly_8552_eu_DataSheet.pdf`. 180°C / 356°F curing matrix. Hexcel Corporation, Mar. 2023. URL: `https://www.hexcel.com/user_area/content_media/raw/HexPly_8552_eu_DataSheet.pdf`.

[33] Jörg Hohe et al. “Performance of fiber reinforced materials under cryogenic conditions—A review”. In: *Composites Part A: Applied Science and Manufacturing* 141 (2021), p. 106226.

[34] Ghalib Ibrahim. “Progressive Damage Modelling of Composite Materials”. PhD thesis. Manchester Metropolitan University, 2020. URL: `https://e-space.mmu.ac.uk/631614/`.

[35] Theodore F. Johnson and Teresa L. O'Neil. "Apparent-Strain Correction for Combined Thermal and Mechanical Testing". In: *Materials in Cryogenic Environments (AIAA SDM-8 Conference)*. Includes correction methods over −450°F to +250°F, with extrapolation approaches. American Institute of Aeronautics and Astronautics. NASA Langley Research Center, Hampton, VA, USA, 2007. DOI: `10.2514/6.2007-2410`.

[36] A. S. Kaddour and M. J. Hinton. "Maturity of 3D failure criteria for fibre-reinforced composites: Comparison between theories and experiments: Part B of WWFE-II". In: *Journal of Composite Materials* 47.6-7 (2013), pp. 925–966.

[37] A. S. Kaddour, M. J. Hinton, and P. D. Soden. *Failure Criteria in Fibre Reinforced Polymer Composites: The World-Wide Failure Exercise*. 1st. Oxford: Elsevier Ltd, 2004.

[38] M. B. Kasen et al. *Mechanical, Electrical, and Thermal Characterization of G-10CR and G-11CR Glass-Cloth/Epoxy Laminates Between Room Temperature and 4 K*. Advances in Cryogenic Engineering 26. National Bureau of Standards (now NIST), 1980, pp. 235–243.

[39] C. Kassapoglou. *Design and Analysis of Composite Structures: With Applications to Aerospace Structures*. Aerospace Series. Wiley, 2011. ISBN: 9781119957065. URL: `https://books.google.nl/books?id=gOXm2HnEzBIC`.

[40] C. Kassapoglou. *Modeling the Effect of Damage in Composite Structures: Simplified Approaches*. Aerospace Series. Wiley, 2015. ISBN: 9781119013211. URL: `https://onlinelibrary.wiley.com/doi/book/10.1002/9781119013228`.

[41] Josef Koord. "Design methodology for highly loaded composite bolted joints with local metal hybridization at low temperature". PhD thesis. Braunschweig, Germany: Braunschweig University of Technology, Sept. 2023.

[42] J. Kosmann et al. "Digital image correlation strain measurement of thick adherend shear test specimen joined with an epoxy film adhesive". In: *International Journal of Adhesion and Adhesives* 90 (2019), pp. 32–37. ISSN: 0143-7496. DOI: `https://doi.org/10.1016/j.ijadhadh.2019.01.024`. URL: `https://www.sciencedirect.com/science/article/pii/S0143749619300247`.

[43] H. Kumazawa and J. Whitcomb. "Numerical modeling of gas leakage through damaged composite laminates". In: *Journal of Composite Materials* 42.16 (2008), pp. 1619–1638. DOI: `10.1177/0021998308092210`.

[44] Hisashi Kumazawa et al. "Modeling of propellant leakage through matrix cracks in composite laminates". In: June 2001, pp. 3–4. DOI: `10.2514/6.2001-1217`.

[45] Mateusz Lentner. "Internship Report". In: (May 2023). Embargo date: 2026-03-13.

[46] Mateusz Lentner. "Numerical analysis of multiaxial test setup for composite cryogenic hydrogen tank development". Master's thesis. Delft, Netherlands: Delft University of Technology, Feb. 2024. URL: `http://resolver.tudelft.nl/uuid:d8d7f2a0-d1ba-46b6-affd-c2903a527fc1`.

[47] Luna Innovations Incorporated. *ODiSI 6100 User's Guide*. ODiSI 6000 Series User Documentation. Blacksburg, VA, USA, 2018. URL: `https://www.lunainc.com/sites/default/files/assets/files/resource-library/ODiSI%206100%20User%20Guide.pdf`.

[48] MakeItFrom.com. *AISI 304 (S30400) Stainless Steel*. `https://www.makeitfrom.com/material-properties/AISI-304-S30400-Stainless-Steel`. Accessed: 2025-07-24. 2017.

[49] Avyadhish Malladi. "Numerical Modelling of Skin-Stringer Separation in Thermoplastic Composite Stiffened Panels". Master's thesis. Faculty of Aerospace Engineering, 2024. URL: `https://repository.tudelft.nl/record/uuid:d217b773-e8c7-4f42-8d10-64bbc4ed9a63`.

[50] Kathrin Marquardt et al. "A novel interferometric dilatometer in the 4–300 K temperature range". In: *Measurement Science and Technology* 24.10 (2013). Data on thermal expansion of SS-304 sample at cryogenic temperatures 4–300 K, p. 105203. DOI: `10.1088/0957-0233/24/10/105203`.

[51] Tommaso Mazzanti. "Internship Report". In: (Nov. 2023). Embargo date: 2026-11-07.

[52] Micro-Measurements (Vishay Measurements Group). *Strain Gage Thermal Output and Gage Factor Variation with Temperature (Tech Note TN-504-1)*. Tech. rep. Tech Note TN-504-1. Vishay Measurements Group / Micro-Measurements, 1989. URL: `https://intertechnology.com/Vishay/pdfs/TechNotes_TechTips/TN-504.pdf`.

[53] MicroMeasurements / Vishay Intertechnology. *Strain Gage Selection: Criteria, Procedures, Recommendations (Tech Note TN□505□4)*. Tech. rep. TN□505□4. Tech Note in the “TechNotes& TechTips” series by Vishay Intertechnology. MicroMeasurements (Vishay Intertechnology), 2013. URL: https://intertechnology.com/Vishay/pdfs/TechNotes_TechTips/TN-505.pdf.

[54] Shraeya Mithal and Dan Rutherford. “ICAO’s 2050 net-zero CO”. In: *POLICY* (2023).

[55] MTU Aero Engines. *Flying Fuel Cell – The Hydrogen-Powered Future of Aviation*. Accessed: 2025-02-25. 2025. URL: https://www.mtu.de/de/technologie/clean-air-engine/flying-fuel-cell/.

[56] National Institute of Standards and Technology (NIST). *G□10 CR Fiberglass Epoxy – Cryogenic Material Properties Database*. Accessed July 16, 2025. 2025. URL: %5Curl%7Bhttps://trc.nist.gov/cryogenics/materials/G-10%20CR%20Fiberglass%20Epoxy/G10CRFiberglassEpoxy_rev.htm%7D.

[57] Netherlands Aerospace Centre (NLR). *Case: Liquid Hydrogen Composite Tanks for Civil Aviation*. Accessed: 2025-02-25. 2025. URL: https://www.nlr.org/case/case-liquid-hydrogen-composite-tanks-for-civil-aviation/.

[58] Dick Ng and John H. S. Lee. “Comments on explosion problems for hydrogen safety”. In: *Journal of Loss Prevention in the Process Industries* 21.2 (2008), pp. 136–146.

[59] Nickel Institute. *36% Nickel–Iron Alloy for Low Temperature Service (INCO No. 410)*. Technical Report. Republished from the 1976 INCO handbook. Nickel Institute, 2020. URL: https://nickelinstitute.org/media/4687/ni_inco_410_nickelironalloy.pdf.

[60] Mindy Niedermeyer and R. G. Clinton Jr. “X-33 LH2 tank failure investigation findings”. In: *Aerospace Materials, Processes and Environmental Technology*. 2000.

[61] Stanley T. Oliver. “Analysis of a Circular Composite Disk Subjected to Edge Rotations and Hydrostatic Pressure”. Master’s thesis. Hustsville, USA: The University of Alabama in Huntsville, 2004.

[62] Florian Pape. “Localisation of cracks in structural bonded joints using fibre optic sensors”. Bachelor’s thesis. Braunschweig, Germany: FH Aachen University of Applied Sciences, Jan. 2025.

[63] Yu. P. Perelygin and D. V. El’chenko. “Electrodeposition of chromium□indium alloys”. In: *Zhurnal Prikladnoj Khimii (Journal of Applied Chemistry, USSR/USA translation)* 64.2 (Feb. 1991). Translated by USINT, originally published in USSR.

[64] Pfeiffer Vacuum GmbH. *Leak Detection Compendium*. 2014.

[65] Silvestre Pinho et al. “Material and Structural Response of Polymer-Matrix Fibre-Reinforced Composites”. In: *Journal of Composite Materials* 46.19-20 (Sept. 2012), pp. 2313–2341. DOI: 10.1177/0021998312454478.

[66] Y. Qiu et al. “Research Progress of Cryogenic Materials for Storage and Transportation of Liquid Hydrogen”. In: *Metals* 11 (2021), p. 1234. DOI: 10.3390/met11091234.

[67] Leonardo Raffaelli. “Thermomechanics of Fibre Reinforced Epoxies for Cryogenic Pressurized Containment”. PhD thesis. Munich, Germany: Munich University of Technology, May 2006.

[68] Carolin Rauh, Thomas Reimer, and Jascha Wilken. “Leakage Investigation of Epoxy-Based Composite Laminates for Reusable Cryogenic Propellant Tanks”. In: *AIAA SciTech Forum*. Accessed May 22, 2025. German Aerospace Center (DLR). 2023. URL: https://elib.dlr.de/187090/.

[69] R. P. Reed et al. “Tensile Strength and Ductility of Indium”. In: *Materials Science and Engineering: A* 102 (1988), pp. 227–236. DOI: 10.1016/0025-5416(88)90229-3.

[70] Samit Roy and Michael Benjamin. “Modeling of permeation and damage in graphite/epoxy laminates for cryogenic fuel storage”. In: *Composites Science and Technology* 64 (Oct. 2004), pp. 2051–2065. DOI: 10.1016/j.compscitech.2004.02.014.

[71] Michael Scheerer et al. “Analyses and Testing of the Thermo□Mechanical Behaviour of Cryogenic Composite Propellant Feed Lines”. In: *13th European Conference on Spacecraft Structures, Materials & Environmental Testing*. Conference paper, Bibcode: 2014ESASP.727E.124S. ESA/ESTEC, Noordwijk, The Netherlands, 2014.

[72] Daniel Schultheiß. “Permeation Barrier for Lightweight Liquid Hydrogen Tanks”. PhD thesis. Augburg, Germany: University of Ausburg, Apr. 2007.

[73] C. Y. Shih and D. A. Rigney. “Sliding friction and wear of tin-, indium- and lead-coated 52100 steel”. In: *Wear* 134 (1989), pp. 165–184.

[74] Y. Shindo et al. “Cryomechanics and Short□Beam Interlaminar Shear Strength of G□10CR Glass-Cloth/Epoxy Laminates”. In: *Advances in Cryogenic Engineering Materials*. Ed. by U. B. Balachandran et al. Vol. 44. Springer, Boston, MA, 2000, pp. 167–174. DOI: 10.1007/978-1-4615-9056-6_22.

[75] International Digital Image Correlation Society, E. M. C. Jones, and M. A. (Eds.) Iadicola. *A Good Practices Guide for Digital Image Correlation*. Tech. rep. Electronic Version (V5g, 22-October-2018). International Digital Image Correlation Society (iDICs), 2018. DOI: 10.32720/idics/gpg.ed1. URL: https://doi.org/10.32720/idics/gpg.ed1.

[76] Eric Qiuli Sun. *Shear Locking and Hourglassing in MSC Nastran, ABAQUS, and ANSYS*. Tech. rep. Accessed via internal technical report; publication date not specified. Thomas Jefferson National Accelerator Facility (Jefferson Lab), 2006.

[77] Technia. *What are the key considerations for surface-to-surface contact?* 2023. URL: https://www.technia.com/en/faqs/what-are-the-key-considerations-for-surface-to-surface-contact/.

[78] The Engineering ToolBox. *Bolt Torque Calculator: Loads & Preloads Data and Calculator*. Accessed: 2025-07-22. 2018. URL: https://www.engineeringtoolbox.com/bolt-torque-load-calculator-d_2065.html.

[79] Thermophysical Properties of Matter Database (TPMD). *6061-T6 Aluminum*. https://trc.nist.gov/cryogenics/materials/6061%20Aluminum/6061_T6Aluminum_rev.htm. Accessed: 2025-07-26. 2011.

[80] John F Timmerman et al. “Matrix and fiber influences on the cryogenic microcracking of carbon fiber/epoxy composites”. In: *Composites Part A: Applied Science and Manufacturing* 33.3 (2002), pp. 323–329. ISSN: 1359-835X. DOI: https://doi.org/10.1016/S1359-835X(01)00126-9. URL: https://www.sciencedirect.com/science/article/pii/S1359835X01001269.

[81] U.S. Nuclear Regulatory Commission. *EMC^2 Crack Growth Modeling XFEM Experience: ABAQUS*. Technical Report ML24198A091. Accessed: 2025-07-20. U.S. Nuclear Regulatory Commission, 2024. URL: https://www.nrc.gov/docs/ML2419/ML24198A091.pdf.

[82] Oliver Völkerink. “Simulation-driven design of bonded joints in fibre composite aircraft structures using progressive damage analyses”. PhD thesis. Braunschweig, Germany: Braunschweig University of Technology, Mar. 2022.

[83] Robert Wagner, Dietmar Klingbeil, and Claus Berger. “Fracture Mechanical Characterization of AISI 304 and 316L at Cryogenic Temperatures”. In: *AIP Conference Proceedings*. Vol. 1219. 1. AIP Publishing, 2009, pp. 33–40. DOI: 10.1063/1.3295240. URL: https://pubs.aip.org/aip/acp/article/1219/1/33/1007956/Fracture-Mechanical-Characterization-of-AISI-304.

[84] M. et al. Wiedemann. *Innovation Report 2022*. Braunschweig: Institute of Lightweight Systems, German Aerospace Centre (DLR), 2022.

[85] M. et al. Wiedemann. *Innovation Report 2024*. Braunschweig: Institute of Lightweight Systems, German Aerospace Centre (DLR), 2024.

[86] Donald W. Wisander. *Lead, Indium, and Tin as Potential Lubricants in Liquid Hydrogen*. NASA Technical Note NASA TN□D□6455 (E□5880). National Aeronautics and Space Administration, Lewis Research Center, Aug. 1971. URL: https://ntrs.nasa.gov/citations/19710022717.

[87] Marina Wolff and Markus Quadt. “Maturation of selected and promising CFRP-technologies for bare tanks and structures of a representative future launcher upper stage demonstrator”. In: *European Conference on Spacecraft Structures Materials and Environmental Testing*. Vol. 103. 2023.

[88] T. Yokozeki et al. “Experimental evaluation of gas permeability through damaged composite laminates for cryogenic tank”. In: *Composites Science and Technology* 69.9 (2009). Special Issue on the 12th European Conference on Composite Materials (ECCM12), organized by the European Society for Composite Materials (ESCM), pp. 1334–1340. ISSN: 0266-3538. DOI: `https://doi.org/10.1016/j.compscitech.2008.05.019`. URL: `https://www.sciencedirect.com/science/article/pii/S026635380800211X`.

[89] Tomohiro Yokozeki, Toshio Ogasawara, and Takashi Ishikawa. “Evaluation of gas leakage through composite laminates with multilayer matrix cracks: Cracking angle effects”. In: *Composites Science and Technology* 66.15 (2006), pp. 2815–2824. ISSN: 0266-3538. DOI: `https://doi.org/10.1016/j.compscitech.2006.02.024`. URL: `https://www.sciencedirect.com/science/article/pii/S0266353806000832`.

[90] Sergei Zimbelmann. “Development of a test concept for determining the permeability of CFRP test specimens at cryogenic temperatures”. Master’s thesis. Stade, Germany: Hamburg University of Applied Sciences, Sept. 2022.